High-Power Induction Motor Drives: Configurations, PWM Techniques and Control Methodologies

SHAYAK CHAUDHURI



DEPARTMENT OF ELECTRICAL ENGINEERING
INDIAN INSTITUTE OF TECHNOLOGY, DELHI

APRIL 2026

© Indian Institute of Technology Delhi (IITD), New Delhi, 2026

High-Power Induction Motor Drives: Configurations, PWM Techniques and Control Methodologies

by

Shayak Chaudhuri

DEPARTMENT OF ELECTRICAL ENGINEERING

Submitted

in fulfilment of the requirements of the Degree of

Doctor of Philosophy

to the



INDIAN INSTITUTE OF TECHNOLOGY DELHI

APRIL 2026

Certificate

It is certified that the thesis entitled "**High-Power Induction Motor Drives: Configurations, PWM Techniques and Control Methodologies**" being submitted by **Mr. Shayak Chaudhuri** for award of the degree of **Doctor of Philosophy** in the Department of Electrical Engineering, Indian Institute of Technology Delhi, is a record of the work carried out by him under our supervision and guidance. The matter embodied in this thesis has not been submitted for award of any other degree or diploma. This work was done wholly or mainly while in candidature for a research degree at IIT, Delhi.

Date:

Prof. Amit Kumar Jain
Thesis supervisor
Department of Electrical Engineering
Indian Institute of Technology Delhi,
Hauz Khas, New Delhi-110016, India

Date:

Prof. Avanish Tripathi
Thesis supervisor
Department of Energy Science and Engineering
Indian Institute of Technology Delhi,
Hauz Khas, New Delhi-110016, India

Acknowledgements

Ph.D is a commitment and the list of people who impact this journey seems almost endless. However, I will try my best to name all those who has helped me in my journey of research.

I bow my head in gratitude to Lord *Radhramanlal* for giving me the strength and love in life.

I would like to convey my deep gratitude to my supervisors, **Prof. Amit Kumar Jain** and **Prof. Avanish Tripathi** for their continuous guidance and help during the course of my research work. The rich technical discussions with them have given the final shape of my thesis in its present form. Apart from technical and professional discussions, both of them have guided me in my personal life with their words of wisdom.

I would like to thank the members of my doctoral research review committee, **Prof. M Veerachary, Prof. Shubhendu Bhasin** and **Prof. Sumit Chattopadhyay** for their invaluable suggestions during the progress review sessions. I am equally grateful to various faculty members from the Machine Drives and Power electronics Group in the Electrical Engineering Department, IIT Delhi, namely **Prof. Bhim Singh, Prof. Anandarup Das, Prof. Sumit Pramanick, Prof Soumya Subhra Nag** and **Prof. Sheryam Sinha**. My research was greatly enriched by attending the courses on Power Electronics, Digital Control and Wireless Power Transfer taught by Prof. Das, Prof. Paramnick and Prof. Sinha respectively.

I will be completely failing in my duty as a student if I do not acknowledge the impact, that professors from Electrical Engineering Department, IIT Kharagapur, had on my journey as power electronics engineer. Two names, which have deeply impacted my life, are **Prof. Souvik Chattopadhayay** and **Prof. Gautam Poddar**. I had the honour of doing my M.Tech thesis under the supervision of Prof. Chattopadhayay. It is during that one year in his lab, that I learnt how to design, build and develop power converters. I have no hesitation in admitting that whatever I know in power electronics even now, it is mostly from Prof. Chattopadhayay. Prof. Poddar taught me a course on Electric Machine Drives and laid the foundation of my interest in the area. He is simply one of the best minds in the area I have come across. The clarity he possesses on the intricacies of the subject and his willing to share the same with his students is something I aspire to gain sometime in my life. Other professors like **Prof. Debprasad Kastha, Prof. Chandan Chakraborty, Prof Suman Maiti, Prof. Tanmoy Bhattacharya** also had profound impact on

my research journey. I am also extremely grateful to **Prof. Shiladri Chakroborty** from Electrical engineering Department, IIT Bombay who was my senior in my lab in IIT Kharagpur. I still remember the enriching late-night technical discussions I had with him.

Personal friendships are equally important along with professional collaborations. I am extremely lucky to have some amazing colleagues in my lab, with whom I not only had some great and lively technical discussions but also personal relationship. I am thankful to **Mr. Sumit Singh, Mr. Shashank Parrikar, Mr. Ashish Panda, Mr. Vaibhav Bharadwaj and Ms Keerthi R Gopan**. I worked closely with all of them during my course of PhD. I would also like to thank my seniors **Dr. Khushboo Kumari, Dr. Chestha Jain, Dr. Apurva Verma, Dr. Nidhi Bisht, Dr. Navneet Vaishnav**, **Dr. Himanshu Swami** and **Mr. Sagar Gupta** for their continuous support. I extend my best wishes to my juniors, **Mr. Indrasis Roy, Mr. Surajit Saha, Ms. Saumya Tripathi** and **Mr. Abhishek Shaw**.

Ph.D is a journey of ups and downs. And all impact of the downs faced by me during this journey was equally shared by two people in my life. They are my sister **Mrs Pritha Chaudhuri** and my friend **Mr. Rohit Kumar**. I have no words to thank them enough for keeping me motivated when I was at my lowest. They dealt with my anger and frustration during challenging times and kept reminding me the purpose with which I started my PhD. A third name that adds to this list, is my brother in-law **Mr. Sudeepta Bhadra** who was also there with me at every step of this journey.

My parents, **Late Ranajit Chaudhuri** and **Late Maya Chaudhuri** were always there with me in spirit. They provided me all the support, financial and emotional, even if they were not present with me physically. The values that they had taught me in life continues to shape my life long after they are gone.

Finally, I have no qualms to admit that I could finish this PhD journey only because I could find my spiritual self as a servant at the lotus feet of **Shri Radharaman Lal**. I am forever in gratitude to my *Guru* **Vaishanavacharya Shri Chandan Goswami** and my *Guruma* **Shrimati Radhika Goswami** for being beacons of guidance in my spiritual life.

SHAYAK CHAUDHURI

Abstract

This thesis deals with addressing various challenges associated with induction motor (IM) drives used for high-power applications like railway traction, industrial fans, pumps and blowers. Squirrel-cage induction motors are generally used in these applications because of their rugged and robust structure. Power rating of these motors varies from few hundreds of kilowatts (≈500 kW) to a couple of megawatts (≈2-3 MW). Voltage rating of these motors varies in the range of 2-5 kV. Insulated gate bipolar transistor (IGBT) based two-level voltage source inverters (2L-VSI) are most popularly used to drive these medium-voltage, high-power motors. Rotor-flux oriented vector control is generally employed to ensure satisfactory dynamic performance of the drive. Such systems suffer from various challenges. In a 2L-VSI, each IGBT blocks the complete DC-link voltage in off state. Thus, voltage rating of these devices should be rated at 4.5 kV or higher. Semiconductor devices with such high-voltage blocking capabilities exhibit compromised switching characteristics both in terms of switching speed and switching energy losses. Thus, the switching frequency (f_{sw}) of these power converters is generally limited to the range of few hundred Hertz (≈ 500-750 Hz). Limited f_{sw} affects both the harmonic and dynamic performance of the drive under closed-loop control. Synchronous pulse-width modulation (PWM) techniques are generally employed in order to ensure satisfactory harmonic performance. Here, the number of switching pulses in the inverter pole-voltages in one fundamental cycle is kept constant. This is also referred to as the pulse number, P. As the modulation frequency of the drive, f_m, increases with the speed of the motor, P is sequentially reduced in order to maintain f_{sw} under the prescribed limits.

Synchronous sine-triangle (SST) PWM is popular among the other synchronous PWM techniques because of simplicity of implementation. For SST PWM scheme, P can also be defined as the ratio of carrier-frequency, f_c and f_m ($P = \frac{f_c}{f_m}$). P is restricted to be only odd-triplen integers, e.g. 21,15,9,3 in case of SST PWM. Thus, beyond $P = 9$, the harmonic performance of SST PWM degrades considerably. This thesis proposes a hybrid synchronous PWM technique which is a combination of synchronous sine-triangle (SST) PWM and synchronous optimal (SO) PWM for SCIM drives. For higher values of P (e.g. $P = 21, 15, 9$), SST PWM scheme is employed. At $P = 9$, the proposed scheme shifts from SST to SO PWM. Odd non-triplen values, such as $P = 7, 5$ are also incorporated in the proposed PWM scheme using SO PWM. SO PWM suffers from the drawback of increased burden on the memory allocation of the digital control platform as optimal switching angles

are required to be stored in a look-up table as a function of modulation index. This thesis proposes a method to implement the PWM scheme without using any look-up table.

Another challenge faced by these drives, under closed-loop operation, comes due to the transition in pulse-pattern applied by the 2L-VSI to the motor as the value of P changes. Such a transition, if done in an unconstrained manner, can lead to huge transients in the line current and electromagnetic torque developed. This thesis proposes a pulse-pattern transition strategy to ensure minimum transient in the line current. The strategy is based on matching the instantaneous stator-flux trajectory for the outgoing and incoming pulse patterns.

Further, this thesis proposes a modified railway traction drive based on open-end winding induction motor (OWIM) drive which consists of two 2L-VSIs feeding power from both the ends of the stator winding of the IM drive. Railway traction drive consists of two single-phase active front-end converters (AFEC) where the AC side is connected to the two secondary windings of a three-winding transformer. Thus, two isolated DC sources are formed which makes OWIM drive very suitable for this application. A SST PWM scheme is proposed for this drive which incorporates even triplen ($P = 6, 12..$) and odd non-triplen integers ($P = 5, 7..$) along with odd triplen integers ($P = 3, 9..$) as pulse numbers. With the introduction of intermediate values of pulse numbers, large change in f_c is restricted as the value of P changes. A double-fourier series (DFS) based mathematical framework has been developed to predict the harmonic profile for the proposed PWM scheme. Further analyses, such as stator-flux trajectory based analysis, fourier-series based analysis are also done in order to establish the harmonic performance of the proposed PWM scheme.

Following this, another SST PWM scheme for OWIM drive is proposed in this thesis where dissimilar carrier signals are used for the two VSIs in the OWIM drive. Only triplen values (odd and even) of P are considered in the proposed PWM scheme. The value of P corresponding to the two VSIs, P_1, P_2, may not remain equal unlike in the conventional drive. The effective pulse number of the drive, $\overline{P}$, is taken to be the average of P_1 and P_2. When $\overline{P}$ takes odd-triplen values, P_1 and P_2 are kept equal. However, a phase-shift is introduced between the two carrier signals. On the other hand, for even triplen values of $\overline{P}$, P_1 and P_2 take different values. P_1 is kept as the odd-triplen number higher than $\overline{P}$ and P_2 is kept lower than $\overline{P}$. For example, for $\overline{P} = 6$, P_1 is kept at 9 and P_2 is kept at 3. Through extensive mathematical analysis based on double fourier series, simulation and experimental validations, it

is shown that the proposed PWM scheme exhibits improved harmonic performance than the conventional scheme.

Another challenge faced by high-power IM drives in terms of control techniques is the performance of speed-sensorless control algorithms specially in the low-speed operating region. This thesis considers a multi-induction motor drive system (MMDS) wherein two or more Y-connected SCIMs are coupled together on the same shaft driving a common load. The load under consideration has a specific torque-speed characteristics wherein the torque-demand from the drive increases with increases in speed, like industrial fans, blowers and pumps. For a MMDS driving such a load, atleast one of the motor need not produce any torque at low speed. It may just rotate and maintain its rated flux. It is established in this thesis that a PLL designed used the stator-current of the zero torque producing motor gives accurate information about the rotor-speed of the MMDS even at very low speed.

Performance of the proposed PWM techniques and control algorithms has been validated on simulation using MATLAB/Simulink and then verified experimentally on lower power laboratory set-up. Relevant simulation and experimental results establish the improved performance of the propositions over the conventional methods.

सार (Abstract)

यह शोधप्रबंध उच्च-शक्ति अनुप्रयोगों जैसे रेलवे ट्रैक्शन, औद्योगिक पंखे, पंप और ब्लोअर्स में प्रयुक्त इंडक्शन मोटर (IM) ड्राइव से संबंधित विभिन्न चुनौतियों के समाधान पर केंद्रित है। इन अनुप्रयोगों में स्क्विरल-केज इंडक्शन मोटर का उपयोग उनकी मजबूत और टिकाऊ संरचना के कारण व्यापक रूप से किया जाता है। इन मोटरों की पावर रेटिंग कुछ सौ किलोवाट (≈500 kW) से लेकर कुछ मेगावाट (≈2–3 MW) तक होती है, जबकि वोल्टेज रेटिंग 2–5 kV के बीच होती है।

इंसुलेटेड गेट बाइपोलर ट्रांजिस्टर (IGBT) आधारित टू-लेवल वोल्टेज सोर्स इन्वर्टर (2L-VSI) इन मध्यम-वोल्टेज, उच्च-शक्ति मोटरों को चलाने के लिए सबसे अधिक उपयोग किए जाते हैं। ड्राइव के संतोषजनक डायनामिक प्रदर्शन के लिए सामान्यतः रोटर-फ्लक्स ओरिएंटेड वेक्टर कंट्रोल अपनाया जाता है। तथापि, ऐसे सिस्टम कई चुनौतियों का सामना करते हैं। 2L-VSI में प्रत्येक IGBT ऑफ-स्टेट में संपूर्ण DC-लिंक वोल्टेज को ब्लॉक करता है, इसलिए इन उपकरणों की वोल्टेज रेटिंग 4.5 kV या उससे अधिक होनी चाहिए। इतनी उच्च वोल्टेज-ब्लॉकिंग क्षमता वाले सेमीकंडक्टर उपकरणों की स्विचिंग विशेषताएँ (स्विचिंग गति और स्विचिंग ऊर्जा हानि दोनों के संदर्भ में) प्रभावित होती हैं। परिणामस्वरूप, इन पावर कन्वर्टरों की स्विचिंग फ्रीक्वेंसी (fsw) सामान्यतः कुछ सौ हर्ट्ज (≈500–750 Hz) तक सीमित रहती है। सीमित fsw, क्लोज्ड-लूप नियंत्रण के अंतर्गत ड्राइव के हार्मोनिक तथा डायनामिक प्रदर्शन को प्रभावित करता है।

संतोषजनक हार्मोनिक प्रदर्शन सुनिश्चित करने के लिए सामान्यतः सिंक्रोनस पल्स-विथ मॉड्यूलेशन (PWM) तकनीकों का उपयोग किया जाता है, जिसमें एक मूलभूत चक्र में इन्वर्टर के पोल-वोल्टेज में स्विचिंग पल्स की संख्या स्थिर रखी जाती है। इसे पल्स संख्या (P) कहा जाता है। जैसे-जैसे ड्राइव की मॉड्यूलेशन फ्रीक्वेंसी (fm) मोटर की गति के साथ बढ़ती है, fsw को निर्धारित सीमा में बनाए रखने के लिए P को क्रमशः घटाया जाता है।

सिंक्रोनस साइन-ट्रायंगल (SST) PWM अपनी सरलता के कारण अन्य सिंक्रोनस PWM तकनीकों में लोकप्रिय है। SST PWM में P को कैरियर फ्रीक्वेंसी (fc) और fm के अनुपात (P = fc/fm) के रूप में परिभाषित किया जाता है। P केवल विषम ट्रिप्लेन पूर्णांकों (जैसे 21, 15, 9, 3) तक सीमित रहता है। अतः P = 9 के बाद SST PWM का हार्मोनिक प्रदर्शन काफी हद तक खराब हो जाता है। इस शोध में एक हाइब्रिड सिंक्रोनस PWM तकनीक प्रस्तावित की गई है, जो SST PWM और सिंक्रोनस ऑप्टिमल (SO) PWM का संयोजन है। उच्च P मान (जैसे 21, 15, 9) पर SST PWM का उपयोग किया जाता है, जबकि P = 9 पर यह SO PWM में परिवर्तित हो जाता है। प्रस्तावित तकनीक में P = 7, 5 जैसे विषम गैर-ट्रिप्लेन मानों को भी शामिल किया गया है। SO PWM की एक कमी यह है कि इसमें मॉड्यूलेशन इंडेक्स के अनुसार ऑप्टिमल स्विचिंग एंगल्स को लुक-अप टेबल में संग्रहीत करना पड़ता है, जिससे मेमोरी पर भार बढ़ता है। इस शोध में बिना लुक-अप टेबल के इस PWM तकनीक को लागू करने की विधि भी प्रस्तावित की गई है।

क्लोज्ड-लूप संचालन में एक अन्य चुनौती तब उत्पन्न होती है जब P के बदलने के साथ 2L-VSI द्वारा लागू पल्स-पैटर्न में परिवर्तन होता है। यदि यह परिवर्तन नियंत्रित तरीके से न किया जाए, तो लाइन करंट और विद्युतचुंबकीय टॉर्क में बड़े ट्रांजिएंट्स उत्पन्न हो सकते हैं। इस शोध में एक ऐसी रणनीति प्रस्तावित की गई है, जो न्यूनतम ट्रांजिएंट सुनिश्चित करती है। यह रणनीति आउटगोइंग और इनकमिंग पल्स-पैटर्न के लिए तत्क्षण स्टेटर-फ्लक्स ट्रैजेक्टरी के मिलान पर आधारित है।

इसके अतिरिक्त, इस शोध में ओपन-एंड वाइंडिंग इंडक्शन मोटर (OWIM) आधारित एक संशोधित रेलवे ट्रैक्शन ड्राइव प्रस्तावित किया गया है, जिसमें दो 2L-VSI स्टेटर वाइंडिंग के दोनों सिरों से मोटर को शक्ति प्रदान करते हैं। इस प्रणाली में दो सिंगल-फेज एक्टिव फ्रंट-एंड कन्वर्टर (AFEC) होते हैं, जिनकी AC साइड एक तीन-वाइंडिंग ट्रांसफॉर्मर की द्वितीयक वाइंडिंग से जुड़ी होती है, जिससे दो पृथक DC स्रोत प्राप्त होते हैं। यह OWIM ड्राइव को इस अनुप्रयोग के लिए उपयुक्त बनाता है।

इस ड्राइव के लिए एक SST PWM तकनीक प्रस्तावित की गई है, जिसमें सम ट्रिप्लेन (P = 6, 12...), विषम गैर-ट्रिप्लेन (P = 5, 7...) और विषम ट्रिप्लेन (P = 3, 9...) सभी को शामिल किया गया है। मध्यवर्ती P मानों के उपयोग से fc में बड़े बदलाव को रोका जा सकता है। प्रस्तावित PWM तकनीक के हार्मोनिक विश्लेषण हेतु डबल-फूरियर सीरीज़ (DFS) आधारित गणितीय ढांचा विकसित किया गया है। साथ ही, स्टेटर-फ्लक्स ट्रैजेक्टरी और फूरियर-सीरीज़ आधारित विश्लेषण भी किए गए हैं।

इसके पश्चात, OWIM ड्राइव के लिए एक अन्य SST PWM तकनीक प्रस्तावित की गई है, जिसमें दो VSIs के लिए भिन्न कैरियर सिग्नल उपयोग किए जाते हैं। इसमें केवल ट्रिप्लेन (सम और विषम) P मानों को ही लिया गया है। दोनों VSIs के लिए P1 और P2 समान नहीं होते, और प्रभावी P को इनके औसत के रूप में परिभाषित किया गया है। इस योजना से पारंपरिक विधि की तुलना में बेहतर हार्मोनिक प्रदर्शन प्राप्त होता है, जिसे गणितीय विश्लेषण, सिमुलेशन और प्रयोगों द्वारा सत्यापित किया गया है।

उच्च-शक्ति IM ड्राइव में एक अन्य चुनौती स्पीड-सेंसरलेस नियंत्रण तकनीकों के निम्न गति क्षेत्र में प्रदर्शन से संबंधित है। इस शोध में एक मल्टी-इंडक्शन मोटर ड्राइव सिस्टम (MMDS) पर विचार किया गया है, जिसमें दो या अधिक Y-कनेक्टेड मोटर एक ही शाफ्ट पर जुड़े होते हैं। ऐसे लोड में, कम गति पर कम से कम एक मोटर को टॉर्क उत्पन्न करने की आवश्यकता नहीं होती। इस शोध में यह दर्शाया गया है कि शून्य टॉर्क उत्पन्न करने वाली मोटर के स्टेटर करंट पर आधारित PLL, बहुत कम गति पर भी रोटर स्पीड का सटीक अनुमान प्रदान करता है।

अंततः, प्रस्तावित PWM तकनीकों और नियंत्रण एल्गोरिद्म का सत्यापन MATLAB/Simulink के माध्यम से सिमुलेशन द्वारा किया गया और तत्पश्चात कम-शक्ति प्रयोगशाला सेटअप पर प्रयोगात्मक रूप से प्रमाणित किया गया। सिमुलेशन और प्रयोगात्मक परिणामों से यह स्पष्ट होता है कि प्रस्तावित विधियाँ पारंपरिक तरीकों की तुलना में बेहतर प्रदर्शन प्रदान करती हैं।

Contents

Certificate i

Acknowledgements iii

Abstract v

Contents ix

List of Figures xiii

List of Tables xxi

Abbreviations xxiii

Symbols xxv

1 Introduction 1
- 1.1 Three-Phase Induction Motor Drives . . . 1
- 1.2 Review of Modelling and Control of SCIM . . . 6
  - 1.2.1 Modelling . . . 6
  - 1.2.2 Field Oriented Control with Speed Sensor . . . 10
  - 1.2.3 Sensorless Field Oriented Control . . . 11
- 1.3 Literature Review . . . 13
  - 1.3.1 Configuration: Motor and Power Converter Topologies . . . 14
  - 1.3.2 Pulse-Width Modulation Techniques . . . 16
  - 1.3.3 Speed-Sensorless Motor Control Algorithms . . . 18
- 1.4 Research Problem . . . 20
- 1.5 Objectives and Scope of Work . . . 22
- 1.6 Outline of the Thesis . . . 23

2 Synchronous PWM Scheme and Pulse Pattern Transition Strategy: Y-connected SCIM 25
- 2.1 Introduction . . . 25
- 2.2 Limitations in Performance of SCIM Drives Employing SST PWM . . . 27
  - 2.2.1 Impact of unconstrained pulse transition on the performance of drive under closed-loop control . . . 28
  - 2.2.2 SST PWM scheme for SCIM drive with intermediate non-triplen values of P . . . 31
    - 2.2.2.1 Single Carrier V/s Multi-carrier Implementation . . . 31
    - 2.2.2.2 Harmonic analysis using Double-Fourier Expansion . . . 34
    - 2.2.2.3 Simulation Results . . . 36
    - 2.2.2.4 Experimental Results . . . 40
    - 2.2.2.5 Inferences from Results . . . 42
- 2.3 Synchronous Optimal Hybrid PWM Scheme . . . 43
  - 2.3.1 Realisation of proposed SOH PWM scheme . . . 45

2.3.2 Estimation of θ_s and M . . . 49
2.3.3 Implementation of SST PWM . . . 50
2.3.4 Implementation of SO PWM . . . 51
2.3.5 Performance of the drive with proposed PWM technique during unconstrained pulse transition . . . 53
2.4 Pulse Pattern Transition Strategy . . . 56
2.4.1 Analysis from fundamental model perspective . . . 57
2.4.2 Harmonic Model Analysis . . . 59
2.4.3 Proposed stator-flux trajectory based pulse-transition strategy 61
2.4.3.1 Required Compensation in SST PWM . . . 63
2.4.4 Implementation of the proposed strategy . . . 65
2.5 Validation of Proposed SOH PWM Technique and Pulse transition Strategy . . . 65
2.5.1 Simulation Results . . . 66
2.5.2 Experimental Results . . . 70
2.6 Conclusion . . . 77

3 Synchronous PWM Scheme: Open-End Winding Induction Motor 81
3.1 Introduction . . . 81
3.2 Proposed modification in traction drive to incorporate OWIM configuration . . . 82
3.3 Proposed Multi-Carrier based Synchronized Sin-Triangle PWM Strategy for OWIM drive . . . 85
3.3.1 Double Fourier Series based Analysis to Predict Harmonic Profile of the inverter pole-voltages in an OWIM drive . . . 86
3.3.2 Proposed Multi-Carrier SST PWM for OWIM Drive . . . 89
3.4 Further Analysis of Proposed PWM Technique . . . 91
3.4.1 Space vector based analysis . . . 91
3.4.2 Analytical estimation of harmonic spectrum . . . 93
3.4.3 Stator-flux Analysis . . . 94
3.5 Validation of Proposed PWM Technique . . . 95
3.5.1 Simulation Results . . . 95
3.5.2 Experimental Results . . . 107
3.6 Impact of Orientation of Carrier Signal with respect to the modulating signal on the harmonic performance of the drive . . . 117
3.6.1 Validation through Simulations and Experiments . . . 119
3.7 Conclusion . . . 119

4 Dissimilar Carrier based Synchronous PWM Scheme for Open-End Winding Induction Motor 127
4.1 Introduction . . . 127
4.2 Proposed SST-PWM Scheme for OWIM Drive . . . 128
4.2.1 Expression of phase-voltage of OWIM using DFS . . . 130

4.2.2 Impact of phase-shift in modulating signals ($\Delta\gamma$) and carrier signals ($\Delta\phi$) on fundamental phase-voltage . . . 131
4.3 Harmonic Optimization Using Phase-Shift in Carrier Signals ($\Delta\phi$) for $\overline{P} = 9$ . . . 132
4.4 Harmonic performance pertaining to $\overline{P} = 6$ . . . 135
4.4.1 Case I: Conventional PWM, $P_1 = P_2 = 6$ . . . 135
4.4.2 Case II: Proposed PWM, $P_1 = 9$ and $P_2 = 3$ . . . 135
4.5 Analysis based on Stator-flux ripple . . . 137
4.6 Validation of Proposed PWM Technique . . . 139
4.6.1 Simulation Results . . . 140
4.6.2 Experimental Results . . . 146
4.6.2.1 Open-Loop Results . . . 146
4.6.2.2 Closed-Loop Operation . . . 146
4.7 Conclusion . . . 151

5 Speed Sensorless Control of Multi-Induction Motor Drives 155
5.1 Introduction . . . 155
5.2 Sensorless Control Architecture for MMDS . . . 157
5.2.1 Modes of Operation of the Drive . . . 157
5.2.2 Control of DMDS in TSM . . . 159
5.3 Proposed Speed Estimation Technique . . . 160
5.3.1 PLL Based Speed Estimation Scheme . . . 160
5.3.2 Estimation of Erroneous Operating Speed, $\tilde{\omega}_m$ . . . 162
5.3.3 Impact of Operating Frequency on the Estimation of $\tilde{\omega}_m$ . . . 164
5.3.4 Design of the PLL . . . 167
5.3.5 Impact of Variation in $T_{r,1}$ and δ_1 on the Closed-Loop Performance of the PLL . . . 169
5.3.6 Control of DMDS in SCM . . . 172
5.3.7 Transition from SCM to TSM . . . 173
5.3.8 Power Flow Analysis . . . 173
5.4 Torque-sharing strategy for minimum copper loss . . . 174
5.5 Validation of Proposed Algorithm . . . 177
5.5.1 Smooth Starting and Speed Reversal . . . 179
5.5.2 Smooth Operation in SCM and Transition to TSM . . . 180
5.5.3 Low-Speed Operation of the Drive . . . 182
5.5.4 Comparison with Conventional Sensorless Algorithm . . . 183
5.5.5 Performance of the Drive Under Load Dynamics . . . 184
5.5.6 Impact of Parameter Variation on Drive Performance . . . 185
5.5.7 Impact of LPF Cutoff Frequency, ω_o on Drive Performance . . . 188
5.5.8 Experimental validation of torque sharing strategy . . . 190
5.5.9 Simulation based validation . . . 191
5.6 Conclusion . . . 193

6 Conclusion and Future Scope 195

6.1 General 195
6.2 Major Conclusions 195
6.3 Future Scope 197

Bibliography **199**

Appendix A: Double Fourier Series **211**

Appendix B: Controller Design **213**

Appendix C: Experimental Setups and Parameters **217**

List of Publications **221**

Biography **223**

List of Figures

1.1 Torque-speed characteristic of a SCIM with constant voltage constant frequency supply . . . 1
1.2 General block diagram of an IMD. . . . 3
1.3 Torque-speed characteristics of an IMD . . . 3
1.4 Schematic representation of an OWIM drive . . . 5
1.5 (A) Equivalent circuit of IM and (B) corresponding phasor diagram . 7
1.6 Control block diagram of RFOC of SCIM with speed sensor . . . 10
1.7 Control block diagram of RFOC of SCIM without speed sensor . . . 12
1.8 Developments in high-power IMD. . . . 14

2.1 Schematic of SCIM based railway traction drive . . . 25
2.2 Variation of carrier frequency with modulating signal frequency for SST PWM . . . 26
2.3 m_r and normalised V_{ro} during the transition between $P = 9$ and 3 . . 28
2.4 Performance of simulated vector controlled IM drive in terms of (a) i_{mr} (b) i_{sd} (c) speed and (d) i_{sq} with SST PWM. . . . 29
2.5 (a) Electromagnetic torque and (b) three-phase current through the complete range of f_m with SST PWM. . . . 30
2.6 Modulating and carrier signal for (a) $P = 7$ (b) $P = 5$ with same carrier and for (c) $P = 7$, (d) $P = 5$ with different carrier signals for three-phases. . . . 32
2.7 Normalised pole-voltages for (a) $P = 7$ and (b) $P = 5$ with same carrier and for (c) $P = 7$ and (d) $P = 5$ with different carriers for three phases. . . . 33
2.8 Simulation results pertaining to three-phase line current for (a) $P = 7$, (b) $P = 5$ with common carrier and (c) $P = 7$, (d) $P = 5$ with different carrier . . . 37
2.9 Simulation results pertaining to FFT of line current for (a)$P = 7$ ($i_{THD} = 118.17\%$) (b)$P = 5$ ($i_{THD} = 200.39\%$) with common carrier signal and (c) $P = 7$ ($i_{THD} = 248.41\%$) (d) $P = 5$ ($i_{THD} = 354.31\%$) with different carrier signals . . . 38
2.10 Experimental results pertaining to three-phase line modulating and carrier signal for (a) $P = 7$, (b) $P = 5$ with common carrier and (c) $P = 7$, (d) $P = 5$ with different carrier signals (x axis: 5ms/div) . . . 40
2.11 Experimental results pertaining to three-phase line current for (a)$P = 7$ (b) $P = 5$ with common carrier and (c)$P = 7$, (d) $P = 5$ with different carrier signals (x axis: 5ms/div) . . . 41
2.12 Experimental results pertaining to FFT of three-phase line current for (a)$P = 7$, (b) $P = 5$ with common carrier and (c) $P = 7$ (d)$P = 5$ with different carrier signals . . . 42
2.13 (a) Type A and (b) type B pulse pattern for $P = 5$ . . . 44
2.14 Plot of f_{sw} over complete range of f_m for SOH PWM . . . 45
2.15 Theoretically estimated V_{WTHD} for both Type A and type B pulse pattern for (a) $P = 5$ (b) $P = 7$ (c) $P = 9$ [1] . . . 46

2.16 Variation of α_i over the complete range of M 47
2.17 Vectors A, Z_A, B and Z_B in sector I based on α_i for (a) $P = 9A$ (b) $P = 9B$ (c) $P = 7A$ (d) $P = 7B$ (e) $P = 5A$ 48
2.18 Phasor Diagram consisting of IM in (a) motoring and (b) generating modes 50
2.19 Block diagram to implement SST PWM 51
2.20 Change in PP (a) $P = 9B$ to $7A$ (b) $P = 7B$ to $5A$ 53
2.21 Block diagram to implement SO PWM 53
2.22 m_r and normalised V_{ro} during the transition SST P=9 to SO P=9A . 54
2.23 (a) i_{sd} and (b) i_{sq} axis current through the complete range of f_m with proposed SOH PWM. 54
2.24 i_{sd} and i_{sq} captured during transitions from (a) $P = 9$ to $P = 9A$ (b) $P = 9b$ to $P = 7A$ (c) $P = 7A$ to $P = 7b$ (d) $P = 7B$ to $P = 5A$ . . . 55
2.25 Experimental result corresponding to three-phase current during the transition from SST P=9 to SO P=9A [x axis: 10ms/div, y axis: 20A/div] 56
2.26 Current control loop for traction motor drive. 57
2.27 Bode plots of loop transfer function (G_{ol}) pertaining to transitions in P from (a) Asyn to P=21 at $f_m = 10Hz$ (b) P=21 to 15 at $f_m = 23Hz$ (c) P=15 to 9 at $f_m = 33Hz$ (d) P=9 to 3 at $f_m = 55Hz$. 58
2.28 Mismatch in ripple currents pertaining to $P = 9$ and 3 at $f_m = 55Hz$. 60
2.29 Normalized $\overrightarrow{\psi}_s$ trajectories pertaining to (a) SST (b) SO PWM . . . 62
2.30 Block diagram of proposed algorithm for transition of P in vector controlled IM drive 64
2.31 Complete control block diagram of the motor drive 66
2.32 Simulation results pertaining to (a) i_{sd} and (b) i_{sq} through the complete range of f_m with proposed SOH PWM with proposed pulse transition strategy 67
2.33 Simulation results pertaining to i_{sd} and i_{sq} captured during transitions from (a) $P = 9$ to $P = 9A$ (b) $P = 9b$ to $P = 7A$ (c) $P = 7A$ to $P = 7b$ (d) $P = 7B$ to $P = 5A$ with proposed pulse transition strategy 68
2.34 Simulation results pertaining to (a) i_{sd} and (b) i_{sq} axis current through the complete range of f_m with conventional SST PWM with proposed pulse transition strategy 69
2.35 Simulation results pertaining to i_{sd} and i_{sq} captured during transitions from (a) $P = 15$ to $P = 9$ (b) $P = 9$ to $P = 3$ with proposed pulse transition strategy 69
2.36 Experimental result showing synchronization of θ_s and V_{ro} with m_r [x axis: 10ms/div] 70
2.37 Continuity in ψ_α and ψ_β (5Wb/div) with the proposed strategy during transition from (a)SST P=9 to SST P=3 (b)SST P=9 to SO P=9A [x axis: 10ms/div] 70

2.38 Experimental results showing i_{sd} (5A/div), i_{sq} (8A/div), normalised V_{ro} and m_r with proposed strategy at the instant of transition from (a) P=9 to 9A (b) P=9A to P=9B (c) P=9B to P=7A (d) P=7A to P=7B and (e) P=7B to P=5A [x axis: 10ms/div] 71
2.39 Experimental results showing i_{sd} (4A/div), i_{sq} (8A/div), normalised V_{ro} and m_r with proposed strategy at the instant of transition from (a) P=5A to P=7B (b) P=7B to P=7A (c) P=7A to P=9B and (d) P=9B to P=9A during deceleration. [x axis: 10ms/div] 73
2.40 Experimental performance of vector controlled IM drive in terms of (a) i_{mr} [Scale: 5A/div, 5s/div] (b) i_{sd} [Scale: 5A/div, 5s/div] (c) speed [Scale: 600RPM/div, 5s/div]and (d) i_{sq} [Scale: 8A/div, 5s/div] with proposed strategy under proposed SOH PWM scheme 74
2.41 i_{THD} for actual and approximated values of α_i. 75
2.42 Rise in temperature of motor casing due to SST and SO PWM . . . 75
2.43 Experimental results showing i_{sd} (5A/div) and i_{sq} (8A/div) along with normalised V_{ro} and m_r with proposed strategy during the transition from (a) SST P=9 to SST P=3 (b) SST P=9 to SO P=9A [x axis: 10ms/div] 77
2.44 Experimental performance of vector controlled IM drive in terms of (a) i_{mr} [Scale: 5A/div, 5s/div] (b) i_{sd} [Scale: 5A/div, 5s/div] (c) speed [Scale: 600RPM/div, 5s/div]and (d) i_{sq} [Scale: 8A/div, 5s/div] with proposed strategy under SST PWM. 78

3.1 (a) Conventional 2L-VSI fed SCIM and (b) proposed OWIM based modified drives for railway propulsion system 83
3.2 Plot of f_{sw} against f_m for standard SCIM and OWIM based modified drives 84
3.3 Three-phase modulating signals and triangular carriers for inverter 1 at (a) f_m=35Hz, M=0.5384 (P=9) (b) f_m=45Hz, M=0.6923 (P=7) (c) f_m=55Hz, M=0.8461 (P=6) and (d) f_m=65Hz, M=1 (P=5) pertaining to proposed OWIM drive. 90
3.4 Voltage vectors corresponding to individual inverters and combined phase voltages pertaining to OWIM drive. 91
3.5 Illustration of voltage vector applied over sector I by individual inverters and resultant voltage vector corresponding to (a) Fig. 3.3a (b) Fig. 3.3b (c) Fig. 3.3c and (d) Fig. 3.3d 92
3.6 R-phase modulating signal, carrier and normalized pole voltages of (a) Inverter 1 and (b) Inverter 2 94
3.7 Magnitude of normalized (a) 13^{th} (b) 11^{th} (c) 7^{th} and (d) 5^{th} harmonic over the complete range of frequency 95
3.8 Trajectory of tip of normalized $\overrightarrow{\psi_s}$ corresponding to (a) Fig. 3.3a (b) Fig. 3.3b (c) Fig. 3.3c and (d) Fig. 3.3d 96

3.9 Pole voltages of individual inverters (v_{Ro_1}, v_{ro_2}) and resultant phase voltage (v_{Rr}) corresponding to (a) Fig. 3.3a (b) Fig. 3.3b (c) Fig. 3.3c and (d) Fig. 3.3d 97
3.10 Harmonic spectrum of v_{Ro_1}, v_{ro_2}, v_{Rr} corresponding to (a) Fig. 3.9a (b) Fig. 3.9b (c) Fig. 3.9c and (d) Fig. 3.9d 98
3.11 Three-phase current (i_R, i_Y, i_B) pertaining to proposed OWIM based modified drive under no-load corresponding to (a) Fig. 3.9a (b) Fig. 3.9b (c) Fig. 3.9c and (d) Fig. 3.9d 100
3.12 Harmonic-spectrum of i_R corresponding to (a) Fig. 3.11a (b) Fig. 3.11b (c) Fig. 3.11c and (d) Fig. 3.11d 101
3.13 Three-phase current (i_R, i_Y, i_B) pertaining to proposed OWIM based modified drive under full-load corresponding to (a) Fig. 3.9a (b) Fig. 3.9b (c) Fig. 3.9c and (d) Fig. 3.9d 102
3.14 Three-phase currents (i_R, i_Y, i_B) pertaining to standard SCIM drive at (a) f_m=35Hz (P=9) (b) f_m=45Hz (P=3) (c) f_m=55Hz (P=3) and (d) f_m=65Hz (P=3) under no-load 103
3.15 Harmonic-spectrum of i_R corresponding to (a) Fig. 3.14a (b) Fig. 3.14b (c) Fig. 3.14c and (d) Fig. 3.14d 104
3.16 Three-phase current (i_R, i_Y, i_B) pertaining to proposed SCIM based modified drive under full-load corresponding to (a) Fig. 3.9a (b) Fig. 3.9b (c) Fig. 3.9c and (d) Fig. 3.9d 105
3.17 Simulated torque ripple waveform corresponding to (a) Fig. 3.3a (b) Fig. 3.3b (c) Fig. 3.3c and (d) Fig. 3.3d 106
3.18 Comparison of I_{THD} under full-load pertaining to 850kW standard SCIM and proposed OWIM drive 106
3.19 Comparison of total power converter losses under full-load condition for 850kW traction system 108
3.20 Experimentally measured pole voltages of individual inverters (v_{Ro_1}, v_{ro_2}) and resultant phase voltage (v_{Rr}) corresponding to (a) Fig. 3.3a (b) Fig. 3.3b (c) Fig. 3.3c and (d) Fig. 3.3d [Scale: 200V/div, 5ms/div] 109
3.21 Experimentally obtained harmonic spectra of voltages (v_{Ro_1}, v_{ro_2}, v_{Rr}) corresponding to (a) Fig. 3.20a (b) Fig. 3.20b (c) Fig. 3.20c and (d) Fig. 3.20d 110
3.22 Measured three-phase currents (i_R, i_Y, i_B) under no-load corresponding to (a) Fig. 3.20a (b) Fig. 3.20b (c) Fig. 3.20c and (d) Fig. 3.20d [Scale: 2A/div, 5ms/div] 111
3.23 Measured harmonic-spectrum of i_R corresponding to (a) Fig. 3.22a (b) Fig. 3.22b (c) Fig. 3.22c and (d) Fig. 3.22d 112
3.24 Measured three-phase currents (i_R, i_Y, i_B) under full load corresponding to (a) Fig. 3.20a (b) Fig. 3.20b (c) Fig. 3.20c and (d) Fig. 3.20d [Scale: 10A/div, 10ms/div] 113

3.25 Measured three-phase currents pertaining to 3.7kW SCIM drive (a) f_m=35Hz (P=9) [Scale: 7A/div, 5ms/div] (b) f_m=45Hz (P=3) (c) f_m=55Hz (P=3) and (d) f_m=65Hz (P=3) under no-load [Scale: 10A/-div, 5ms/div] 114
3.26 Measured harmonic-spectrum of i_R corresponding to (a) Fig. 3.25a (b) Fig. 3.25b (c) Fig. 3.25c and (d) Fig. 3.25d 115
3.27 Comparison of experimentally measured I_{thd} under no-load condition. 116
3.28 Various carrier configuration for 2L-VSI fed SCIM (a)Positive quadrature phase (b)Negative quadrature phase (c)In-phase (d)Out-of-phase 118
3.29 Individual inverter pole volatges (v_{Ro1}, v_{ro2}) and machine phase voltage (v_{Rr}) at $f_m = 35Hz$ for $P = 9$ for (a)Positive quadrature phase (b)Negative quadrature phase (c)In-phase (d)Out-of-phase carrier signals 120
3.30 Three-phase line-currents (i_R, i_Y, i_B) under full-load corresponding to (a) Fig.3.29a (b) Fig.3.29b(c)Fig.3.29c(d)Fig.3.29d 121
3.31 Harmonic spectrum of line-currents (i_R) corresponding to (a) Fig.3.30a (b) Fig.3.30b(c)Fig.3.30c(d)Fig.3.30d 122
3.32 Experimentally measured Individual inverter pole volatges (v_{Ro1}, v_{ro2}) and machine phase voltage (v_{Rr}) at $f_m = 35Hz$ for $P = 9$ for (a)Positive quadrature phase (b)Negative quadrature phase (c)In-phase (d)Out-of-phase carrier signals [Scale: 200V/div, 5ms/div] 123
3.33 Experimentally measured three-phase current (i_R, i_Y, i_B) corresponding to (a)Fig.3.32a (b)Fig.3.32b (c)Fig.3.32c(d)Fig.3.32d [Scale: 5A/-div, 5ms/div] 124
3.34 Experimentally measured spectrum of line-current (i_R) corresponding to (a)Fig.3.33a (b)Fig.3.33b (c)Fig.3.33c (d)Fig.3.33d. 125

4.1 Variation of (a) f_c for conventional scheme and (b) f_c^{inv1}, f_2^{inv2} and $\overline{f}_c$ for proposed scheme with f_m 129
4.2 R-phase modulating and carrier signal for both inverter 1 and 2 showing $\Delta\phi$ and $\Delta\gamma$ 131
4.3 Variation of optimal value of $\Delta\phi$ for $\overline{P} = 9$ 134
4.4 Comparison of V_{WTHD} for the two cases corresponding to $\overline{P} = 6$ . . . 136
4.5 (a) $\tilde{\psi}_{sd}$ (b) $\tilde{\psi}_{sq}$ for conventional PWM (c) $\tilde{\psi}_{sd}$ (d) $\tilde{\psi}_{sq}$ for proposed PWM for $\overline{P} = 9$ 138
4.6 (a) $\tilde{\psi}_{sd}$ (b) $\tilde{\psi}_{sq}$ for conventional PWM (c) $\tilde{\psi}_{sd}$ (d) $\tilde{\psi}_{sq}$ for proposed PWM for $\overline{P} = 6$ 139
4.7 Variation of i_{THD} for $\overline{P} = 9$ for various modulation indices as $\Delta\phi$ is varied. 140
4.8 Simulation results for $\overline{P} = 9$ with $\Delta\phi = 0^o$ (a) pole voltages (v_{Ro1}, v_{ro2}) and phase voltage (v_{Rr}) (b) corresponding harmonic spectrum (c) three-phase current (d) corresponding harmonic spectrum. 141

4.9 Simulation results for $\overline{P} = 9$ with $\Delta\phi = 74^o$ (a) pole voltages (v_{Ro1}, v_{ro2}) and phase voltage (v_{Rr}) (b) corresponding harmonic spectrum (c) three-phase current (d) corresponding harmonic spectrum. 142
4.10 Simulation results for $P_1 = P_2 = \overline{P} = 6$ (a) pole voltages (v_{Ro1}, v_{ro2}) and phase voltage (v_{Rr}) (b) corresponding harmonic spectrum (c) three-phase current (d) corresponding harmonic spectrum. 143
4.11 Simulation results for $\overline{P} = 6$, $P_1 = 9$, $P_2 = 3$ (a) pole voltages (v_{Ro1}, v_{ro2}) and phase voltage (v_{Rr}) (b) corresponding harmonic spectrum (c)three-phase current (d) corresponding harmonic spectrum. 144
4.12 Experimental results pertaining to $\overline{P} = 9$ and $\Delta\phi = 0$ (a) Individual inverter pole voltages (v_{Ro1}, v_{ro2}) and machine phase voltage (v_{Rr}) (500V/div, 5ms/div) (b) corresponding harmonic spectrum (c) three-phase current (2A/div, 5ms/div) (d) corresponding harmonic spectrum. 147
4.13 Experimental results for $\overline{P} = 9$ and $\Delta\phi = 74^o$ (a) pole voltages (v_{Ro1}, v_{ro2}) and phase voltage (v_{Rr}) (500V/div, 5ms/div) (b) corresponding harmonic spectrum (c) three-phase current (2A/div, 5ms/div) (d) corresponding harmonic spectrum. 148
4.14 Experimental results for $\overline{P} = P_1 = P_2 = 6$ (a) pole voltages (v_{Ro1}, v_{ro2}) and phase voltage (v_{Rr}) (500V/div, 5ms/div) (b) corresponding harmonic spectrum (c) three-phase current (2A/div, 5ms/div) (d) corresponding harmonic spectrum. 149
4.15 Experimental results for $\overline{P} == 6$, $P_1 = 9$ and $P_2 = 3$ (a) pole voltages (v_{Ro1}, v_{ro2}) and phase voltage (v_{Rr}) (500V/div, 5ms/div) (b) corresponding harmonic spectrum (c) three-phase current (2A/div, 5ms/div) (d) corresponding harmonic spectrum. 150
4.16 Comparison of i_{THD} for conventional and proposed PWM over range of f_m. 151
4.17 Experimental performance of vector controlled OWIM drive in terms of (a) i_{mr} [Scale: 3A/div, 20s/div] (b) i_{sd} [Scale: 3A/div, 20s/div] (c) speed [Scale: 500RPM/div, 20s/div]and (d) i_{sq} [Scale: 3A/div, 20s/div] with proposed PWM technique 152
4.18 Experimental results showing three-phase currents at the instant of transition from (a) Asynchronous PWM to $\overline{P} = 21$ (b) $\overline{P} = 21$ to $\overline{P} = 18$ (c) $\overline{P} = 12$ to $\overline{P} = 9$ (d) $\overline{P} = 9$ to $\overline{P} = 6$ [y axis: 2A/div, x axis: 20ms/div] 153

5.1 (a) IM based dual-motor drive system. (b) Load torque-speed profile and region of torque production of individual IM. 156
5.2 Torque demand from motor 2 and the corresponding modes of operation of the DMDS. 158
5.3 Proposed control block diagram for the dual motor drive system. . . . 159
5.4 Phasor diagram of IM under no-load 160

5.5 Control block diagram for stator current based PLL 162
5.6 Proposed speed estimation technique 163
5.7 Inaccuracy in ρ_{mr} estimation 165
5.8 Variation in ω_{er} with $\omega_{mr,1}$ 166
5.9 Experimentally obtained $\alpha - \beta$ components of $\overrightarrow{e}_s$ and estimated $\overrightarrow{\psi}_s$ when the drive operates at (a) $f_s = 4$ Hz [x-axis scale: 100 ms/div] (b) $f_s = 24$ Hz [x-axis scale: 20 ms/div]. 167
5.10 Control block diagram for PLL with $\tilde{\omega}_m$ 168
5.11 Small signal model for PLL 168
5.12 Bode plot of G_{ol}^{PLL} for variation in δ_1 170
5.13 Bode plot of G_{ol}^{PLL} for variation in $T_{r,1}$ 170
5.14 Variation in bandwidth of the G_{cl}^{PLL} with δ_1 and $T_{r,1}$ 172
5.15 Flowchart depicting the torque sharing strategy. 176
5.16 Experimentally obtained (a) ω_m^*, ω_m^{est} , $i_{sq,1}$ and $i_{sq,2}$ (b) $i_{y,1}$ and $i_{y,2}$ and $i_{sd,1}$ and $i_{sd,2}$ for motor 1 and 2 for a positive speed command of $\omega_m^* = 600$ r/min followed by reversal command upto $\omega_m^* = -600$ r/min. 177
5.17 Experimentally measured ω_m, ω_m^{est}, $i_{sq,1}$ and $i_{sq,2}$ for motor 1 and 2 for a initial speed command of $\omega_m^* = 200$ r/min followed by a speed command of 600 r/min in (a) positive and (b) negative direction. . . 179
5.18 Active power-flow as the mode changes from SCM to TSM and vice versa. 180
5.19 (a) Experimentally measured ω_m^*, ω_m^{est}, $i_{sq,1}$ and $i_{sq,2}$ during load dynamics at low speed (b) ω_m, ω_m^{est}, $i_{sq,1}$ and $i_{sq,2}$ during speed reversal command at low speed. 181
5.20 Performance of the drive with successive low speed command. 183
5.21 Experimental comparison of performance between proposed and conventional sensorless algorithm in low speed of operation. 184
5.22 Experimentally obtained ω_m^*, ω_m^{est}, $i_{sq,1}$ and $i_{sq,2}$ during load dynamics in TSM. 185
5.23 Performance of the drive with (a) 100% (b) 50% variation in $R_{r,1}$. . . 186
5.24 Performance of the drive with 100% variation in $R_{s,1}$ 187
5.25 Performance of the drive with 100% variation in $R_{r,2}$ 188
5.26 Accuracy in speed estimation with $\omega_o = 2$ Hz. 188
5.27 Performance of the drive with $\omega_o = 2$ Hz with offset in R-phase current 189
5.28 Performance of the drive with $\omega_o = 5$ Hz with offset in R-phase current 190
5.29 Performance of the PLL without $\tilde{\omega}_m$ as feedforward 191
5.30 Experimentally obtained $i_{sd,1}$, $i_{sd,2}$, $i_{sq,1}$ and $i_{sq,2}$ for (a) equal and (b) unequal sharing of torque as the load is increased sequentially. (c) Estimated copper loss using (5.28) for both the cases. 192
5.31 ω_m^*, ω_m^{est} and ω_m obtained through simulation to (a) validate the performance of conventional sensorless algorithm at low speed (b) to test the proposed algorithm with faster rates of change of speed (c) to test the performance of PLL with reference speed added to the output of PLL 194

1 (A) Inner current control loop (B) Outer speed control loop 214

2 Experimental setup of Y-connected SCIM 217
3 Experimental set-up for OWIM drive 218
4 Experimental setup for MMDS 219

List of Tables

2.1 Combination of (m, n) for dominant lower order harmonics 34
2.2 39
2.3 Optimal Vector Sequence 47

3.1 γ_β for Inverter I and II 87
3.2 ϕ_β for Inverter I and II 87
3.3 Predicted harmonic profile of pole voltage for various P 88
3.4 Comparison of various PWM schemes for OWIM drive 91
3.5 I_{THD} under full load 99
3.6 ϕ_R for different carrier configuration 118

4.1 Values of P_1, P_2 and $\overline{P}$ for complete range of f_m 130
4.2 (m, n) giving rise k for various values of $\overline{P}$ 132

5.1 Controller parameters 178
5.2 Code execution time 184
5.3 Error in ω_m^{est} with variation in $R_{r,1}$ 185

1 Machine parameters for Y-connected SCIM 217
2 Machine parameters for OWIM Drive 218
3 Machine parameters for MMDS 219

Abbreviations

IM	**I**nduction **M**otor
SCIM	**S**quirrel **C**age **I**nduction **M**otor
OWIM	**O**pen-end **W**inding **I**nduction **M**otor
WRIM	**W**ound **R**otor **I**nduction **M**otor
MMDS	**M**ulti **M**otor **D**rive **S**ystem
DMDS	**D**ual **M**otor **D**rive **S**ystem
AFEC	**A**ctive **F**ront **E**nd **C**onverter
PWM	**P**ulse **W**idth **M**odulation
SST	**S**ynchronous **S**ine **T**riangle
SO	**S**ynchronous **O**ptimal
SOH	**S**ynchronous **O**ptimal **H**ybrid
VSI	**V**oltage **S**ource **I**nverter
DTC	**D**irect **T**orque **C**ontrol
FOC	**F**lux **O**riented **C**ontrol
DFS	**D**ouble **F**ourier **S**eries
LPF	**L**ow **P**ass **F**ilter
PLL	**P**hase **L**ocked **L**oop
PP	**P**ulse **P**attern
THD	**T**otal **H**armonic **D**istortion
DSP	**D**igital **S**ignal **P**rocessor

Symbols

Symbol	Definition	Unit
System parameters and the associated variables		
R_s, R_r	Stator and rotor resistance per phase	Ω
L_s, L_r	Stator and rotor self inductance per phase	H
L_{ls}, L_{lr}	Stator and rotor leakage inductance per phase	H
L_m	Magnetising inductance	H
σ_s, σ_r	Stator and rotor leakage factor	
σ	Total leakage factor	
p	Number of poles	
J	Moment of inertia	kgm^2
m_d	Electromagnetic torque of the motor	Nm
m_d^*	Reference electromagnetic torque (output of speed controller)	Nm
V_{dc}	DC bus voltage	V
P	Pulse Number	
Reference frames		
$\alpha - \beta$	Stationary reference frame	
$d - q$	Rotor flux ($\bar{\psi_{rs}}$) reference frame as seen from ($\alpha - \beta$)	
Frequencies		
f_m	Modulating Signal Frequency	Hz
f_c	Carrier Signal Frequency	Hz
f_{sw}	Switching Frequency	Hz

Chapter 1

Introduction

1.1 Three-Phase Induction Motor Drives

Three-phase induction motors (3P-IM) are extremely popular for high power applications like industrial fans, pumps, blowers and railway traction propeller. Such motors can be primarily classified into two categories, namely squirrel caged rotor induction motors (SCIM) and wound rotor induction motor (WRIM). Out of these two, WRIM offers more controllability due to the availability of rotor terminals. However, they suffer from the disadvantage of reduced ruggedness and robustness primarily due to the presence of slip-rings on rotor terminals. SCIM, on the other hand, offers very high reliability and robustness due to its simple rotor structure. Traditionally, these motors were operated by directly connecting them to three-phase AC power grid which is essentially a constant frequency and voltage power supply. The torque-speed, $(m_d - \omega_m)$ characteristics of SCIM when directly connected to the grid is shown in Fig.1.1. The figure shows the $(m_d - \omega_m)$ characteristics for two cases that is when the motor is connected to the grid maintaining the phase-sequence of the grid (positive sequence, RYB) or in the opposite phase-sequence of the grid (negative sequence, RBY).

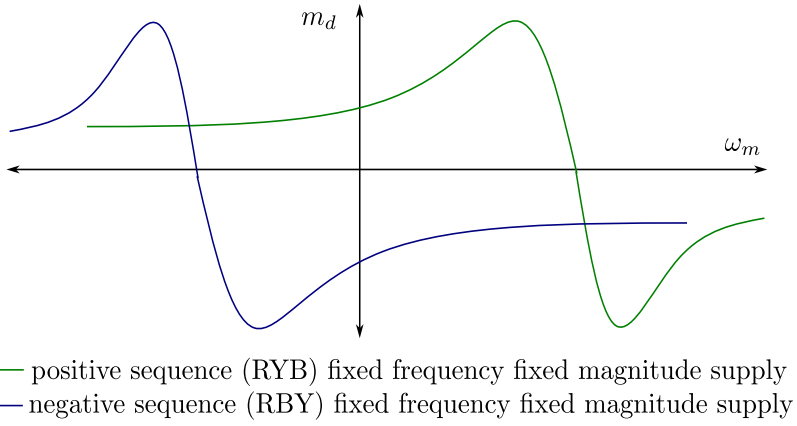


FIGURE 1.1: Torque-speed characteristic of a SCIM with constant voltage constant frequency supply

However, such operation where the motor is directly connected with the grid suffers from several disadvantages. They are listed below,

1. The region of operation is restricted to a narrow speed zone below the synchronous speed.
2. Speed regulation, defined as the percentage change in speed from no-load to full-load, can be high.
3. Such a motor draws excessive reactive power from the grid, resulting in poor voltage regulation of the grid.
4. Such a grid connected motor has zero degrees of freedom in terms of control of both speed and torque.

However, with the advent of power electronic technologies, variable voltage and variable frequency power supplies can easily be created from either a DC source or a fixed frequency and voltage AC source. Thus, this lead to the possibility of operating the 3P-IM over a wide range of speed with variable as well as constant load-torque. 3P-IM when operated with a power electronics based power converter is termed as 3P-IM drive (3P-IMD). Three-phase voltage source inverter (3P-VSI) based induction motor drives are extremely popular for high-power industrial and traction application. Three-phase voltages of variable magnitude and frequency can be generated using 3P-VSI. Magnitude and frequency of the required voltage from the 3P-VSI are decided based on the algorithm implemented in order to control the motor. Generally, the motor currents and motor speed are taken as feedback in order to implement the control algorithm. Finally, semiconductor devices like insulated gate bipolar transistors (IGBT) are switched in accordance to a pulse-width modulation (PWM) technique in order to generate to generate AC voltages from a fixed DC source in the 3P-VSI. Thus, an induction motor drive broadly has three units: the motor and power converter (configuration), PWM technique and control algorithm. This is shown in Fig. 1.2. With a power converter which supplies variable frequency and voltage to the SCIM, the torque speed characteristic of the motor changes into a region as shown in Fig.1.3.

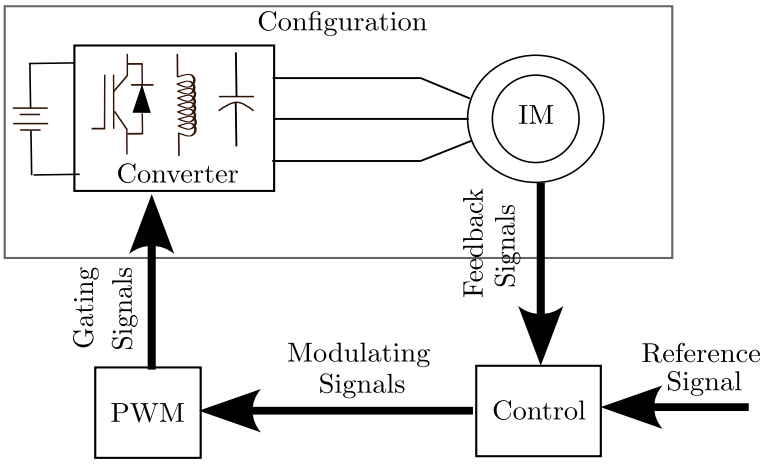


FIGURE 1.2: General block diagram of an IMD.

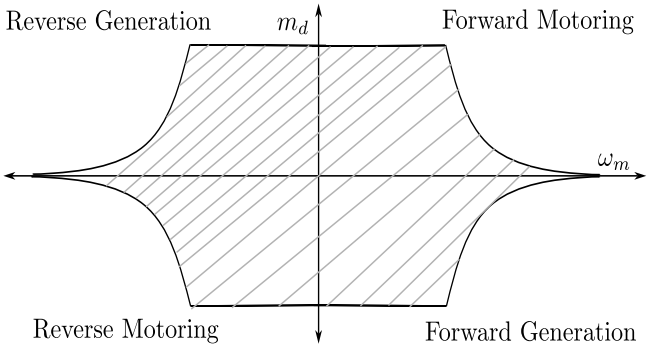


FIGURE 1.3: Torque-speed characteristics of an IMD

Traditionally, a caged rotor induction motor with a Y/Δ connected three-phase winding on the stator fed with a three-phase two-level VSI (2L-VSI) had become popular. Rotor-flux oriented vector control (RFO-VC) algorithm was developed to ensure fast and decoupled control of the motor. Triangular carrier based sine-triangle PWM or space-vector PWM were the popular modulation techniques. However, in the last few decades, tremendous developments have taken place in all three units of induction motor drives. Generally, the control algorithm and PWM techniques are implemented on digital platforms like DSP/FPGA. New topologies pertaining to both the power converter and induction motor have come up. New control algorithms have been developed to ensure fast dynamic control and newer PWM techniques have come up to enhance the performance of the drive.

With increasing power level, the rated voltage of the motor also increases. This

is done in order to primarily limit the currents flowing through the machine. Lesser winding currents lead to lesser losses, specially conduction losses in the motor. Thus, for the power level in the range of few megawatts $(1-2)$ MW, the rated voltage of the motor goes into the range of few kilovolts $(2-5)$kV. This range is generally termed as medium voltage range.

With increased voltage rating of the motor, the AC voltage required to be generated from the 3P-VSI also increases. In a 2L-VSI, increase in the output AC voltage leads to increased DC voltage of the same. Further, the power semiconductor devices block the entire DC voltage under off-state in a 2L-VSI. Thus, with increasing voltage level, IGBTs of higher blocking capabilities are required. The commercially available IGBTs on the high-voltage spectrum are generally rated at 4.5kV. However, they have limited switching capabilities both in terms of reduced switching speed and increased switching losses. Further, if the DC bus goes beyond the rating of the devices, they are required to be connected in series.

Series connected IGBTs require very precise control in their gate-circuitry during both turn on and off which requires complex gate driving circuitry. This paved the way for development of multilevel converters like neutral point clamped (NPC) multi-level converters where the converter topology is designed in a such a manner which ensures that each IGBT block only a fraction of the total DC-link voltage. Further, more advanced topologies like cascaded H-bridge (CHB) converter and modular multi-level converters (MMC) were developed wherein several modules generating a fraction of the required AC voltage are connected in series. Thus, multi-level power converters are slowly becoming a very popular choice for high-power medium voltage drive.

From the machine side, instead of using a Y-connected machine, the neutral point of the stator winding can be opened up and both the ends of the stator winding can be made accessible. Thus, voltage and power can be applied to the stator both the ends. Thus, the voltage requirement from each end directly becomes half, reducing the DC voltage requirement. This configuration of IM is also known as open-end

winding induction motor (OWIM). A schematic representation of an OWIM drive is shown in Fig.1.4.

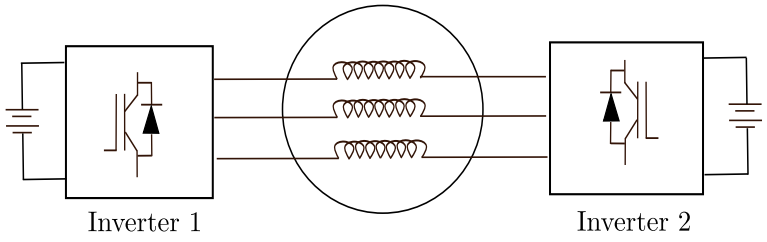


FIGURE 1.4: Schematic representation of an OWIM drive

Although RFO-VC is a very popular control technique and is extensively used in industry, it suffers from several serious challenges. A major challenge in RFO-VC is dependency on sensors. The motor currents and the speed are required to be sensed in order to implement RFO-VC. Of these, speed sensors are generally expensive which increases the overall cost of the drive. Further, information from the speed sensors are extremely susceptible to noise and disturbances in practical situation. For some applications, the machine is kept at distance from the power converter and digital controller. Information from the speed sensor attached to the machine is transmitted over the distance. Thus, such a practical challenge paves the way to the development of speed-sensorless control algorithms.

Another challenge of RFO-VC is dependency on machine parameters like rotor resistance of the machine. This parameter changes as the machine is run for a long time due to its dependence on temperature. Thus, control algorithms involving estimation and adaptation of rotor-resistance have been developed. Control algorithms like direct-torque control (DTC) also have reduced dependency on machine parameters along with faster dynamic response.

PWM techniques are an intrinsic part of an IMD. AC voltage is generated on a volt-second average basis from the DC voltage using these techniques. However, an instantaneous error in the desired AC voltage and the voltage output from the VSI exits. Induction machine primarily being inductive in nature, the instantaneous volt-second error manifests into switching ripple in currents of the motor. Consequently,

this leads to ripples in the torque developed by the motor. One way of minimizing this ripples is to switch the power converters at a higher frequency. However, as mentioned earlier, semiconductor devices with higher power/voltage ratings have poor switching characteristics. This limits their switching frequency. Hence, a high-power, medium voltage 2L-VSI is inherently switched at much lower frequencies in comparison to their low-powered counterparts. This has a direct impact on the harmonic performance of the drive. Thus, specialized modulation methods like synchronous PWM techniques have been developed to ensure satisfactory harmonic performance of the drive. Further more advanced techniques like optimal PWM ensure considerably reduced harmonic distortion in motor currents and torque.

This thesis is primarily about high-power induction motor drives for industrial and railway traction application and focusses on all the three aspects mentioned before. Before delving into the discussions related the various PWM and control algorithms employed for IM, it is important to briefly review the modelling and field oriented control of the motor. Modelling of SCIM is generally done in a synchronous (d-q) frame where the d-axis is aligned along the rotor-flux vector of the motor. Field oriented control of SCIM is done either using a speed sensor or without one. Modelling of SCIM along with both the control techniques are reviewed in the next section.

1.2 Review of Modelling and Control of SCIM

1.2.1 Modelling

As mentioned earlier, modelling of SCIM can be done in various reference frames. First, the equations governing the dynamics of the motor in stator frame of reference (FOR) $(\alpha - \beta)$ are presented. The various vector quantities associated in IM are listed below.

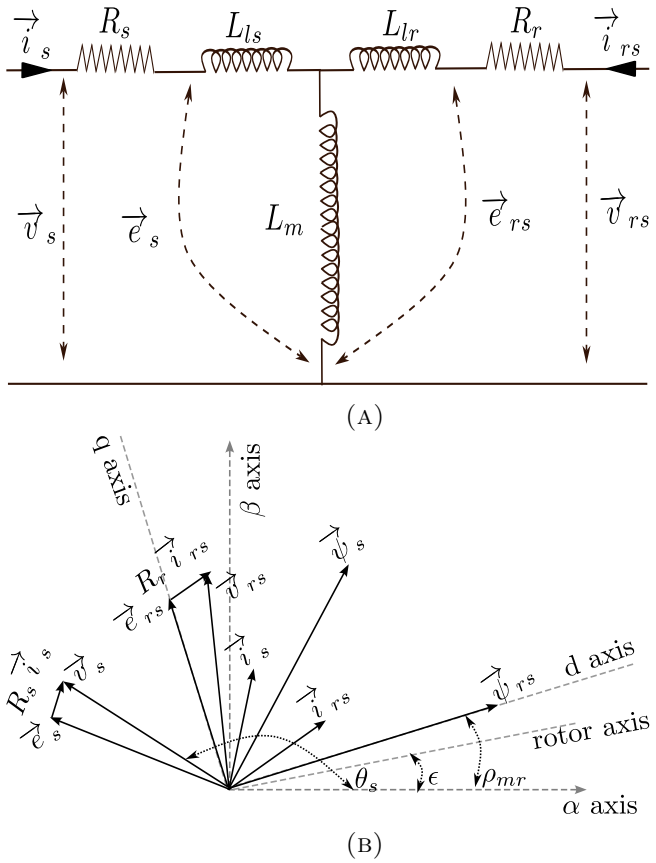


FIGURE 1.5: (A) Equivalent circuit of IM and (B) corresponding phasor diagram

$$
\begin{aligned}
\vec{v}_s &= v_{s\alpha} + jv_{s\beta} && \text{stator voltage vector in stator FOR} \\
\vec{v}_r &= v_{r\alpha} + jv_{r\beta} && \text{rotor voltage vector in rotor FOR} \\
\vec{v}_{rs} &= v_{rs\alpha} + jv_{rs\beta} = \vec{v}_r e^{j\epsilon} && \text{rotor voltage vector in stator FOR} \\
\vec{i}_s &= i_{s\alpha} + ji_{s\beta} && \text{stator current vector in stator FOR} \\
\vec{i}_r &= i_{r\alpha} + ji_{r\beta} && \text{rotor current vector in rotor FOR} \\
\vec{i}_{rs} &= i_{rs\alpha} + ji_{rs\beta} = \vec{i}_r e^{j\epsilon} && \text{rotor current vector in stator FOR} \\
\vec{\psi}_s &= \psi_{s\alpha} + j\psi_{s\beta} && \text{stator flux vector in stator FOR} \\
\vec{\psi}_r &= \psi_{r\alpha} + j\psi_{r\beta} && \text{rotor flux vector in rotor FOR} \\
\vec{\psi}_{rs} &= \psi_{rs\alpha} + j\psi_{rs\beta} = \vec{\psi}_r e^{j\epsilon} && \text{rotor flux vector in stator FOR}
\end{aligned} \tag{1.1}
$$

The equivalent circuit of IM and the corresponding phasor diagrams are shown in Fig.1.5a and 1.5b respectively.

The differential equations governing the dynamics of the motor are given by (1.2).

$$\begin{aligned}
\overrightarrow{v}_s &= R_s \overrightarrow{i}_s + \frac{d\overrightarrow{\psi}_s}{dt} \\
\overrightarrow{v}_{rs} &= R_s \overrightarrow{i}_{rs} + \frac{d\overrightarrow{\psi}_{rs}}{dt} \\
\overrightarrow{\psi}_s &= L_s \overrightarrow{i}_s + L_m \overrightarrow{i}_{rs} \\
\overrightarrow{\psi}_{rs} &= L_r \overrightarrow{i}_{rs} + L_m \overrightarrow{i}_r
\end{aligned} \tag{1.2}$$

Here, R_s and R_r are the stator and rotor resistances respectively, L_m is the magnetising inductance, L_{ls} and L_{lr} are the stator and rotor leakage inductances respectively. The stator and rotor inductance, L_s and L_r, are given by, $L_s = L_{ls} + L_m$ and $L_r = L_{lr} + L_m$.

Since the rotor is short-circuited in a SCIM, $\overrightarrow{v}_r = \overrightarrow{v}_{rs} = 0$. Further, since the mutual coupling between the coils continuously varies as the coils rotate. it is convenient to transform the stator and rotor coils into two orthogonal coils rotating in reference frame $(d-q)$ rotating at synchronous speed (ω_e). Transforming (1.2) into $d-q$ frame, separating the real and imaginary parts and using $\overrightarrow{v}_{rs} = 0$, the following equations are obtained

$$\begin{aligned}
v_{sd} &= R_s i_{sd} + \frac{d\psi_{sd}}{dt} - \omega_e \psi_{sq} \\
v_{sq} &= R_s i_{sq} + \frac{d\psi_{sq}}{dt} + \omega_e \psi_{sd} \\
v_{rd} &= R_r i_{rd} + \frac{d\psi_{rd}}{dt} - (\omega_e - \omega_r)\psi_{rq} = 0 \\
v_{rq} &= R_r i_{rq} + \frac{d\psi_{rq}}{dt} + (\omega_e - \omega_r)\psi_{rd} = 0 \\
\psi_{sd} &= L_s i_{sd} + L_m i_{rd} \\
\psi_{sq} &= L_s i_{sq} + L_m i_{rq} \\
\psi_{rd} &= L_r i_{rd} + L_m i_{sd} \\
\psi_{rq} &= L_r i_{rq} + L_m i_{sq}
\end{aligned} \tag{1.3}$$

The electromagnetic torque developed by the motor, (m_d), is given by

$$m_d = -\frac{2}{3}\frac{p}{2}\frac{L_m}{L_r} Im[(\psi_{rd} + j\psi_{rq})(i_{sd} + j i_{sq})^*] \tag{1.4}$$

Here, Im refers to the imaginary part of a complex number. If the synchronously rotating FOR is chosen such that $\psi_{rq} = 0$, the same gets aligned with the rotor-flux vector, $\overrightarrow{\psi_{rs}}$ of the machine. The synchronous speed, ω_e becomes equal to the speed of the rotating vector $\overrightarrow{\psi}_{rs}$, denoted by ω_{mr}. This results into the following mathematical relationships,

$$
\begin{aligned}
i_{rq} &= -\frac{L_m}{L_r} i_{sq} \\
\omega_{mr} - \omega_r &= -R_r \frac{i_{rq}}{\psi_{rd}} = R_r \frac{L_m}{L_r} \frac{i_{sq}}{\psi_{rd}} \\
i_{rd} &= \frac{1}{L_r}(\psi_{rd} - L_m i_{sd}) \\
\frac{d\psi_{rd}}{dt} &= -R_r i_{rd} = -\frac{R_r}{L_r}(\psi_{rd} - L_m i_{sd}) \\
\psi_{sd} &= L_s i_{sd} + \frac{L_m}{L_r}(\psi_{rd} - L_m i_{sd}) \\
\psi_{sq} &= L_s i_{sq} - \frac{L_m^2}{L_r} i_{sq}
\end{aligned} \tag{1.5}
$$

The term $\frac{\psi_{rd}}{L_m}$ can be defined as the rotor-flux magnetising current and is denoted by i_{mr} in this thesis. Similarly, the term $\frac{L_r}{R_r}$ is defined as the rotor time constant and is denoted by T_r in this thesis.

Using the notation of i_{mr} and T_r and substituting the expression of ψ_{sd} and ψ_{sq} from (1.5) into expression of v_{sd} and v_{sq} in (1.3) and simplifying the torque expression in (1.4), the dynamic equations of SCIM in $d-q$ FOR where the d-axis is aligned with along $\overrightarrow{\psi}_{rs}$, are given by [2], [3],

$$
\begin{aligned}
v_{sd} &= R_s i_{sd} + \sigma L_s \frac{di_{sd}}{dt} + \frac{L_m^2}{L_r}\frac{di_{mr}}{dt} + -\sigma L_s \omega_{mr} i_{sq} \\
v_{sq} &= R_s i_{sq} + \sigma L_s \frac{di_{sq}}{dt} + \frac{L_m^2}{L_r} i_{mr}\omega_{mr} + -\sigma L_s \omega_{mr} i_{sd} \quad \text{where} \quad \sigma = 1 - \frac{L_m^2}{L_s L_r} \\
i_{mr} + T_r \frac{di_{mr}}{dt} &= i_{sd} \quad \text{where} \quad T_r = \frac{L_r}{R_r} \\
\omega_{sl} &= \omega_{mr} - \omega_r = \frac{1}{T_r}\frac{i_{sq}}{i_{mr}} \\
m_d &= \frac{2}{3}\frac{p}{2}\frac{L_m^2}{L_r} i_{mr} i_{sq} \\
J\frac{2}{p}\frac{d\omega_r}{dt} &= m_d - m_l
\end{aligned} \tag{1.6}
$$

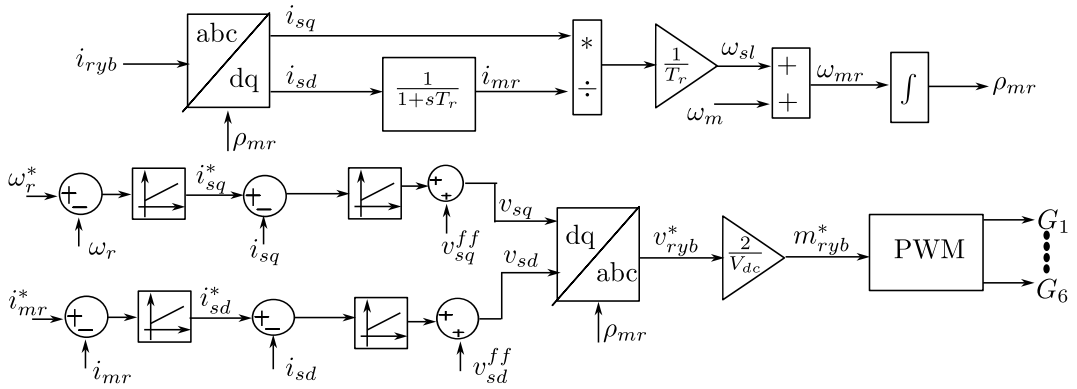


FIGURE 1.6: Control block diagram of RFOC of SCIM with speed sensor

Here, ω_{mr} is the angular synchronous frequency of $\overrightarrow{\psi}_{rs}$, ω_r is the electrical rotor speed, m_d is the developed electromagnetic torque, m_l is the load torque and J coefficient of mechanical inertia. v_{sd} and v_{sq} are the d-q axes components of stator voltage, i_{sd} and i_{sq} are the d-q components of stator current, i_{mr} is the rotor-flux magnetising current. p is the number of poles of the IM.

1.2.2 Field Oriented Control with Speed Sensor

Fig.1.6 shows the block diagram of a sensored rotor flux-oriented control (RFOC) scheme for a squirrel-cage induction motor (SCIM). The primary objective of RFOC is to achieve independent control of rotor flux and electromagnetic torque by aligning the synchronously rotating reference frame with the rotor flux vector. The measured three-phase stator currents, denoted by i_{ryb}, are first transformed into the stationary $\alpha\beta$ reference frame using the Clarke transformation and subsequently into the rotating dq reference frame through the Park transformation. The transformation angle ρmr corresponds to the electrical position of the rotor flux and is obtained from the speed-sensing and flux computation blocks. This transformation enables the decomposition of stator current into the direct-axis component i_{sd}, which controls the rotor flux magnitude, and the quadrature-axis component i_{sq}, which governs electromagnetic torque production.

The outer speed control loop compares the reference speed ω_r^* with the measured rotor speed ω_r, acquired using a shaft-mounted sensor such as an encoder or resolver. The resulting speed error is processed by a proportional–integral (PI) controller to

generate the reference torque-producing current i^*_{sq}. Simultaneously, the reference flux-producing current i^*_{mr} is set according to the desired flux level, typically chosen to ensure rated flux operation below base speed. The inner current control loops independently regulate i_{sd} and i_{sq} using PI controllers. To improve dynamic performance and ensure effective decoupling between the d and q-axes, feedforward compensation and cross-coupling terms (v^{ff}_{sq}, v^{ff}_{sd}) derived from the machine model are added to the output of the PI controllers to generate the d and q-axes components of the reference voltages, v_{sd} and v_{sq}. v^{ff}_{sq} and v^{ff}_{sd} are given by,

$$\begin{aligned} v^{ff}_{sq} &= (1-\sigma)L_s\omega_{mr}i_{mr} + \sigma L_s\omega_{mr}i_{sd} \\ v^{ff}_{sd} &= (1-\sigma)L_s\frac{di_{mr}}{dt} - \sigma L_s\omega_{mr}i_{sq} \end{aligned} \tag{1.7}$$

The reference voltages v_{sd} and v_{sq} are transformed back into the stationary frame via inverse Park and Clarke transformations, yielding the three-phase voltage references v^*_{ryb}. Further, these are normalized with respect to $\frac{V_{dc}}{2}$ to obtain the modulation indices, m^*_{ryb}, which further are applied to the voltage-source inverter (VSI) through a pulse-width modulation (PWM) block, which generates the gating signals G_1–G_6. The inverter supplies the SCIM, thereby closing the inner current loop through feedback of the measured stator currents.

The rotor flux producing current i_{mr} and slip angular frequency ω_{sl} are computed using measured variables and motor parameters. The synchronous electrical speed is obtained as $\omega_{mr} = \omega_m + \omega_{sl}$, and its integration yields the electrical angle ρ_{mr} required for coordinate transformations. Owing to the use of direct speed feedback, the sensored FOC scheme ensures accurate flux orientation, fast torque response, and robust operation over a wide speed range, making it suitable for high-performance SCIM drive applications.

1.2.3 Sensorless Field Oriented Control

Fig.1.7 illustrates the block diagram of a sensorless rotor flux-oriented control (RFOC) scheme for a squirrel-cage induction motor (SCIM), in which the mechanical speed sensor is eliminated and the required speed and rotor flux information are obtained through estimation. Similar to sensored FOC, the fundamental objective is to

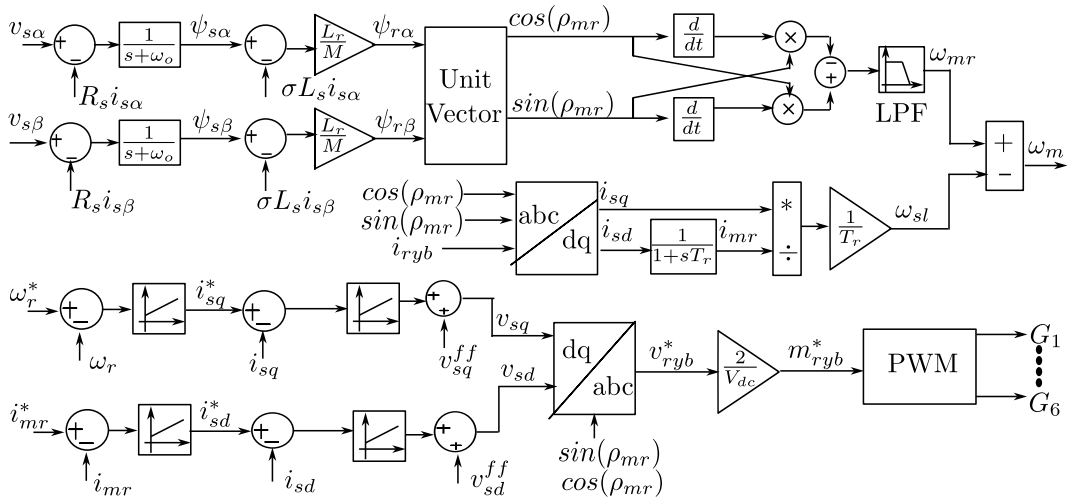


FIGURE 1.7: Control block diagram of RFOC of SCIM without speed sensor

achieve decoupled control of electromagnetic torque and rotor flux by aligning the synchronously rotating reference frame with the rotor flux vector. The measured three-phase stator currents i_{ryb} are transformed into the stationary $\alpha - \beta$ reference frame and subsequently into the rotating dq reference frame using the estimated electrical angle ρ_{mr}. This transformation yields the direct-axis current i_{sd}, associated with rotor flux control, and the quadrature-axis current i_{sq}, responsible for torque production. The outer speed control loop compares the reference speed ω_r^* with the estimated rotor speed ω_r. The resulting speed error is processed by a PI controller to generate the reference torque-producing current i_{sq}^*. The reference flux-producing current i_{mr}^* is set based on the desired operating flux level. The inner current control loops independently regulate i_{sd} and i_{sq} using PI controllers, producing the reference voltages v_{sd}^* and v_{sq}^*. Feedforward decoupling and compensation terms are included to mitigate the inherent cross-coupling between the d- and q-axis dynamics of the induction motor, thereby improving transient response and current tracking accuracy.

A key component of the sensorless FOC scheme is the speed and flux estimation block. $\alpha - \beta$ components of the stator flux vector, $\overrightarrow{\psi}_s$ is first estimated by integrating the $\alpha - \beta$ components of stator-voltage vector. Pure integration leads to several challenges in practical implementation. Thus, a low pass filter with a very small cut-off frequency is used. The transfer-function of the same is given by $\frac{1}{s+\omega_o}$. $\alpha - \beta$

components of the rotor flux vector is further estimated using machine model. The corresponding unit vectors are then calculated as,

$$cos(\rho_{mr}) = \frac{\psi_{r\alpha}}{\sqrt{\psi_{r\alpha}^2 + \psi_{r\beta}^2}}$$
$$sin(\rho_{mr}) = \frac{\psi_{r\beta}}{\sqrt{\psi_{r\alpha}^2 + \psi_{r\beta}^2}} \tag{1.8}$$

Further, the synchronous angular frequency, ω_{mr} is calculated from the unit-vector information. ω_{sl} is then estimated using i_{sq}, i_{mr} and T_r. Finally, the rotor speed is estimated from ω_{mr} and ω_{sl}.

Integration of ω_{mr} yields the estimated electrical angle ρ_{mr}, which is fed back to the coordinate transformation blocks to maintain flux orientation. The reference voltages v_{sd} and v_{sq} are transformed back into the stationary frame using inverse Park and Clarke transformations, producing the three-phase voltage references v_{ryb}^*. These voltages are applied to the voltage-source inverter (VSI) through a pulse-width modulation (PWM) block that generates the gating signals for the power semiconductor devices.

By eliminating the mechanical speed sensor, sensorless RFOC improves system reliability, reduces cost, and enhances suitability for harsh operating environments. However, the overall performance of the drive strongly depends on the accuracy of the flux and speed estimation, particularly at low speeds and under parameter variations. Despite these challenges, sensorless RFOC remains a widely adopted control strategy for SCIM drives in industrial and traction applications due to its favourable balance between performance, robustness, and cost.

A detailed literature review of various aspects of an IMD is presented next.

1.3 Literature Review

Based on the discussion from the previous sections, the various developments happening in the three aspects of high-power IMD is shown in Fig. 1.8. This list is a general one and not exhaustive in any sense. Each aspect of the drive will be discussed in

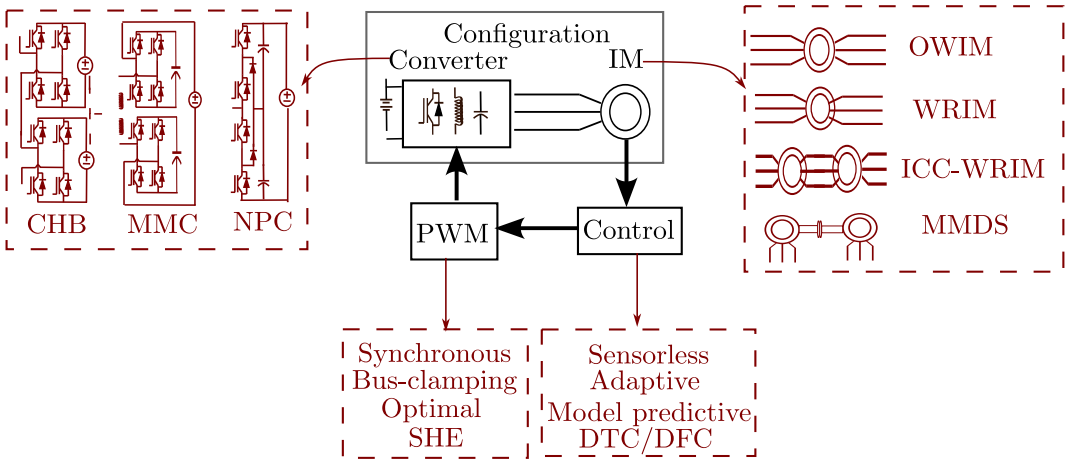


FIGURE 1.8: Developments in high-power IMD.

details starting from the machine and power converter topology. A detailed literature review on the various aspects of the IMD is presented next.

1.3.1 Configuration: Motor and Power Converter Topologies

As mentioned earlier, with increasing voltage level, power converter topologies shift from conventional 2L-VSI to multi-level VSI [4]. Introduced in the 1980s, the Neutral-Point Clamped (NPC) or diode-clamped topology [5] was the first significant development in this domain, offering improved performance over traditional two-level inverters by using multiple voltage levels to approximate a sinusoidal waveform. The NPC converter uses clamping diodes to divide the DC-link voltage, enabling the use of lower-rated power devices. This topology laid the groundwork for further exploration into high-performance inverters for industrial applications.

Subsequent advancements led to the development of other popular multilevel topologies such as the Flying Capacitor (FC) converter [6] and the Cascaded H-Bridge (CHB) converter [7]. While FC topology offers redundant switching states and high reliability, it suffers from complex voltage balancing and increased component count, especially for higher voltage levels. The CHB topology, in particular, has gained widespread attention due to its modular structure, ease of scalability, and the ability to use isolated DC sources, making it well-suited for renewable energy integration and motor drive systems. However, for application where a single high-voltage DC source is available, CHB topology fails due to requirement of multiple isolated DC

source. More recently, the Modular Multilevel Converter (MMC) [8] has become the preferred choice in high-voltage direct current (HVDC) transmission systems and other grid-connected applications. MMCs offer superior harmonic performance, modularity, and fault tolerance, though at the cost of increased control complexity and communication requirements.

From the perspective of electric machines, open-end winding induction motor (OWIM) drives are well-known to reduce the line current distortion and $\frac{dv}{dt}$ stress in high-power systems. In general, OWIM drives are operated with VSIs having half VA rating compared to equivalent SCIM drives. Both VSIs may have common [9], [10], [11] or isolated DC bus [12]. To reduce line current distortions and losses in VSIs, optimal [13], [14] and discontinuous PWM techniques [15] have been proposed.

Wound-rotor induction machines (WRIM) have become popular because of the great freedom of control that the machine offers. With both the stator and rotor windings accessible and connected to individual power converters, both rotor and stator current can be controlled independently to some extent. Vector control [16] and Direct Torque Control (DTC) [17] strategies have been applied to WRIMs, offering precise dynamic responses and decoupled control of flux and torque. For instance, research has demonstrated the efficacy of DTC in achieving fast torque and flux control in WRIMs, enhancing their performance in variable-speed applications. New field oriented control techniques [18] and DTC techniques [19] based on current reference frame have also been developed. Further, maximum-torque per ampere (MTPA) control for WRIM has been reported in [20]. A new series connected topology for WRIM drive has been presented in [21].

An inverse connected cascaded wound rotor induction machine (ICC-WRIM) is one of the configurations of WRIM which completely eliminates the need of using slip-rings. An ICC-WRIM consists of two WRIMs whose rotors are mechanically coupled to a common shaft, as well as, electrically connected in reverse phase sequence. Since the rotor terminals are not required to make electrical connection with any static electrical circuitry, slip-rings or brushes are not required for ICC-WRIM which

is a huge advantage over conventional WRIM. To make the machine size compact, both the WRIMs can be designed to be held in one mechanical frame. A model of cascaded doubly-fed induction machine in an arbitrary reference frame is presented in [22]. A standalone generator application is presented in [23], wherein the stator of WRIM 1 is connected to a power converter and the stator of WRIM 2 supplies an isolated load.

The concept of multiple motors mechanically coupled to a common shaft introduces modularity in the mechanical drive level. Each motor operates at the same speed and collectively shares the load torque. Such a configuration enhances system-level modularity by allowing selective motor redundancy, scalability in torque/power capability, and improved fault resilience. Thus, multi-motor drive systems (MMDS) are becoming popular for high power industrial applications like industrial pumps, fans and blowers [24]. Cage-rotor induction motor (IM) drives are generally chosen for such applications due to their ruggedness and low-maintenance. Each motor in such an MMDS is driven by its dedicated power converter which can commonly be a 2-level voltage source inverter (2L-VSI). Further, rotor-flux oriented vector control algorithm is implemented for the individual motor to control the torque produced by them. Series-connected, multiphase, multi-motor drive with independent vector control is presented in [25], [26].

1.3.2 Pulse-Width Modulation Techniques

As have been discussed earlier, switching frequency (f_{sw}), for such high-power converters, is maintained below 500Hz on account of high switching energy losses in IGBTs [9], [10]. Due to such low switching frequency, harmonic distortion in motor line-current [27], poor efficiency and degradation in overall performance of drive becomes prominent. In such cases synchronous PWM techniques are employed in order to ensure satisfactory harmonic performance. In such modulation methods, the number of pulses in the inverter pole-voltage in one fundamental cycle is maintained as an odd-triplen integer. This is termed as pulse number, P which can also be defined as the ratio of f_{sw} and modulating frequency, (f_m).

$$P = \frac{f_{sw}}{f_m} \tag{1.9}$$

Further, Synchronous PWM techniques ensure that half-wave, quarter-wave and three-phase symmetry are maintained in the inverter pole-voltages. It is thus clear that the constraint of low f_{sw} manifest as operation with low value of P. P is generally maintained as odd integer. [28], [29]. Low pulse number operation leads to high distortion in line current. Synchronized sine-triangle (SST) [30], selective harmonic elimination (SHE), optimal [31], [32], [33] and space vector [29], [34], [35], [36] PWM techniques are quite popular.

Due to simple and computationally efficient implementation of SST PWM, it is preferred over optimal and SV PWM schemes. In case of SST PWM¡ the gating pulses are generated by comparing the modulating signals with a triangular carrier. For a 2L-VSI, f_{sw} becomes equal to the frequency of the carrier signal, f_c. Thus, in case of SST PWM, P can be defined as

$$P = \frac{f_c}{f_m} \tag{1.10}$$

However, P for SST PWM is restricted to only odd-triplen integers (e.g. 3,9,15..) to ensure all waveform symmetries [37] and good line current quality [30]. Further, the triangular carrier must be synchronized with modulating signals to have common zero-crossings [30]. Restrictions on P and upper-limit on f_{sw} introduce sudden jumps in f_{sw} for SST PWM. Therefore, motor drive often suffers from huge transients on line-current [38]. Fundamental current extraction based methods have been proposed in literature for minimization of transients in line-current during pulse transitions [27]. Further, these techniques impose additional computational burden on micro-controllers. Multi-carrier sine triangle PWM has been proposed for 2L-VSI fed SCIM drive to reduce the common-mode voltage. However, differential mode harmonics components increase significantly in magnitude [39], [40]. It may lead to very poor current quality at low P.

Vector controlled high-power IM drives operated with SST or SO PWM, also suffer from transients during transition in P [36], [35]. At the junction of P changeover,

pulse-pattern (PP) applied by the 2L-VSI to the IM changes abruptly. An unconstrained change in PP may result into transients in line current and electromagnetic torque (m_d) [38].

Several pulse transition techniques have been proposed in the literature for mitigating the transients in motor drive. These techniques involve complex gain based stator voltage vector compensation for stator flux matching [35], fundamental current estimation based space vector to synchronous optimal PWM transition [27], sequential transition of phases for synchronous to selective harmonic elimination PWM [38], strategy considering sampling delays in space vector PWM [34] and optimal flux trajectory based pulse transition for synchronous optimal PWM. However, these techniques require complex offline and online computation [35] [27]. This increases either the computational burden or the storage capacity of the digital platform to be used to implement the strategy. Also, sequential transition of phases may lead to loss of waveform symmetry in the output voltages. Most of the strategies, proposed in the literature, are based on matching the fundamental output voltage of 2L-VSI. However, it is interesting to note that as the pulse pattern applied by the 2L-VSI changes, the magnitude and phase of harmonic voltages applied to the motor also change significantly. This leads to a transient in the harmonic current which can be extremely severe. The impact of transition in pulse pattern on the harmonic current of the motor has not been analysed mathematically in literature.

1.3.3 Speed-Sensorless Motor Control Algorithms

Speed sensorless operation of these drives is preferred in order to improve the overall reliability and robustness of the system [41]. Performance of sensorless field oriented control (FOC) of induction motor is highly dependent on the accurate estimation of stator flux vector, $\overrightarrow{\psi}_s$, using the information of applied stator voltage vector $\overrightarrow{v}_s$, stator-current vector, $\overrightarrow{i}_s$ and machine parameters. Simple integration of motor back-emf, $\overrightarrow{e}_s$, may not work due to issues like small DC-offset in measured currents [42], [43], [44]. Hence, a low-pass filter (LPF) with a small cut-off frequency ($\omega_o = 2\pi f_o$) is used to estimate the stator flux as shown below,

$$\Psi(s)_\alpha + j\Psi(s)_\beta = \frac{1}{(s+\omega_o)}[E(s)_\alpha + jE(s)_\beta] \tag{1.11}$$

Here,$\Psi(s)_x$ and $E(s)_x$, where $x \in (\alpha, \beta)$, are the s-domain transfer functions of the two quadrature components of $\overrightarrow{\psi}_s$ and $\overrightarrow{e}_s$. This method works well when the operating frequency of the motor, f_s, is fairly higher than f_o. However, at lower f_s, the phase and magnitude error in the estimated $\overrightarrow{\psi}_s$ due to the LPF becomes significant and degrades the over-all performance of the sensorless drive.

Several methods have been reported in the literature to improve the performance of a sensorless IM drive at very low speed [45] [46]. Generally, most of these methods can be divided into three categories:

1. Utilising anisotropic properties of the machine [47], [48].
2. Observer-based methods [49], [50].
3. Phase-locked loop (PLL) or Frequency-locked loop (FLL) based methods [51] [52].

For the first category, high-frequency (HF) signals are injected in the motor along with the fundamental voltage and the motor-speed is estimated by analysing the response of the motor to these HF signals due to its structural non-idealities like slot harmonics, rotor-saliency etc [53]. For the second category, popularly implemented observers are full-order [54], [55] and reduced order adaptive observers [56], model-reference adaptive schemes [57] [58], sliding-mode observers [59], extended-kalman filter based observers [60]. However, both the kinds of techniques have their own disadvantages. On one hand, speed estimation techniques using the machine non-idealities may lead to unwanted torque ripples and excessive power-loss in the machine [61] and on the other hand, machine-model based speed observer schemes are complex and computationally intensive.

Implementation of PLL is extremely popular for grid-connected inverters. However, variable frequency operation makes PLL based angle estimation methods quite challenging for motor drives. Moreover, PLL provides information pertaining to the synchronous frequency of the drive. For synchronous machine based drives, the rotor

speed is same as the synchronous frequency. However, for induction machine based drives, the difference of slip speed has to be accounted in to estimate the rotor speed.

Sensorless algorithms for different configurations of induction motor apart from the popular squirrel cage rotor structure are also explored in the literature. For example, two such control techniques for double inverter fed slip-ring induction machines are proposed in [16], [62]. Novel frequency profiles for the stator side and rotor side converters are proposed in these papers which ensures that both stator and rotor frequencies do not approach the filter-cutoff frequency even when the machine operates at lower speed. A model-reference adaptive system observer is proposed in [63] for stand-alone doubly fed induction generator. Speed estimation using adaptive full-order observer for dual inverter fed open-end winding induction motor is reported in [64]. Similarly, an adaptive speed observer for a dual-stator winding induction generator is presented in [65].

This presents a broad literature survey of high-power induction drives. Based on this literature survey, a few research gaps have been identified which became motivation of the research problem. The same is discussed next.

1.4 Research Problem

From the literature review, it is clear that a lot of work has been done in all the three aspects of a induction-machine based high-power drive. However, there are still some significant research gaps. Though multi-level converters have gained extreme interest in the research community, the industry is still reluctant to accept such power converters for electric drive applications mainly because of issues like reliability. Thus, the thesis focuses on different configurations of SCIM with 2L-VSI as the power converter. Further, the focus is also on PWM techniques and the challenges associated with these PWM techniques under closed-loop control of the drive. The main research gaps identified in this thesis are enumerated below:

- High-power IMD are invariably operated using rotor-flux oriented vector-control with synchronous PWM techniques. As mentioned earlier, P is restricted only to be odd-triplen integer in case of SST PWM and transitions in P has significant

impact on the performance of the closed-loop control of the drive. Particularly, the transition from $P = 9$ to $P = 3$ is very critical. Sudden unconstrained change in pulse number of the 2L-VSI leads to severe transients in the motor line-currents and torque. and invariably leads to very large transients in the line-current. The instantaneous values of current can go to as high as three or four times the rated current. This may activate the over-current protection of the drive and stop the motor. This is a practical problem faced in many industrial and traction drives. However, a theoretical study to identify the cause of these transients is required to be done.

- Further, efforts should be made to incorporate intermediate values of P, such as $P = 7$ and 5. This will limit the change in f_c as opposed to when the transition directly from $P = 9$ to $P = 3$ happens. A detailed theoretical and experimental study is required to establish the performance of the drive operated with SST PWM with odd non-triplen values of P such as 7&5.
- SST PWM is extremely popular for such applications due to ease of its implementation. On the other hand, optimal PWM techniques offer much superior harmonic performance at the cost of increased computational and memory related burden on the micro-controller. Thus, a combination of both SST PWM and SO PWM wherein SST PWM is employed for higher values of P and SO PWM is employed for lower values of P can be developed.
- OWIM drives with two 2L-VSI feeding power from both ends of the stator of SCIM allows many flexibilities while implementing modulation methods. The suitability of OWIM drives particularly for railway traction application should be investigated. New SST modulation schemes can be developed for OWIM drives.
- OWIM drive consists of two inverters and hence two sets of carrier signals in case of SST PWM. Optimization of SST PWM schemes for OWM drives based on creating phase shift between the carrier signals can be explored.
- From the perspective of closed-loop control, sensorless control techniques for

caged-rotor induction motor drives have been clearly established in the literature. However, performance of such control algorithms under low-speed operation is still a challenge. It will be interesting to see if a sensorless control algorithm can be developed for other topologies of IMD like the MMDS which can give better performance at low-speed.

1.5 Objectives and Scope of Work

Based on the research gaps identified in the previous section, the broad objectives and the scope of the work is presented below.

- A detailed theoretical and experimental study regarding the performance of SCIM drive operated with SST PWM with $P = 7$ and $P = 5$ is done.
- A synchronous optimal hybrid (SOH) PWM scheme consisting of asynchronous PWM (AST), SST and SO PWM has been developed for a high-power drive. In this scheme, the drive is started with AST PWM, and then at $f_m = 10Hz$, the operation changes to SST PWM and finally at $f_m = 28Hz$, SO PWM is used. A particularly interesting way of implementing SO-PWM has been developed which ensures no extra computational and memory related burden on the DSP.
- A pulse transition strategy for vector-control induction motor drive has been developed which ensures transition between various pulse patterns in the 2L-VSI with insignificant transient in the motor current and torque.
- Another method of tackling this problem of transient due to change in P is by reducing the jump in carrier frequency by introducing intermediate pulse numbers like even triplen and odd non-triplen. However, voltage waveform symmetry with these pulse numbers is not maintained for 2l-VSI. However, for another topology like the OWIM drive, such pulse numbers can be implemented with while maintaining waveform symmetry. Moreover, due to the presence of two isolated active front end converters, OWIM can be a very suitable substitute for 2L-VSI fed Y-connected IM drive for railway traction application.

- Another SST PWM scheme employing triplen values of P for OWIM drive is developed in order to further improve the harmonic performance of the drive. Here, dissimilar carrier signals are utilised for the two VSIs in the drive.
- Finally from the control point of view, a sensorless control algorithm has been developed for MMDS drive for applications which require low torque at low speed, like fans and pumps. For such loads, atleast one of the motor does not need to produce torque at low speed. Under no-load condition, the stator current, stator flux and rotor flux vector of the non-torque producing machine get aligned with each other. Thus, a PLL based on the stator current will accurately give the angle and speed of the rotor flux vector. Further, the speed of the rotor-flux vector becomes equal to the rotor speed under such condition.

1.6 Outline of the Thesis

Abstract

Table of Contents

Chapter 1 presents an introduction of the thesis with a detailed literature review on all three-aspects of the IMD. Further, research gaps that have been identified will also be presented and the motivation of the research work will be developed.

Chapter 2 initially discusses the issues regarding the operation of SCIM drive with conventional SST PWM with odd triplen values of P under closed-loop control. Further, it presents a detailed theoretical experimental study on the performance of Y-connected SCIM drive with SST PWM for $P = 7$ and $P = 5$. Following this, a synchronous optimal PWM scheme for Y-connected SCIM drive with the a pulse transition strategy in order to curb the transients in motor currents and torque will be proposed. Necessary mathematical analysis using the fundamental and harmonic model of the IM will be presented.

Chapter 3 introduces the suitability of using OWIM drive for railway traction application. A modified topology based on OWIM machine will be presented for railway traction application. Further, a SST PWM scheme will be developed for the

OWIM drive where all triplen and odd non-triplen pulse numbers can be utilised without affecting the waveform symmetries. A double-fourier series based mathematical framework will be developed in order to predict the harmonic profile of the motor phase voltages and currents.

Chapter 4 presents another SST PWM scheme for OWIM drive where the two inverters in the OWIM are operated using dissimilar carrier configurations. The drive is operated with triplen values of P only. For odd triplen values of P, the individual pulse numbers of the two VSIs are kept the same but a phase-shift is introduced between the two triangular carriers. For even triplen values of P, the two inverters are operated with consecutive odd triplen integers. The harmonic performance of the drive under the proposed PWM scheme is shown to be improved compared to the conventional PWM method. .

Chapter 5 will focus on multi-motor drive used industrial applications here the load torque demand from the drive is low at lower speed. This include loads such as fans/pumps etc. A speed-sensorless control algorithm for such a drive will be developed based on a PLL using the stator currents of the non-torque producing machine. A torque-sharing algorithm for a dual-motor drive system will also be developed with aim of reducing the copper losses.

Chapter 6 will present the final conclusions of the thesis and highlight the future-scope of work.

Bibliography and Appendix

Chapter 2

Synchronous PWM Scheme and Pulse Pattern Transition Strategy: Y-connected SCIM

2.1 Introduction

High-power induction motors drives are employed for industrial applications, like fans, blowers and pumps, and also for traction application like in railways. In India, electric locomotives are driven by multiple two-level VSI fed SCIM drives connected to a common DC bus. This DC bus voltage is maintained at 2.8 kV by two interleaved single phase front end conveters (FECs). SCIMs are rated at 2.2kV, 850kW having a rated fundamental frequency of 65Hz [66]. Typically, IGBTS rated at 4.5kV, 1000A are used in VSIs. Complete schematic of a traction converter is shown in Fig. 2.1. Switching frequency (f_{sw}) of IGBTs, used in traction converter, is restricted below 500Hz to curb switching energy losses [67], [28] [68]. Restrictions on f_{sw} reduces the number of PWM pulses generated within a fundamental cycle. This is quantified as pulse number (P), i.e. ratio between f_{sw} and the fundamental frequency (f_m). Operation of motor drive at low P leads to poor line current quality and unsatisfactory dynamic response of induction motor (IM) drive. Hence, synchronous

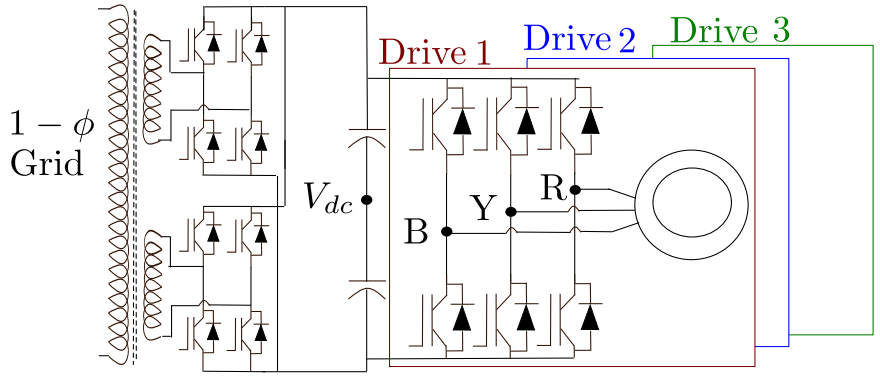


FIGURE 2.1: Schematic of SCIM based railway traction drive

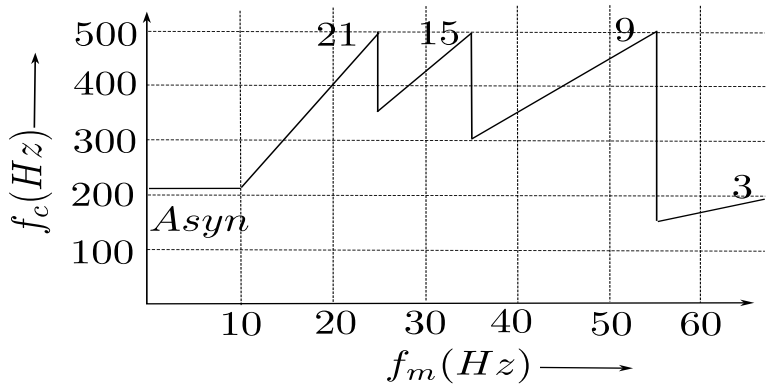


FIGURE 2.2: Variation of carrier frequency with modulating signal frequency for SST PWM

PWM techniques are used for achieving reasonable line current quality [37], [69], [70].

Synchronous sine-triangle (SST) PWM is a very popular modulation scheme employed for such applications. Since carrier signal frequency (f_c) is the same as the switching frequency, (f_{sw}) in a two-level VSI, P is also defined as the ratio between, f_c and modulating signal frequency, f_m as given by (1.10). The variation of f_c with f_m in case of SST PWM is shown in Fig.2.2. The corresponding values of P in different range of f_m is also shown in the same figure.

Various conditions of waveform symmetry are required to be maintained in the inverter pole-voltages during operation under low values of P. For example, half-wave symmetry is maintained to ensure there are no even-order harmonic and three-phase symmetry is maintained to ensure there are no triplen order harmonics. Further, quarter-wave symmetry is also maintained by ensuring that the zero-crossing of the modulating signal coincides with the zero-crossing of the carrier signal. This restricts P to be limited only to odd-triplen integers like $21, 15, 9$ and 3 as shown in Fig.2.2.

The objective of this chapter is to analyse the various issues regarding the operation of two-level VSI fed SCIM drive operated with SST PWM, specially under closed-loop control and then propose suitable solutions. First, the issue which arises due to the adverse impact of sudden change in f_c as P changes will be demonstrated through results from simulation of such a drive. It will be established that such transitions if done in an unconstrained manner leads to severe transients in

line-current. The severity of these transients become significant particularly for the transition from $P = 9$ to $P = 3$. Following this, a solution to incorporate intermediate odd non-triplen pulse numbers such as $P = 7$ and 5 is proposed. However, with suitable mathematical analysis it will be established that these values of P lead to very high harmonic distortion in the line-current. The harmonic performance improves significantly if these pulse numbers are implemented using synchronous optimal (SO) PWM technique. Thus, a new PWM scheme, namely, synchronous optimal hybrid (SOH) PWM scheme, which is a combination of SST and SO PWM techniques, will presented. Implementation of the proposed PWM scheme will be discussed in details. Moving forth, the issue regarding the transients in line current due to transition in P will be revisited and a thorough analytical study will be done for the same. From the findings of the study, a strategy to ensure smooth transition in pulse-patten will be presented. The developed strategy is generalized in the sense that the same can be used to ensure smooth transition between any two values of P within SST PWM, from SST PWM to SO PWM and within different values of P within SO PWM. Finally, the performance of the proposed SOH PWM scheme with the proposed pulse-transition strategy under closed-loop control will be verified through both simulation and experimental results.

2.2 Limitations in Performance of SCIM Drives Employing SST PWM

As shown in Fig.2.2, SCIM drive operated with conventional SST PWM is started with a constant value of f_c (fixed at 210Hz here). This is referred to as asnychronous PWM. At $f_m = 10$Hz, the modulation scheme is changed from asynchronous to synchronous PWM, with $P = 21$. In this region of operation, the value of f_c increases with f_m. As f_c reaches the maximum value of 500Hz, the value of P is changed to the next allowable value, that is 15. This happens at about $f_m = 24$Hz. Further, f_c again reaches 500Hz when f_m becomes 33Hz. At this point, P is changed to 9. Finally, at $f_m = 55$Hz, f_c becomes 500Hz with $P = 9$. Thus, the value of P is changed to 3.

It can be observed that, at the value of f_m corresponding to which P changes it

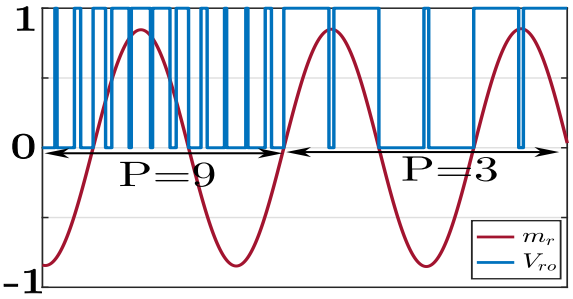


FIGURE 2.3: m_r and normalised V_{ro} during the transition between $P = 9$ and 3

value, the change in f_c becomes equal to $6f_m$. The value of f_m at which the transition from $P = 9$ to $P = 3$ (i.e. $f_m = 55$Hz) occurs, happens to be the highest among the values of f_m at which other transitions happen (i.e. $f_m = 10, 24$ and 33Hz). Thus, the change in f_c corresponding to the transition from $P = 9$ to $P = 3$ is maximum.

When the drive is operated with this PWM scheme and under rotor-flux oriented vector control, it is anticipated that such change in f_c or pulse pattern if done in an unconstrained manner will surely impact the performance of the drive. The impact is expected to be severe for the transition corresponding to $P = 9$ and 3. Simulation results demonstrating the performance of the drive with unconstrained pulse pattern transition are presented next.

2.2.1 Impact of unconstrained pulse transition on the performance of drive under closed-loop control

As the value of P changes in SST PWM, the pulse pattern (PP) applied by the 2L-VSI to the motor changes. Such transition in pulse pattern during the change of P from 9 to 3 is shown in Fig.2.3. The R-phase modulating signal and normalized pole-voltage of 2L-VSI corresponding to $P = 9$ and $P = 3$ are shown in this figure. The impact of unconstrained transition in pulse pattern for a vector controlled traction drive is demonstrated in this section. A 2.2kV, 850kW, 65Hz drive is operated in vector control mode over complete range of f_m, having variable f_c as shown in Fig.2.2. The complete set of parameters of the motor is presented in Appendix 1. There are four instances of pulse-pattern transition over complete range of f_m. Fig.2.4 presents the performance of the drive as obtained over simulation in Matlab/Simulink. Rotor flux

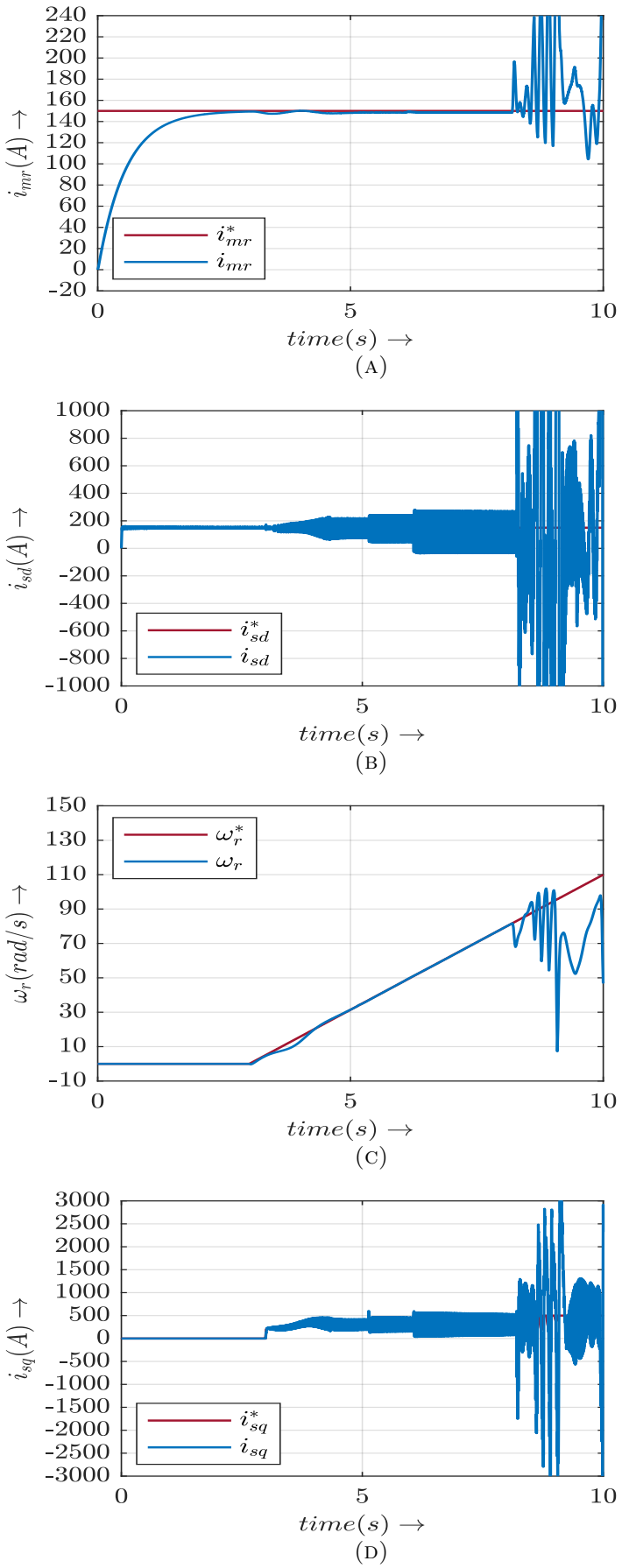


FIGURE 2.4: Performance of simulated vector controlled IM drive in terms of (a) i_{mr} (b) i_{sd} (c) speed and (d) i_{sq} with SST PWM.

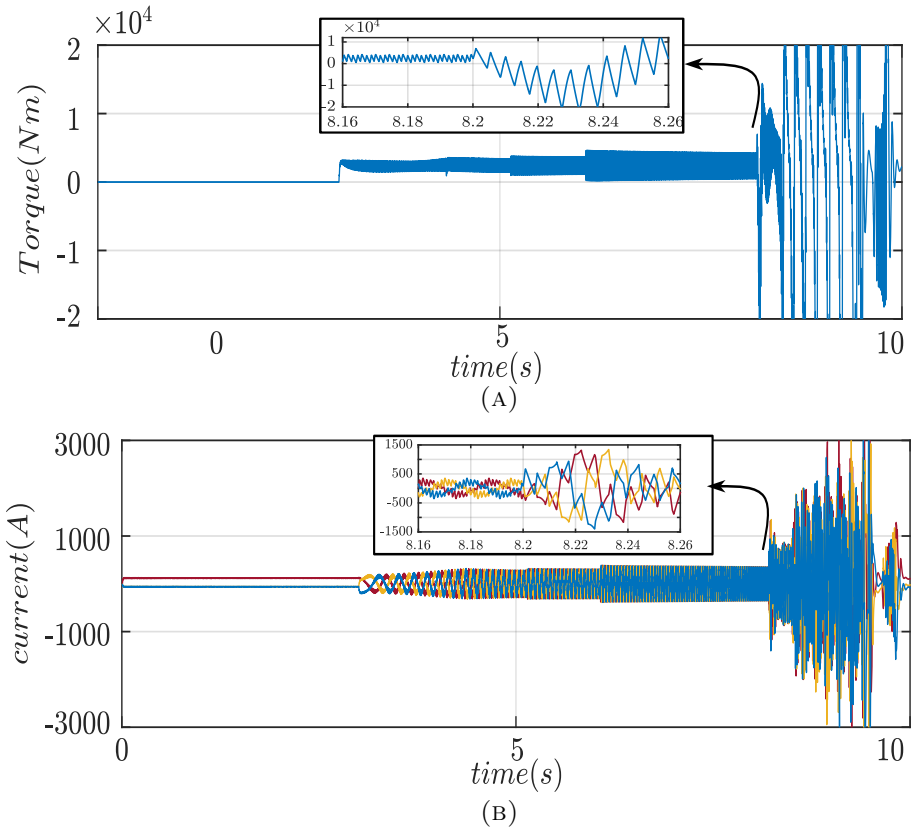


FIGURE 2.5: (a) Electromagnetic torque and (b) three-phase current through the complete range of f_m with SST PWM.

magnetising current (i_{mr}) and its reference (i^*_{mr}); d-axis current (i_{sd}) and its reference (i^*_{sd}); speed (ω_r) and its reference (ω^*_r); and q-axis current (i_{sq}) and its reference (i^*_{sq}) are shown in Fig.2.4a -2.4d, respectively. It is seen that these quantities are tracking their respective reference values until the IM drive is operated with $P = 9$. At $t = 8.2s$, an unconstrained transition from $P = 9$ to 3 is initiated. It is evident from these control quantities that the motor drive becomes unstable as P is changed from 9 to 3 and eventually the speed of the drive falls down to zero (Fig.2.4c). The same is reflected in the electromagnetic torque (m_d) and three-phase currents (i_R, i_Y, i_B) of the motor as shown in Fig.2.5. Such transients on hardware setup would result into over current trip. Thus, it is clear that an unconstrained transition from $P = 9$ to $P = 3$ has to be avoided.

2.2.2 SST PWM scheme for SCIM drive with intermediate non-triplen values of P

One possible way of to avoid a direct transition from $P = 9$ to $P = 3$ is to incorporate intermediate values of P such as $P = 7$ and 5. However, with SST PWM, for these non-triplen values of P, three-phase symmetry is lost in the inverter-pole voltages. This can be remedied by using multi-carrier PWM technique. However, that degrades the harmonic performance of the drive considerably. Performance of the drive with the non-triplen values of P is analysed using double-fourier series in this sub section. Further, the analytical findings are validated through simulations and experiments.

2.2.2.1 Single Carrier V/s Multi-carrier Implementation

A triangular carrier signal is compared with the three-phase modulating signals (m_R, m_Y, m_B)in order to generate the gating pulses in case of SST PWM. Quarter wave symmetry in the inverter pole voltages is ensured by keeping the positive zero-crossing of the modulating signals coincident with the positive or negative zero-crossing of the carrier signal. Since f_c is maintained as $f_c = P * f_m$, the angle pertaining to the carrier signal, θ_c is related to the angle pertaining to the modulating signal θ_m as

$$\theta_c = P * \theta_m \quad \text{where} \quad \theta_c = \int 2\pi f_c d\theta \quad \text{and} \quad \theta_m = \int 2\pi f_m d\theta \tag{2.1}$$

Thus, it can be inferred from (2.1), if P is maintained as an odd triplen integer, the zero-crossings of the modulating signals of all the three phases can be ensured to be coincident with the zero-crossing of the same triangular carrier. However, if P is made an odd non-triplen integer, the same is not possible. This is illustrated in Fig.2.6. For example, in case $P = 7$, the triangular carrier which is coincident with the the R-phase modulating signal will be lagging the Y-phase modulating by a phase-angle of 120^o leading the B-phase modulating signal by 120^o as shown in Fig. 2.6a. The same is shown for $P = 5$ in Fig.2.6b.

Such condition leads to the loss of three-phase symmetry in the inverter pole voltages and consequently triplen-order harmonics are introduced in the motor line-current. One possible way to mitigate this is to use three different carrier signals for

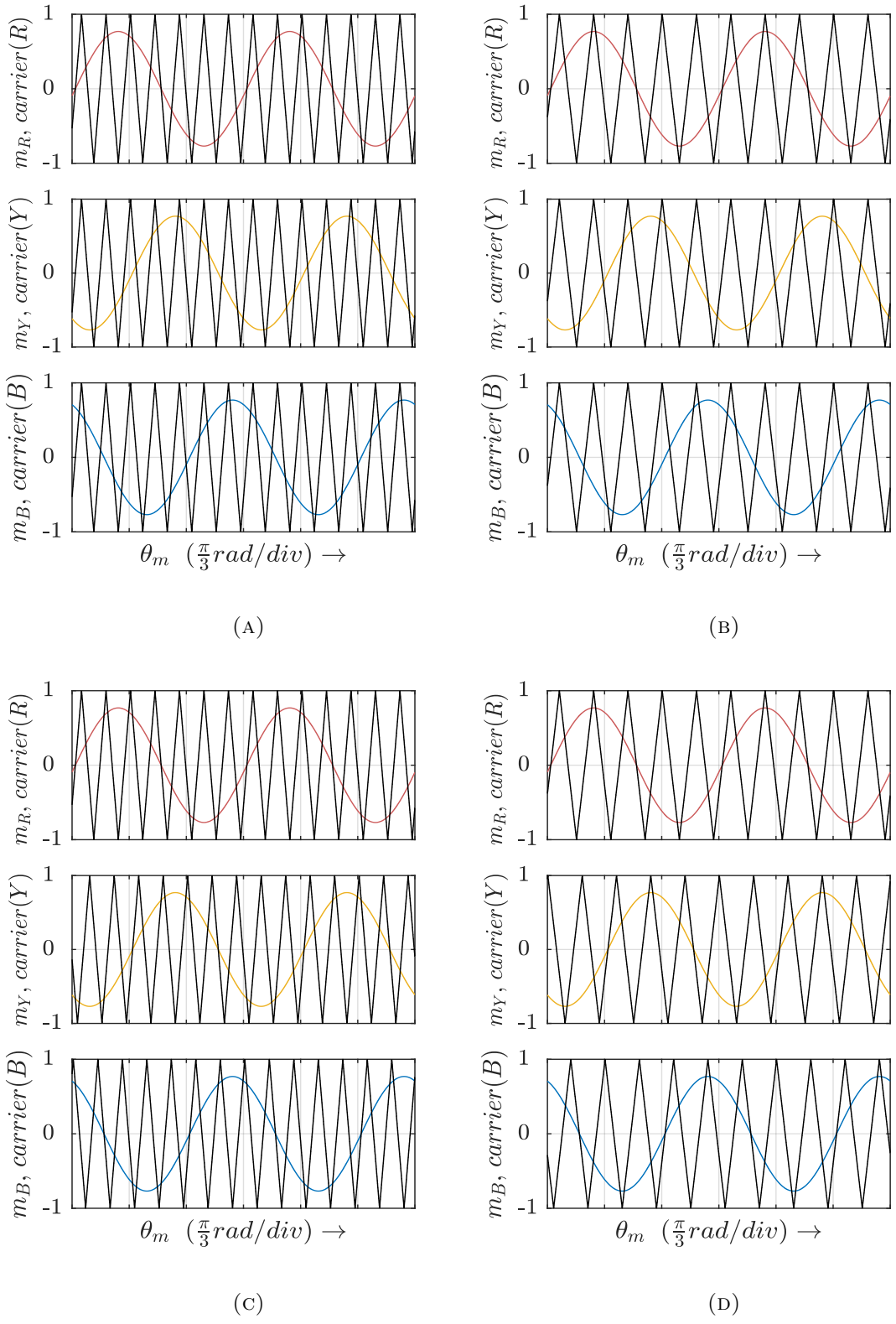


FIGURE 2.6: Modulating and carrier signal for (a) $P = 7$ (b) $P = 5$ with same carrier and for (c) $P = 7$, (d) $P = 5$ with different carrier signals for three-phases.

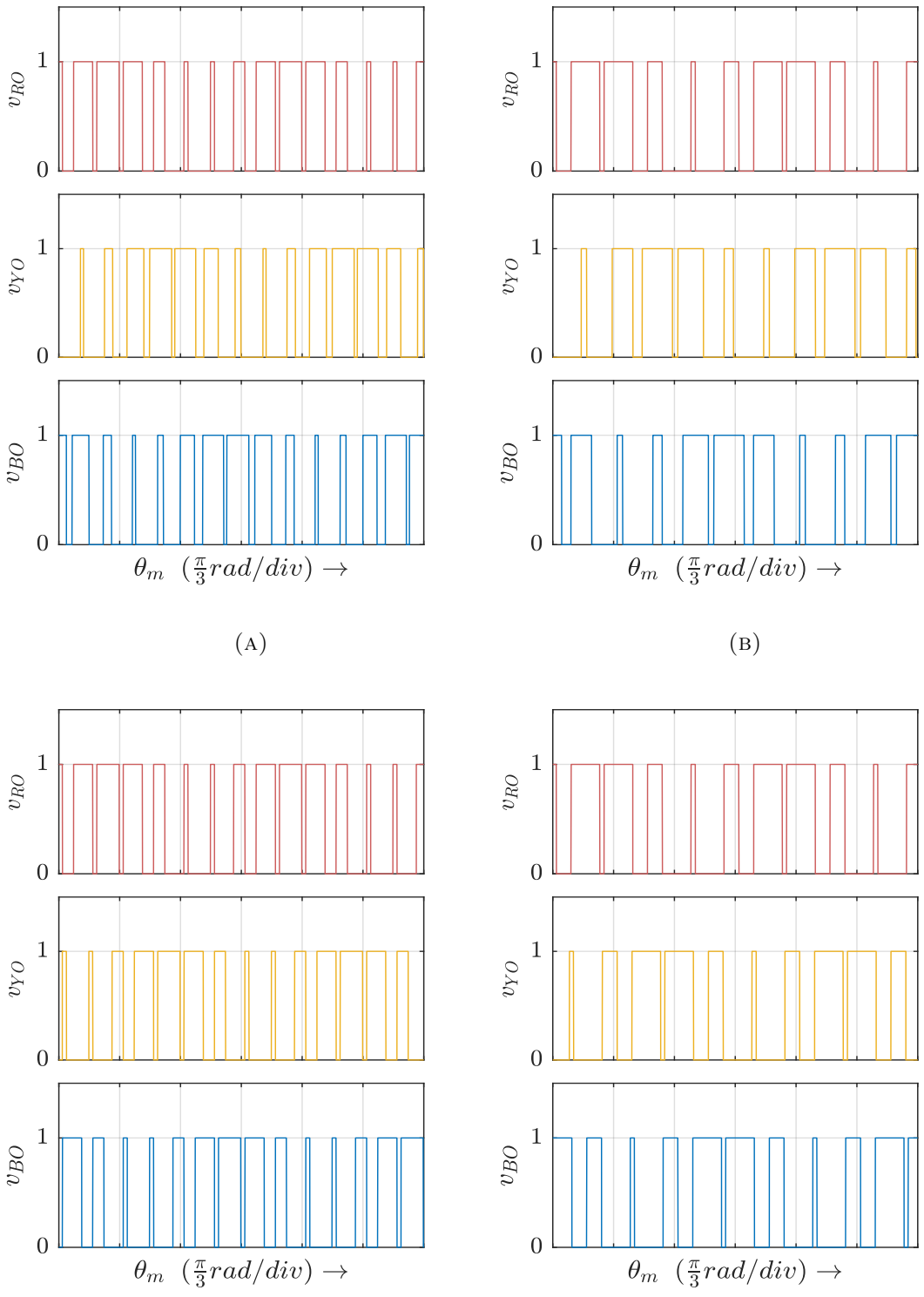


FIGURE 2.7: Normalised pole-voltages for (a) $P = 7$ and (b) $P = 5$ with same carrier and for (c) $P = 7$ and (d) $P = 5$ with different carriers for three phases.

TABLE 2.1: Combination of (m, n) for dominant lower order harmonics

Harmonic Order	$P = 7$	$P = 5$
$k = 5$	$(1, -2)$	$(1, 0)$
$k = 7$	$(1, 0)$	$(1, 2)$
$k = 9$	$(1, 2)$	$(2, -1)$

each phase of the modulating signal. Each carrier signal phase shifted with respect to each other by 120^o. In other words, three carrier signals can be used such that their respective zero-crossings coincides with the zero-crossings of the three-phase modulating signals. This is shown in Fig. 2.6c for $P = 7$ and for $P = 5$ in Fig. 2.6d. Three-phase pole voltages normalized with respect of DC bus voltage, V_{dc}, for $P = 7$ and 5 for both the cases, that is, with the same carrier and three different carrier signals are shown in Fig 2.7. Three phase symmetry can be seen missing in Fig. 2.7a and 2.7b whre the same carrier signal is used whereas the same is maintained in Fig. 2.7c and 2.7d wherein different carrier signals are used.

However, It is imperative to predict the harmonic profile of the inverter pole-voltages and consequently, the machine line-current for both the cases, namely, with a common carrier and with phase-shifted carrier for both $P = 7$ and $P = 5$. A mathematical framework based on double-fourier series is utilised in this thesis. Details about the basics of double-fourier series can be found in Appendix 7.

2.2.2.2 Harmonic analysis using Double-Fourier Expansion

Details of double-fourier expansion can be found in Appendix 7. The expression for the various harmonic components present in the inverter pole-voltages is given by (2). It is clear from (2), that a combination of (m, n, P) gives rise to k^{th} order harmonics in the pole voltages. Here, $k = mP + n$. Further, the values of (m, n) only within the range of $-3 \leq m, n \leq 3$ are to be considered. Based on this, the various combinations of (m, n) which gives rise to 5^{th}, 7^{th} and 9^{th} order harmonics in the inverter pole voltages for $P = 7$ and $P = 5$ is given in table 2.1.

The case pertaining to 9^{th} harmonic $(k = 9)$ is first considered. It is established in Appendix 7, that all odd order harmonics are present in the inverter pole-voltages.

However, it will be interesting to examine if they are present in the machine phase-voltages. The machine phase voltages (v_{RN}, v_{YN}, v_{BN}) is related to the inverter pole-voltages (v_{RO}, v_{YO}, v_{BO}) as

$$\begin{aligned} v_{RN} &= v_{RO} - \frac{v_{RO} + v_{YO} + v_{BO}}{3}; \\ v_{YN} &= v_{YO} - \frac{v_{RO} + v_{YO} + v_{BO}}{3}; \\ v_{BN} &= v_{BO} - \frac{v_{RO} + v_{YO} + v_{BO}}{3} \end{aligned} \tag{2.4}$$

The term $\frac{v_{RO}+v_{YO}+v_{BO}}{3}$ is also called as the common mode voltage or v_{CM}. Using (2), for the case of using a common carrier, the expression for v_{CM} corresponding to $k = 9$ and $P = 7$ is given in (2.5). Thus, 9^{th} harmonic component of v_{CM} becomes zero for $P = 7$ when a common carrier signal is used for all three phases. Consequently, from (2.4), it can be said that 9^{th} harmonic present in the inverter pole-voltages will also be present in the machine phase voltages leading to a 9^{th} harmonic component in the line-current. Thus, it is inferred that as three-phase symmetry is lost when using the same carrier for odd non-triplen P, triplen harmonics are introduced in the motor phase-voltage and consequently motor line-current.

$$v_{CM}|_{k=9} = \frac{A_1^2 cos(9\omega_o t + \frac{\pi}{2}) + A_1^2 cos(9\omega_o t - \frac{4\pi}{3} + \frac{\pi}{2}) + A_1^2 cos(9\omega_o t + \frac{4\pi}{3} + \frac{\pi}{2})}{3} = 0 \tag{2.5}$$

However, for the case of using different carriers for $P = 7$ and $k = 9$, v_{CM} is given by (2.6). It can be inferred that in this case, the 9^{th} harmonic component present in v_{RO} is also present in v_{CM} in equal magnitude and phase. Hence, they get cancelled in the v_{RN}. It is thus inferred that when three-phase symmetry is maintained using three-different carrier signals u for odd non-triplen P, triplen order harmonics are absent from the motor line current.

$$\begin{aligned} v_{CM}|_{k=9} &= \frac{A_1^2 cos(9\omega_o t + \frac{\pi}{2}) + A_1^2 cos(9\omega_o t - \frac{4\pi}{3} + \frac{7\pi}{6}) + A_1^2 cos(9\omega_o t + \frac{4\pi}{3} - \frac{\pi}{6})}{3} \\ &= A_1^2 cos(9\omega_o t + \frac{\pi}{2}) \end{aligned} \tag{2.6}$$

Now the case of 7^{th} harmonics or $k = 7$ is considered. When the same carrier signal is used for $P = 7$, 7^{th} harmonic component of v_{CM} is given by (2.7). On the other hand, 7^{th} harmonic component of v_{CM} when different carrier signals are used,

is given by (2.8). Thus, 7^{th} harmonic gets cancelled due to common mode voltage when a common carrier is used and it remains in the machine phase-voltage when different carriers are used.

$$\begin{aligned} v_{CM}|_{k=7} &= \frac{A_1^2 cos(7\omega_o t + \frac{\pi}{2}) + A_1^2 cos(7\omega_o t + \frac{\pi}{2}) + A_1^2 cos(7\omega_o t + \frac{\pi}{2})}{3} \\ &= A_1^2 cos(7\omega_o t + \frac{\pi}{2}) \end{aligned} \tag{2.7}$$

$$v_{CM}|_{k=7} = \frac{A_1^2 cos(7\omega_o t + \frac{\pi}{2}) + A_1^2 cos(7\omega_o t + \frac{\pi}{2} - \frac{2\pi}{3}) + A_1^2 cos(7\omega_o t + \frac{\pi}{2} - \frac{4\pi}{3})}{3} = 0 \tag{2.8}$$

A similar analysis for 5^{th} harmonic or $k = 5$ for $P = 7$ is also done. The expression for v_{CM} for the two cases, that is same carrier and different carrier signals for three-phases are given by (2.9) and (2.10) respectively. It can be that v_{CM} becomes zero for the case of same different signal but it cancels the same in pole-voltages for the case of same carrier signal. Thus, it can be concluded that that 5^{th} harmonic will be present in the machine phase-voltages for when different carrier signals are used whereas they cancel when a common carrier signal is used.

$$\begin{aligned} v_{CM}|_{k=5} &= \frac{A_1^{-2} cos(5\omega_o t + \frac{\pi}{2}) + A_1^{-2} cos(5\omega_o t + \frac{\pi}{2}) + A_1^{-2} cos(5\omega_o t + \frac{\pi}{2})}{3} \\ &= A_1^{-2} cos(5\omega_o t + \frac{\pi}{2}) \end{aligned} \tag{2.9}$$

$$v_{CM}|_{k=5} = \frac{A_1^{-2} cos(5\omega_o t + \frac{\pi}{2}) + A_1^{-2} cos(5\omega_o t + \frac{\pi}{2} - \frac{2\pi}{3}) + A_1^{-2} cos(5\omega_o t + \frac{\pi}{2} - \frac{4\pi}{3})}{3} = 0 \tag{2.10}$$

The same analysis can be extended for $P = 5$ for all the three harmonics. Table 2.2 presents the results obtained from this analysis and predicts the order of harmonics present for $P = 7$ and $P = 5$ for both when a common and different carriers are used. This analysis is corroborated with results obtained on simulation and experiments in the next section.

2.2.2.3 Simulation Results

The conclusions obtained from analysis done using the double fourier series regarding operation of the Y-connected SCIM using SST PWM with $P = 7$ and $P = 5$ are validated by simulating a 850kW, 2.2kV, 65Hz SCIM drive on MATLAB/Simulink and running it using SST PWM with $P = 7$ and 5 with constant V/f operation.

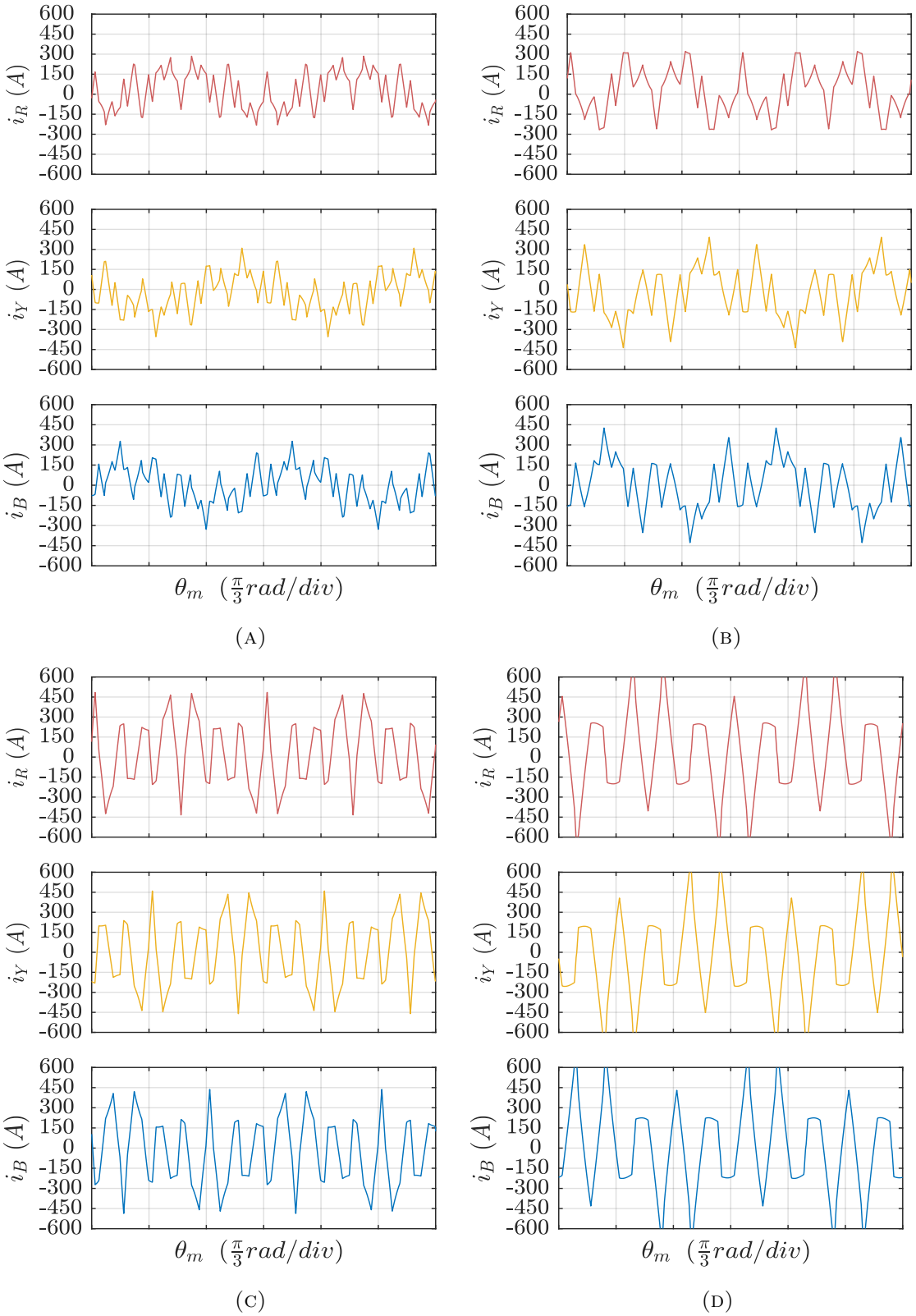


FIGURE 2.8: Simulation results pertaining to three-phase line current for (a) $P = 7$, (b) $P = 5$ with common carrier and (c) $P = 7$, (d) $P = 5$ with different carrier

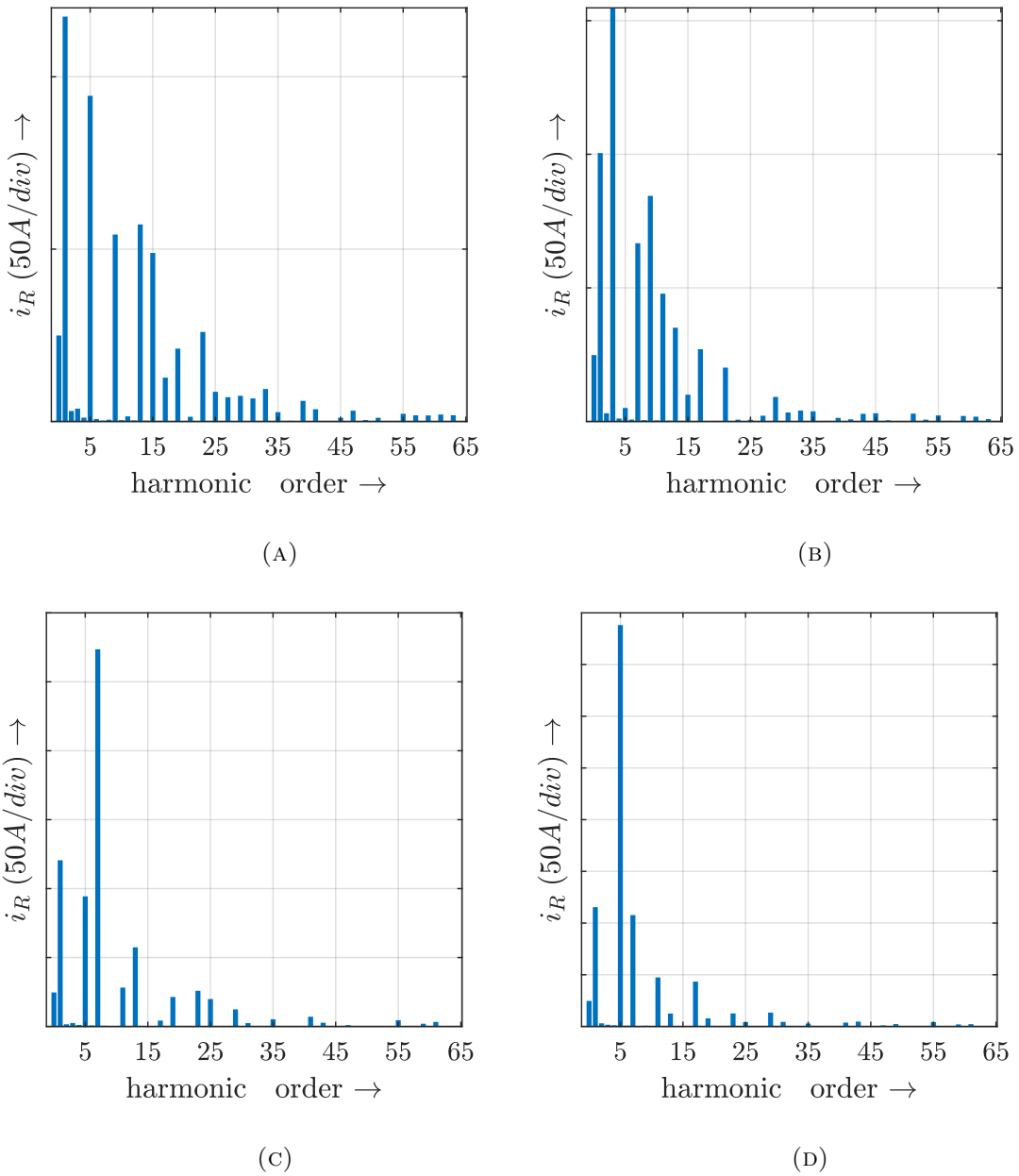


FIGURE 2.9: Simulation results pertaining to FFT of line current for (a)$P = 7$ ($i_{THD} = 118.17\%$) (b)$P = 5$ ($i_{THD} = 200.39\%$) with common carrier signal and (c) $P = 7$ ($i_{THD} = 248.41\%$) (d) $P = 5$ ($i_{THD} = 354.31\%$) with different carrier signals

TABLE 2.2

	$P = 7$		$P = 5$	
	Common Carrier	Different carrier	Common carrier	Different Carrier
$k = 5$	Absent	Present	Absent	Present
$k = 7$	Absent	Present	Absent	Present
$k = 9$	Present	Absent	Present	Absent

Further, experiments are performed on a 3.7kW, 415V, 65Hz laboratory prototype to verify the analytical findings. The parameters of the motor used for simulation and experiments are mentioned in Appendix 7 (Table 1).

The three phase lines current obtained in simulation for the four cases of $P = 7$ and 5 with common and different carriers are presented in Fig. 2.8. The operating modulating frequency in the present case is $f_m = 50Hz$. The cases corresponding to using same carrier signal for three-phases are shown in Fig. 2.8a and 2.8b for $P = 7$ and $P = 5$ respectively. Further, the cases corresponding to using different carrier signal for three-phases are shown in Fig. 2.8c and 2.8d for $P = 7$ and $P = 5$ respectively. It can be clearly seen from Fig. 2.8a and 2.8b, the shape of the current waveform for the three phases are quite distinct from each other. This is due to the fact that three-phase symmetry is lost in the machine phase voltage. However, upon using three different carrier signals, three-phase symmetry is restored in the currents as shown in Fig. 2.8c and 2.8a. The harmonic spectrum corresponding to the R-phase current (i_R) corresponding to all four cases is shown in Fig. 2.9. The harmonic spectrum of i_R corresponding to the case of common carrier signal for $P = 7$ and $P = 5$ are shown in Fig.2.8a and 2.8b respectively, while the same for the case of different carrier signals for $P = 7$ and $P = 5$ are shown in Fig.2.8c and 2.8d respectively. Triplen-order harmonics are present in the line-current in Fig.2.8a and 2.8b and they are absent in Fig.2.8c and 2.8d. However, the magnitude of other lower order harmonics like 5^{th} and 7^{th} significantly increase for the case of different carrier signals as can be seen in Fig.2.8c and 2.8d. The THD values corresponding to i_R are mentioned in the caption of the figure. From the THD values, it can be

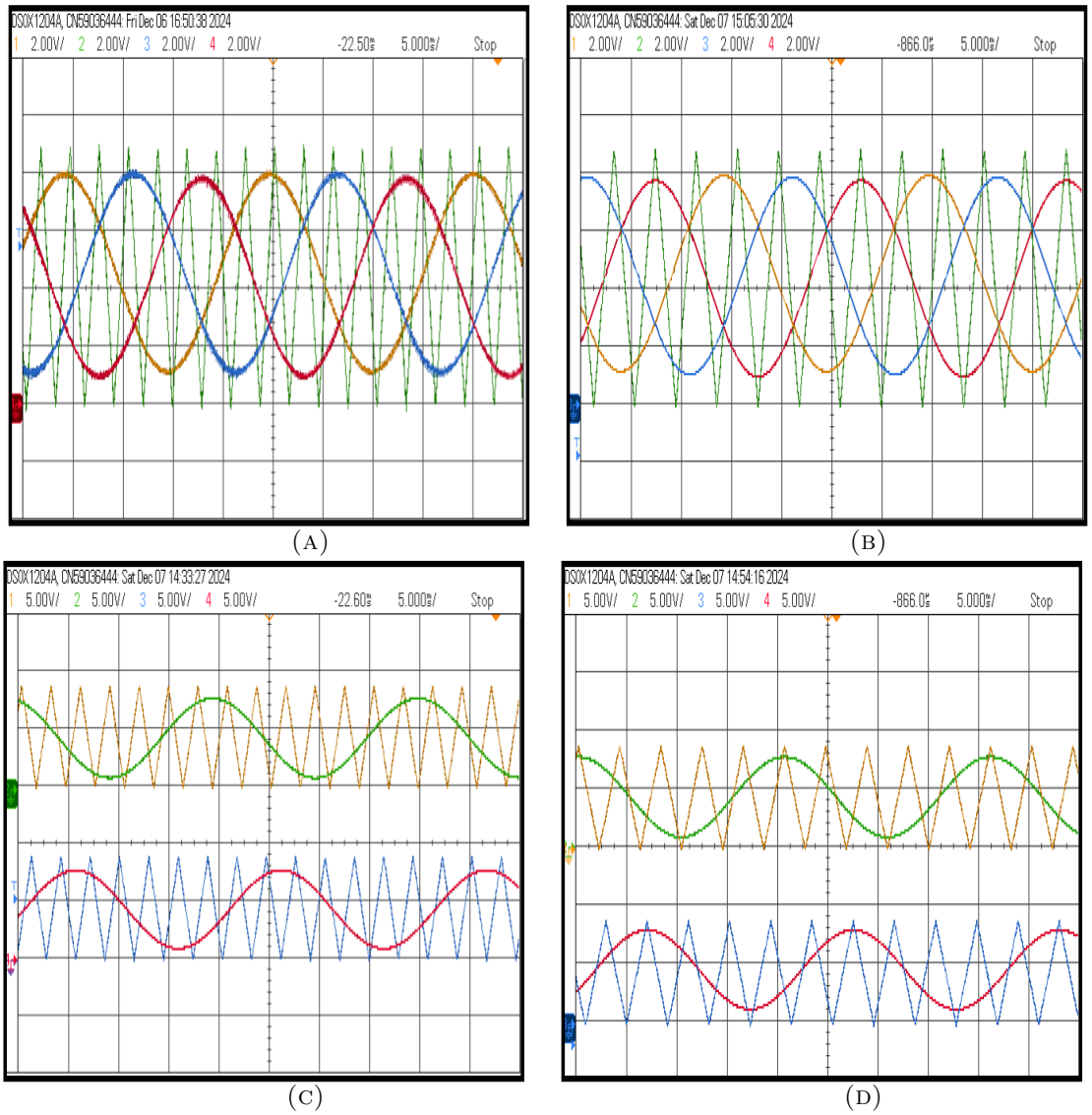


FIGURE 2.10: Experimental results pertaining to three-phase line modulating and carrier signal for (a) $P = 7$, (b) $P = 5$ with common carrier and (c) $P = 7$, (d) $P = 5$ with different carrier signals (x axis: 5ms/div)

inferred that harmonic performance with three different carriers is worse even though three-phase symmetry is maintained. This is due to significant increase in other lower order harmonics.

2.2.2.4 Experimental Results

Both the cases of having the same carrier and three different carrier signals for the three-phases are implemented experimentally for both $P = 7$ and $P = 5$. The modulating and carrier signals for four cases is shown in Fig. 2.10. In case of having

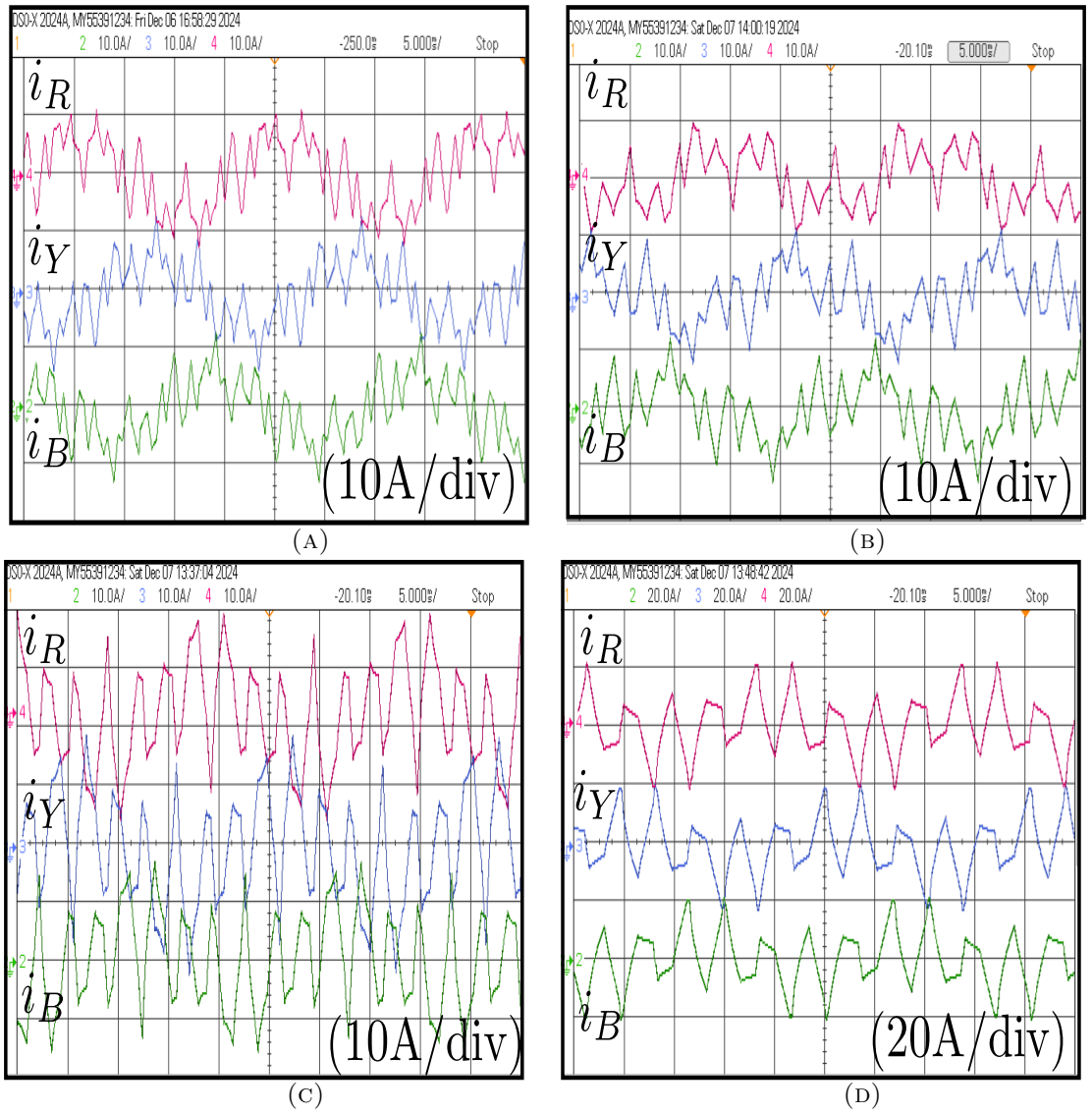


FIGURE 2.11: Experimental results pertaining to three-phase line current for (a)$P = 7$ (b) $P = 5$ with common carrier and (c)$P = 7$, (d) $P = 5$ with different carrier signals (x axis: 5ms/div)

different carriers for the three-phases shown in Fig. 2.10c and 2.10d, only two phases have been shown because of the restriction of four channels in the oscilloscope. The experimentally measured three-phase current corresponding to the simulation results in Fig. 2.8 is presented in Fig. 2.11. The overall shape of the current waveform as obtained in simulation and experiment are similar. It is experimentally corroborated that three phase symmetry is lost when the same carrier signal is used for all the three-phases for an odd triplen value of P. However, the same is restored when

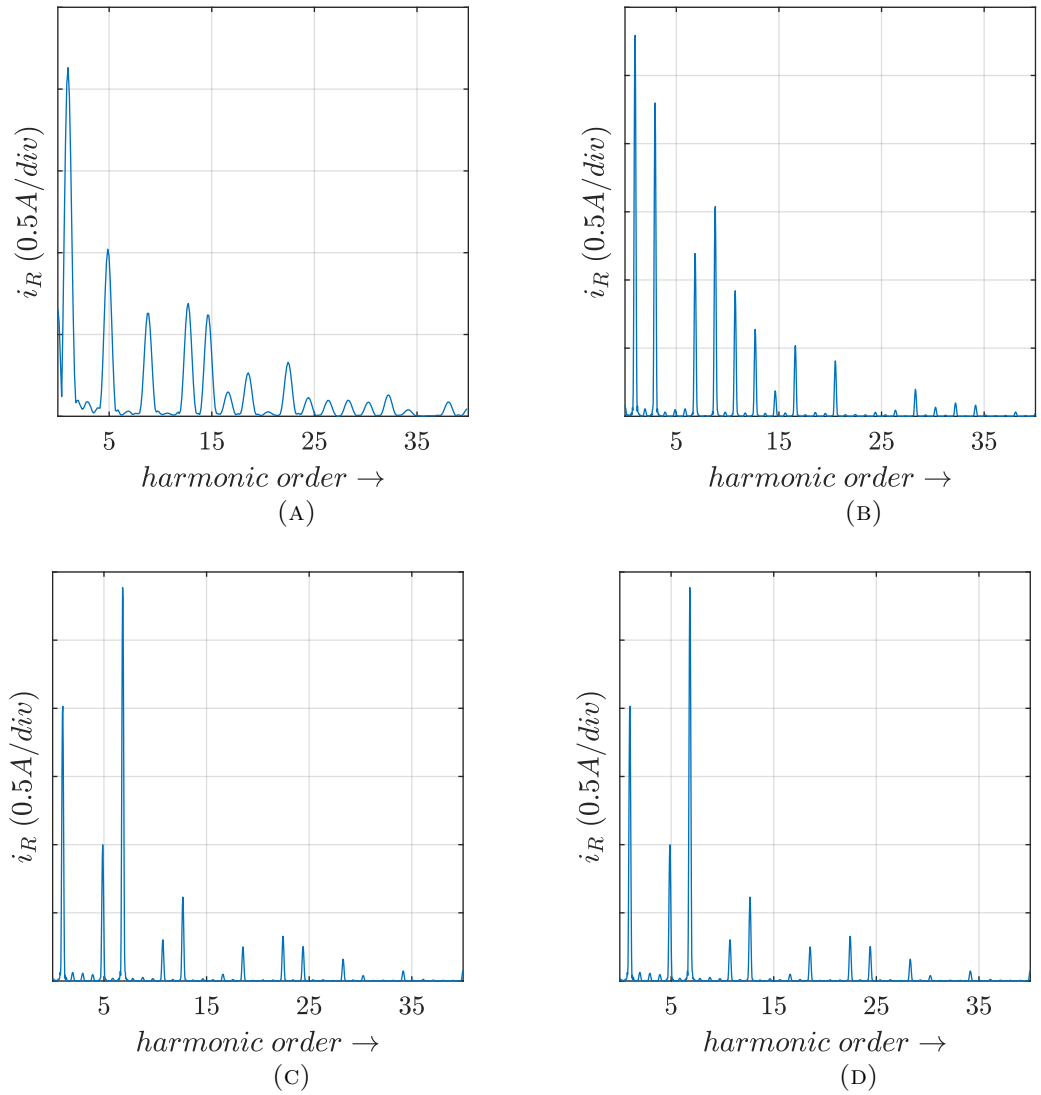


FIGURE 2.12: Experimental results pertaining to FFT of three-phase line current for (a)$P = 7$, (b) $P = 5$ with common carrier and (c) $P = 7$ (d)$P = 5$ with different carrier signals

three-different carrier signals are utilised. The experimentally FFT of the R-phase current is presented in Fig. 2.12. The harmonic spectrum obtained experimentally matches with that of simulation. Thus, all the inferences drawn from the simulation results hold true for the experimental results also.

2.2.2.5 Inferences from Results

From the mathematical analysis, simulation and experimental results, it can be inferred that for SCIM drive operated SST PWM with non-triplen values of P, using

a common carrier signal, leads to the triplen order harmonics in the machine-phase voltages and current. On the other hand, using three different carrier signals for three-phases, while triplen order harmonic are cancelled, 5^{th} and 7^{th} order harmonics increase significantly in the machine phase-voltage and current. Harmonic distortion for both the cases are quite high.

Thus, it can be concluded that simple implementation of non-triplen values of P in SST PWM for Y-connected SCIM is not advisable. However, such values of P can be implemented with more advanced PWM techniques like selective harmonic elimination (SHE) or synchronous optimal (SO) PWM technique. Out of these, SO PWM offers the best harmonic performance. For the range of f_m wherein the value of P is high, such as $P = 21, 15, 9$, implementation of SO PWM comes computationally intensive and requires high storage memory in the digital controllers like DSP. SST PWM in this region offers acceptable harmonic performance along with ease of implementation. Thus, a hybrid PWM technique, combining SST and synchronous optimal (SO) PWM, is proposed in the next section.

2.3 Synchronous Optimal Hybrid PWM Scheme

In the last section, it has been clearly established that implementation of odd non-triplen value of P directly with SST PWM, both a common carrier and different carrier signals for three-phases is not recommended from the point of view of the harmonic performance for a Y-connected SCIM drive. However, as established earlier,a direct transition from $P = 9$ to $P = 3$ in SST PWM is also not recommended due to the instability that comes in the closed-loop performance of the drive. Thus, this thesis proposes a PWM scheme which is a combination of SST and SO PWM for such drives.

The harmonic performance of SO PWM is found to be superior among the other synchronized PWM techniques [71], [72]. In this case, the switching in the pole-voltages of 2L-VSI are done at pre-determined angles, α_i, $(i = 1, 2...q)$. These angles are obtained by minimizing the weighted total harmonic distortion (THD) in voltages (V_{WTHD}) which is a measure of the line-current THD [1]. V_{WTHD} is given

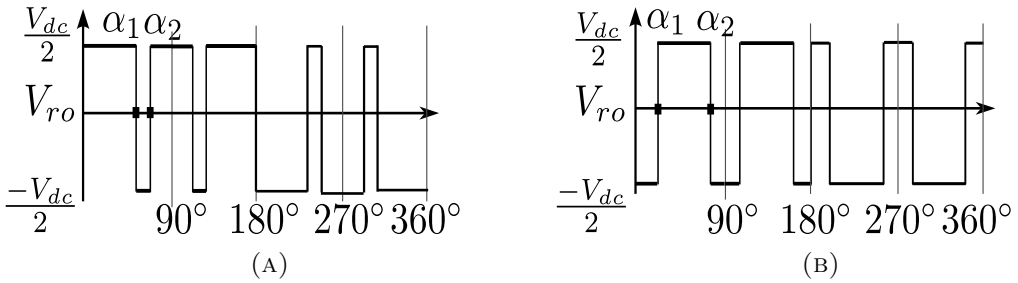


FIGURE 2.13: (a) Type A and (b) type B pulse pattern for $P = 5$

by

$$V_{WTHD} = \sqrt{\frac{\sum F_n^2/n^2}{F_1^2}} \tag{2.11}$$

Here, F_n is the magnitude of n^{th} harmonic voltage and F_1 is the magnitude of the fundamental voltage. Two kinds of optimal pulse patterns are possible for any given P, namely, type A and type B. This is depicted in Fig. 2.13. The expression of F_n for type A and B pulse pattern is given by [1],

$$\begin{aligned} F_n^A &= \frac{2V_{dc}}{n\pi}[1 + \sum_{i=1}^{N}(-1)^i 2cos(n\alpha_i)] \\ F_n^B &= \frac{2V_{dc}}{n\pi}[-1 + \sum_{i=1}^{N}(-1)^{(i-1)} 2cos(n\alpha_i)] \end{aligned} \tag{2.12}$$

Thus, for a given P, $\alpha_i s$ are obtained by minimizing (2.11) under the constraints [1],

$$\frac{F_1}{\frac{2V_{dc}}{\pi}} = M = M^* \text{ and } 0 < \alpha_1 < .... < \alpha_q < \frac{\pi}{2} \tag{2.13}$$

Here, M is the modulation index and M^* is the desired modulation index.

A synchronous optimal hybrid PWM technique which is a combination of asynchronous sine-triangle (AST), SST and SO PWM is proposed in this thesis for high-power application. SST PWM is utilised when P is high (i.e. $P = 21, 15, 9$) and SO PWM is utilised when P is low (i.e. $P = 9, 7, 5$). Each PWM technique is applied over suitable range of f_m. Fig. 2.14 shows the variation of f_{sw} as f_m varies.

The realisation and implementation of the PWM technique as the drive is operated in rotor flux oriented (RFO) vector control mode is discussed in detail in this section. Correct information pertaining to θ_s, which is the angle associated with

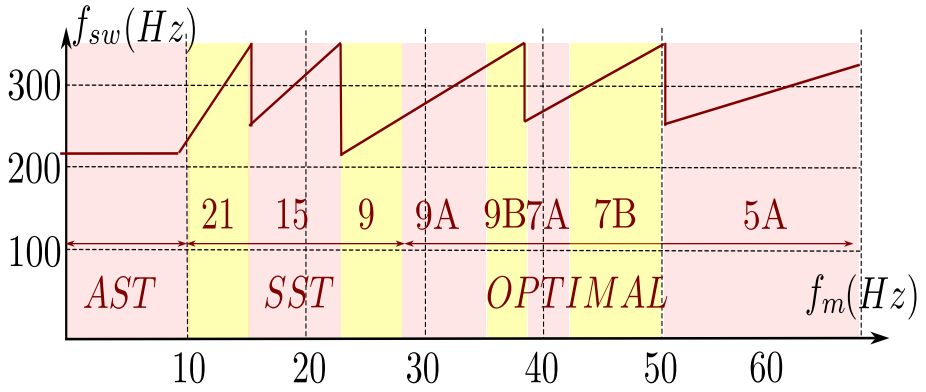


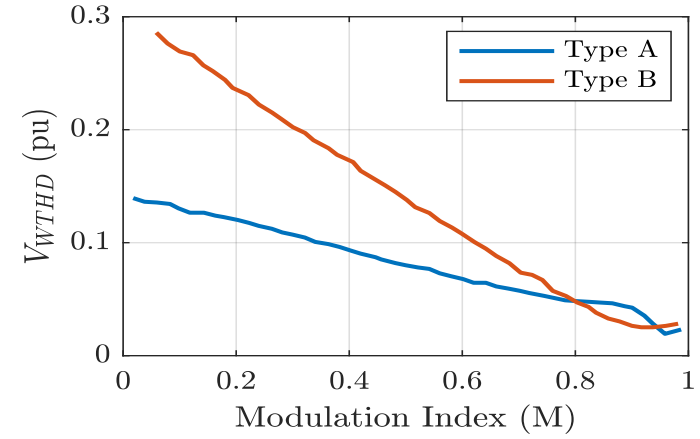
FIGURE 2.14: Plot of f_{sw} over complete range of f_m for SOH PWM

stator voltage vector ($\overrightarrow{v}_s$), is very crucial for proper implementation of both SST and SO PWM. However, θ_s is not directly available when the drive operates under vector-control mode. Moreover, in case of SO PWM, α_i, $(i = 1, 2..q)$ are usually pre-calculated for discrete values of modulation index (M) and stored a look-up table in the DSP/micro-controller. This requires additional memory. Since α_i are available corresponding to discrete value of M, the need to extrapolate these angles arises as M varies smoothly with speed. This leads to under-fluxing or over-fluxing the machine which impacts its performance.

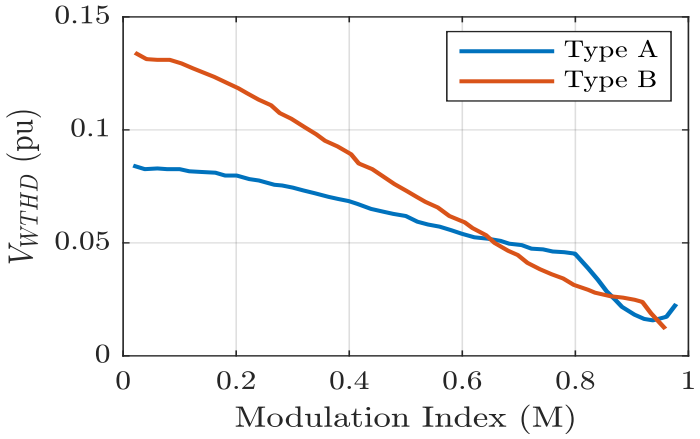
2.3.1 Realisation of proposed SOH PWM scheme

As indicated in Fig. 2.14, the drive is operated using AST for $f_m \leq 10$Hz with a constant $f_{sw} = 210$Hz. Beyond 10Hz, a triangular carrier with $P = 21, 15$ and 9 is utilised sequentially to implement SST PWM. At higher values of P, SST PWM exhibits satisfactory harmonic performance. However, its performance deteriorates at lower values of P. Further, in case of SST PWM, the next allowed value of P after $P = 9$ is $P = 3$, which becomes substantially small. Thus, in order to incorporate intermediate values, such as $P = 7, 5$, a transition is made from SST to SO PWM with $P = 9$ at $f_m = 28$Hz.

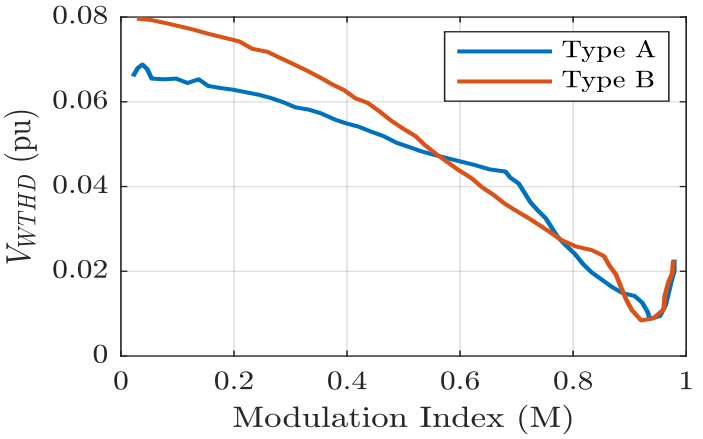
Theoretically estimated V_{WTHD} for both type A and B pulse patterns for $P = 5, 7$ and 9 over the complete range of modulation index is shown in Fig. 2.15a-2.15c respectively. It is evident from the figures that for each value of P, type A offers better harmonic performance over certain range of M, while type B outperforms



(A)



(B)



(C)

FIGURE 2.15: Theoretically estimated V_{WTHD} for both Type A and type B pulse pattern for (a) $P = 5$ (b) $P = 7$ (c) $P = 9$ [1]

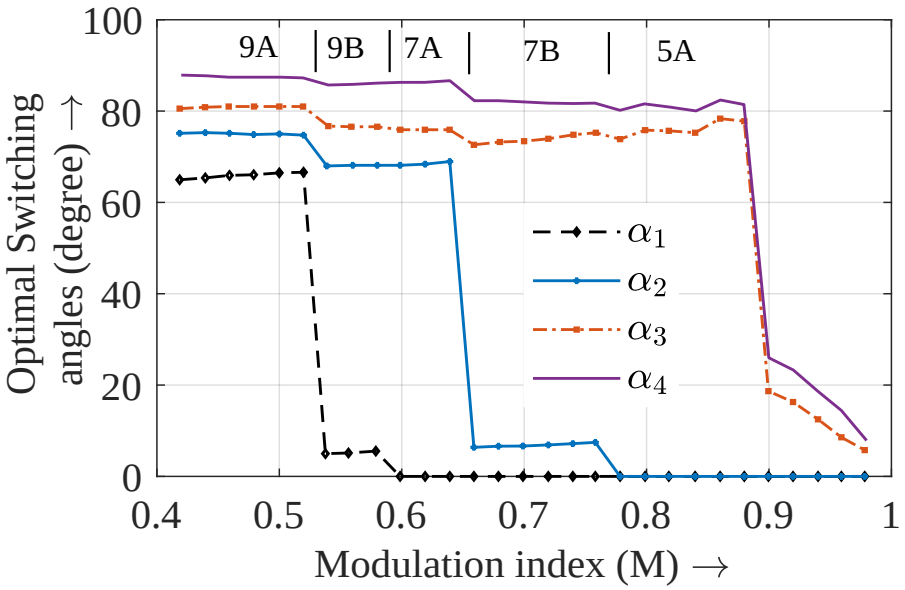


FIGURE 2.16: Variation of α_i over the complete range of M

TABLE 2.3: Optimal Vector Sequence

P	Vector Sequence
9A	$A - Z_A - A - Z_A - A - B - Z_B - B - Z_B - B$
9B	$Z_A - A - Z_A - A - B - A - B - Z_B - B - Z_B$
7A	$Z_A - A - Z_A - A - B - Z_B - B - Z_B$
7B	$A - Z_A - A - B - A - B - Z_B - B$
5A	$A - Z_A - A - B - Z_B - B$

in other range. As seen in Fig. 2.15c, for SO PWM with $P = 9$, the harmonic performance of the type B pulse pattern surpasses that of type A at approximately $M = 0.55$, which corresponds to $f_m = 36$ Hz. Consequently, as shown in Fig. 2.14, the pulse pattern is switched from type A to B at $f_m = 36$ Hz for $P = 9$. Furthermore, as f_{sw} reaches its maximum value, P is sequentially reduced to the next allowed values, namely 7 and then 5. Similar to the case of $P = 9$, both Type A and B pulse patterns have been employed for $P = 7$ within the modulation ranges where each offers superior harmonic performance, as illustrated in Fig. 2.14. The change in pulse pattern due to change in pulse numbers and also transition from type A to B within a pulse number is highlighted by change of background color in Fig.2.14.

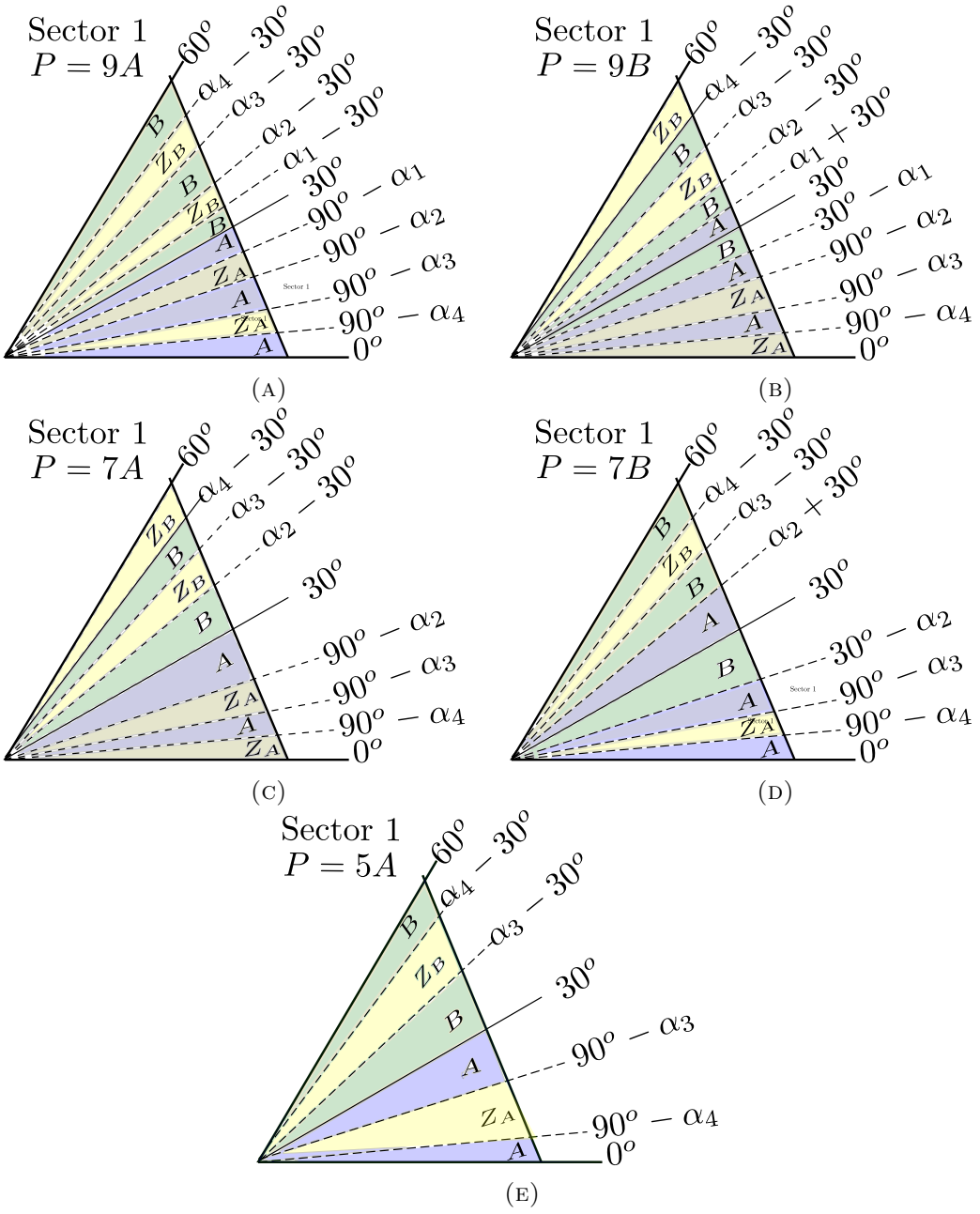


FIGURE 2.17: Vectors A, Z_A, B and Z_B in sector I based on α_i for (a) $P = 9A$ (b) $P = 9B$ (c) $P = 7A$ (d) $P = 7B$ (e) $P = 5A$

SST PWM is realised by comparing the sinusoidal modulating signals with triangular carrier. On the other hand, a space vector based approach is followed to realise SO PWM. The variation of optimal angles (α_i) with M considering the different P applied over specific region is presented in Fig. 2.16. Further, each pulse pattern leads to a specific sequence of voltage vectors applied by the 2L-VSI. This sequence, termed as optimal vector sequence, is given in table 2.3 for a sector. Here, A and B are the nearest active vectors associated with the sector, while Z_A and Z_B are the respective nearest zero-vectors. For examples, for $P = 9A$, the optimal vector sequence in sector 1 is given by $10101 - 27272$.

The switching in the pole-voltages of 2L-VSI can be directly correlated to the vectors applied by it. Thus, α_i can be mapped to the particular values of θ_s at which the vector within the optimal sequence changes. Such a mapping is shown in Fig. 2.17 for pulse pattern $P = 9A, 9B, 7A, 7B$ and $5A$ for sector I. Thus, SO PWM can be realised by applying the suitable vector from the sequence for the duration obtained by comparing θ_s with the mapped value of α_i.

2.3.2 Estimation of θ_s and M

It is stated in the last subsection that accurate information pertaining to θ_s is crucial for proper implementation of both SST and SO PWM. Under open-loop operation of IM drive, θ_s is readily available. However, the same is not true for RFO vector control mode of operation. In this case, v_{sd} and v_{sq} are directly converted to the sinusoidal three-phase reference voltages (v_r, v_y and v_b) using ρ_{mr} which is the angle associated with rotor-flux vector, $\overrightarrow{\psi}_r$.

Thus, an indirect way to estimate θ_s using ρ_{mr}, v_{sd} and v_{sq} is proposed in the chapter. The relation between these quantities becomes clear from the phasor-diagram of the IM under RFO vector control mode. It is shown in Fig. 2.18a and Fig. 2.18b, for both motoring and generating modes, respectively. The angular difference between θ_s and ρ_{mr} is termed as γ as shown below

$$\gamma = \theta_s - \rho_{mr} \tag{2.14}$$

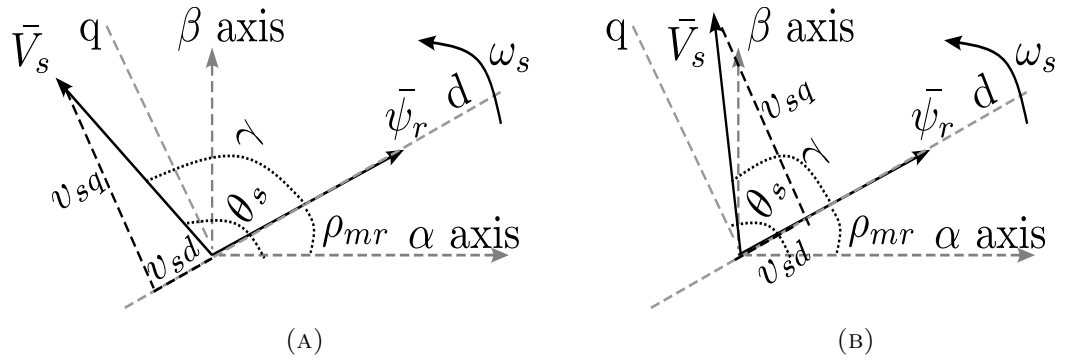


FIGURE 2.18: Phasor Diagram consisting of IM in (a) motoring and (b) generating modes

For RFO indirect vector control drive, ρ_{mr} is computed as shown in (2.15), where ω_r and ω_{sl} are the rotor speed and slip speed, respectively.

$$\rho_{mr} = \int_0^t (\omega_r + \omega_{sl})dt \tag{2.15}$$

Further, γ is computed on basis of mode of operation as

$$\begin{aligned} \gamma &= \frac{\pi}{2} + tan^{-1}\frac{|v_{sd}|}{|v_{sq}|} \quad (\text{if } v_{sd} \leq 0); \\ &= tan^{-1}\frac{|v_{sq}|}{|v_{sd}|} \qquad (\text{if } v_{sd} \geq 0); \end{aligned} \tag{2.16}$$

Since the DC component of v_{sd} and v_{sq} is sufficient to generate the information pertaining to fundamental component of $\overrightarrow{v}_s$, a simple low-pass filter can be designed to extract that. Thus θ_s can be computed once ρ_{mr} and γ are known.

2.3.3 Implementation of SST PWM

As θ_s is accurately obtained, the same can be utilized to generate the triangular carrier for SST PWM. A saw-tooth signal in time, θ_{cr}, can be generated from θ_s as given using

$$\theta_{cr} = \frac{P(\theta_s + \frac{\pi}{2})}{2\pi} - floor\big(\frac{P(\theta_s + \frac{\pi}{2})}{2\pi}\big) \tag{2.17}$$

Here, *floor* denotes the nearest lowest integer function. Thus, zero-crossings of θ_{cr} and modulating signals are always synchronized. With suitable manipulation, θ_{cr} can be converted into a triangular carrier. The block diagram to represent the implementation of SST PWM is shown in Fig. 2.19.

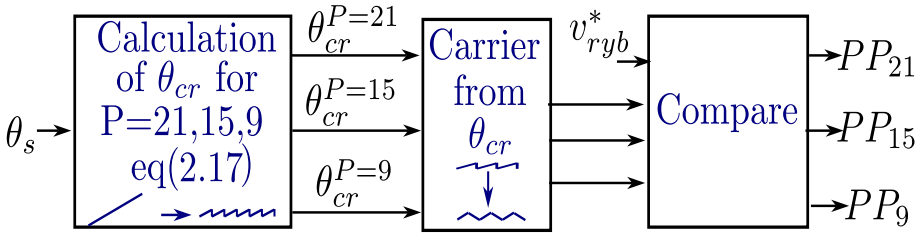


FIGURE 2.19: Block diagram to implement SST PWM

2.3.4 Implementation of SO PWM

The optimal switching angles α_i are pre-calculated and stored in a look-up-table. This burdens the micro-controller due to requirement of additional memory. It can be seen in Fig. 2.16 that the α_i vary almost as a linear function of M for a given value of P. Thus these angles can be expressed as piece-wise linear functions of M. In this present case, 4 optimal angles corresponding to each P have been defined. For $P = 9A$ and $9B$, all these 4 angles vary as linear-function of M. As the pulse pattern changes from $P = 9B$ to $7A$, first optimal angle (α_1) becomes constant at 0^o and the remaining 3 vary as a function of M. This is depicted in Fig. 2.20. Further, as the pulse pattern changes to $P = 5B$, α_2 becomes constants at 0^o as well. Thus, the four optimal angles, expressed in terms of linear equations in (2.18)-(2.21), are used for generating optimal PWM voltage waveforms corresponding to $P = 9A, 9B, 7A, 7B$ and $5A$.

$$\alpha_1 = \begin{cases} 5M + 59.75 & \text{if} 0.43 \leq M < 0.52 \\ 12.5M - 1.75 & \text{if } 0.52 \leq M < 0.58 \\ 0 & \text{if } 0.58 \leq M < 0.64 \\ 0 & \text{if } 0.64 \leq M < 0.76 \\ 0 & \text{if } 0.76 \leq M < 0.88 \\ 0 & \text{if } 0.88 \leq M \end{cases} \tag{2.18}$$

$$\alpha_2 = \begin{cases} -6.66M + 74.83 & \text{if} 0.43 \leq M < 0.52 \\ 21.25M + 57 & \text{if} 0.52 \leq M < 0.58 \\ 9.09M + 59.93 & \text{if } 0.58 \leq M < 0.64 \\ -3.33M + 7.5 & \text{if} 0.64 \leq M < 0.76 \\ 0 & \text{if} 0.76 \leq M < 0.88 \\ 0 & \text{if } 0.88 \leq M \end{cases} \tag{2.19}$$

$$\alpha_3 = \begin{cases} 8.3333M + 75.08 & \text{if} 0.43 \leq M < 0.52 \\ 77.75 & \text{if} 0.52 \leq M < 0.58 \\ -12.72M + 81.54 & \text{if} 0.58 \leq M < 0.64 \\ 30M + 53.5 & \text{if} 0.64 \leq M < 0.76 \\ 18.125M + 60.875 & \text{if} 0.76 \leq M < 0.88 \\ -108.33M + 112.4 & \text{if} 0.88 \leq M \end{cases} \tag{2.20}$$

$$\alpha_4 = \begin{cases} -7.5M + 90 & \text{if } 0.43 \leq M < 0.52 \\ 10M + 80.5 & \text{if } 0.52 \leq M < 0.58 \\ 8.18M + 81.81 & \text{if } 0.58 \leq M < 0.64 \\ -1.25M + 83.75 & \text{if } 0.64 \leq M < 0.76 \\ 11.87M + 90.62 & \text{if} 0.76 \leq M < 0.88 \\ -191.66M + 198.05 & \text{if } 0.88 \leq M \end{cases} \tag{2.21}$$

The duration of the vectors A, Z_A, B and Z_B within each sector, remains same for all the six sectors on account of symmetry. As mentioned earlier, the the dwell time for each vector is determined by comparing α_i and θ_s. Thus, the dwell time computed for the vectors in sector 1 will be the same for the corresponding vectors in the other sectors.

As θ_s varies in the other sectors, it can be mapped to sector 1 by obtaining θ_s^{map} using (2.22) wherein S is the number of the sector in which $\overrightarrow{v}_s$ is present. Thus, S

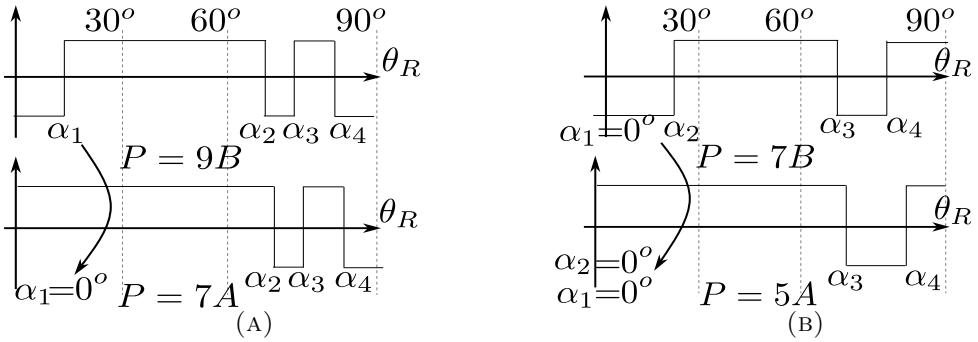


FIGURE 2.20: Change in PP (a) $P = 9B$ to $7A$ (b) $P = 7B$ to $5A$

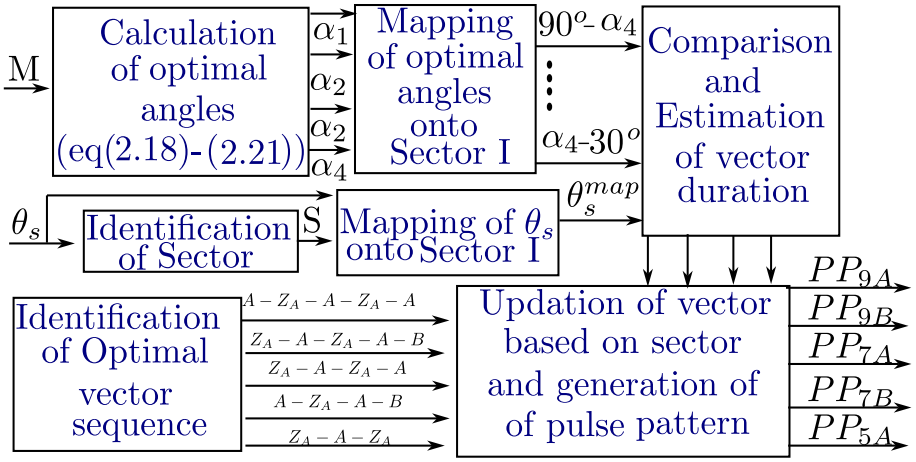


FIGURE 2.21: Block diagram to implement SO PWM

can take the value $1, 2, 3, 4, 5$ and 6. θ_s^{map} remains in the range $0^o$to 60^o as θ_s rotates through 360^o.

$$\theta_s^{map} = \theta_s - (S-1)60^o \tag{2.22}$$

Thus,in a given sector, the vector to be applied is selected from the optimal sequence and applied for their dwell time is obtained by comparing the mapped values of α_i with θ_s^{map}. Three-phase output voltages are generated on basis of voltage vector generated by SO PWM.

2.3.5 Performance of the drive with proposed PWM technique during unconstrained pulse transition

As mentioned earlier, one notable aspect of synchronized PWM technique is the transition in the pulse pattern (PP) applied by the 2L-VSI as P changes. The transition in PP is illustrated in Fig. 2.22 by depicting v_{RO} normalised with respect

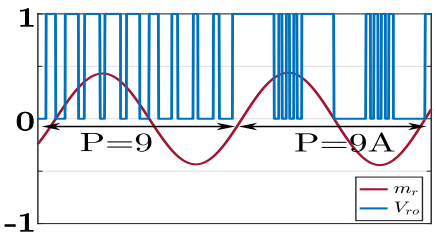


FIGURE 2.22: m_r and normalised V_{ro} during the transition SST P=9 to SO P=9A

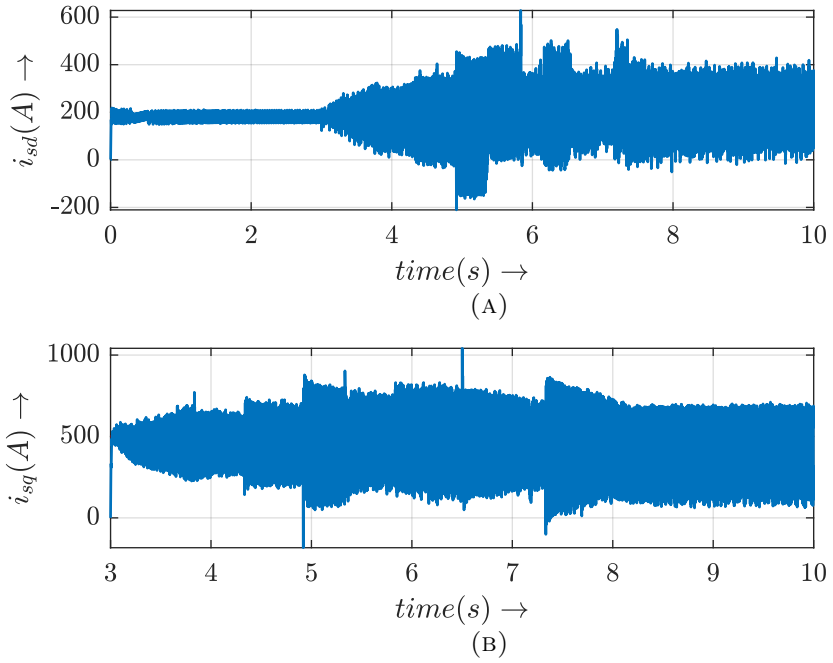


FIGURE 2.23: (a) i_{sd} and (b) i_{sq} axis current through the complete range of f_m with proposed SOH PWM.

to V_{dc} and m_r as P changes from SST $P = 9$ to $P = 9A$ in SO PWM.

A 2.2kV, 850kW, 65Hz drive is simulated in MATLAB/Simulink in vector control mode over complete range of f_m with the proposed SOH PWM scheme. The performance of the drive is evaluated in terms of the transients observed in d and q-axis components (i_{sd} and i_{sq}) of the stator-current vector, $\overrightarrow{i}_s$, over the complete range of f_m. The same is captured and presented in Fig. 2.23. Further, both i_{sd} and i_{sq} are captured at particular time instants corresponding to the transition from $P = 9$ to $P = 9A$, $P = 9B$ to $P = 7A$, $P = 7A$ to $P = 7B$ and $P = 7B$ to $P = 5A$ and shown in Fig. 2.24.Severe transients (2-3 times of steady state value) can be

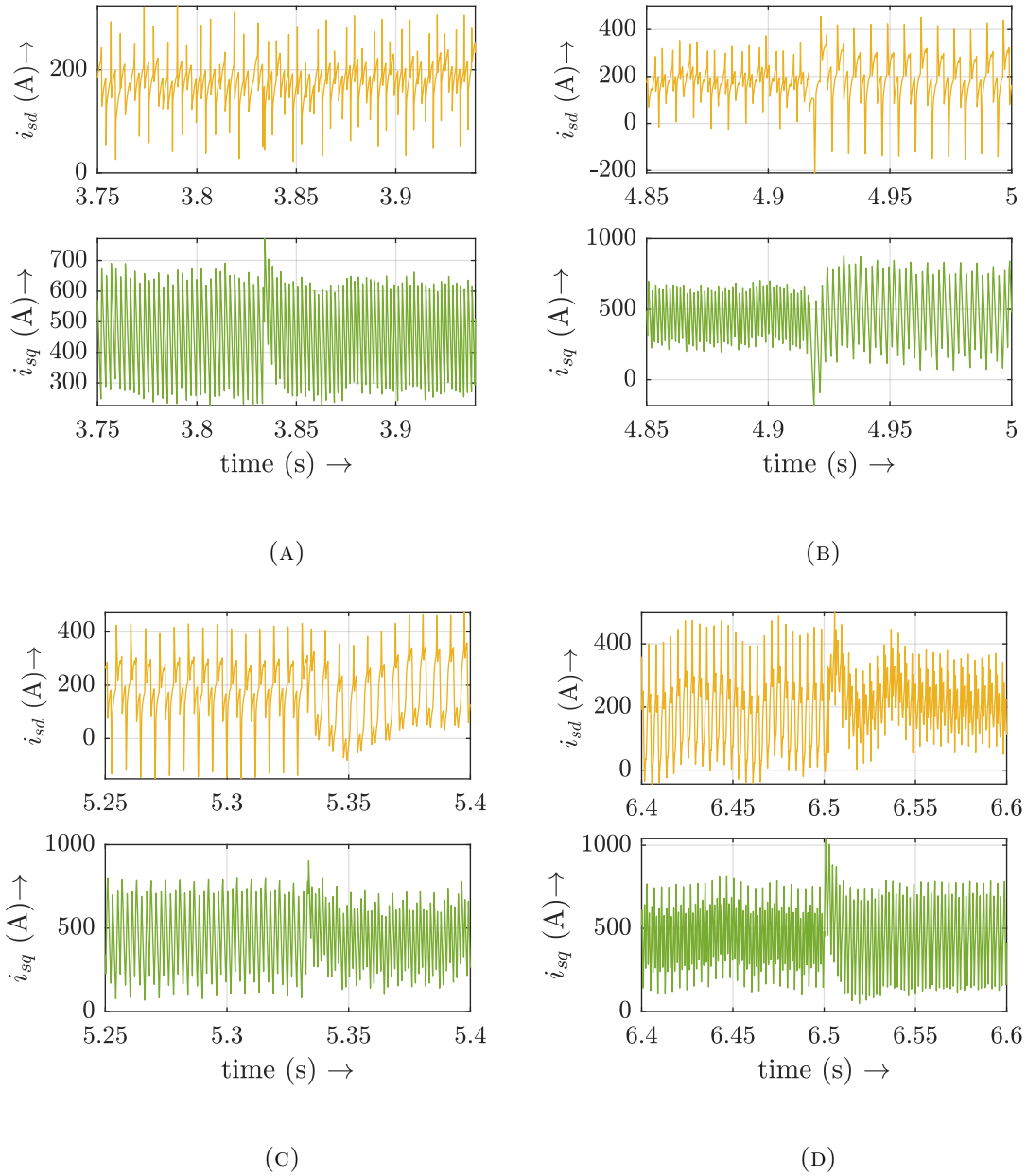


FIGURE 2.24: i_{sd} and i_{sq} captured during transitions from (a) $P = 9$ to $P = 9A$ (b) $P = 9b$ to $P = 7A$ (c) $P = 7A$ to $P = 7b$ (d) $P = 7B$ to $P = 5A$

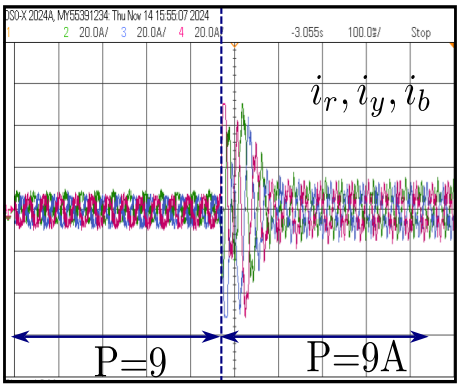


FIGURE 2.25: Experimental result corresponding to three-phase current during the transition from SST P=9 to SO P=9A [x axis: 10ms/div, y axis: 20A/div]

observed in both i_{sd} and i_{sq} for both the cases despite synchronized PWM generation. The same is reflected in the three-phase line-currents of the IM drive. This may activate the over-current protection circuitry and stop the drive. The experimentally observed transients in the three-phase current as the transition from SST $P = 9$ to SO $P = 9A$ takes place is shown in Fig. 2.25. The over-current protection of the VSI is deactivated and this result is captured. Severe transient in three-phase current can be seen in Fig. 2.25.

Thus, it can be inferred from these results that the transients observed in line-current during PP transition is not a problem just restricted to SST PWM scheme. Introduction of intermediate pulse numbers like $P = 7$ and $P = 5$ ensures that the operation of the drive does get unstable but significant transients are still observed in the line-current. Thus more detailed analysis, both from fundamental and harmonic model perspective of the motor is required to be done to investigate the cause of this issue. The same is presented in the section following which a generalized PP transition strategy is proposed in this thesis which ensures such transitions happen smoothly.

2.4 Pulse Pattern Transition Strategy

An analysis from both the perspective of fundamental and harmonic model of the motor is done to identify the cause of the transients observed in current due to transition in pulse-pattern in this section. Based on this analysis, a strategy to ensure

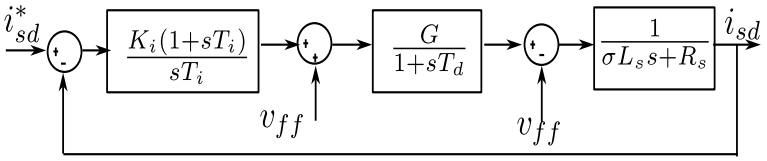


FIGURE 2.26: Current control loop for traction motor drive.

minimum transient in line currents and electromagnetic torque as the pulse pattern applied by the 2L-VSI to the motor changes is developed.

2.4.1 Analysis from fundamental model perspective

Block diagram of current control loop in vector controlled IM drive is shown in Fig. 2.26 [73]. Here, the inverter is modelled as a gain (G) with first-order delay. In case of SST PWM, generally G is taken to be $\frac{V_{dc}}{2}$ whereas time-constant T_d is considered as $\frac{1}{4f_{sw}}$. The parameters of current controller are designed by considering the worst possible T_d.

The voltage gain of the inverter deviated from $\frac{V_{dc}}{2}$ by a factor of 1.22 when the inverter operates with SST PWM with $P = 3$. Therefore, the modulating signals should be suitably adjusted in magnitude around the f_m where 9 to 3 transition in P is expected.

Open loop transfer function of current control (G_{ol}) is given by (2.23). Fig. 2.27a -2.27d present Bode plots of G_{ol} at PWM transitions, AST PWM to SST PWM, $P = 21$ to $P = 15$, $P = 15$ to $P = 9$ and $P = 9$ to $P = 3$, respectively.

$$G_{ol} = \frac{K_i(1 + sT_i)}{sT_i} \frac{G}{(1 + sT_d)} \frac{1}{(R_s + \sigma L_s)} \tag{2.23}$$

The magnitude plot is found to be nearly overlapping for previous and next PWM scheme whereas phase plot is observed to have lower value at gain cross-over frequency. The change in phase value is found to be most prominent in case of transition from $P = 9$ to $P = 3$ (see Fig. 2.27d). Thus, the phase margin of the system changes abruptly with P transition. Since, the phase margin is always positive, the current control loop stays stable. However, abrupt change in phase margin affects the dynamic performance of control-loop without making it unstable.

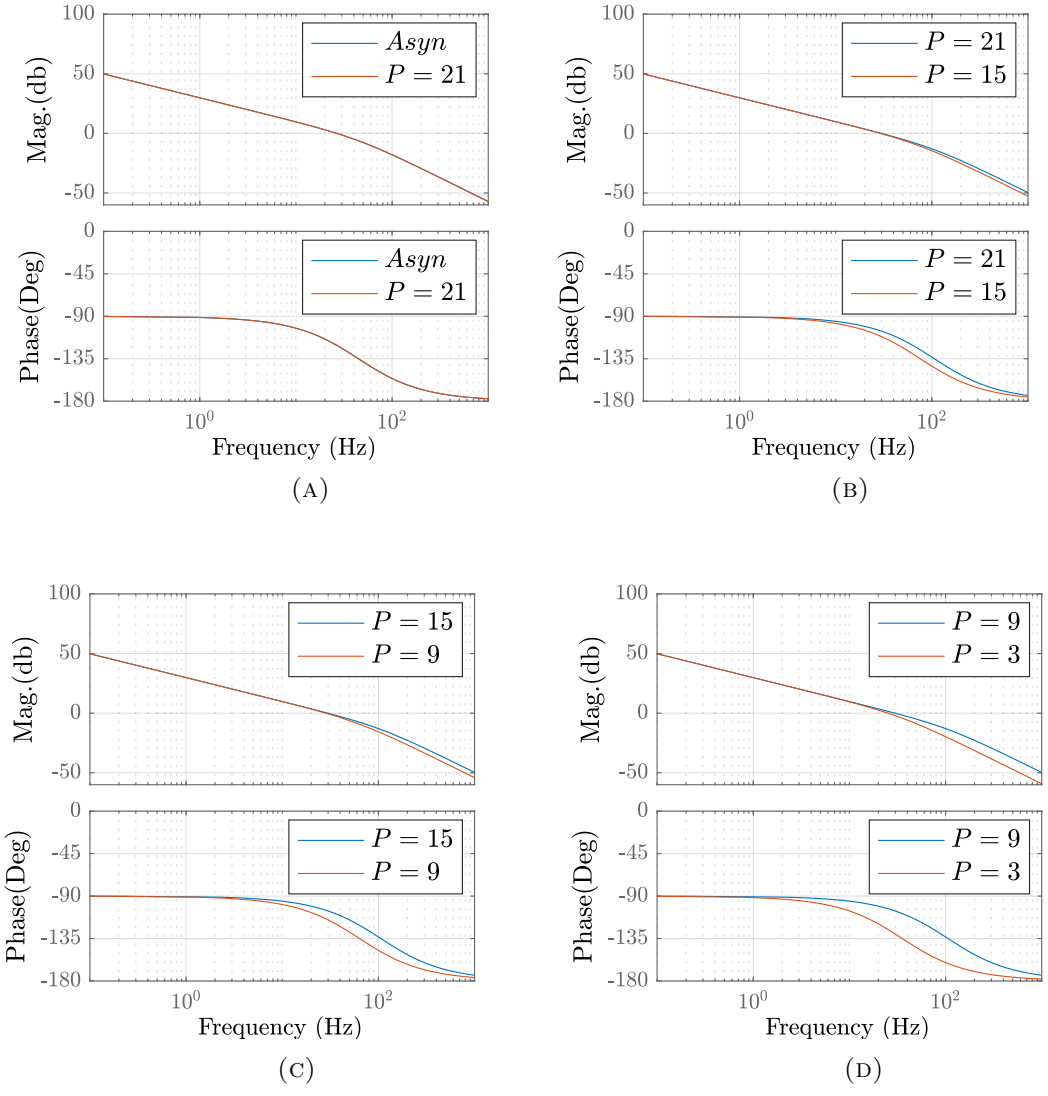


FIGURE 2.27: Bode plots of loop transfer function (G_{ol}) pertaining to transitions in P from (a) Asyn to P=21 at $f_m = 10Hz$ (b) P=21 to 15 at $f_m = 23Hz$ (c) P=15 to 9 at $f_m = 33Hz$ (d) P=9 to 3 at $f_m = 55Hz$.

2.4.2 Harmonic Model Analysis

PWM output voltage of VSI comprises of harmonic components which leads to ripple in line current. The same, for R-phase is represented in (2.24) as

$$v_{rn} = v_{RN_1} + \tilde{v}_{RN}; \quad i_r = i_{R_1} + \tilde{i}_R; \tag{2.24}$$

where, v_{rn}, v_{rn_1} and $\tilde{v}_{rn}$ denotes R-phase to neutral voltage, its fundamental and harmonic component, respectively. Similarly, i_r, i_{r_1} and $\tilde{i}_r$ are R-phase line-current, its fundamental and ripple components respectively.

Due to low switching frequency, $\tilde{v}_{rn}$ consists of 5^{th} and 7^{th} order harmonics and can be written as

$$\tilde{v}_{RN}(t) = \sum_{m=5,7..} V_m sin(m\omega t + \phi_m) \tag{2.25}$$

At a given f_m, change in P leads to a change in the magnitude and phase of $\tilde{v}_{rn}$. The response, $\tilde{i_r}$ to these changes in $\tilde{v}_{rn}$ can be computed using the dynamical equation (2.26). This is obtained from the harmonic model [30] of IM as

$$\frac{d\tilde{i}_R}{dt} = \frac{\tilde{v}_{RN} - R_{eq}\tilde{i_R}}{L_{eq}} \tag{2.26}$$

Here, $R_{eq} = R_s + R_r$ where R_s and R_r are per-phase stator and rotor resistances, respectively of IM and $L_{eq} = L_{ls} + L_{lr}$, where L_{ls} and L_{lr} are per-phase stator and rotor leakage inductances , respectively of IM.

In s-domain, (2.26) can be written as

$$\tilde{I}_R(s) = H(s)\tilde{V}_{RN}(s) \text{ where } H(s) = \frac{1}{R_{eq} + sL_{eq}} \tag{2.27}$$

The time domain expression of $\tilde{i}_r(t)$ consists of a transient response and a steady-state response. It is is given by

$$\tilde{i}_R(t) = C_1 e^{\frac{-R_{eq}t}{L_{eq}}} + \tilde{i}_R^{SS}(t) \tag{2.28}$$

Here, time $t = 0$ is taken as the instant at which P changes its value. $C_1 e^{\frac{-R_{eq}t}{L_{eq}}}$ is the transient component of the total response and $\tilde{i}_r^{SS}(t)$ is the steady state response of the current. The latter can be estimated using superposition theorem as,

$$\tilde{i}_R^{SS}(t) = \sum_{m=5,7..} |H(jm\omega)|V_m sin(m\omega t + \phi_m + \angle H(jm\omega)) \tag{2.29}$$

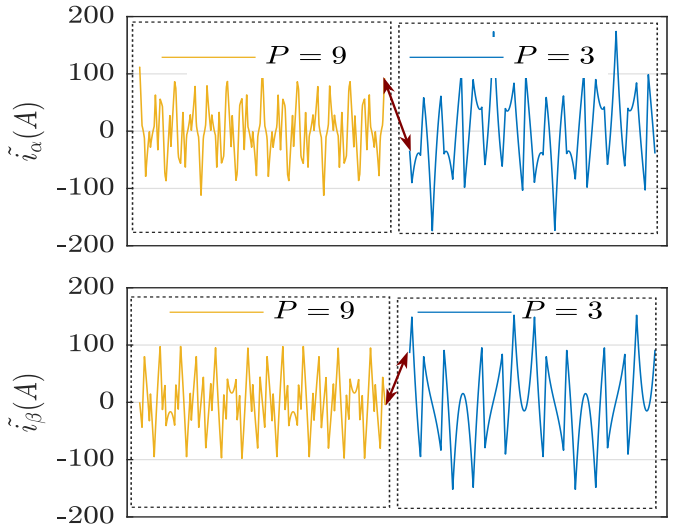


FIGURE 2.28: Mismatch in ripple currents pertaining to $P = 9$ and 3 at $f_m = 55Hz$.

Here, $|H(jm\omega)|$ and $\angle H(jm\omega)$ are the magnitude and phase of $H(s)$ at $s = jm\omega$.

If the constant C_1 in (2.28), can be made zero, the transient in the current can be made zero. C_1 is determined by using initial conditions. C_1 can be made zero, if time instant $(t = 0)$ is chosen such that the following condition is true

$$\tilde{i}_R(t = 0^-) = \tilde{i}_R^{SS}(t = 0^+) \tag{2.30}$$

Here, $\tilde{i}_r(t = 0-)$ corresponds to the instantaneous value of the steady-state ripple current due to the pulse pattern before the transition (i.e. for the outgoing P) and $\tilde{i}_r^{SS}(t = 0^+)$ corresponds to the instantaneous value of the steady-state ripple current due the pulse pattern after the transition (i.e. for the incoming P). Thus, it can be said, that the transient in the ripple current can be minimized if it is ensured that the transition in P takes place at an instant when the steady-state value of the ripple current matches closely for the incoming and outgoing pulse pattern.

Current ripples in R, Y and B-phases (i.e. $\tilde{i_r}$, $\tilde{i_y}$ and $\tilde{i_b}$, respectively) can be represented in vector form in stationary $\alpha - \beta$ reference frame given in (2.31).

$$\overrightarrow{\tilde{i_s}} = \tilde{i_\alpha} + j\tilde{i_\beta} = \tilde{i}_R + \tilde{i}_Y e^{j\frac{2\pi}{3}} + \tilde{i}_B e^{j\frac{4\pi}{3}} \tag{2.31}$$

where, $\overrightarrow{\tilde{i_s}}$ is the ripple current vector and $\tilde{i_\alpha}$ and $\tilde{i_\beta}$ are components of $\overrightarrow{\tilde{i_s}}$ in stationary $\alpha - \beta$ reference frame.

Fig. 2.28 demonstrates $\tilde{i_\alpha}$ and $\tilde{i_\beta}$ for $P = 9$ and $P = 3$ under steady-state operation for SST PWM. Peak-peak ripple in $\tilde{i_\alpha}$ and $\tilde{i_\beta}$ is found to be nearly 200A and 300A for $P = 9$ and 3, respectively. It should be noted that instantaneous values of $\tilde{i_\alpha}$ and $\tilde{i_\beta}$ may have mismatch for unconstrained transition in P. The same is illustrated through a double headed arrow in Fig. 2.28. This mismatch leads to transients in line-current and consequently in i_{sq}, i_{sd} and i_{mr}. Therefore, to minimize the line current transients, $\overrightarrow{\tilde{i_s}}$ for incoming and outgoing P must also be matched.

Hence, to minimize the transients, both, fundamental and ripple components of current vector must be matched for present and next P.

2.4.3 Proposed stator-flux trajectory based pulse-transition strategy

It is well established in the previous subsection that $\overrightarrow{i_s}$ for outgoing and incoming P must be matched. However, estimation of $\overrightarrow{i_s}$ requires motor parameters and exact solution of IM model. For SCIM, $\overrightarrow{i_s}$ can be represented in terms of stator flux vector $\overrightarrow{\psi_s}$ and rotor flux vector ($\overrightarrow{\psi_r}$)as

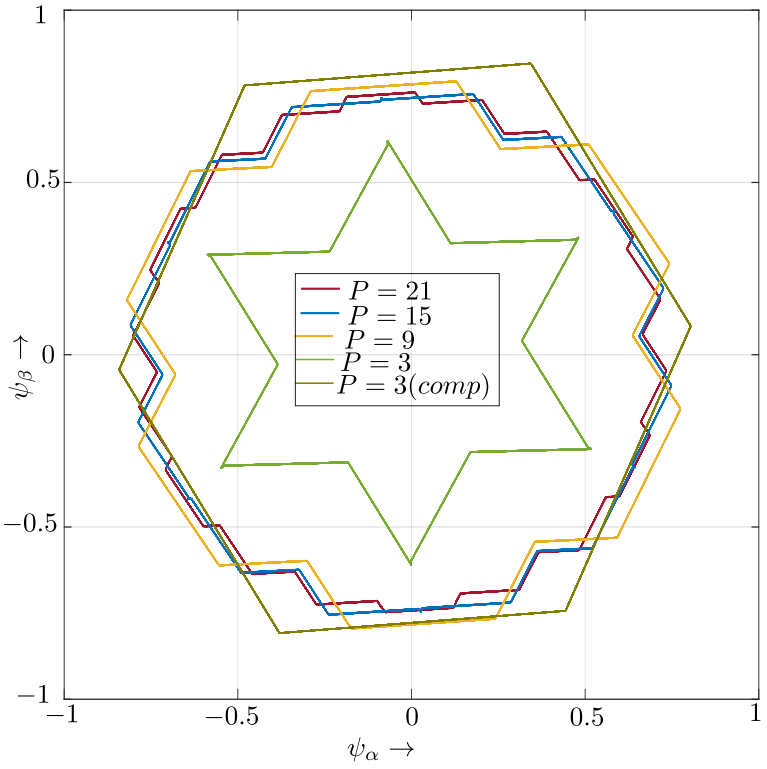
$$\overrightarrow{i_s} = \frac{(\overrightarrow{\psi_s} - \frac{L_m}{L_r}\overrightarrow{\psi_r})}{\sigma L_s} \tag{2.32}$$

where, L_m, L_s and l_r are magnetising, stator and rotor inductances, respectively and σ is the total leakage coefficient.

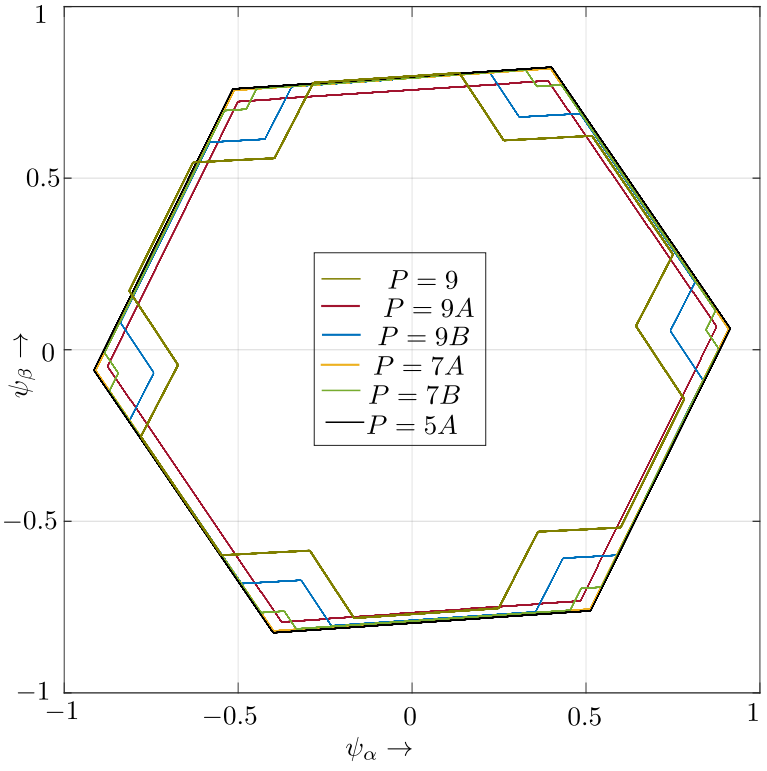
It should be noted that $\overrightarrow{\psi_r}$ is sluggish in nature due to the involvement of rotor-time constant [73]. So, an instantaneous change in $\overrightarrow{i_s}$ can be correlated to instantaneous change in $\overrightarrow{\psi_s}$. Hence, it is proposed in this thesis that values of $\overrightarrow{\psi_s}$ for outgoing and incoming P must be matched to ensure minimum transient during P transition. This can be ensured by enabling the pulse transition at an instant when the difference between the components of $\overrightarrow{\psi_s}$ for outgoing and incoming P are below a specified limit as given in (2.33).

$$\sqrt{(\psi_{s\alpha}^{out} - \psi_{s\alpha}^{in})^2 + (\psi_{s\beta}^{out} - \psi_{s\beta}^{in})^2} \leq l \tag{2.33}$$

Here, $\psi_{s\alpha}^{x}$ and $\psi_{s\beta}^{x}$ are α and $\beta-$ axis components of $\overrightarrow{\psi_s^x}$; $x \in \{out, in\}$ and l is a constant which can be chosen suitably to ensure pulse transition with minimum



(A)



(B)

FIGURE 2.29: Normalized $\overrightarrow{\psi}_s$ trajectories pertaining to (a) SST (b) SO PWM

transient.

$\psi^x_{s\alpha}$ and $\psi^x_{s\beta}$ can be computed from the stator voltage vector components $v^x_{s\alpha}$ and $v^x_{s\beta}$ as shown below [73].

$$\psi^x_{s\alpha,s\beta}(t) = \int_0^t (v^x_{s\alpha,s\beta}(t) - r_s i_{s\alpha,s\beta})\, dt \tag{2.34}$$

$v^x_{s\alpha}$ and $v^x_{s\beta}$ can be determined from the machine -phase-voltages which are further obtained from the inverter pole-voltages for a given P.

2.4.3.1 Required Compensation in SST PWM

Fig.2.29 presents the steady state $\overrightarrow{\psi}_s$ trajectories for both the PWM schemes namely, SST (Fig. 2.29a) and SO PWM (Fig. 2.29b) schemes. It can be seen in Fig. 2.29a, the trajectory for $P = 3$ is quite different from rest of pulse patterns. Thus, the transition from $P = 9$ to $P = 3$ in SST PWM leads to most severe transient as evident in Fig. 2.4. The trajectories for SO PWM in Fig. 2.29b are more-or-less overlapping each other.

Thus, in order to ensure a smooth transition between $P = 9$ and $P = 3$, the flux trajectory pertaining to $P = 3$ must be brought closer to the other trajectories by suitably compensation the PP pertaining to $P = 3$. Two step which are required to be taken in that direction are listed below,

1. The synchronized carrier pertaining to $P = 3$ is inverted. That is, the carrier is generated such that the positive zero-crossing of the carrier coincides with the negative zero-crossing of the modulating signals.
2. The modulating signals are adjusted with a gain of $\frac{1}{1.227}$.

With the above modifications, the flux-trajectory pertaining to $P = 3$ with compensation is shown in Fig. 2.29a with the legend $P = 3(comp)$. It can be seen that the flux trajectory for $P = 3$ now has several points of intersection with the remaining trajectories. Thus, compensating the pulse pattern for $P = 3$ with these two steps would ensure a smooth transition form $P = 9$ to $P = 3$.

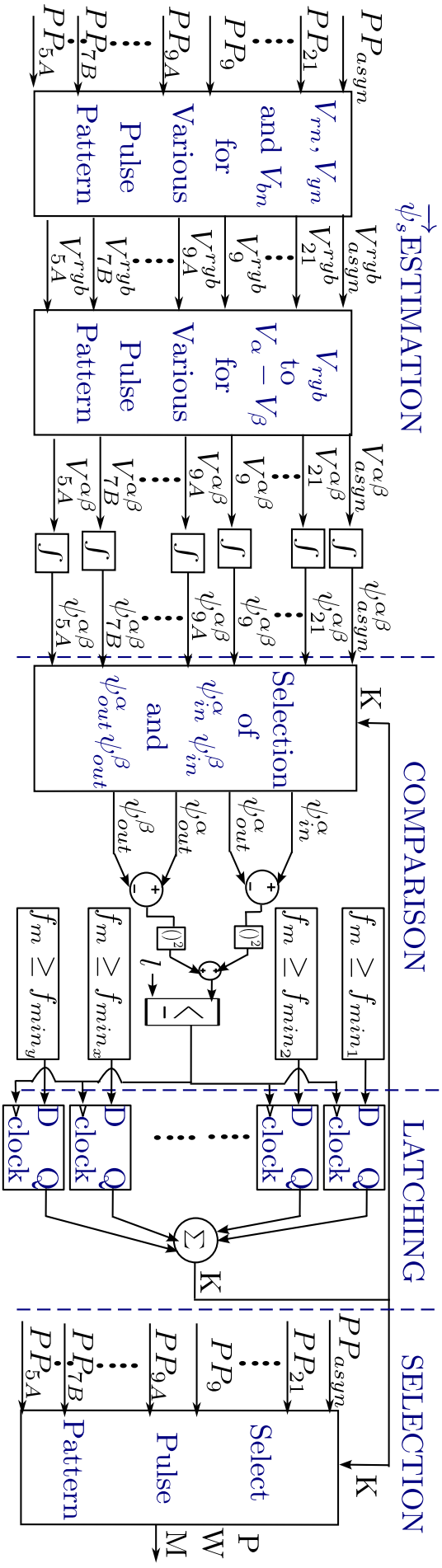


FIGURE 2.30: Block diagram of proposed algorithm for transition of P in vector controlled IM drive

2.4.4 Implementation of the proposed strategy

Fig.2.30 represents the block diagram of the implementation of the proposed pulse transition algorithm. The block diagram is divided into four stages, namely, $\overrightarrow{\psi}_s$ estimation, comparison, latching and carrier selection. The first stage, involves simultaneous estimation of $\alpha - \beta$ components of $\overrightarrow{\psi}_s$, $\psi^{\alpha\beta}$, corresponding to the PP pertaining to all values of P. Following this, the comparison stage starts. The variable K indicates the current state of the PP being applied by the 2L-VSI. For example, K=0 indicates that the PP corresponding to asynchronous PWM is being applied by the 2L-VSI. Similarly, K=1 implies synchronous PWM with $P = 21$ and so on. Based on the present value of K, $\overrightarrow{\psi}^{in}$ and $\overrightarrow{\psi}^{out}$ are selected from all the available estimated $\overrightarrow{\psi}_s$. The magnitude of difference vectors is compared with a constant l using a comparator. Also, another comparator is used for comparing f_m with specified values, f_{min_x}. The output of both the comparators are fed to D-flipflop to latch the output to a specific value in the latching stage. Output of the frequency comparator is fed as D input and that of the flux magnitude comparator is fed as clock. Output Q of the flipflop latches to input D only when the clock pulse is received else it holds its previous value. In other words, after the frequency condition is met, the output of the flipflop becomes 1 only at the instant when the flux condition is met and the then latches to the output 1. The outputs of all such flip-flops are added to update the value of K. Updation of the value K would result in the selection of the new incoming pulse-pattern in the selection stage. Thus, change P happens only when the drive crosses a specified range of f_m and $\overrightarrow{\psi_s}$ for incoming and outgoing P are nearly matching. This ensures a smooth transition between the various pulse patterns as the IM drive operates in RFO vector control mode.

2.5 Validation of Proposed SOH PWM Technique and Pulse transition Strategy

The complete block diagram of the proposed SOH PWM scheme along with the pulse transition strategy is shown in Fig. 5.3. The reference three-phase voltage

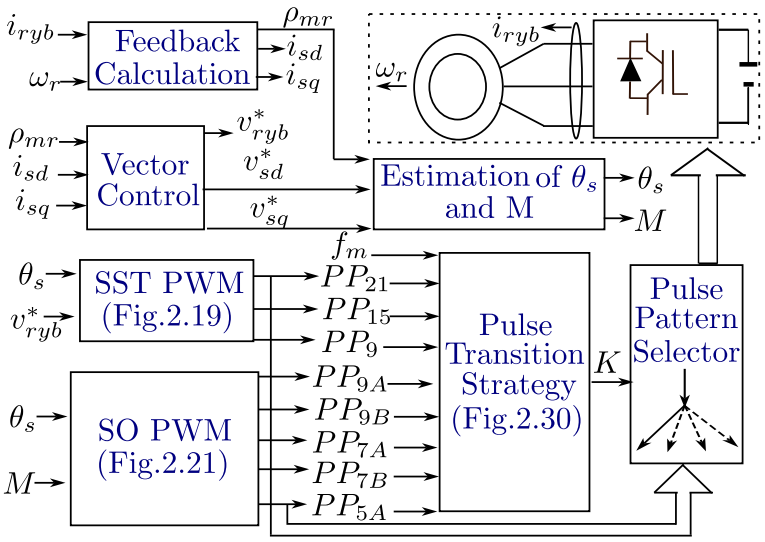


FIGURE 2.31: Complete control block diagram of the motor drive

signal v^*_{ryb}, is obtained from the vector control algorithm. Following this, the angle θ_s and the modulation index M are estimated using v_{sd} and v_{sq} and ρ_{mr}. The PP corresponding to SST PWM for all three pulse numbers i.e. $P = 21, 15$ and 3 are constructed by generating the triangular carrier using θ_s and comparing it with v^*_{ryb}. Simultaneously, the PP corresponding to SO PWM for $P = 9A, 9B, 7A, 7B$ and $5A$ are also constructed by comparing α_i (which are obtained from M) and θ_s^{map} using the optimal vector sequence. Finally, as all the pulse patterns become available, the suitable one is selected based on the proposed pulse-transition strategy.

The performance of the proposed SOH PWM technique and the effectiveness of the proposed pulse transition strategy with proposed SOH PWM technique and conventional SST PWM technique are validated using both simulation in MATLAB/Simulink and experimental results. The parameters of the motor used for simulation and experiments are mentioned in Appendix 7 (Table 1).

2.5.1 Simulation Results

The performance drive in terms of i_{sd} and i_{sq} as obtained in simulation corresponding to proposed SOH PWM technique with the proposed pulse transition strategy is shown in Fig. 2.32. Further, both i_{sd} and i_{sq} are captured at particular time instants corresponding to the transition from $P = 9$ to $P = 9A$, $P = 9B$ to $P = 7A$, $P = 7A$

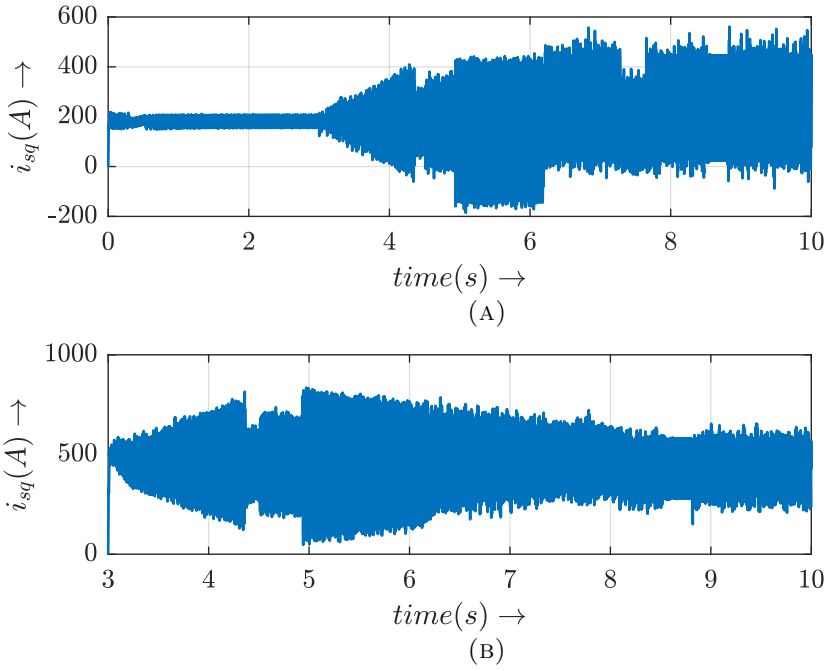
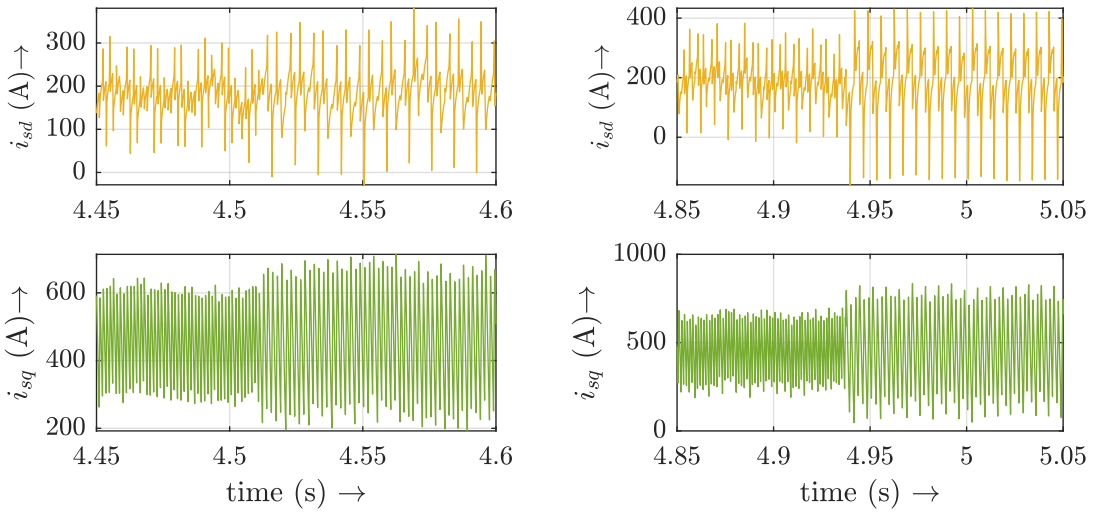


FIGURE 2.32: Simulation results pertaining to (a) i_{sd} and (b) i_{sq} through the complete range of f_m with proposed SOH PWM with proposed pulse transition strategy

to $P = 7B$ and $P = 7B$ to $P = 5A$ and shown in Fig. 2.24. It can be clearly seen that the transients in both i_{sd} and i_{sq} are reduced with respect to the one obtained without the strategy. The small transient observed in Fig.2.33d can be attributed to the fact that these transitions do not occur exactly at the instant when the stator flux trajectories intersect. However, the close proximity of the trajectories at the instant of transition ensure every limited transient in current.

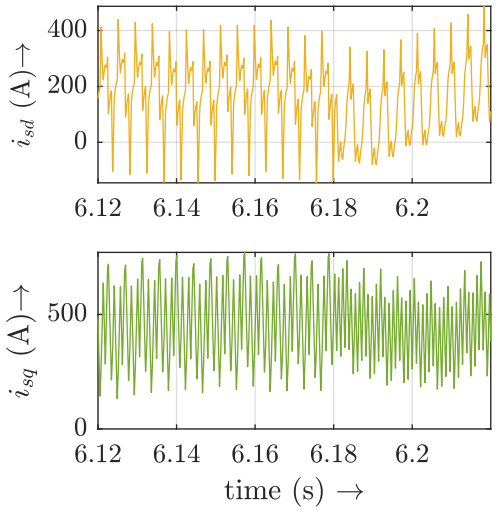
Further, the effective of the pulse transition strategy with conventional SST PWM is also established through simulation by operating the drive through the complete range of f_m. i_{sd} and i_{sq} for complete operation of the drive are shown in Fig.2.34. Further, time instants specific to the transition from $P = 15$ to $P = 9$ and $P = 9$ to $P = 3$ are shown in Fig.2.35a and Fig.2.35b respectively. Stable operation of the drive is achieved with the conventional SST PWM using the proposed pulse transition strategy.

Thus, it is established that with the proposed pulse-pattern transition strategy,

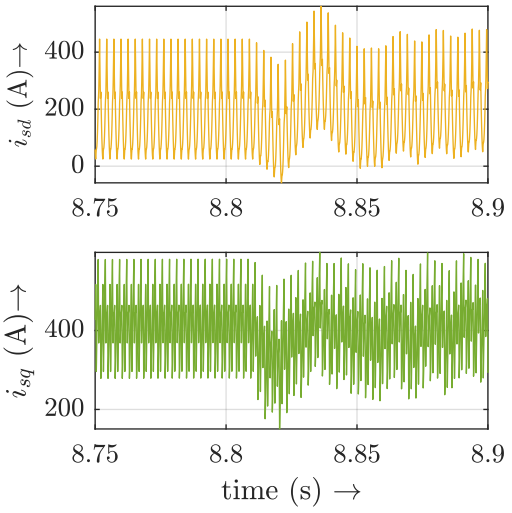


(A)

(B)



(C)



(D)

FIGURE 2.33: Simulation results pertaining to i_{sd} and i_{sq} captured during transitions from (a) $P = 9$ to $P = 9A$ (b) $P = 9b$ to $P = 7A$ (c) $P = 7A$ to $P = 7b$ (d) $P = 7B$ to $P = 5A$ with proposed pulse transition strategy

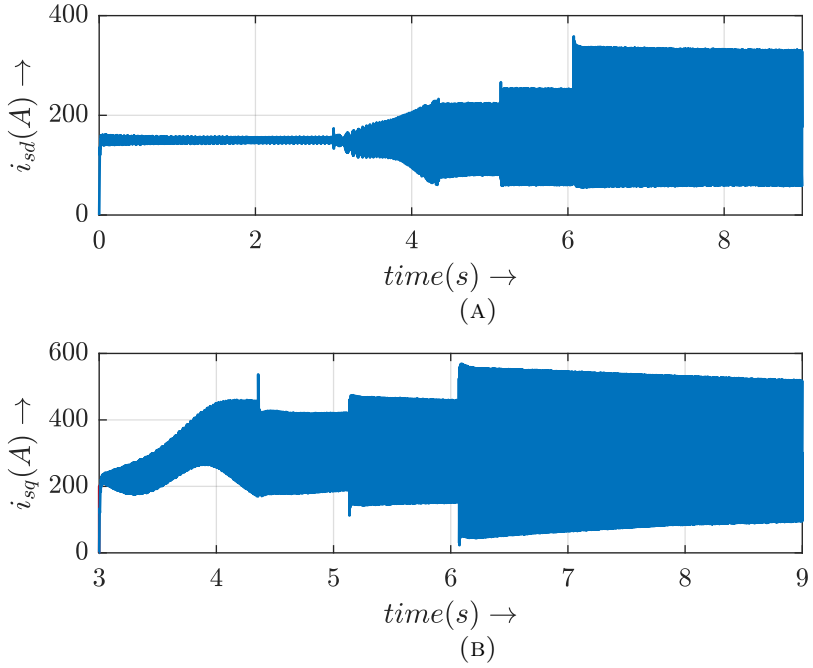
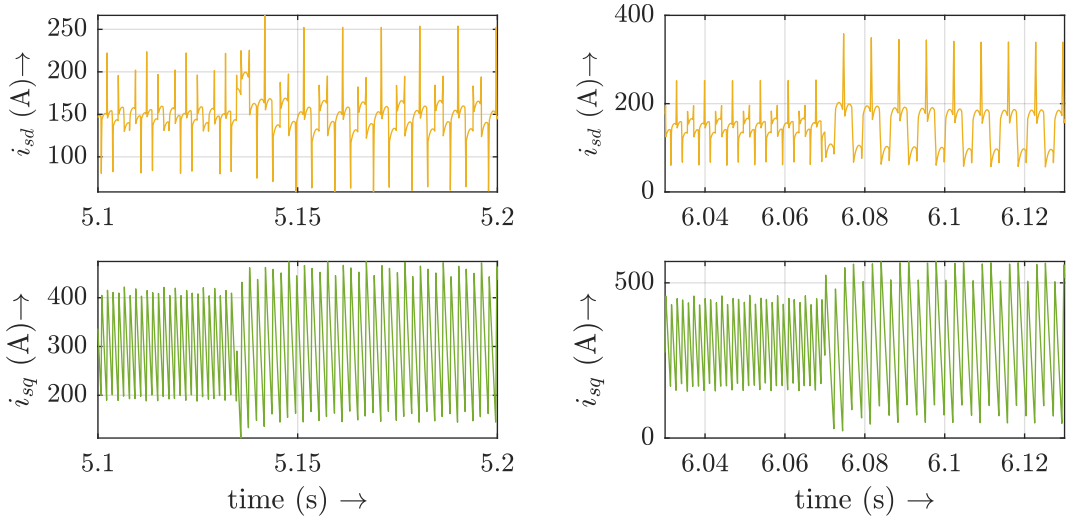


FIGURE 2.34: Simulation results pertaining to (a) i_{sd} and (b) i_{sq} axis current through the complete range of f_m with conventional SST PWM with proposed pulse transition strategy



(A) (B)

FIGURE 2.35: Simulation results pertaining to i_{sd} and i_{sq} captured during transitions from (a) $P = 15$ to $P = 9$ (b) $P = 9$ to $P = 3$ with proposed pulse transition strategy

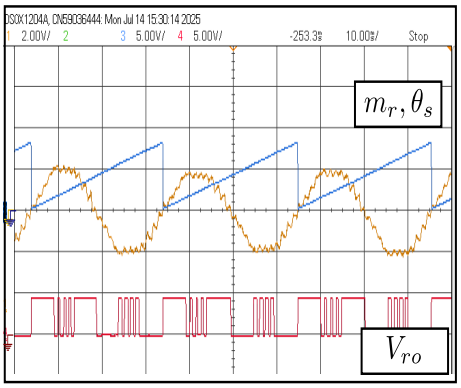
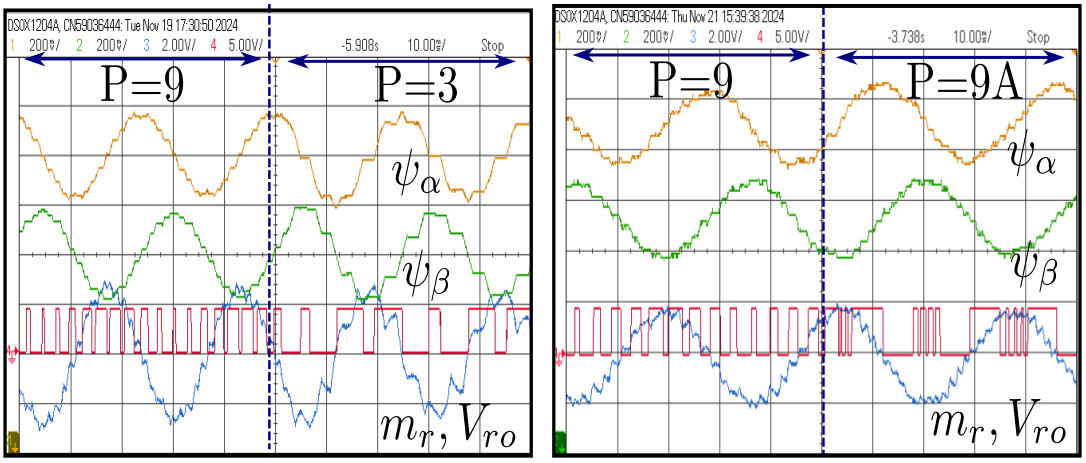


FIGURE 2.36: Experimental result showing synchronization of θ_s and V_{ro} with m_r [x axis: 10ms/div]



(A) (B)

FIGURE 2.37: Continuity in ψ_α and ψ_β (5Wb/div) with the proposed strategy during transition from (a)SST P=9 to SST P=3 (b)SST P=9 to SO P=9A [x axis: 10ms/div]

a high-power Y-connected SCIM drive can be operated smoothly upto $P = 3$ using SST PWM. However, the proposed SOH PWM technqiue offers superior harmonic performance as compared to conventional SST PWM specially at lower values of P due to the optimal PWM technique.

2.5.2 Experimental Results

The performance of the proposed PWM technique and pulse pattern transition strategy with closed-loop control is validated experimentally on a laboratory prototype of a two-level VSI fed Y-connected SCIM drive. The experimental set-up is shown in Appendix 7 (Fig.2). The detailed machine parameters are also presented in Appendix

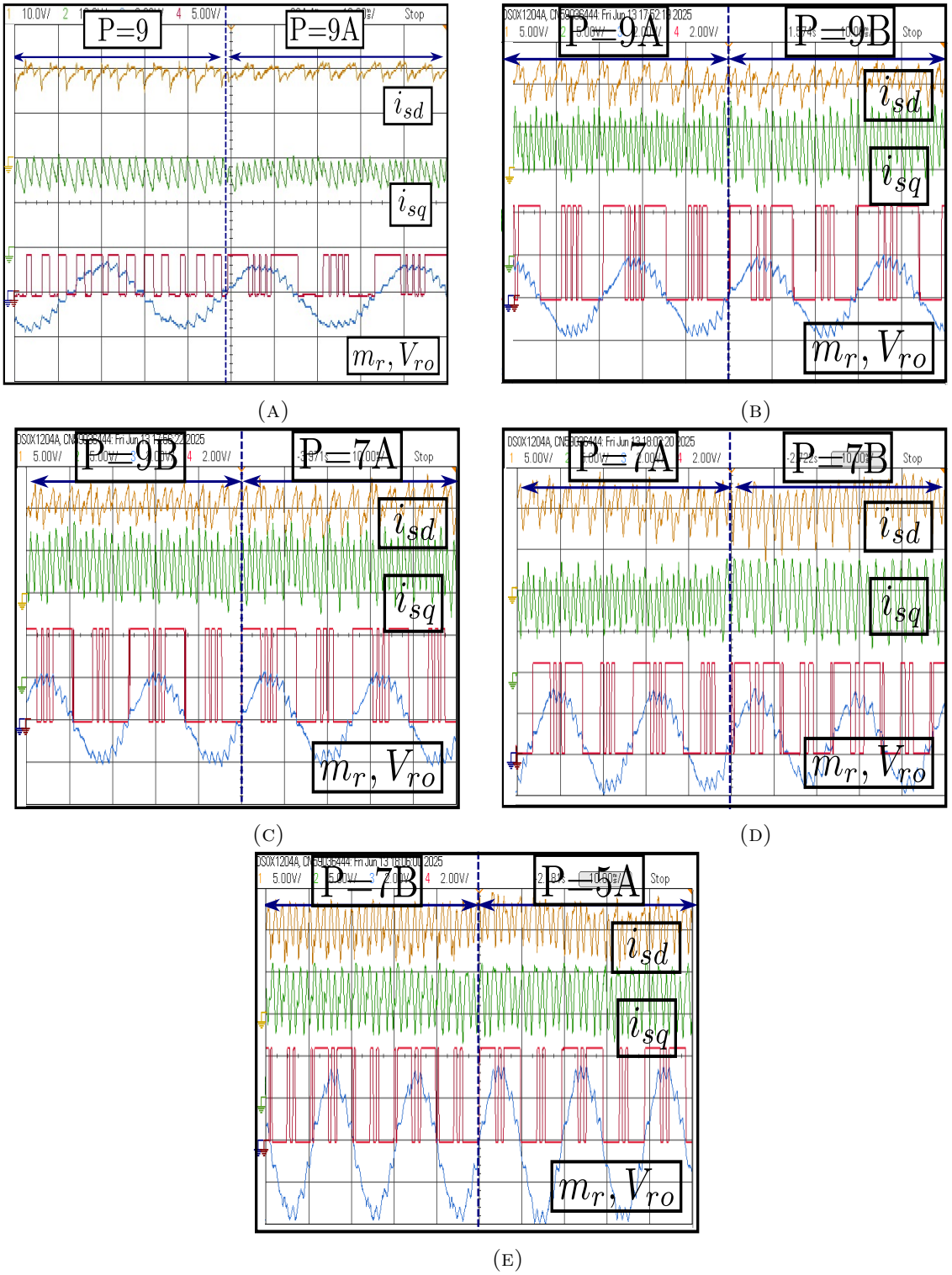


FIGURE 2.38: Experimental results showing i_{sd} (5A/div), i_{sq} (8A/div), normalised V_{ro} and m_r with proposed strategy at the instant of transition from (a) P=9 to 9A (b) P=9A to P=9B (c) P=9B to P=7A (d) P=7A to P=7B and (e) P=7B to P=5A [x axis: 10ms/div]

7 (table 1) The method proposed in this thesis to estimate θ_s which is the angle associated with the stator-voltage vector is first validated experimentally. θ_s along with R-phase modulating signal, m_r and normalised R-phase pole-voltage as obtained experimentally is shown in Fig.2.36. The case with $P = 9A$ is considered here. θ_s can be seen to be perfectly synchronized with m_r in the figure.

The effectiveness of the implementation of the proposed pulse transition strategy is established experimentally by observing the continuity in ψ_α and ψ_β as the transition in P takes place. The same is shown in Fig. 2.37 for the transition from SST $P = 9$ to SST $P = 3$ and SST $P = 9$ to SO $P = 9A$.

Further, the R-phase modulating signal, m_r and the normalised inverter pole voltages V_{ro} are presented along with i_{sd} and i_{sq} in Fig. 2.38 in order to establish the effective implementation of the proposed SOH PWM scheme. The transitions from SST $P = 9$ to SO $P = 9A$, SO $P = 9A$ to $P = 9B$, $P = 9B$ to $P = 7A$, $P = 7A$ to $P = 7B$ and $P = 7B$ to $P = 5A$ are shown in Fig. 2.38a-2.38e respectively. Almost no transient in either i_{sd} or i_{sq} for all the pulse pattern transition under consideration. This establishes the effectiveness of the proposed pulse transition strategy.

The effectiveness of the proposed pulse transition strategy during deceleration of the drive as the pulse pattern changes from $P = 5A$ to $7B$, $P = 7B$ to $7A$, $P = 7A$ to $P = 9B$ and from $P = 9B$ to $9A$ is shown in Fig. 2.39a-2.39d respectively. No transients can be observed in Fig. 2.39 establishing the effectiveness of the proposed pulse transition strategy during deceleration.

Overall dynamic performance of vector-controlled IM drive with proposed pulse transition algorithm on the experimental prototype is shown in Fig. 2.40. A speed reference is ramped up slowly from zero speed to the rated speed first and the speed is ramped down from rated to zero. The load-motor is operated under current-control mode to emulate a speed-dependant friction type of load on the test-motor. The flux producing component of the current, i_{mr} is controlled at its rated value as seen in Fig. 2.40a. The measured speed (ω_r) tracks the ramped reference speed (ω_r^*) as shown in Fig. 2.40c. d and q-components of the stator current vector, i_{sd} and i_{sq},

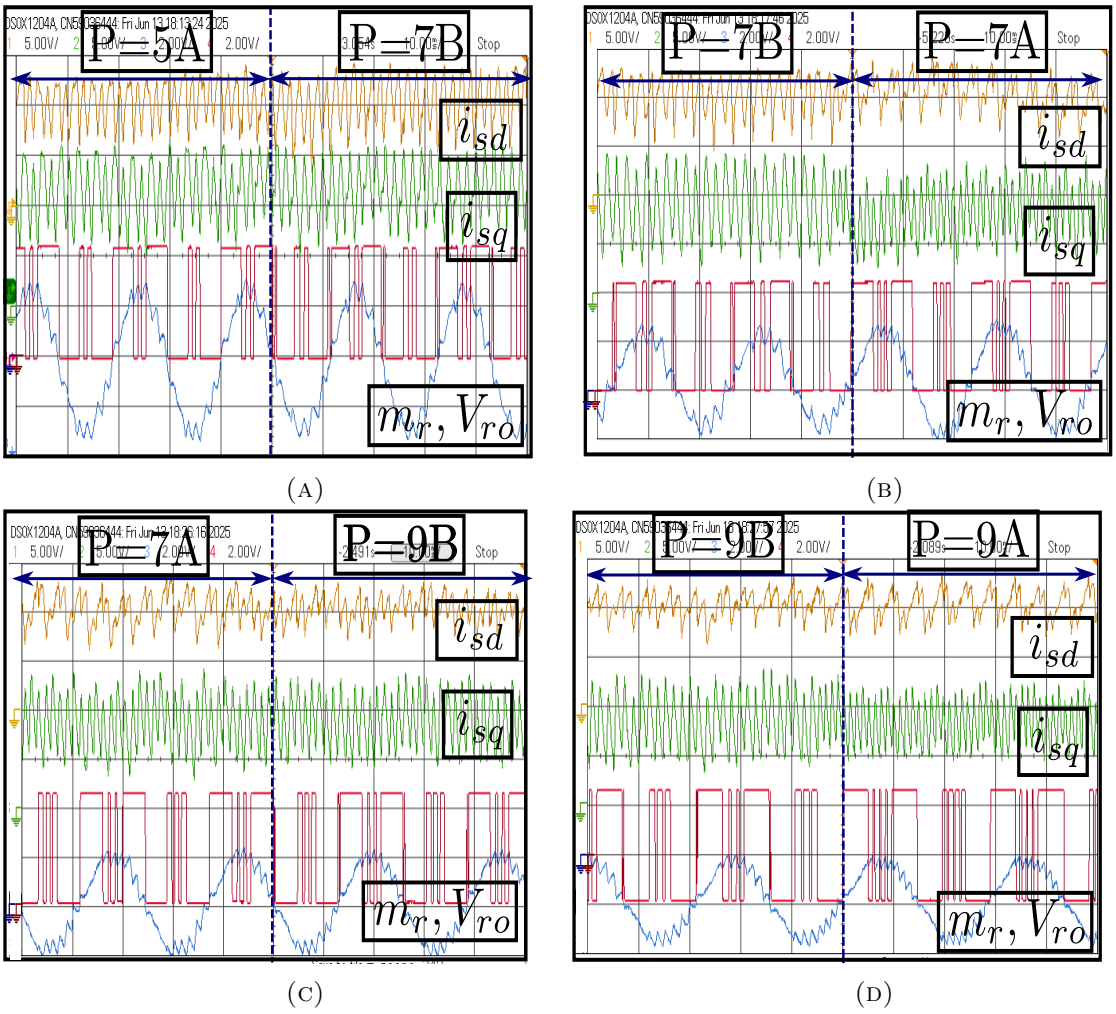


FIGURE 2.39: Experimental results showing i_{sd} (4A/div), i_{sq} (8A/div), normalised V_{ro} and m_r with proposed strategy at the instant of transition from (a) P=5A to P=7B (b) P=7B to P=7A (c) P=7A to P=9B and (d) P=9B to P=9A during deceleration. [x axis: 10ms/div]

are found to be tracking their respective reference values as shown in Fig. 2.40b and 2.40d respectively. Proposed pulse transition strategy ensures negligible transients on these quantities.

Validity of the approximation of the optimal angles α_i by a linear function of M is established by comparing the line current THD i_{thd} obtained when the approximate angles are used with respect to the actual values of α_i. The drive is operated in open-loop control with constant $\frac{V}{f}$ ratio. The line-current THD is measured for both the cases and the same is presented in Fig. 2.41. It can be seen that the i_{thd}

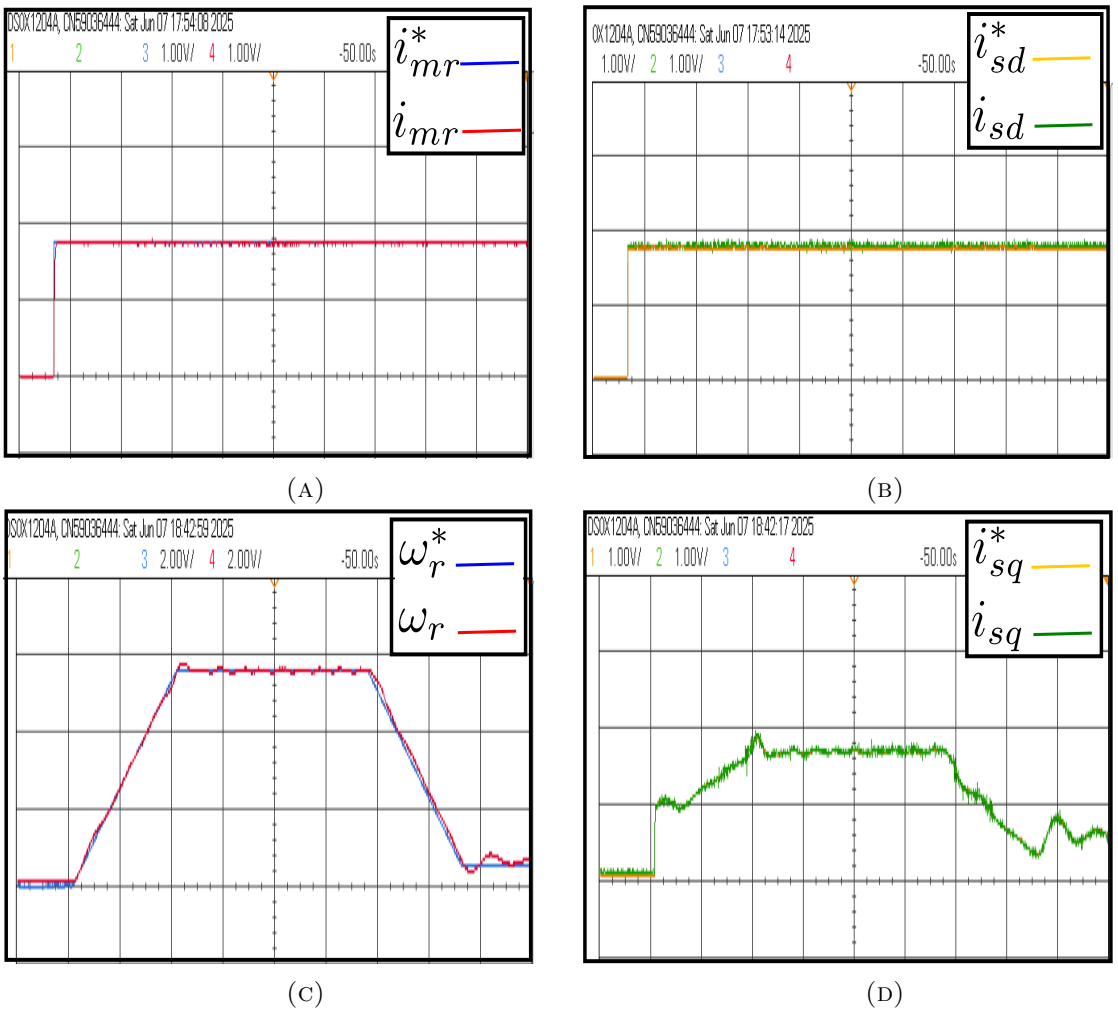


FIGURE 2.40: Experimental performance of vector controlled IM drive in terms of (a) i_{mr} [Scale: 5A/div, 5s/div] (b) i_{sd} [Scale: 5A/div, 5s/div] (c) speed [Scale: 600RPM/div, 5s/div]and (d) i_{sq} [Scale: 8A/div, 5s/div] with proposed strategy under proposed SOH PWM scheme

in both the cases almost overlap each other over the complete range of f_m. This establishes that the harmonic performance of the drive is not compromised when α_i are approximated as a linear function of M. In order to establish the superior harmonic performance of SO PWM with respect to SST PWM, i_{THD} corresponding to SST PWM for the range of modulating frequency, $f_m = 28$Hz to $F_m = 65$Hz is also shown in Fig. 2.41. In case of SST PWM, at $f_m = 39$Hz, the value of P changes from 9 to directly 3 as odd non-triplen values of P (such as 7 and 5) cannot be realised in SST PWM. Thus a steep increase in i_{thd} can be observed in Fig. 2.41.

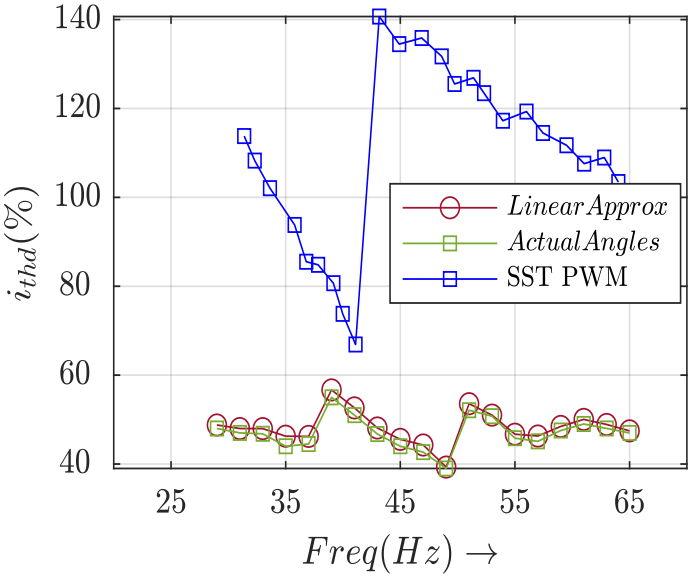


FIGURE 2.41: i_{THD} for actual and approximated values of α_i.

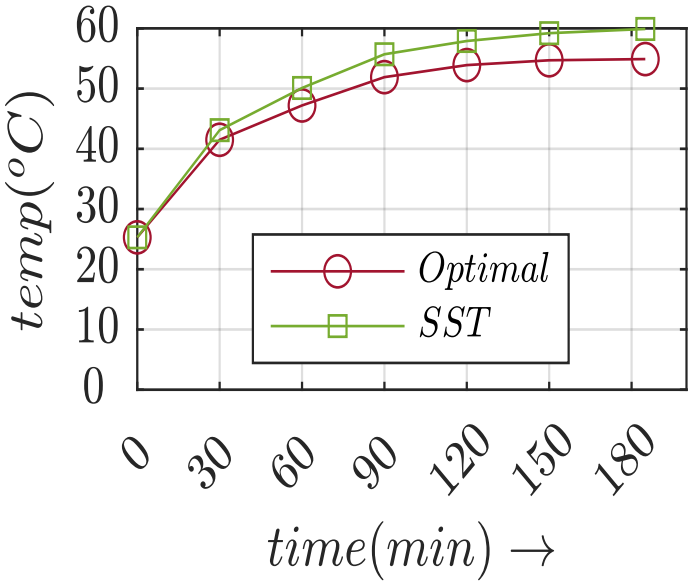


FIGURE 2.42: Rise in temperature of motor casing due to SST and SO PWM

Further, it is clear that the value of i_{thd} corresponding to SO PWM is much lower compared to SO PWM.

In order to establish the superiority of SO PWM over SST PWM, it is also imperative compare the performance of both the PWM techniques in terms of the losses occurring in the motor. However, it is difficult to directly measure the losses

happening in the induction motor. An indirect method to compare the losses in the motor due to the two PWM techniques is to measure the temperature of the stator casing of the motor. Increased rise in temperature would indicate increased losses in the motor.

In that direction, the motor is run for a long time (3 hours), at different fundamental frequencies with the both the PWM techniques. The fundamental frequency is increased at an interval of $5Hz$, starting from $30Hz$ going upto $55Hz$. The motor is made to run at a given fundamental frequency for 30 minutes before the frequency is changed to the next value. The rise in temperature of the motor casing is measured using a infra-red thermometer. The same is plotted for both SO and SST PWM in Fig.2.42. It can be clearly seen in the figure that the side in temperature due to SST PWM is more than that due to SO PWM. This clearly indicates that the occurring in the motor with the VSI operating with SO PWM is lower than when the VSI is operated with SST PWM. The reduction in the losses in motor due to SO PWM can be attributed to reduced harmonic distortion which directly impacts copper losses occurring in the motor. This experiment has been done in a temperature controlled environment where the ambient temperature is maintained constant at 25^oC.

Further, the effectiveness of the proposed pulse-transition strategy with conventional SST PWM scheme is established experimentally in Fig.2.43. i_{sd}, i_{sq}, m_r and V_{ro} are captured experimentally corresponding to the transitions from $P = 21$ to $p = 51$, $P = 15$ to $P = 9$ and $P = 9$ to $P = 3$ and presented in Fig.2.43a-2.43c respectively. All the transitions can be verified to happen smoothly with no transient in i_{sd} and i_{sq}. Further, overall dynamic performance of vector-controlled IM drive with proposed pulse transition algorithm using conventional SST is shown in Fig. 2.44. A speed reference is ramped up slowly from zero speed to the rated speed first. The load-motor is operated under current-control mode to emulate a speed-dependant friction type of load on the test-motor. The flux producing component of the current, i_{mr} is controlled at its rated value as seen in Fig. 2.44a. The measured speed (ω_r) tracks the ramped reference speed (ω_r^*) as shown in Fig. 2.44c. d and q-components

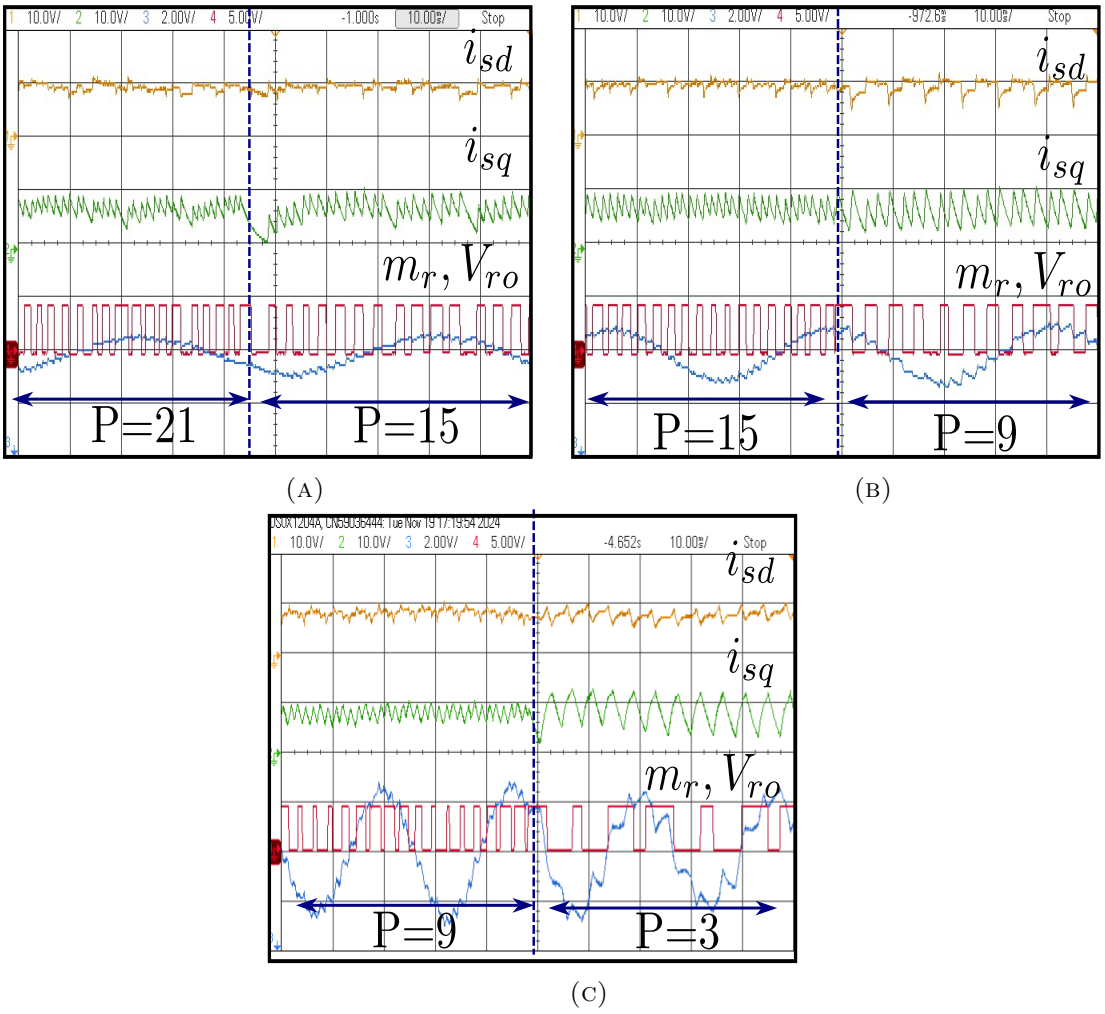


FIGURE 2.43: Experimental results showing i_{sd} (5A/div) and i_{sq} (8A/div) along with normalised V_{ro} and m_r with proposed strategy during the transition from (a) SST P=9 to SST P=3 (b) SST P=9 to SO P=9A [x axis: 10ms/div]

of the stator current vector, i_{sd} and i_{sq}, are found to be tracking their respective reference values as shown in Fig. 2.44b and 2.44d respectively. Proposed pulse transition strategy ensures negligible transients on these quantities.

2.6 Conclusion

Synchronous sine-triangle (SST) PWM scheme for Y-connected SCIM drive is initially investigated in this chapter. Particularly, the harmonic performance of the drive under operation with odd non-triplen values of P, that is $P = 7$ and $P = 5$ is studied using double-fourier series based analysis. Two methods of implementing such values of P are considered, that is, having a common carriers signal for all the three-phases

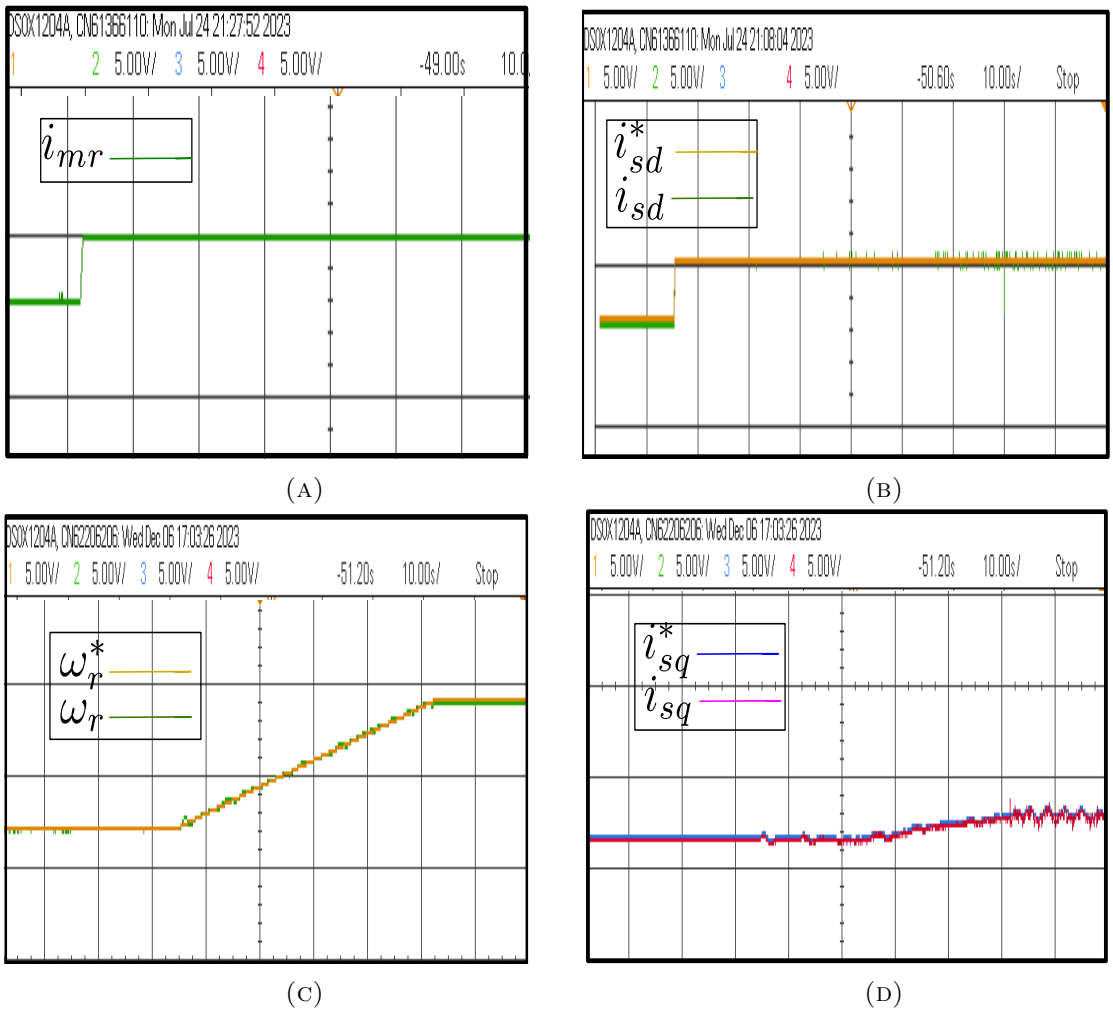


FIGURE 2.44: Experimental performance of vector controlled IM drive in terms of (a) i_{mr} [Scale: 5A/div, 5s/div] (b) i_{sd} [Scale: 5A/div, 5s/div] (c) speed [Scale: 600RPM/div, 5s/div]and (d) i_{sq} [Scale: 8A/div, 5s/div] with proposed strategy under SST PWM.

and having phase-shifted carrier signals for the three phases. It is found that with common carrier, triplen order harmonic appear in machine phase voltage and current whereas with different carrier signals, the magnitude of 5^{th} and 7^{th} order harmonics increase significantly. Both cases, the harmonic distortion in motor-line current becomes very high. Thus, a combination of SST PWM and synchronous optimal (SO) PWM has been proposed in this thesis.

Proposed synchronous optimal hybrid (SOH) PWM consists of asynchronous sine-triangle (AST), synchronous sine-triangle (SST) and synchronous optimal (SO)

PWM techniques applied over $0 < M < 0.15$, $0.15 < M < 0.43$ and $M > 0.43$, respectively. IM drive is operated under vector-control mode for desired dynamic performances. Hence, stator voltage vector ($\overrightarrow{v_s}$) angle θ_s is required to be computed for correct implementation of SST and SO PWMs. A method to estimate θ_s by using the rotor flux ($\overrightarrow{\psi_r}$) angle, ρ_{mr}, and d- and q- axis components of $\overrightarrow{v_s}$ is presented in the chapter. Synchronized triangular carriers corresponding to pulse numbers 21, 15 and 9 are generated from θ_s. Switching angles pertaining to SO PWM are expressed as a function of M through piece-wise linear equations which are generated from pre-determined optimized switching angles. Hence, linear equation based implementation of SO PWM, which does not require storage of optimal switching angles in look-up tables, is also proposed in this chapter.

Since IM drive suffers from severe transients in line currents during abrupt change in PWM pulse pattern, a stator-flux matching strategy is proposed for achieving smooth transition between present and upcoming PWM pulse patterns. The proposed PP transition strategy is independent of machine parameters and can be generalized for any PWM scheme. The proposed PWM technique and pulse transition strategy are thoroughly validated through simulations and experiments on motor drives rated at 2.2kV, 850kW, 65Hz and 415V, 3.7kW, 65Hz, respectively, operated in vector-controlled mode.

Chapter 3

Synchronous PWM Scheme: Open-End Winding Induction Motor

3.1 Introduction

As discussed in the last chapter, limitations in switching frequency (f_{sw}) of power converters in high-power medium voltage drives arise in order to curb the switching energy losses. Synchronous PWM techniques are popular for such applications. For a Y-connected SCIM drive, operation with synchronous sine-triangle (SST) PWM scheme were presented in the last chapter. It was seen that for SST PWM, at higher speeds, transition from pulse number, $P = 9$ to $P = 3$ had adverse impact on the performance of the closed-loop control of the drive. Thus, it was suggested to incorporate intermediate non-triplen pulse numbers, such as $P = 7$ and 5 to reduce the change in carrier frequency, f_c. However, it was established in the previous chapter that with SST PWM, the harmonic performance of the drive when operated with non-triplen values of P deteriorates significantly. Thus, it was proposed to incorporate synchronous optimal PWM technique while operating with these values of P. Hence,a synchronous optimal hybrid (SOH) PWM scheme was proposed.

It is, however, also important to point out here that the simplicity of implementing SST PWM scheme makes it a very popular scheme. Thus, the methods of incorporating non-triplen values of P in SST PWM with acceptable harmonic performance are investigated in this chapter. It was established in the last chapter that using multi-carrier SST PWM scheme, triplen order harmonics get cancelled but the magnitude of 5^{th} and 7^{th} order harmonics increase significantly. If these harmonics can be somehow eliminated, the harmonic performance of the drive can improve significantly.

One method to eliminate these harmonics is to use the open-end winding induction motor (OWIM) configuration. In OWIM drives, two VSIs feed power to the motor

from both the ends of the stator winding. The particular order of harmonics which are generated in equal magnitude and same phase from the two VSIs at both the ends, will cancel each other and not appear in he machine phase-voltage. Thus, this chapter explores the possibility of using an OWIM drive for high-power application such as railway traction. However, it is established in literature that OWIM drives need two isolated DC sources to ensure that no common-mode current flows through the motor windings. In case only one DC source is available, specialized PWM techniques are required to be implemented to ensure zero common-mode current. Thus, it is imperative to first investigate if OWIM drive can be a suitable option for applications such as railway traction.

Once, it is established that OWIM drive can be suitable option for such applications, a SST PWM scheme is proposed for the OWIM drive incorporating odd non-triplen and all triplen values of P for OWIM drive is proposed in this chapter. Double-series based analysis is done to predict the harmonic profile of machine phase-voltage and current. Further, several other analyses, such as space-vector based and stator-flux trajectory based analyses are done for the proposed PWM scheme in this chapter. Finally, the performance of the PWM scheme is validated both in simulation and experiments.

3.2 Proposed modification in traction drive to incorporate OWIM configuration

The existing railway propulsion system with Y-connected SCIM drive is shown in Fig.3.1a. It consists of the induction motor connected to a two-level three-phase VSI. The DC-link of the three-phase VSI is maintained at 2.8kV and is formed by two single-phase front-end converters (FEC) connected in parallel. On the AC side, these FECs are connected to the two secondary windings of a three-winding transformer. Thus, in the present configuration two isolated DC sources are connected in parallel to create the DC-link for the three-phase VSI. Thus, this configuration can be modified to incorporate an OWIM drive without changing the input transformer and single -phase FECs. Fig.3.1b shows the OWIM based modified traction drive with the

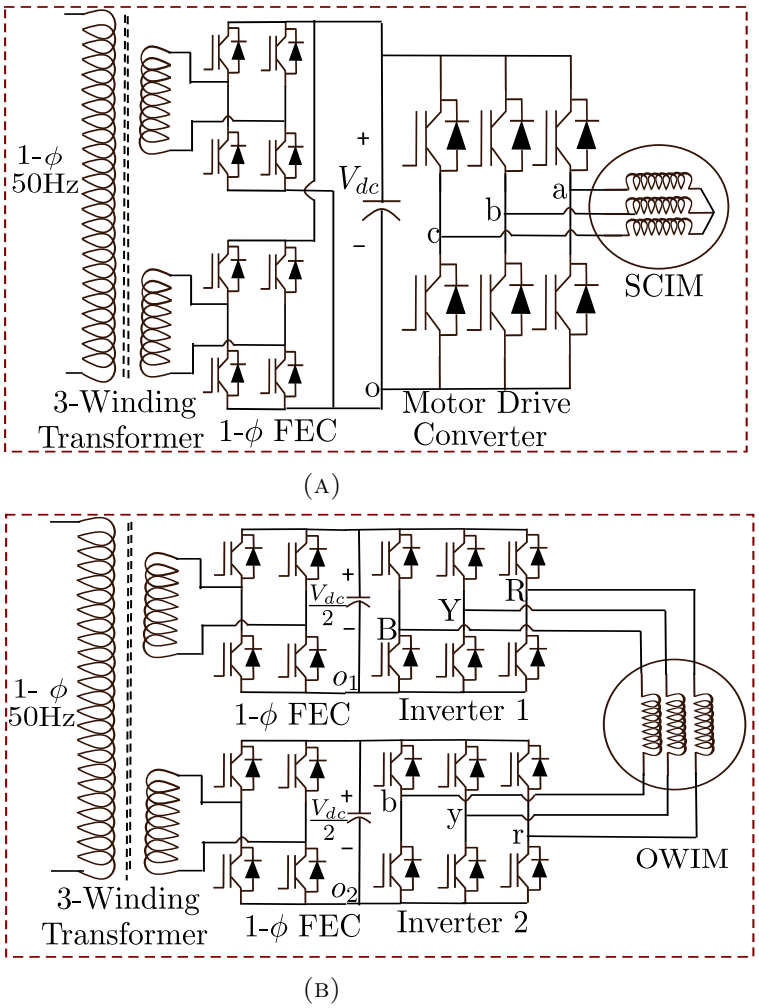


FIGURE 3.1: (a) Conventional 2L-VSI fed SCIM and (b) proposed OWIM based modified drives for railway propulsion system

input transformer and single phase AFECs. Both inverter 1 and inverter 2 are connected to one AFEC each, which are fed from isolated secondary windings of the input transformer. Thus, DC bus voltages of the OWIM are kept isolated from each other to avoid circulating common-mode currents. DC bus voltage of each VSI is maintained at 1.8kV to ensure controllability of AFECs without over-fluxing the induction machine. The Reduction in DC link voltage consequently reduces the voltage requirements for DC bus capacitors and IGBTs by at least 1kV as compared to standard SCIM drive. Therefore, despite adding one extra inverter, proposed OWIM drive does not impose a significant additional cost on the propulsion system. Moreover, in case of failure of one AFEC, the corresponding terminals of OWIM can

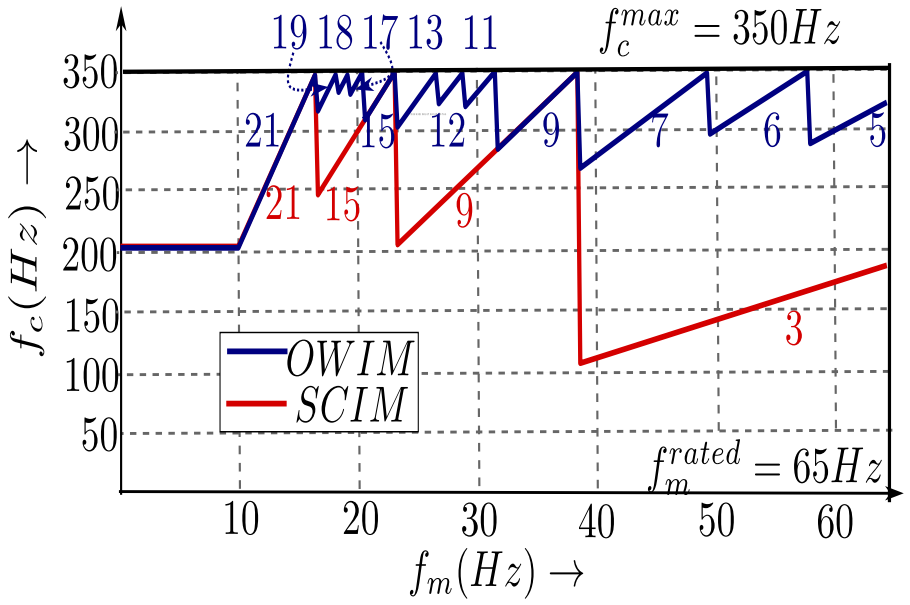


FIGURE 3.2: Plot of f_{sw} against f_m for standard SCIM and OWIM based modified drives

be shorted and the motor can be operated as SCIM at rated torque up to half-rated speed. It is to be noted that the current carried by the motor-side inverter remains same as standard SCIM drive.

The resultant phase voltages (v_{Rr}, v_{Yy}, v_{Bb}) corresponding to the OWIM drive are given by,

$$v_{Xx} = v_{Xo_1} - v_{xo_2} - v_{o_2o_1} \tag{3.1}$$

where v_{Xo_1} $(X \in \{R, Y, B\})$ and v_{xo_2} $(x \in \{r, y, b\})$ are the pole voltages of inverter 1 and 2 w.r.t. negative DC bus points o_1 and o_2, respectively (Fig.3.1b); v_{Xx} $(Xx \in \{Rr, Yy, Bb\})$ is the machine phase voltage and $v_{o_2o_1}$ is the voltage between o_1 and o_2 which is computed as

$$v_{o_2o_1} = \frac{(v_{Ro_1} + v_{Yo_1} + v_{Bo_1})}{3} - \frac{(v_{ro_2} + v_{yo_2} + v_{bo_2})}{3} \tag{3.2}$$

A suitable PWM strategy is developed in the next section to utilise odd non-triplen and even triplen pulse numbers as well.

3.3 Proposed Multi-Carrier based Synchronized Sin-Triangle PWM Strategy for OWIM drive

Standard SCIM drive, operated with SST PWM, involves balanced three-phase modulating signals and a common carrier. f_{sw} is usually restricted below 350Hz (f_{sw}^{max}) in traction converters. As stated in section I, P, is maintained at odd triplen numbers (e.g. 3,9,15...) to retain all waveform symmetries [37]. Therefore, 2L-VSI fed SCIM drive operates with a set of odd-triplen pulse numbers over complete range of f_m. The variation of carrier frequency, f_c with f_m over the complete range of operation is shown in Fig.3.2. It should be noted that there are large transitions in f_c at the junction of two different pulse numbers. Since f_c and f_{sw} are equal in a two-level VSI, a change in P leads to a large change in f_{sw}. As mentioned earlier, these transitions hamper the drive performance. So special provisions must be included to mitigate this [38], [34].

One method to overcome this problem, is to incorporate intermediate values of P, such as odd non-triplen (i.e. 5,7,11..) and even triplen integers (i.e. 6,12,18..). For a conventional SCIM drive, even triplen values of P lead to even harmonics in the machine phase-voltage and current. On the other hand, non-triplen values of P lead to loss of three-phase symmetry in the inverter pole-voltages and consequently leads to triplen-order harmonics in current. Another, way to incorporate these values of P is to use multi-carrier PWM technique. However, at lower values of P, multi-carrier PWM results in high magnitude of 5^{th} and 7^{th} order harmonics in the line current, thereby deteriorating the harmonic performance significantly. This was established in the last chapter analytically and through simulations and experiments. Thus, operation of standard SCIM drive is limited only to odd triplen values of P when it comes to SST PWM.

As it is established in the last section, that OWIM is suitable for railway traction application from the point of view of topology or configuration of the drive, it is interesting to investigate if an OWIM based configuration offers more flexibility in

terms of implementation of PWM technique. For triplen values of P, a common carrier is used for all three-phases. For, non triplen values of P, three different carriers are considered for the three-phases.

(3.1) and (3.2) gives the expression of machine phase-voltage of an OWIM drive in terms of the inverter pole-voltages. These relations hold true for individual order of harmonics as well. It can seen from (3.1) and (3.2), if a particular order of harmonic is generated in equal magnitude and same phase from the two VSIs in the OWIM drive, the same will be eliminated in the machine phase-voltage.

Thus, it is important to predict the harmonic profile of the inverter pole-voltages for even-triplen and odd-non triplen values of P. This is done using double-fourier series based mathematical framework in the following sub-section.

3.3.1 Double Fourier Series based Analysis to Predict Harmonic Profile of the inverter pole-voltages in an OWIM drive

Details of the double fourier series are presented in Appendix 7. The mathematical expression for harmonic components generated in the inverter pole-voltages for SST PWM is given (2). As mentioned in the appendix, a combination of (m, n, P) decides the order of k^{th} harmonic voltage (v_k) in (2). Here, $k = mP + n$.

The appropriate values of γ_β to be used in (2) can be selected from Table 3.1 for inverter I ($\beta \in R, Y, B$) and inverter II ($\beta \in r, y, b$) for various values of P. Here, $P = 9$ (odd-triplen integer), $P = 7, 5$ (odd non-triplen integers) and $P = 6$ (even-triplen integer) are considered. It should be noted that γ_β corresponding to each phase for inverter I and inverter II are shifted by π.

Further, ϕ_β assumes same values for triplen pulse numbers whereas it has a phase shift of $\frac{2\pi}{3}$ between respective phases for non-triplen pulse numbers. Table 3.2 presents the values of for ϕ_β for inverter I ($\beta \in R, Y, B$) and inverter II ($\beta \in r, y, b$) for $P = 9, 7, 6$ and 5.

All harmonic components pertaining to $|m|, |n| \geq 3$ are ignored in this analysis

TABLE 3.1: γ_β for Inverter I and II

	γ_R	γ_Y	γ_B	γ_r	γ_y	γ_b
$P=9$	0	$-\frac{2\pi}{3}$	$-\frac{4\pi}{3}$	π	$\frac{\pi}{3}$	$-\frac{2\pi}{3}$
$P=7$	0	$-\frac{2\pi}{3}$	$-\frac{4\pi}{3}$	π	$\frac{\pi}{3}$	$-\frac{2\pi}{3}$
$P=6$	0	$-\frac{2\pi}{3}$	$-\frac{4\pi}{3}$	π	$\frac{\pi}{3}$	$-\frac{2\pi}{3}$
$P=5$	0	$-\frac{2\pi}{3}$	$-\frac{4\pi}{3}$	π	$\frac{\pi}{3}$	$-\frac{2\pi}{3}$

TABLE 3.2: ϕ_β for Inverter I and II

	ϕ_R	ϕ_Y	ϕ_B	ϕ_r	ϕ_y	ϕ_b
$P=9$	$\frac{\pi}{2}$	$\frac{\pi}{2}$	$\frac{\pi}{2}$	$\frac{\pi}{2}$	$\frac{\pi}{2}$	$\frac{\pi}{2}$
$P=7$	$\frac{\pi}{2}$	$-\frac{\pi}{6}$	$-\frac{5\pi}{6}$	$\frac{\pi}{2}$	$-\frac{\pi}{6}$	$-\frac{5\pi}{6}$
$P=6$	$\frac{\pi}{2}$	$\frac{\pi}{2}$	$\frac{\pi}{2}$	$\frac{\pi}{2}$	$\frac{\pi}{2}$	$\frac{\pi}{2}$
$P=5$	$\frac{\pi}{2}$	$-\frac{\pi}{6}$	$-\frac{5\pi}{6}$	$\frac{\pi}{2}$	$-\frac{\pi}{6}$	$-\frac{5\pi}{6}$

as their magnitude becomes insignificant (Appendix 7). The simplified expression for the relevant harmonic component in the R-phase pole voltage for both the inverters can be written as,

$$\tilde{v_{Ro_i}} = \sum_{m=1}^{2}\sum_{n=-2}^{2}\left(A_m^n cos\big(k\omega_o t + m\frac{\pi}{2} + (i+1)n\pi\big)\right) \tag{3.3}$$

where $i = 1$ and 2 correspond to inverter 1 and inverter 2 respectively.

Thus, the predicted harmonic components of pole voltages for inverter 1 and 2 are tabulated in Table 3.3 corresponding $m = 1$ and 2 only. Here, the magnitude of the $\tilde{v}_{Ro_1}$ and $\tilde{v}_{ro_2}$ have been presented. For all combinations of (m, n) for which, $m+n$ becomes and even integer, the magnitude of corresponding k^{th} order harmonic becomes 0 in Table 3.3 (see (3)).

As seen from Table 3.3a, for $P = 9$, the combination $m = 1$ and $n = -2$ generates v_7 ($k = 7$) in pole-voltages of both inverters, 1 and 2 as determined by (3.3). However, the magnitude and and phase of v_7 are same for both inverters (see (3.3)). Thus, v_7 gets cancelled out in machine phase voltage. Thus, the combinations of (m, n) for which $m + n$ is odd and n is even, the corresponding k^{th} order harmonics appear in

TABLE 3.3: Predicted harmonic profile of pole voltage for various P

(A) $P = 9$, $k = 9m + n$

m	n	k	$v_{\tilde{Ro1}}$	$v_{\tilde{ro2}}$
1	-2	7	A_1^{-2}	A_1^{-2}
	-1	8	0	0
	0	9	A_1^0	A_1^0
	1	10	0	0
	2	11	A_1^{-2}	A_1^{-2}
2	-2	16	0	0
	-1	17	A_2^{-1}	$-A_2^{-1}$
	0	18	0	0
	1	19	A_2^1	$-A_2^1$
	2	20	0	0

(B) $P = 7$, $k = 7m + n$

m	n	k	$v_{\tilde{Ro1}}$	$v_{\tilde{ro2}}$
1	-2	5	A_1^{-2}	A_1^{-2}
	-1	6	0	0
	0	7	A_1^0	A_1^0
	1	8	0	0
	2	9	A_1^2	A_1^2
2	-2	12	0	0
	-1	13	A_2^{-1}	$-A_2^{-1}$
	0	14	0	0
	1	15	A_2^1	$-A_2^1$
	2	16	0	0

(C) $P = 6$, $k = 6m + n$

m	n	k	$v_{\tilde{Ro1}}$	$v_{\tilde{ro2}}$
1	-2	4	A_1^{-2}	A_1^{-2}
	-1	5	0	0
	0	6	A_1^0	A_1^0
	1	7	0	0
	2	8	A_1^{-2}	A_1^{-2}
2	-2	10	0	0
	-1	11	A_2^{-1}	$-A_2^{-1}$
	0	12	0	0
	1	13	A_2^1	$-A_2^1$
	2	14	0	0

(D) $P = 5$, $k = 5m + n$

m	n	k	$v_{\tilde{Ro1}}$	$v_{\tilde{ro2}}$
1	-2	3	A_1^{-2}	A_1^{-2}
	-1	4	0	0
	0	5	A_1^0	A_1^0
	1	6	0	0
	2	7	A_1^2	A_1^2
2	-2	8	0	0
	-1	9	A_2^{-1}	$-A_2^{-1}$
	0	10	0	0
	1	11	A_2^1	$-A_2^1$
	2	12	0	0

inverter pole-voltages but cancel in the machine phase-voltage. The same analysis can be extended for other harmonics as well pertaining to $P = 9$. As highlighted with blue color in Table 3.3, v_{17} and v_{19} are found to harmonics present generated in opposite phase in the inverter pole-voltages. Thus, they will add up in the machine phase-voltage and becomes the dominant harmonics in the phase voltage. Similarly, the analysis is extended for $P = 7, 6$ and 5 as well in Table 3.3. The resultant dominant harmonics are highlighted with blue color in Table 3.3. For $P = 7$ and $P = 5$, the dominant lower order harmonics which appeared in the Y-connected SCIM with multi-carrier PWM gets cancelled in OWIM. Thus, from the above analysis, it can be concluded, that the harmonic performance of OWIM drive with multi-carrier

PWM will for odd non-triplen values of P will be considerably improved with SST PWM. Further, all even order harmonic will also be cancelled in the machine-phase voltage for even triplen values of P.

3.3.2 Proposed Multi-Carrier SST PWM for OWIM Drive

Based on the above analysis, a multi-carrier SST PWM is proposed for OWIM drive. Proposed PWM utilizes odd non-triplen (i.e. 5,7,11..) and even triplen pulse numbers (i.e. 6,12,18..) along with traditional odd triplen (i.e. 3,9,15..) ones. The same is plotted in Fig.3.2 in blue colored line. It is seen that the transitions in f_{sw} have reduced significantly compared to 2L-VSI fed SCIM drive due to the availability of intermediate pulse numbers.

The proposed PWM method uses independent carriers (i.e. C_R, C_Y and C_B) for each modulating signals (i.e m_R, m_Y and m_B, respectively). Carrier frequency is maintained according to P and f_m. Further, each carrier is synchronized to have same zero-crossing as the respective modulating signal. This is achieved by deriving the carriers from the phase angles, θ_R, θ_Y and θ_B corresponding to m_R, m_Y, and m_B, respectively, as represented in (3.4).

$$C_R = \begin{cases} \frac{2}{\pi}\theta_{C_R}; & 0 \leq \theta_{C_R} \leq \frac{\pi}{2} \\ \frac{2}{\pi}(\pi - \theta_{C_R}); & \frac{\pi}{2} \leq \theta_{C_R} \leq \frac{3\pi}{2} \\ \frac{2}{\pi}(\theta_{C_R} - 2\pi); & \frac{3\pi}{2} \leq \theta_{C_R} \leq 2\pi \end{cases} \tag{3.4}$$

Here, θ_{C_R} is obtained as given in (3.5).

$$\theta_{C_R} = mod(P * \theta_R, 2\pi) \tag{3.5}$$

Similarly, C_Y and C_B are also generated from θ_Y and θ_B, respectively.

Fig.3.3a-3.3d present the plot of carriers and modulating signals for inverter 1 corresponding to $P = 9, 7, 6$ and 5, respectively. It should be observed that C_R, C_Y and C_B overlap with each other for triplen P (i.e. 6 and 9) (see Fig.3.3a and Fig.3.3c). Same set of carriers are used for inverter 2 as well. However, modulating signals for inverter 1 and 2 are computed as

$$m_X = -m_x = M\sin(\omega_m t - \gamma), \tag{3.6}$$

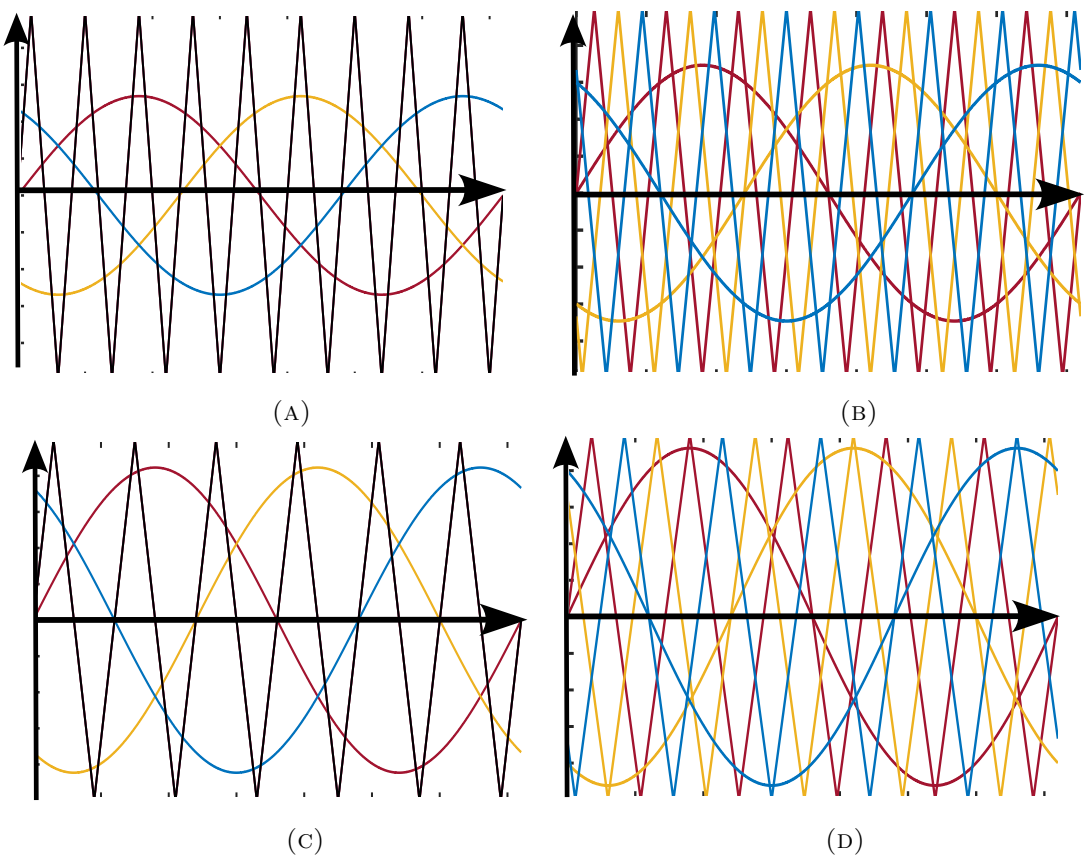


FIGURE 3.3: Three-phase modulating signals and triangular carriers for inverter 1 at (a) f_m=35Hz, M=0.5384 (P=9) (b) f_m=45Hz, M=0.6923 (P=7) (c) f_m=55Hz, M=0.8461 (P=6) and (d) f_m=65Hz, M=1 (P=5) pertaining to proposed OWIM drive.

where, $X \in \{R, Y, B\}$, $x \in \{r, y, b\}$ and $\gamma \in \{0, \frac{2\pi}{3}, \frac{4\pi}{3}\}$; m_R,m_Y and m_B are the modulating signals for inverter 1; m_r, m_y and m_b are that for inverter 2 and M is the desired modulation index.

For open-loop constant V/f drive, M is computed as-

$$M = minimum\langle \frac{f_m}{f_r}, 1 \rangle \tag{3.7}$$

where, f_r is the rated fundamental frequency of the motor.

DC bus voltage is appropriately designed such that the rated phase voltage is supplied to motor at $M = 1$. The proposed PWM scheme is compared with other popular PWM schemes for OWIM drive on various factors in Table 3.4. Here, V_{dc} is the required DC voltage for a 2L-VSI fed SCIM drive operated with SST PWM and

TABLE 3.4: Comparison of various PWM schemes for OWIM drive

Factor for comparison	[10]	[12]	[13]	Present Work
DC Supply	1	1	1	2
V_{dc_1} V_{dc_2}	$0.5V_{dc}$ $0.5V_{dc}$	V_{dc} $0.289V_{dc}$	$0.5V_{dc}$ $0.5V_{dc}$	$0.5V_{dc}$ $0.5V_{dc}$
PWM technique	Space-vector	Dodecagonal SV	Offline Optimal	Sine-Triangle
Non-triplen P	NO	NO	YES	YES
f_{sw} of VSI 1 f_{sw} of VSI 2	$f_{sw} = 1kHz$ $f_{sw} = 1kHz$	$f_{sw} \leq 720Hz$ $f_{sw} \leq 1440Hz$	$f_{sw} \leq 400Hz$ $f_{sw} \leq 400Hz$	$f_{sw} \leq 350Hz$ $f_{sw} \leq 350Hz$

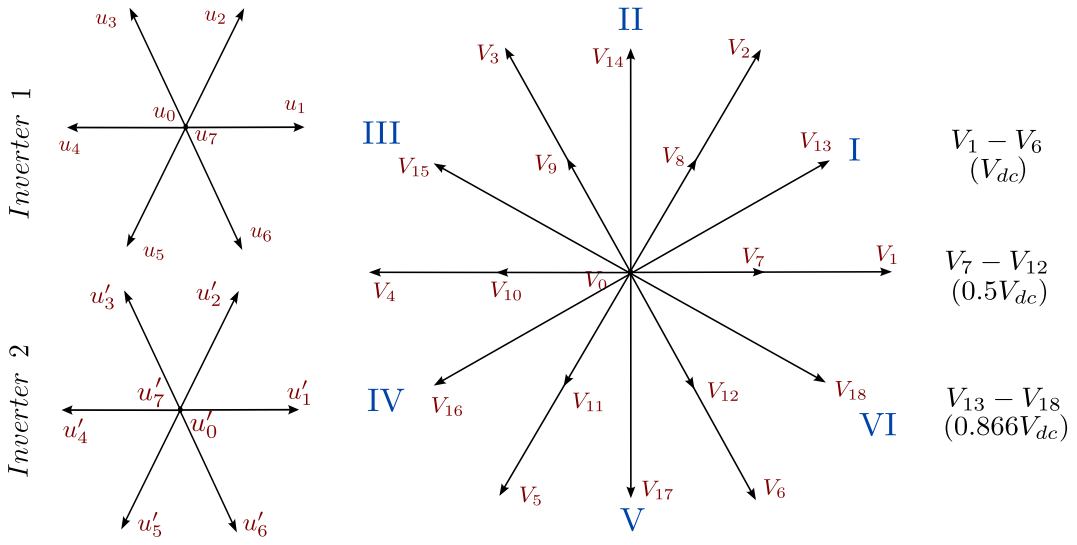


FIGURE 3.4: Voltage vectors corresponding to individual inverters and combined phase voltages pertaining to OWIM drive.

V_{dc_1} and V_{dc_2} correspond to DC link voltages of VSI 1 and 2 respectively.

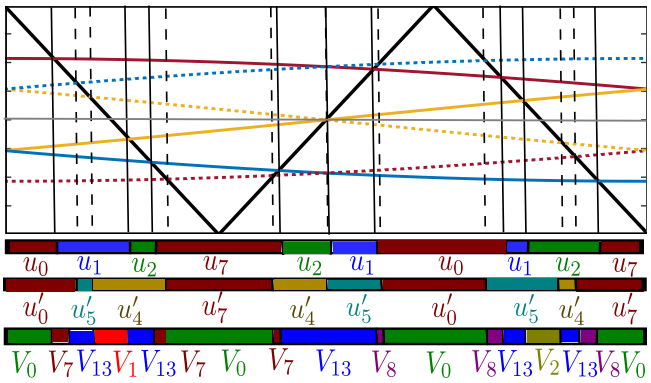
Further analyses, using the notion space vectors, fourier series and stator flux trajectory for the proposed multi-carrier PWM for the OWIM are done in the next section.

3.4 Further Analysis of Proposed PWM Technique

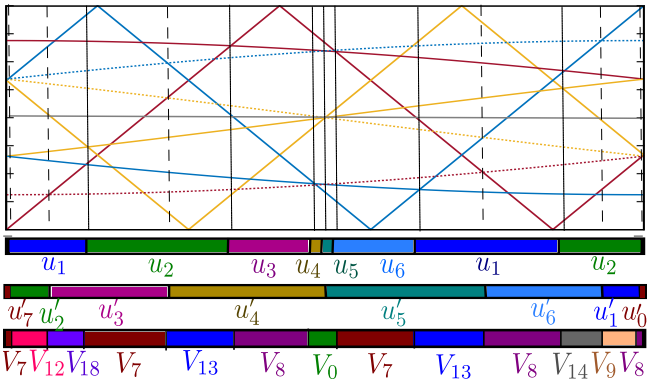
Space vector, fourier series and stator-flux vector based analyses for the proposed PWM technique are performed in this section.

3.4.1 Space vector based analysis

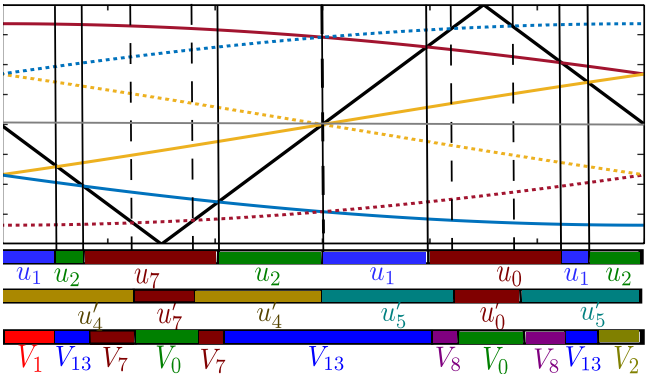
Inverter states applied by two-level VSIs are represented as space vectors for proposed OWIM drive [9], [37]. These are combined vectorially, as shown in (3.8), to determine



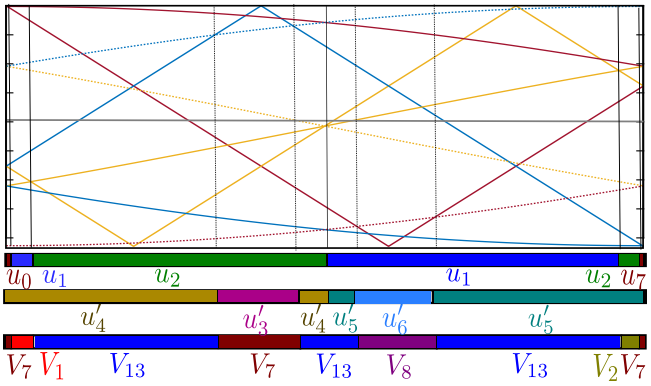
(A)



(B)



(C)



(D)

FIGURE 3.5: Illustration of voltage vector applied over sector I by individual inverters and resultant voltage vector corresponding to (a) Fig. 3.3a (b) Fig. 3.3b (c) Fig. 3.3c and (d) Fig. 3.3d

the resultant voltage vectors applied on OWIM drive [9], [10]. Fig. 3.4 presents all the possible voltage vectors applied from the individual inverters and resultant voltage vectors.

$$\overrightarrow{\mathrm{V}_k} = \overrightarrow{\mathrm{u}_i} - \overrightarrow{\mathrm{u}'_j};\ 0 \leq i, j \leq 7 \text{ and } 0 \leq k \leq 18 \tag{3.8}$$

Individual and combined voltage vectors applied by proposed PWM technique over sector I are identified through the three-phase pole voltages. Fig.3.5a-3.5d illustrate the three-phase modulating signals and carriers of both the inverters for the proposed PWM corresponding to Fig.3.3a-3.3d, respectively, over sector I. Applied voltage vectors are identified and marked on the bottom of the same figure. For clarity, middle of the sector is also marked with a broken vertical line. Vector sequence pertaining to P=9 (Fig.3.5a) indicates that resultant voltage vector sequence starts and ends with a zero-vector over sector I. It also shows that only the nearest voltage vectors are applied to realize the desired voltage vector (see Fig.3.4). Further, voltage vectors applied at sectors angle α (say, V_1) and $\frac{\pi}{3} - \alpha$ (say, V_2) are dual of each other (see Fig.3.5) which establishes the condition of symmetry within a sector [37]. Fig.3.5b-3.5d also follow a similar pattern of voltage vectors. However, the vector sequence starts and ends with an active vector lying at the boundary of the sector (i.e V_1, V_2, V_7 or V_8). It should be noted that proposed PWM applies some active vectors which are beyond sector I (e.g. V_9, V_{12}, V_{14}, V_{18}) for P=7 (Fig.3.5b) without violating the condition of symmetry. Thus, the proposed PWM technique ensures symmetry within a sector for all pulse numbers considered in the PWM technique.

3.4.2 Analytical estimation of harmonic spectrum

Magnitude of the dominant harmonics present, in the machine phase voltages, are analytically calculated in this sub-section through Fourier analysis of the pole voltages generated by the individual inverters. Positive and negative zero-crossings [33] in the pole voltage waveform of each inverter is identified from intersection of modulating signal and corresponding carrier for the proposed PWM. For a particular P, these zero-crossings will remain same irrespective of f_m. This is illustrated in Fig.3.6 for $P = 9$.

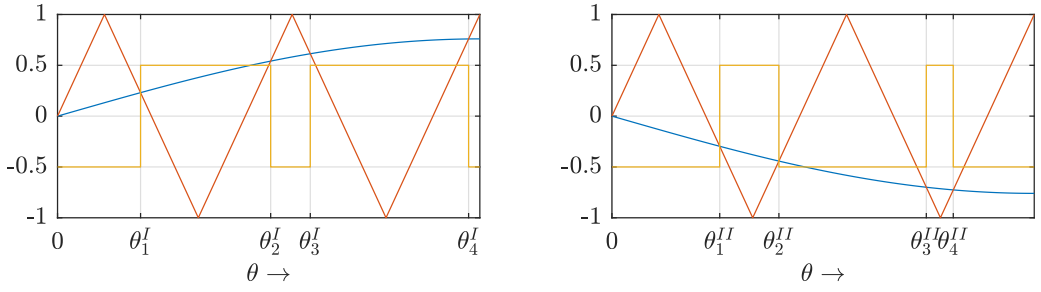


FIGURE 3.6: R-phase modulating signal, carrier and normalized pole voltages of (a) Inverter 1 and (b) Inverter 2

From the general expression of Fourier expansion [37], the coefficient of k^{th} harmonic, B_k, of the inverter pole voltage can be expressed as given in (3.9).

$$B_k = \frac{V_{dc}}{k\pi}\left([\sum_{i=1}^{i=l}(-1)^{i+1}cos(k\theta_i^y)] - 1\right) \quad y \in \{I, II\} \tag{3.9}$$

where $l = 2P - 1$ and θ_i is the corresponding angle of intersection between modulating signal and carrier (see Fig. 3.6). 5^{th}, 7^{th}, 11^{th} and 13^{th} harmonics normalized w.r.t V_{dc} are plotted in Fig.3.7 for $P = 9, 7, 6$ and 5. Voltage harmonics generated with same phase tend to cancel out whereas the harmonics with opposite phase add up in the resultant phase voltage (see Fig.3.7).

3.4.3 Stator-flux Analysis

Tip of the stator-flux vector ($\overrightarrow{\psi_s}$) has a circular trajectory for a balanced three-phase sinusoidal voltage. However, the trajectory deviates from the circle when a PWM voltage is applied to motor. The amount of deviation correlates to the harmonic distortion in the motor line current [31]. Thus, a good PWM technique would have a nearly circular trajectory for the tip of the stator flux vector [31].

$$\overrightarrow{\psi_s} = \int_0^T (v_{Rr} + v_{Yy}e^{j\frac{2\pi}{3}} + v_{Bb}e^{j\frac{4\pi}{3}})\, dt \tag{3.10}$$

$\overrightarrow{\psi_s}$ is computed as (3.10) for a three-phase system. The trajectory of the tip of $\overrightarrow{\psi_s}$ is obtained by plotting real part of $\overrightarrow{\psi_s}$ i.e. ($\psi_{s\alpha}$) against its imaginary part i.e. $\psi_{s\beta}$. Fig.3.8a-3.8d present the trajectory plot pertaining to proposed PWM technique corresponding to Fig.3.3a-3.3d, respectively. Trajectories corresponding to P= 9 and 6 are found to be nearly circular, whereas, those for P =7 and 5 are observed to

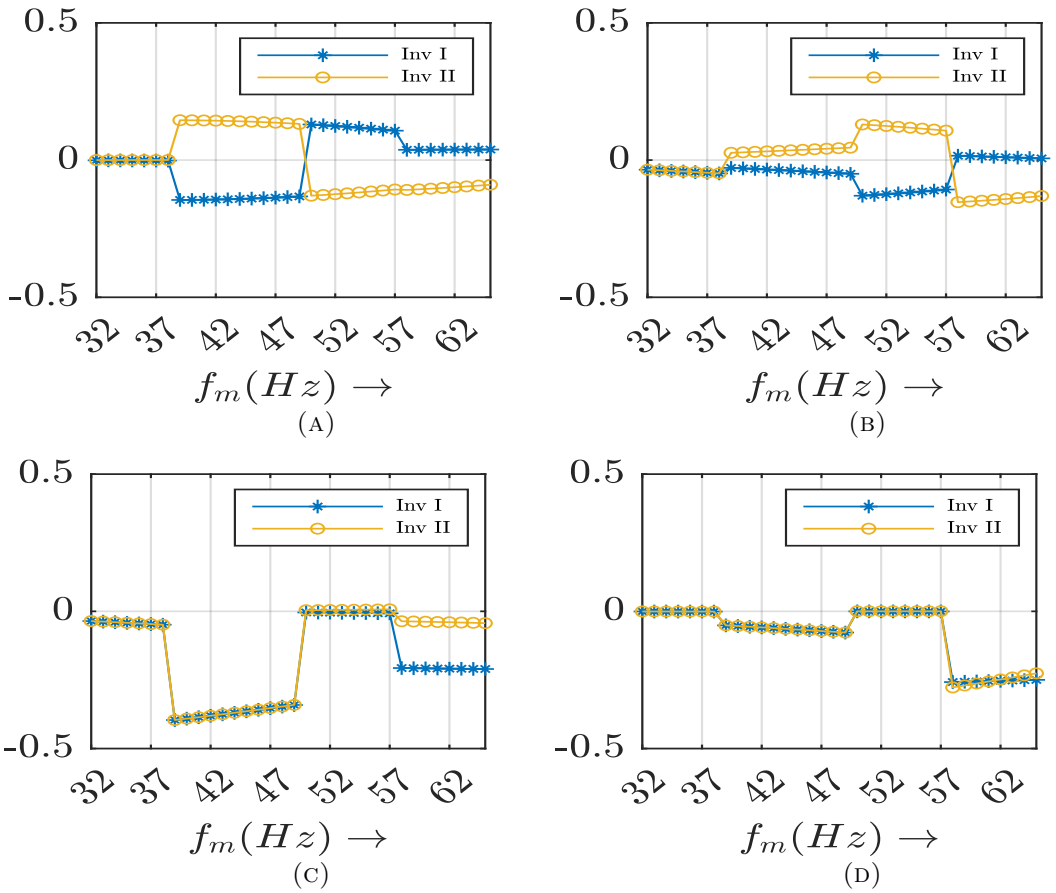


FIGURE 3.7: Magnitude of normalized (a) 13^{th} (b) 11^{th} (c) 7^{th} and (d) 5^{th} harmonic over the complete range of frequency

have some deviations within reasonable limits.

3.5 Validation of Proposed PWM Technique

3.5.1 Simulation Results

Performance of the proposed OWIM and standard SCIM drives are compared through simulation on a 850kW, 2.2kV traction drive system. MATLAB/Simulink based mathematical model of both drives are developed and operated in open loop constant V/f mode with f_{sw} as shown in Fig.3.2. DC bus voltage is maintained at 3.6kV for standard SCIM drive whereas the same is maintained at 1.8kV (both inverters) for proposed OWIM drive. The parameters of the motor are presented in Appendix 7 (Table 2).

Pole voltages of inverter 1 and 2 (v_{Ro_1}, v_{ro2}) and the resultant machine phase

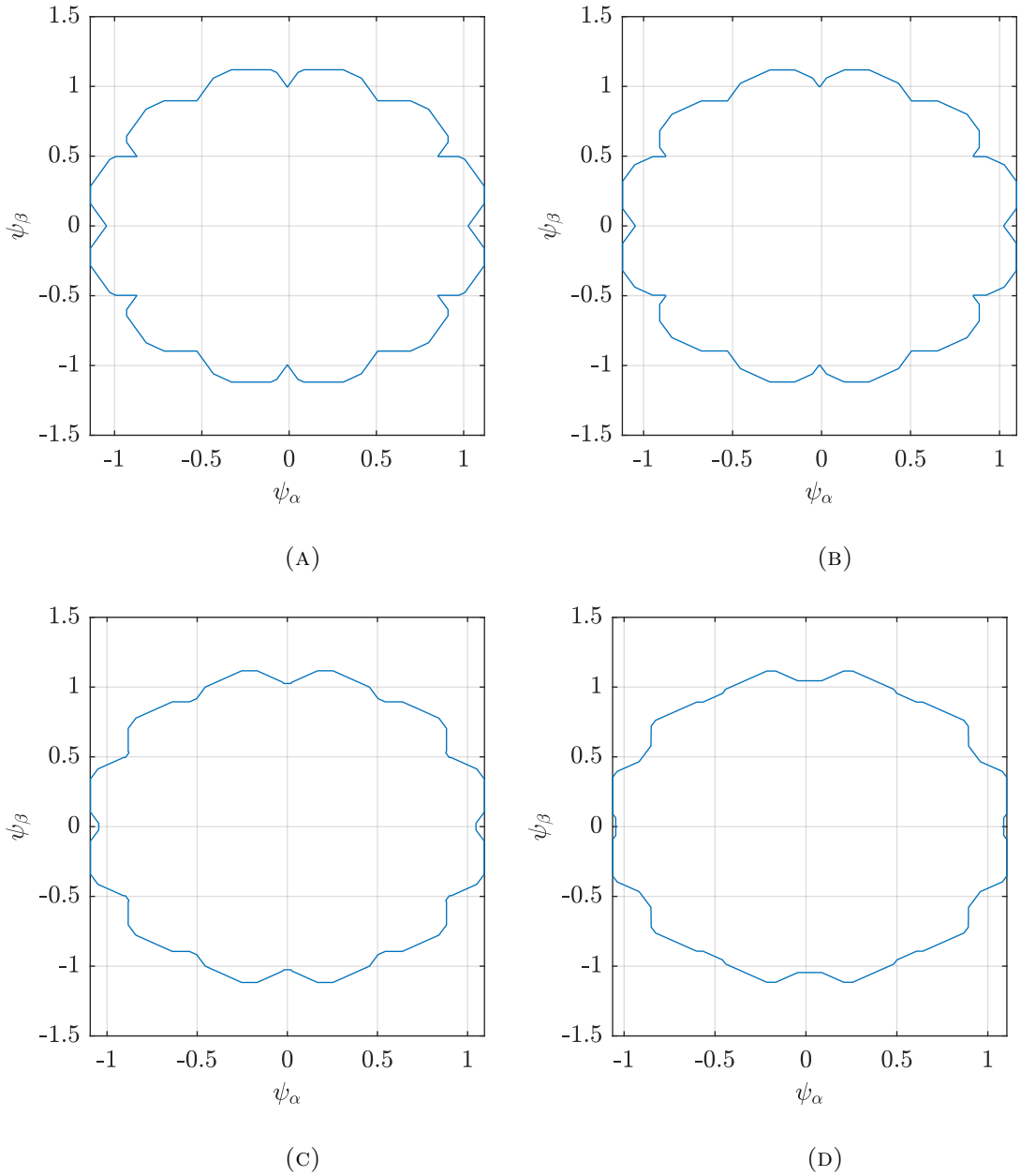


FIGURE 3.8: Trajectory of tip of normalized $\overrightarrow{\psi_s}$ corresponding to (a) Fig. 3.3a (b) Fig. 3.3b (c) Fig. 3.3c and (d) Fig. 3.3d

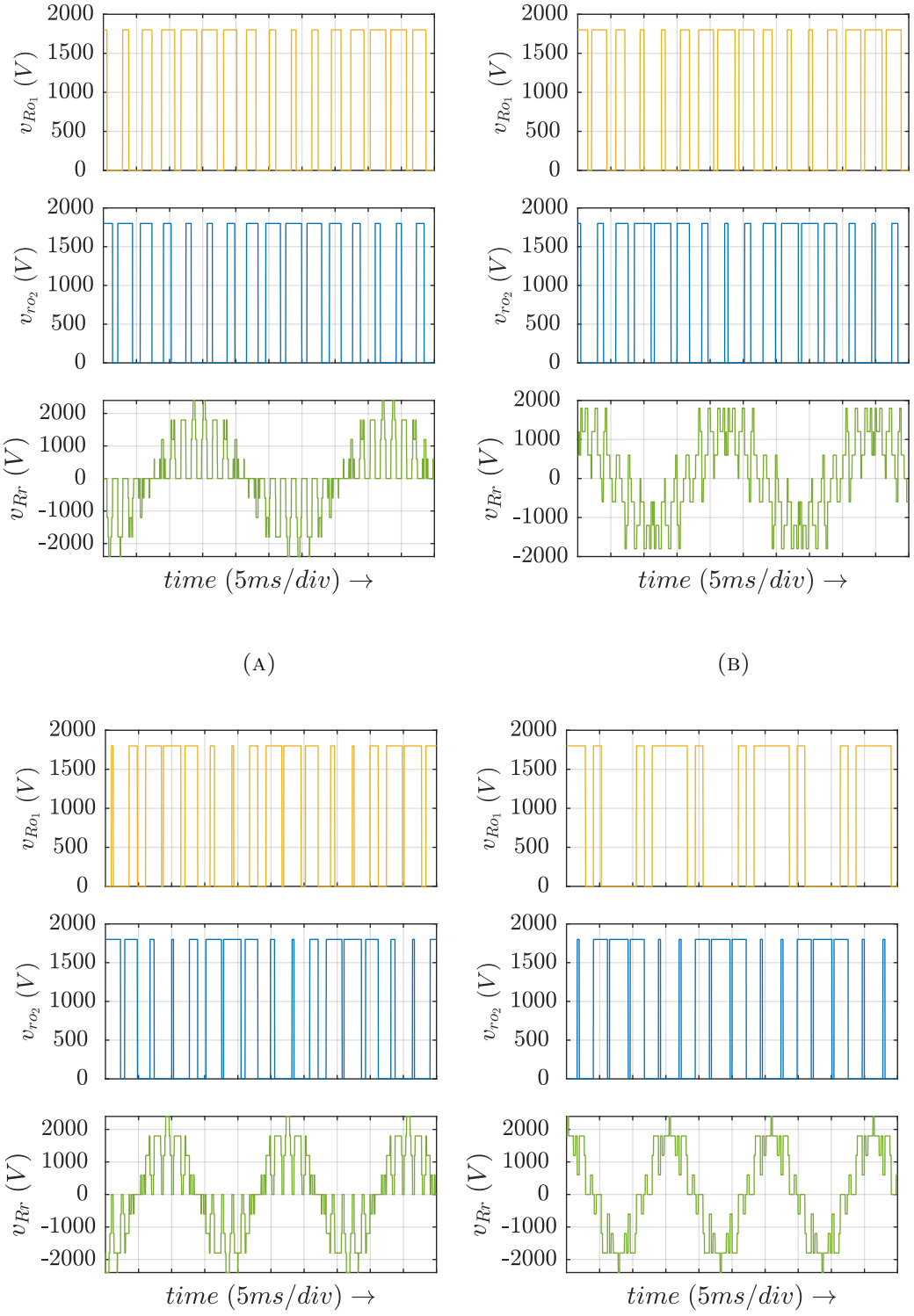


FIGURE 3.9: Pole voltages of individual inverters (v_{Ro_1}, v_{ro_2}) and resultant phase voltage (v_{Rr}) corresponding to (a) Fig. 3.3a (b) Fig. 3.3b (c) Fig. 3.3c and (d) Fig. 3.3d

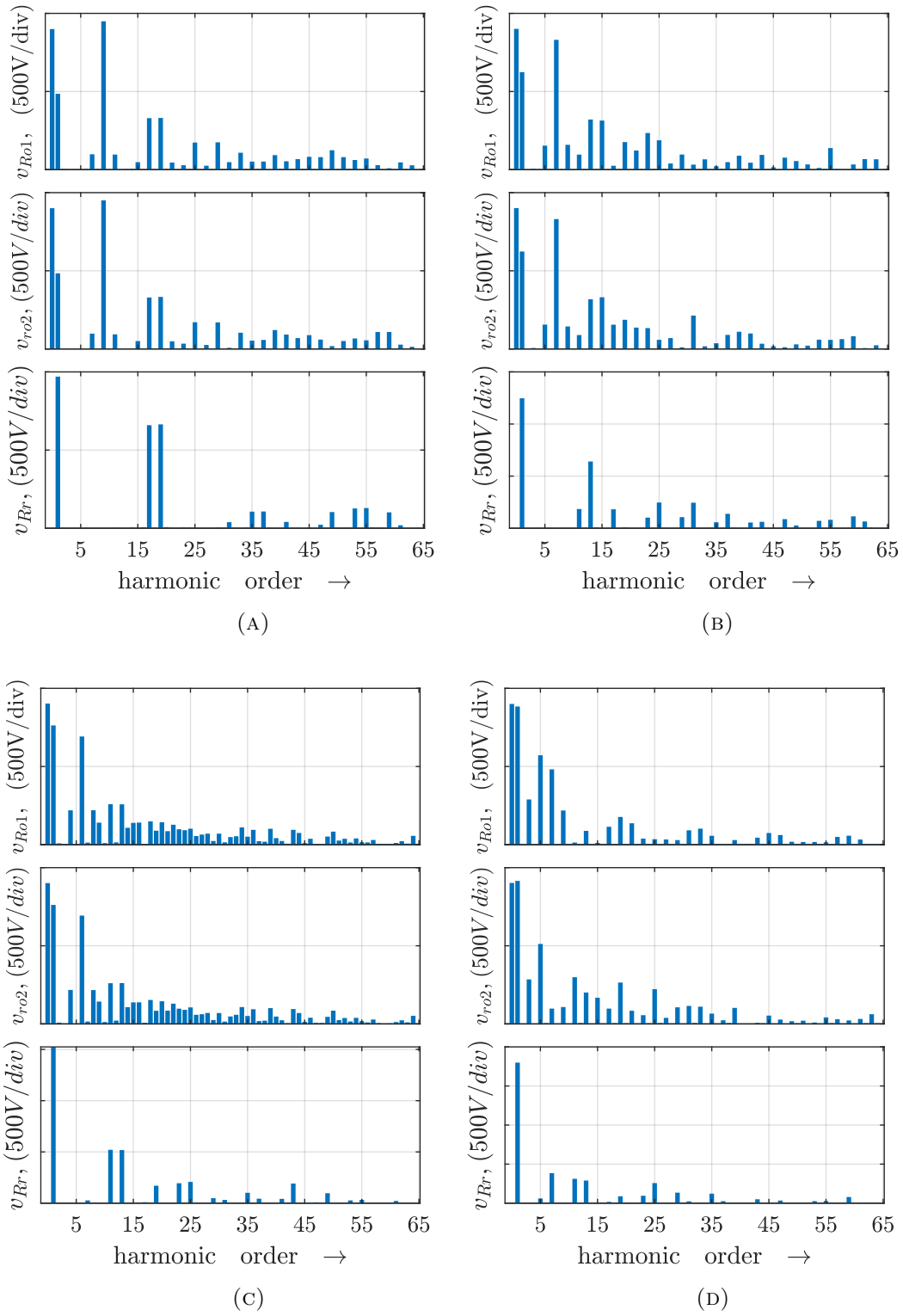


FIGURE 3.10: Harmonic spectrum of v_{Ro_1}, v_{ro_2}, v_{Rr} corresponding to (a) Fig. 3.9a (b) Fig. 3.9b (c) Fig. 3.9c and (d) Fig. 3.9d

TABLE 3.5: I_{THD} under full load

	2L-VSI SCIM	OWIM
$f_m = 35Hz, P = 9$	32.49%	26.45%
$f_m = 45Hz, P = 7$	64.%	21.63%
$f_m = 55Hz, P = 6$	53.06%	20.62%
$f_m = 65Hz, P = 5$	42.94%	18.64%

voltage (v_{Rr}) pertaining to proposed OWIM drive are shown in Fig.3.9a, 3.9b, 3.9c and 3.9d corresponding to f_m=35Hz ($P = 9$), f_m=45Hz ($P = 7$), f_m=55Hz ($P = 6$) and f_m=65Hz ($P = 5$), respectively. It is observed that all pole voltages, except Fig.3.9c (f_m=55Hz, $P = 6$), possess half-wave and quarter-wave symmetries (HWS and QWS). However, all phase voltages are found to retain HWS and QWS due to cancellation of the even harmonics, if any. Harmonic spectra, shown in Fig.3.10a-3.10d corresponding to Fig.3.9a-3.9d, respectively, confirm the presence of dominant low-order harmonics in v_{Ro_1} and v_{ro_2}. On the contrary, harmonic spectra of phase voltage v_{Rr} show significant reduction in the magnitude of low-order harmonics. Even harmonics are found to be cancelled in the phase voltage.

Fig.3.11a-3.11d present three-phase line currents (i_R, i_Y, i_B) corresponding to Fig.3.9a-3.9d, respectively, under full-load conditions. Phase currents are found to be balanced which reconfirms that resultant phase voltages retain all the waveform symmetries. Harmonic spectra of i_R are presented in Fig.3.12a-3.12d corresponding to Fig.3.11a-3.11d, respectively. Low-order dominant phase current harmonics are seen to be suppressed significantly. Simulated i_R, i_Y, and i_B pertaining to SCIM drive are shown in Fig.3.14a-3.14d corresponding to f_m=35Hz ($P = 9$), f_m=45Hz ($P = 3$), f_m=55Hz ($P = 3$) and f_m=65Hz ($P = 3$), respectively, at full-load. Peak-peak current ripple is found to be significantly high compared to proposed OWIM based drive. Fig.3.15a-3.15d present the harmonic spectra of i_R corresponding to Fig.3.14a-3.14d, respectively. Dominant low order harmonics are observed in the harmonic spectra corresponding to SCIM drive. The total harmonic distortion in line current (I_{THD}), for SCIM and OWIM drives is mentioned in Table 3.5. OWIM

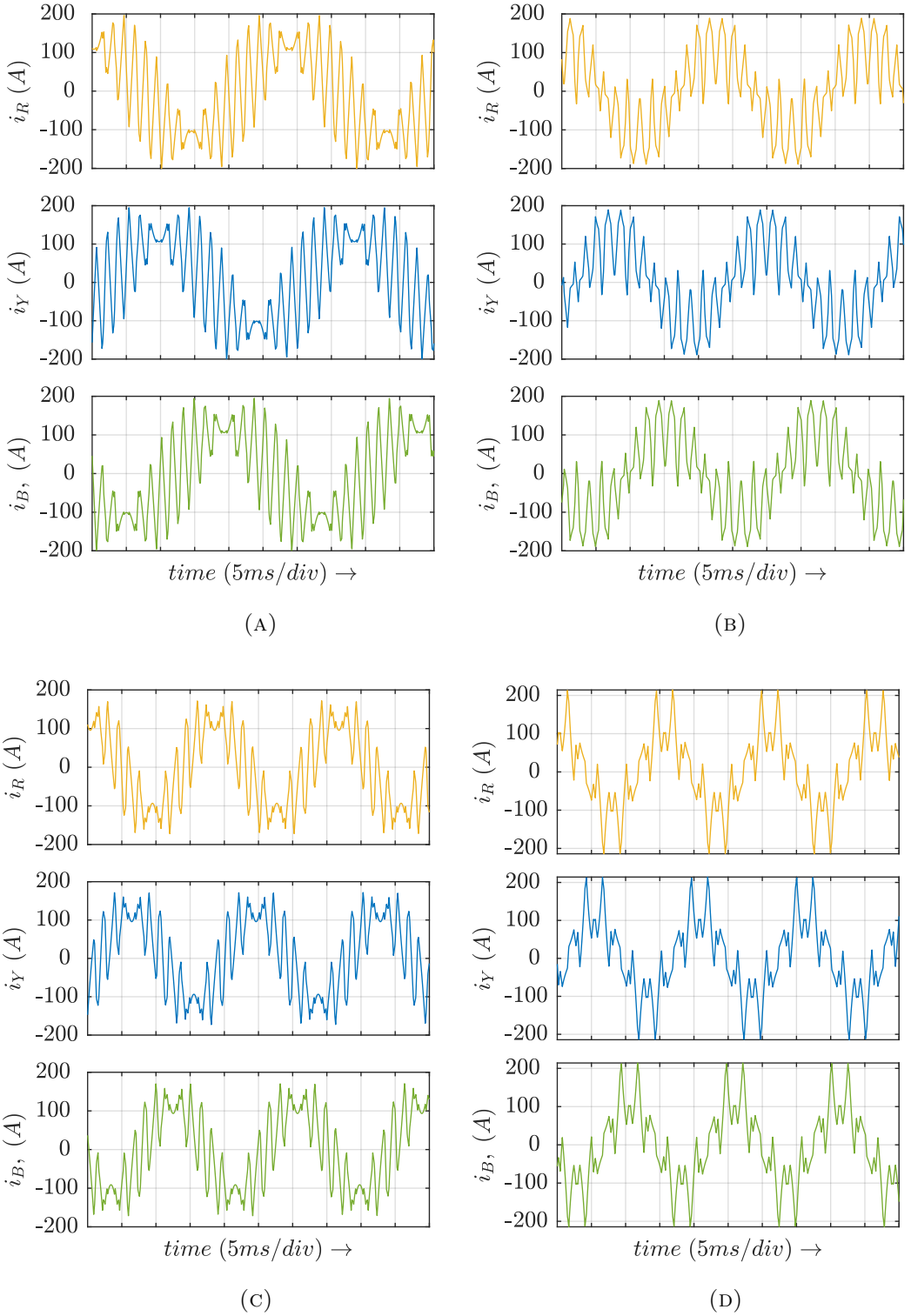


FIGURE 3.11: Three-phase current (i_R, i_Y, i_B) pertaining to proposed OWIM based modified drive under no-load corresponding to (a) Fig. 3.9a (b) Fig. 3.9b (c) Fig. 3.9c and (d) Fig. 3.9d

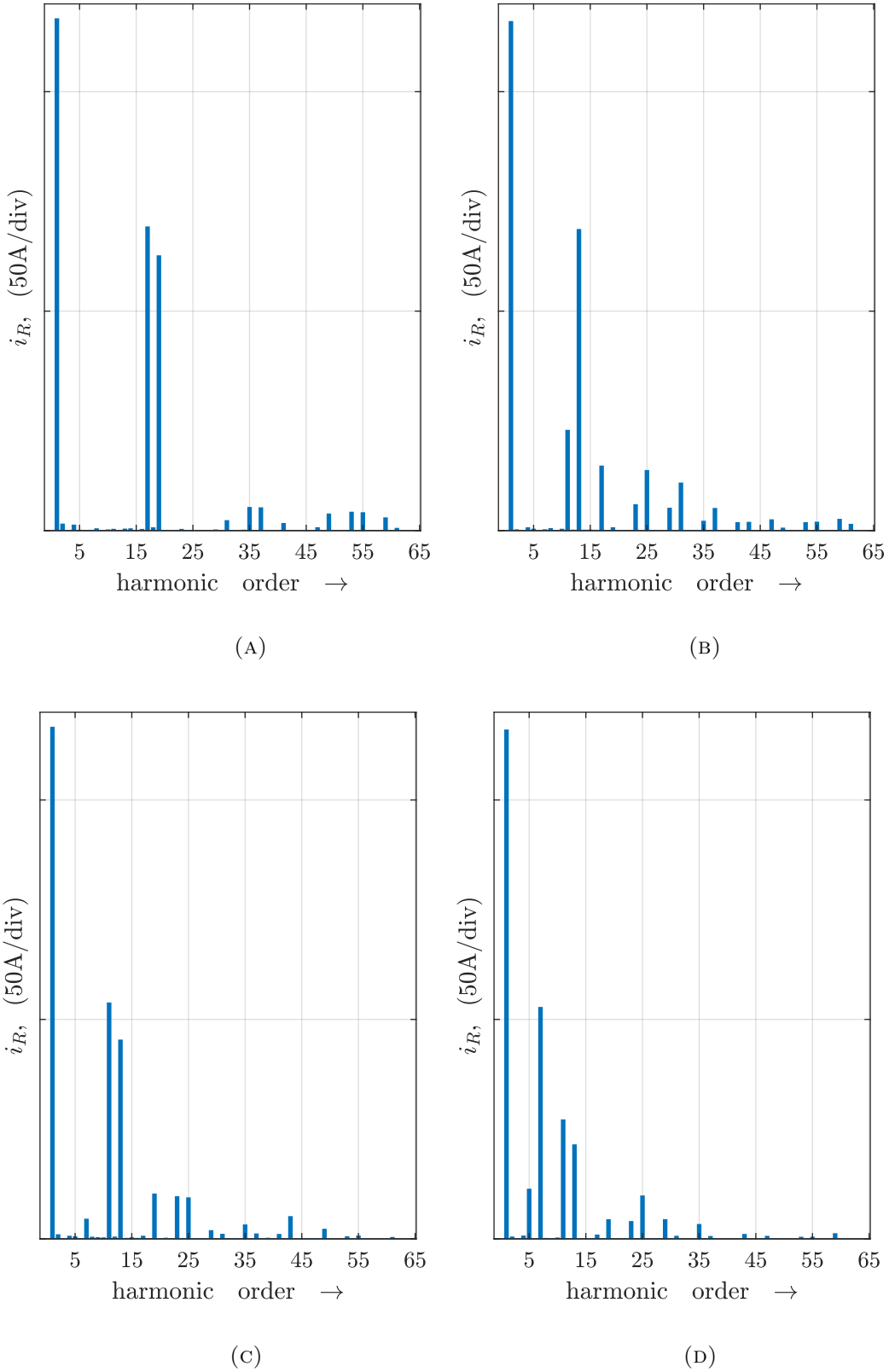


FIGURE 3.12: Harmonic-spectrum of i_R corresponding to (a) Fig. 3.11a (b) Fig. 3.11b (c) Fig. 3.11c and (d) Fig. 3.11d

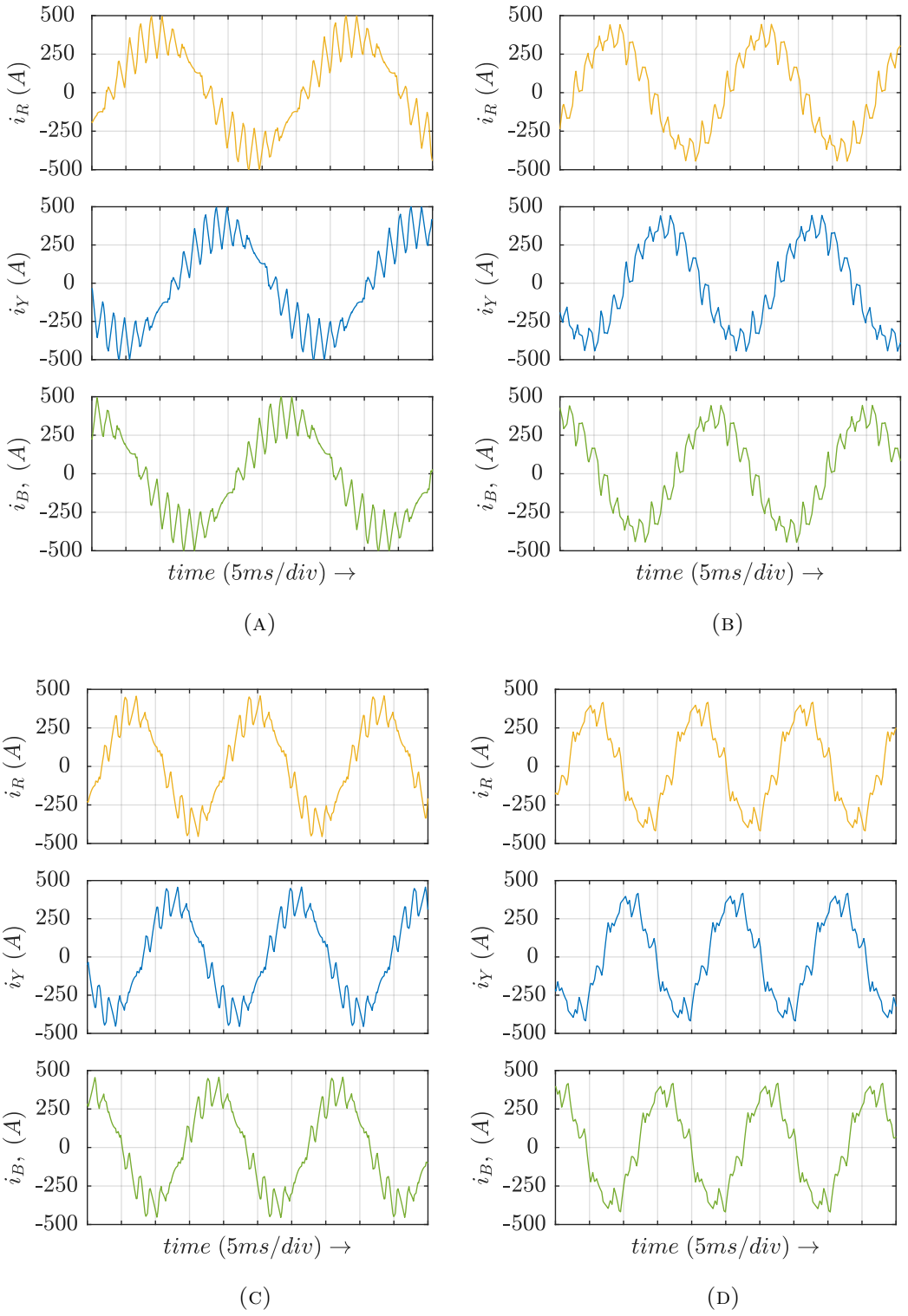


FIGURE 3.13: Three-phase current (i_R, i_Y, i_B) pertaining to proposed OWIM based modified drive under full-load corresponding to (a) Fig. 3.9a (b) Fig. 3.9b (c) Fig. 3.9c and (d) Fig. 3.9d

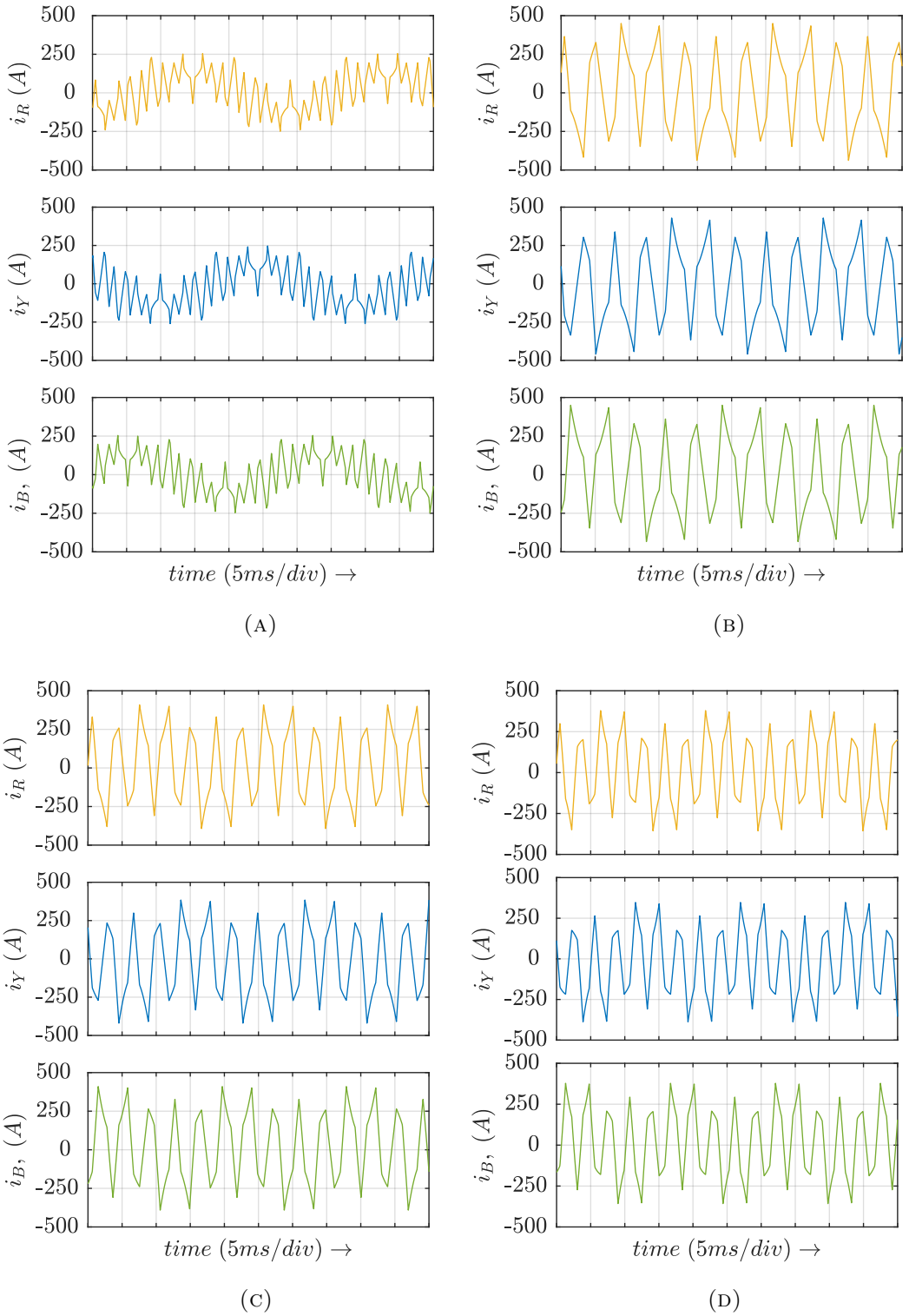


FIGURE 3.14: Three-phase currents (i_R, i_Y, i_B) pertaining to standard SCIM drive at (a) f_m=35Hz (P=9) (b) f_m=45Hz (P=3) (c) f_m=55Hz (P=3) and (d) f_m=65Hz (P=3) under no-load

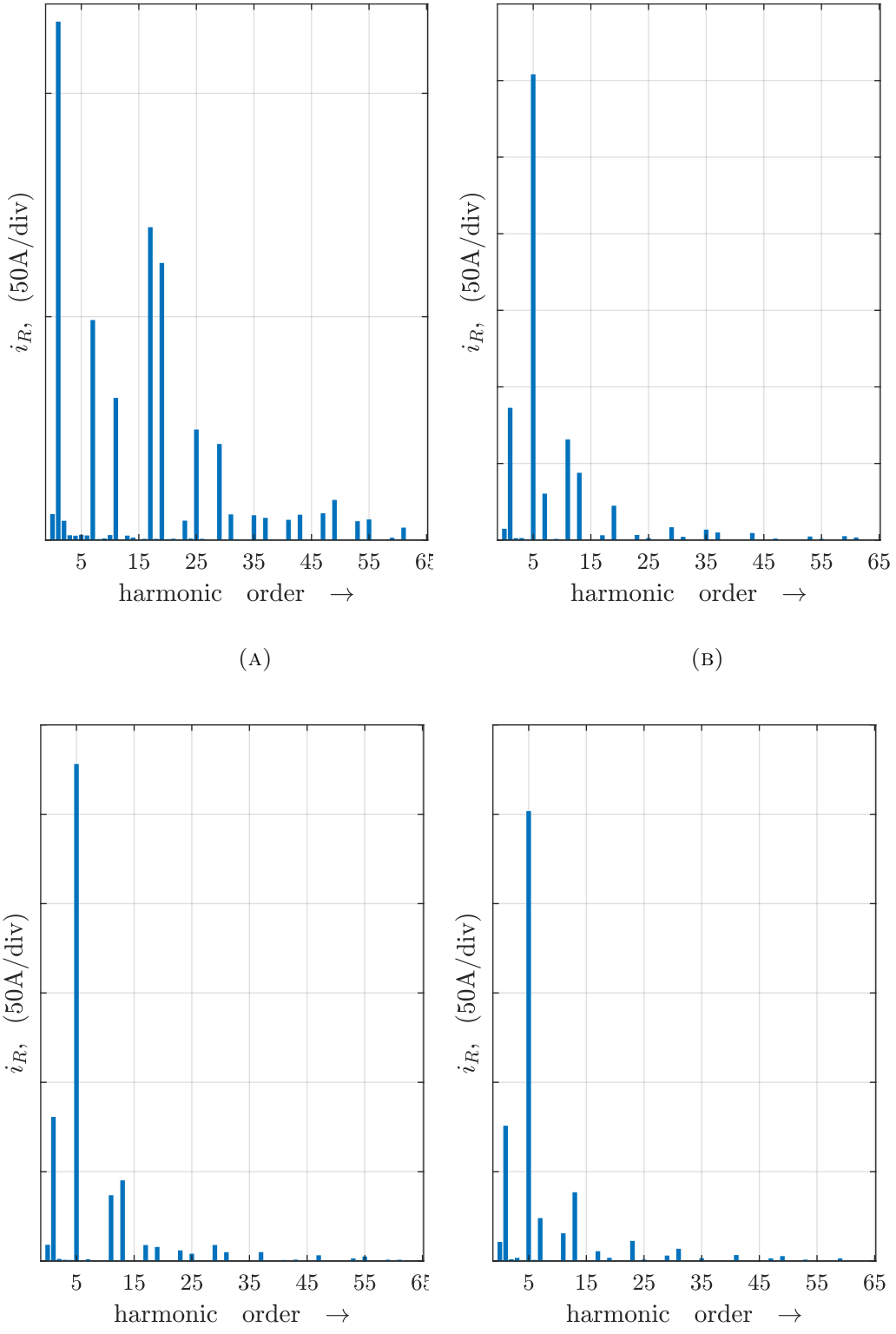


FIGURE 3.15: Harmonic-spectrum of i_R corresponding to (a) Fig. 3.14a (b) Fig. 3.14b (c) Fig. 3.14c and (d) Fig. 3.14d

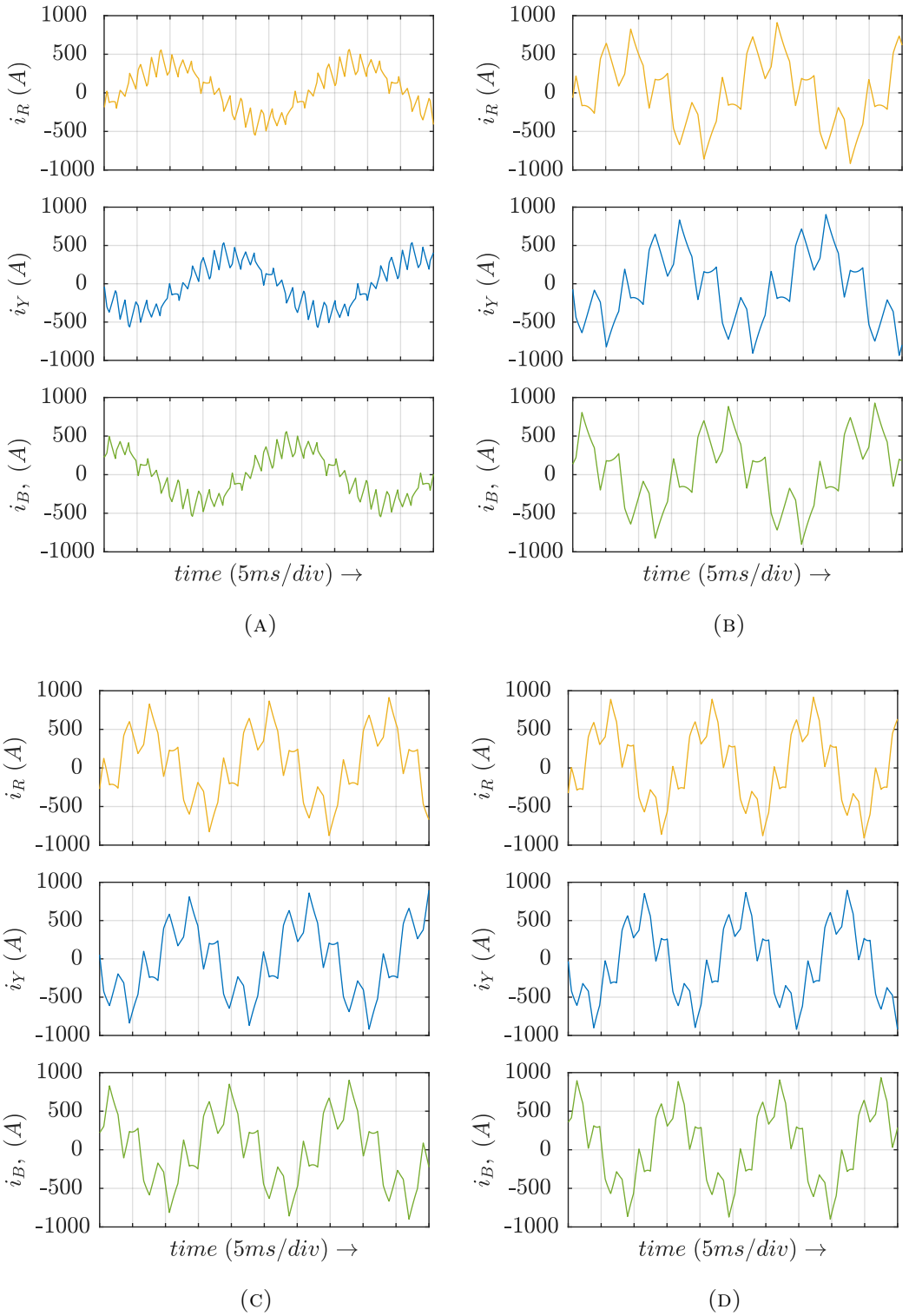


FIGURE 3.16: Three-phase current (i_R, i_Y, i_B) pertaining to proposed SCIM based modified drive under full-load corresponding to (a) Fig. 3.9a (b) Fig. 3.9b (c) Fig. 3.9c and (d) Fig. 3.9d

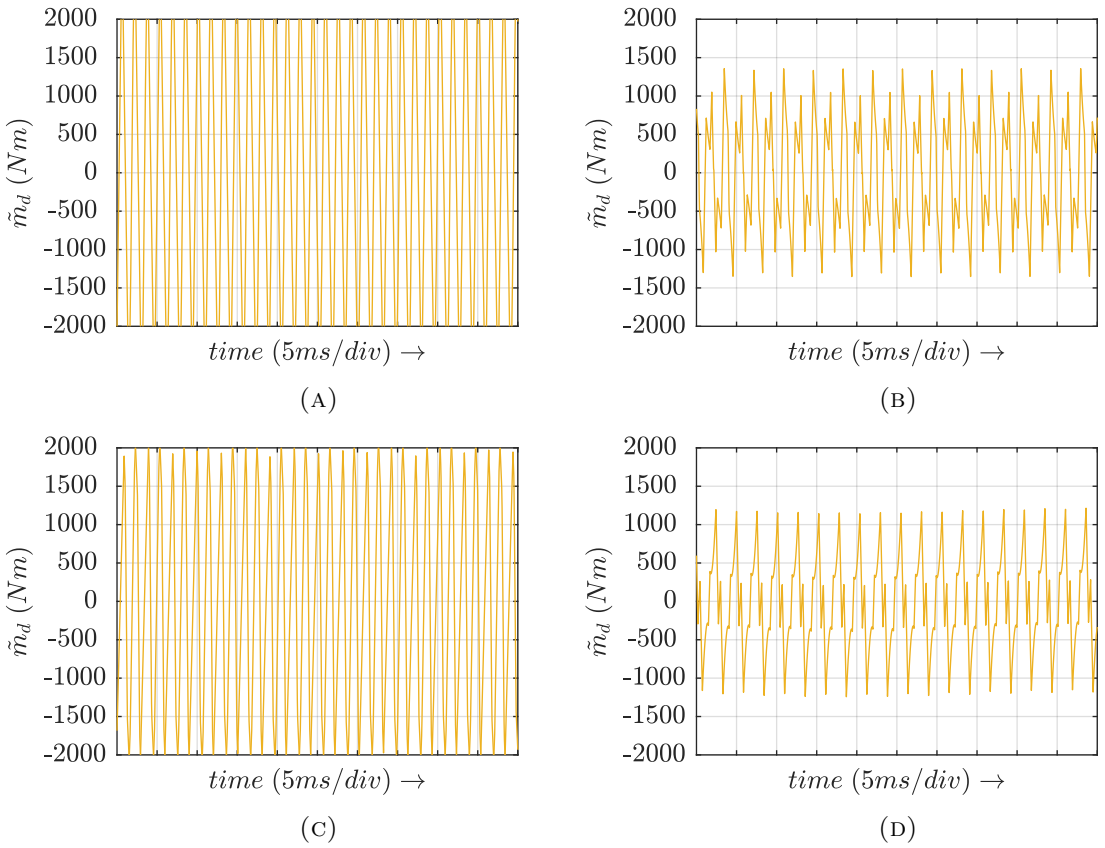


FIGURE 3.17: Simulated torque ripple waveform corresponding to (a) Fig. 3.3a (b) Fig. 3.3b (c) Fig. 3.3c and (d) Fig. 3.3d

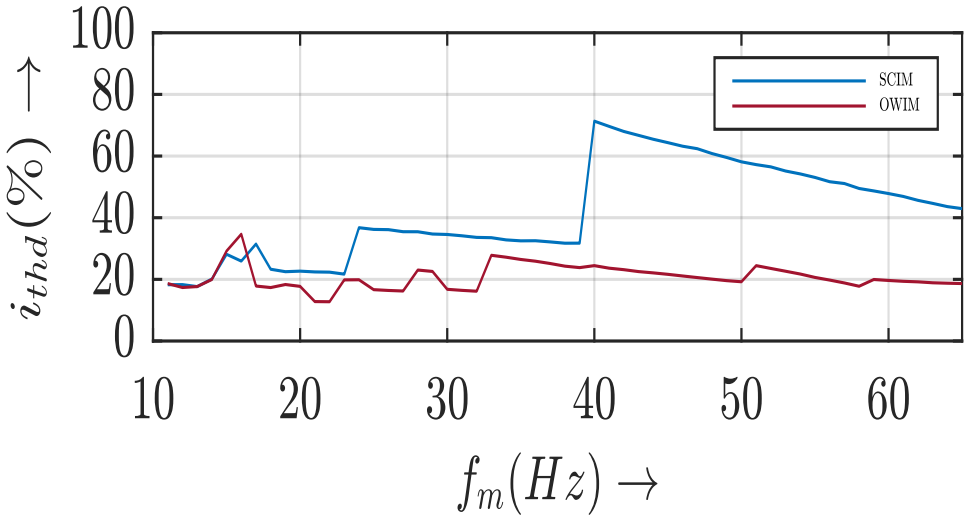


FIGURE 3.18: Comparison of I_{THD} under full-load pertaining to 850kW standard SCIM and proposed OWIM drive

is found to have lower I_{THD} compared to SCIM drive at the tabulated operating conditions. Simulated torque ripple waveform pertaining to OWIM based traction drive is shown in Fig.3.17a-3.17d. It is observed that peak-to-peak torque ripple is confined within 3kNm.

A comparison of I_{THD} over complete range of f_m is presented in Fig.3.18 for both the drives. A significant jump in I_{THD} can be observed at $f_m = 39Hz$ for SCIM drive due to change in pulse number from 9 to 3. Similar observation is made at $f_m = 23Hz$ due to the change in pulse number from 15 to 9. However, such jumps, in I_{THD}, are not observed for the proposed OWIM based drive. SCIM is found to have I_{THD} as high as 70% under full-load conditions whereas proposed OWIM restricts I_{THD} within 25%. Both the drives are further compared in terms of total inverter losses on PLECS software consisting of trial license. A 4.5kV Infineon IGBT ($FZ1200R45KL3$) and 3.3kV Infineon IGBT ($FZ1400R33HE4$) are used for simulation of the SCIM and OWIM based traction drive, respectively. Selection of the devices are made on basis of DC bus voltage and line-current requirements. The switching and conduction energy losses in the inverter pertaining to 850kW IM drive are plotted in Fig.3.19 against f_m. It is observed that despite having 12 IGBT modules in modified drive, it outperforms standard drive significantly in terms of converter losses. This is attributed to the reduced DC bus level and line-current harmonics pertaining to the OWIM based traction drive. Thus, OWIM based modified drive outperforms standard SCIM drive significantly in terms of I_{THD} and inverter losses.

3.5.2 Experimental Results

The theoretical and simulation findings are validated experimentally in this section on a scaled-down laboratory prototype. A 415V, 3.7kW, 50Hz IM is operated in Y-connected and open winding configuration to realise standard SCIM and proposed OWIM drives, respectively. The experimental set-up is shown in Appendix 7 (Fig.3). The detailed machine parameters are also presented in Appendix 7 (table 2). DC bus voltage of the VSIs are maintained, through three-phase diode-bridge rectifiers fed

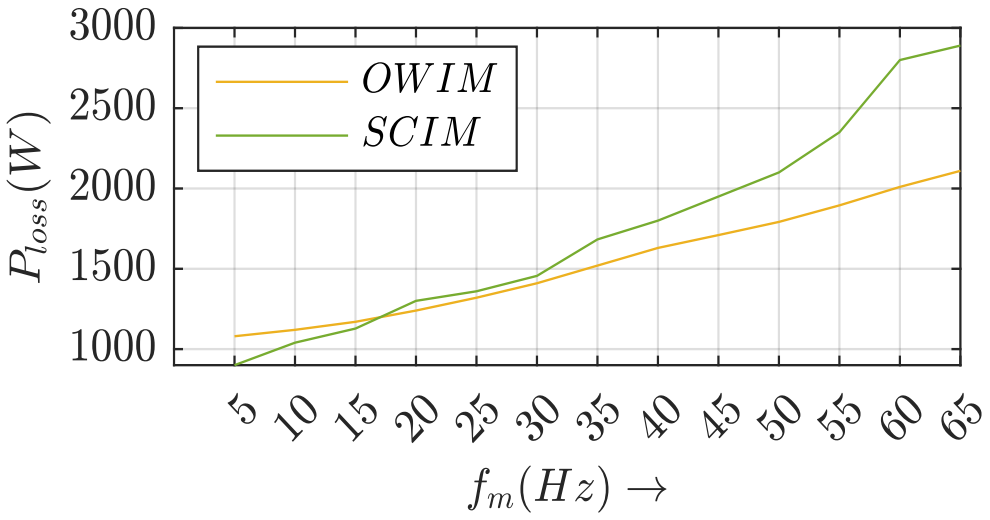


FIGURE 3.19: Comparison of total power converter losses under full-load condition for 850kW traction system

from isolation transformers, at 600V and 300V (for each VSI) for SCIM and OWIM drives, respectively.

Both the drives are operated in open-loop constant V/f mode using TI's TMS320F28379d DSP evaluation module. f_{sw} is followed to be same as that shown in Fig.3.2. Since, IM is rated at 50Hz, M is maintained at 1 for $50Hz \leq f_m \leq 65Hz$.

Experimentally measured v_{Ro_1}, v_{ro_2} and v_{Rr} pertaining to proposed OWIM drive are presented in Fig.3.20a-3.20d corresponding to Fig.3.9a-3.9d, respectively. As stated earlier, v_{Rr} seems to possess all waveform symmetries. Fig.3.21a-3.21d present the harmonic spectra of v_{Ro_1}, v_{ro_2} and v_{Rr} corresponding to Fig.3.20a-3.20d, respectively. Low order dominant harmonics present in v_{Ro_1} and v_{ro_2} are found to be suppressed effectively in v_{Rr}. Fig.3.21c confirms that even harmonics pertaining to $P = 6$ are also cancelled in the resultant phase voltage. The experimentally measured harmonic spectra in Fig.3.21a-3.21d simulated and analytical findings presented in the previous sections.

Measured i_R, i_Y and i_B, under no-load conditions, are captured in Fig.3.22a-3.22d corresponding to Fig.3.20a-3.20d, respectively, pertaining to proposed OWIM

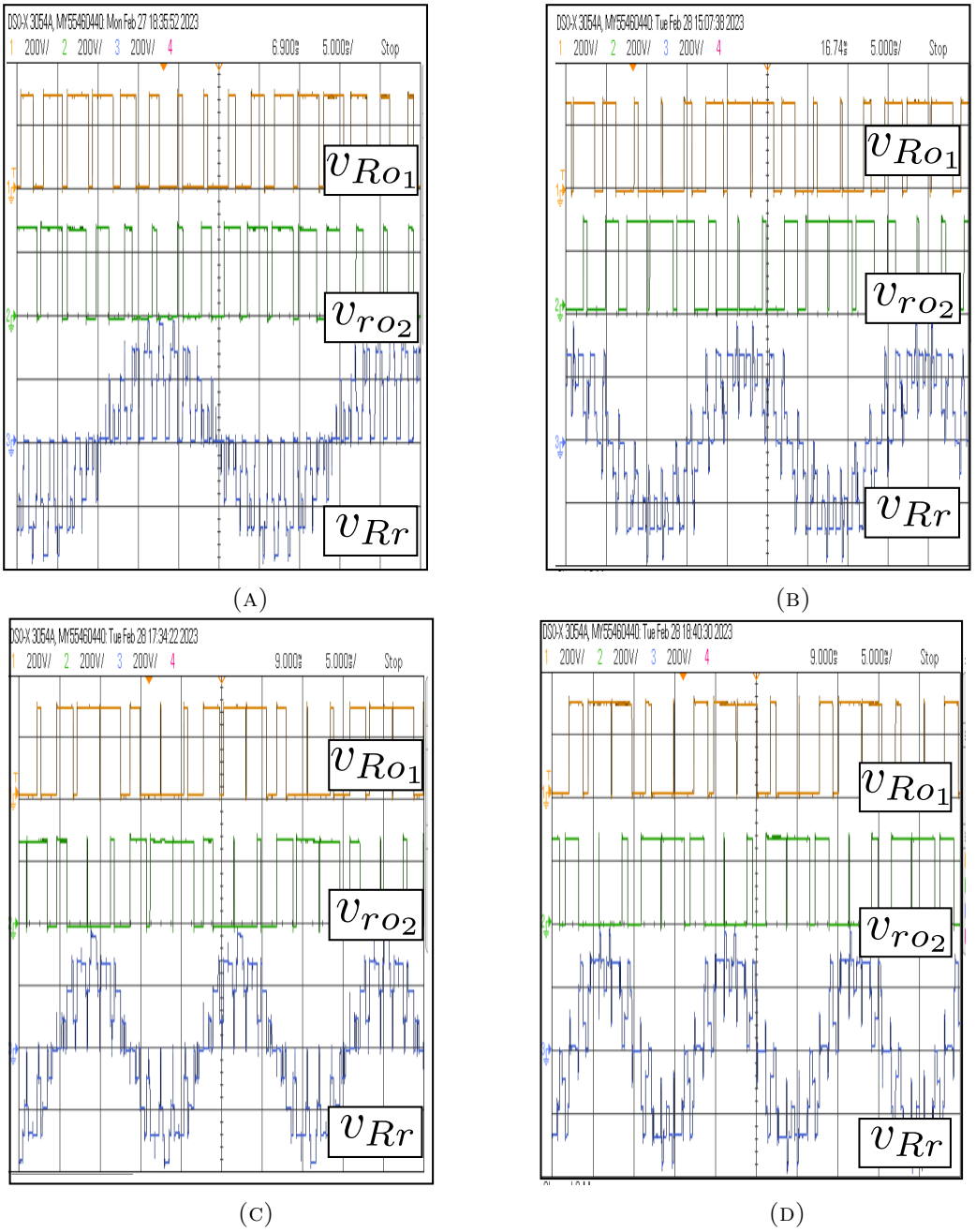


FIGURE 3.20: Experimentally measured pole voltages of individual inverters (v_{Ro_1}, v_{ro_2}) and resultant phase voltage (v_{Rr}) corresponding to (a) Fig. 3.3a (b) Fig. 3.3b (c) Fig. 3.3c and (d) Fig. 3.3d [Scale: 200V/div, 5ms/div]

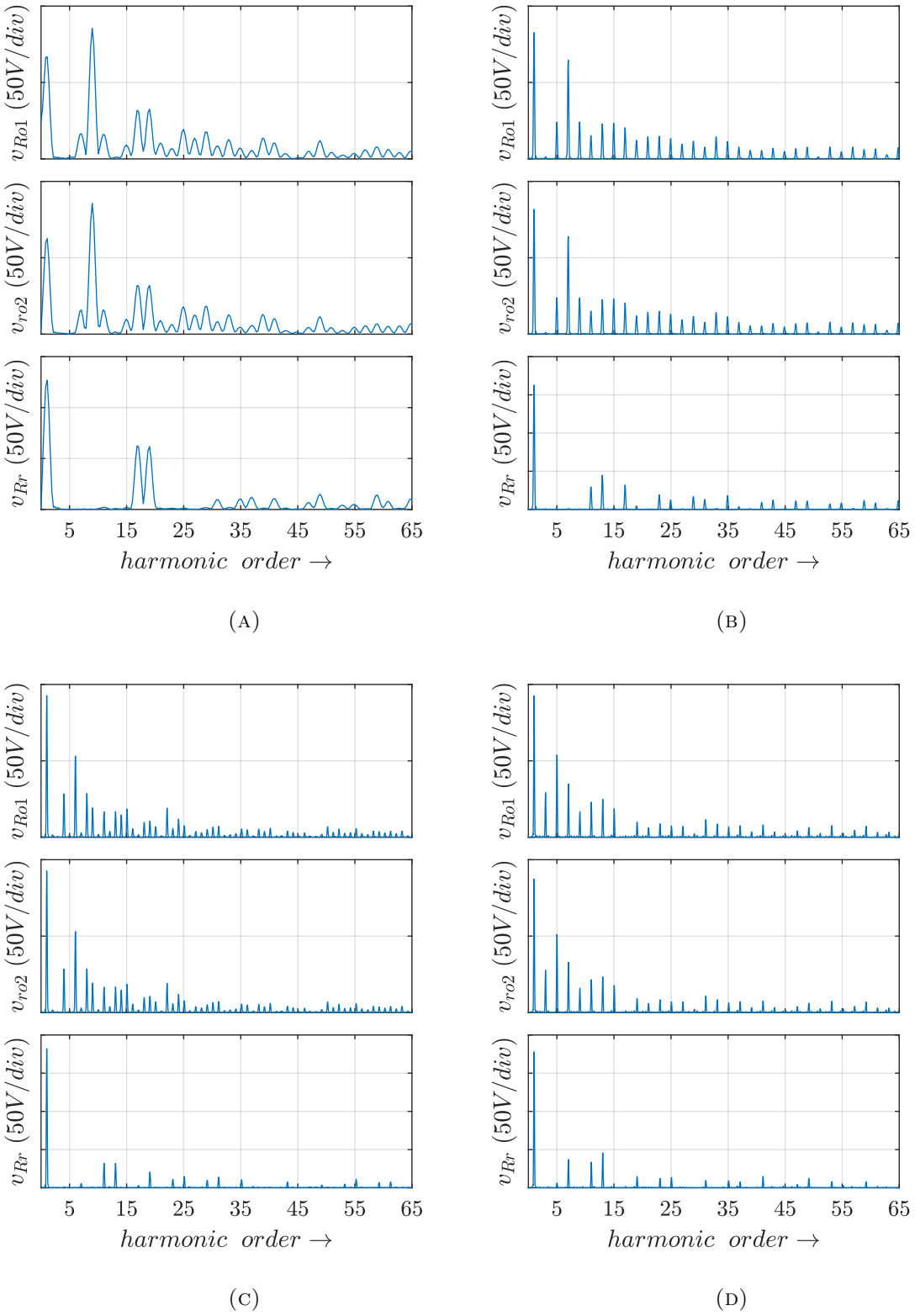


FIGURE 3.21: Experimentally obtained harmonic spectra of voltages (v_{Ro_1}, v_{ro_2}, v_{Rr}) corresponding to (a) Fig. 3.20a (b) Fig. 3.20b (c) Fig. 3.20c and (d) Fig. 3.20d

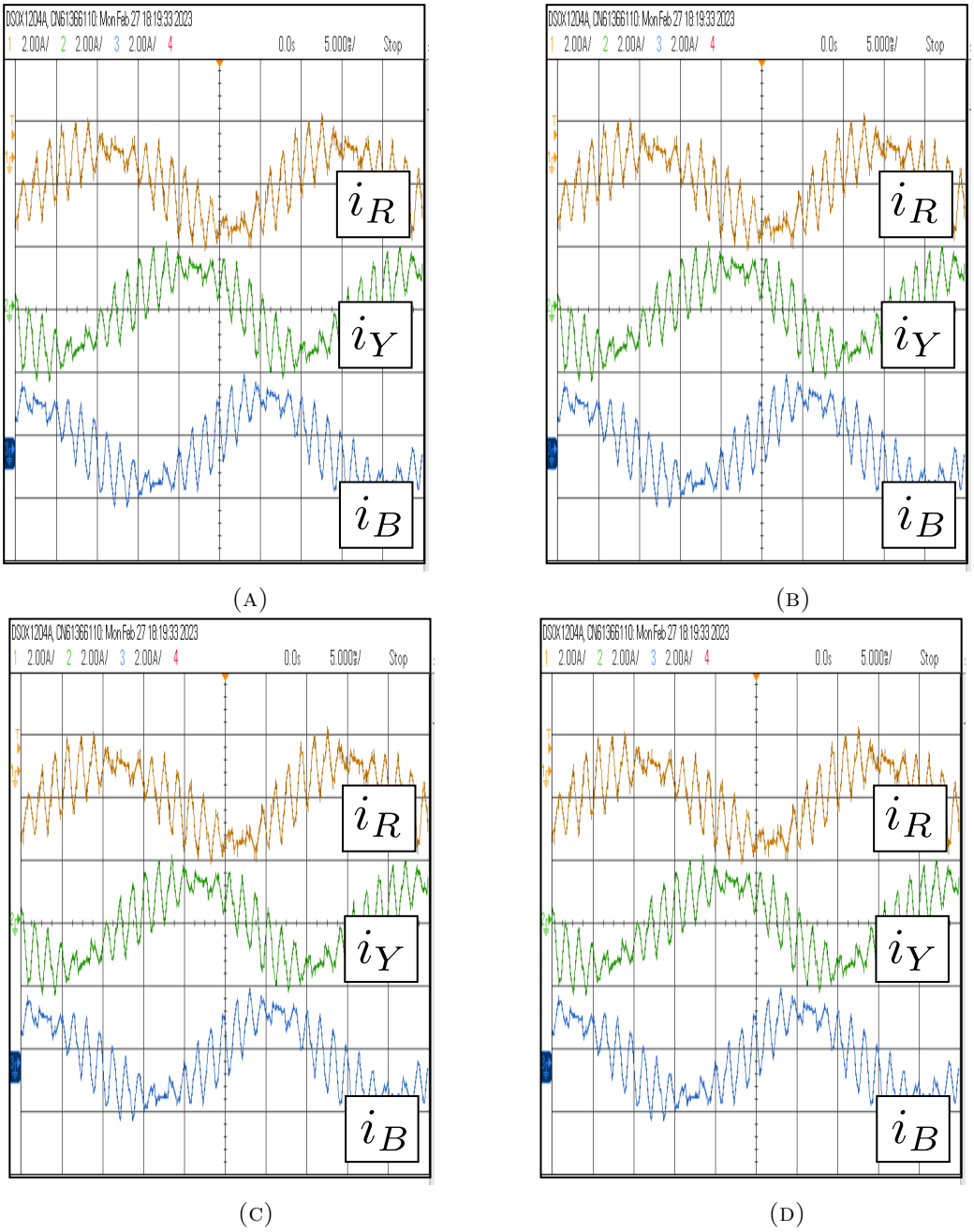


FIGURE 3.22: Measured three-phase currents (i_R, i_Y, i_B) under no-load corresponding to (a) Fig. 3.20a (b) Fig. 3.20b (c) Fig. 3.20c and (d) Fig. 3.20d [Scale: 2A/div, 5ms/div]

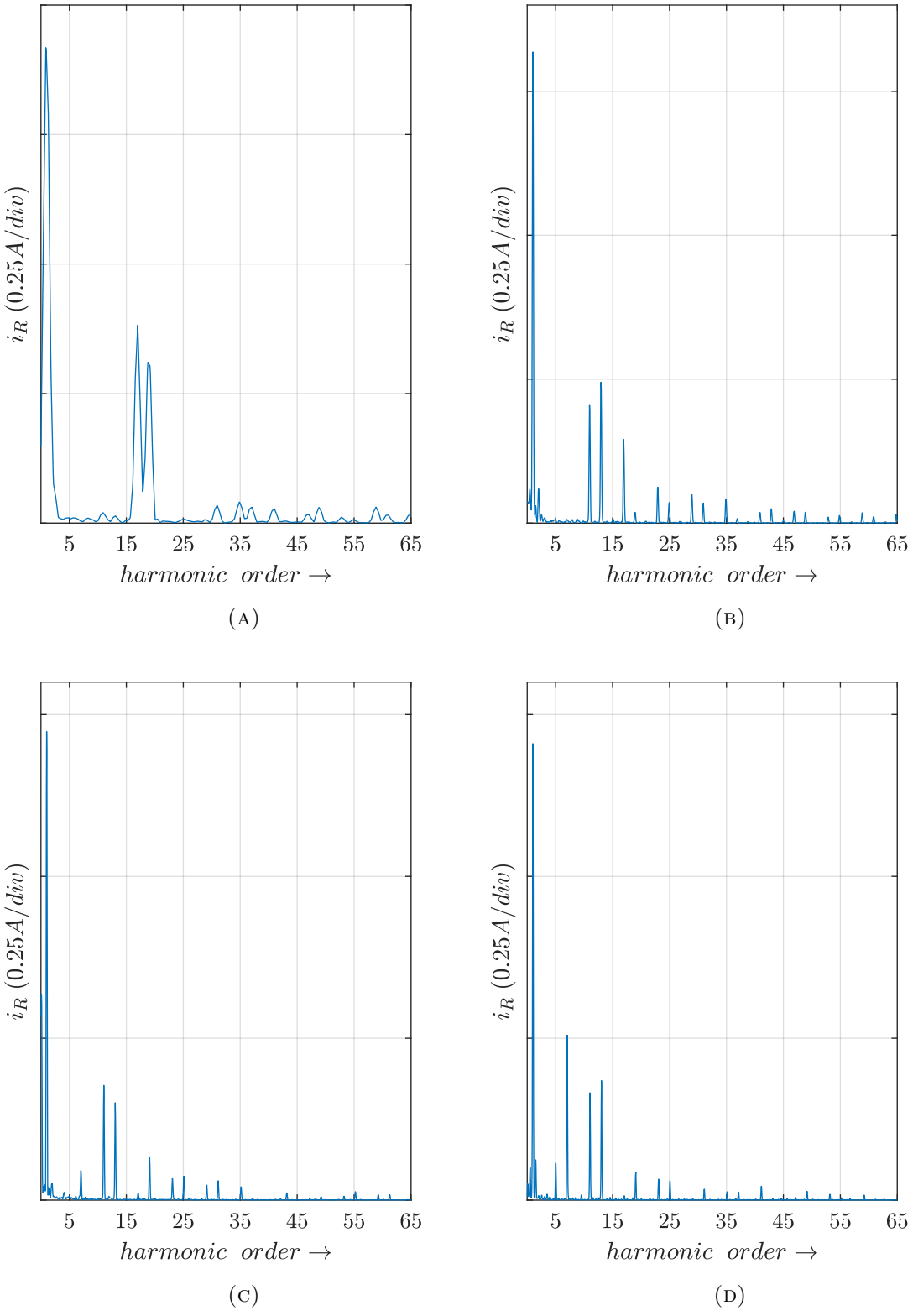


FIGURE 3.23: Measured harmonic-spectrum of i_R corresponding to (a) Fig. 3.22a (b) Fig. 3.22b (c) Fig. 3.22c and (d) Fig. 3.22d

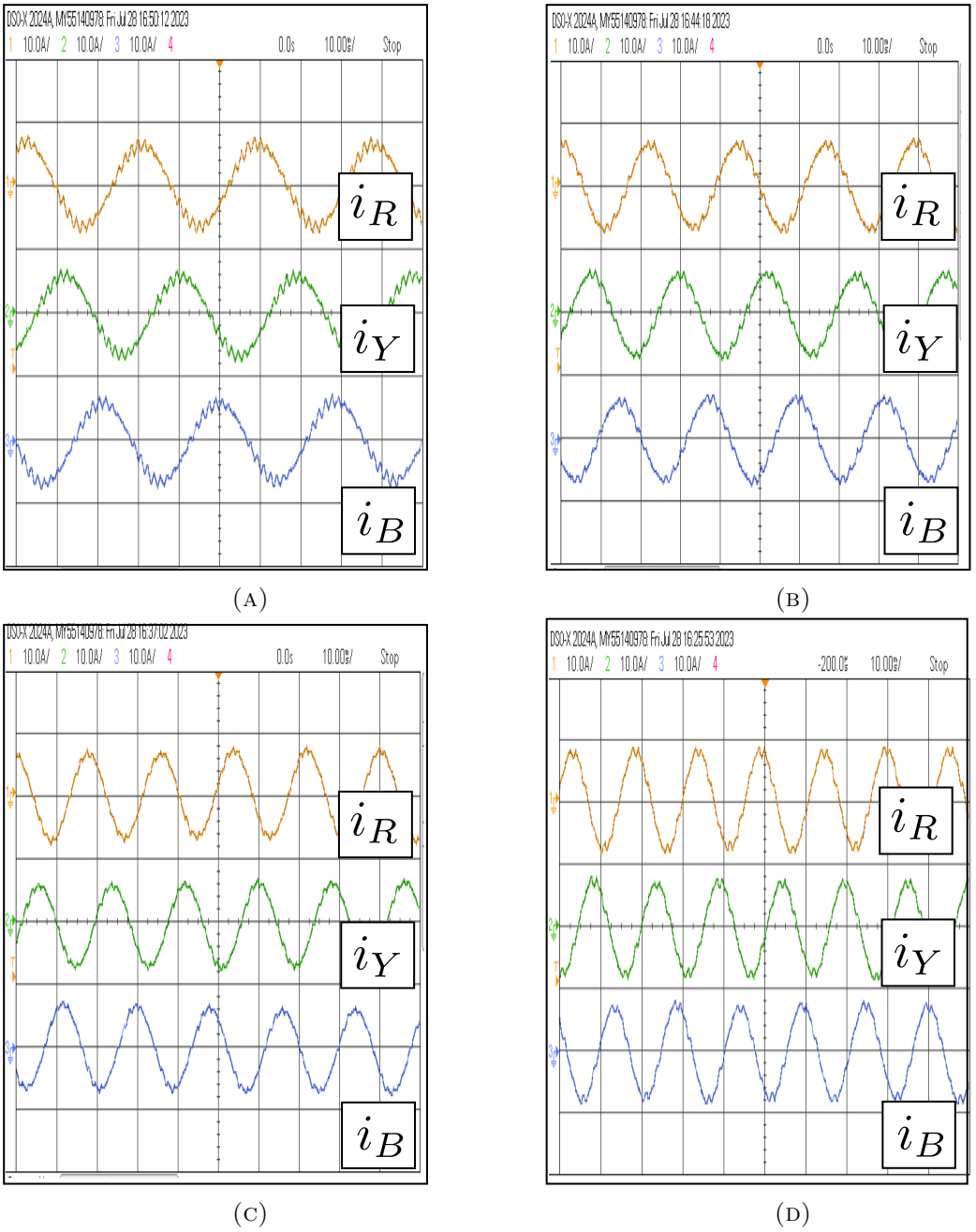


FIGURE 3.24: Measured three-phase currents (i_R, i_Y, i_B) under full load corresponding to (a) Fig. 3.20a (b) Fig. 3.20b (c) Fig. 3.20c and (d) Fig. 3.20d [Scale: 10A/div, 10ms/div]

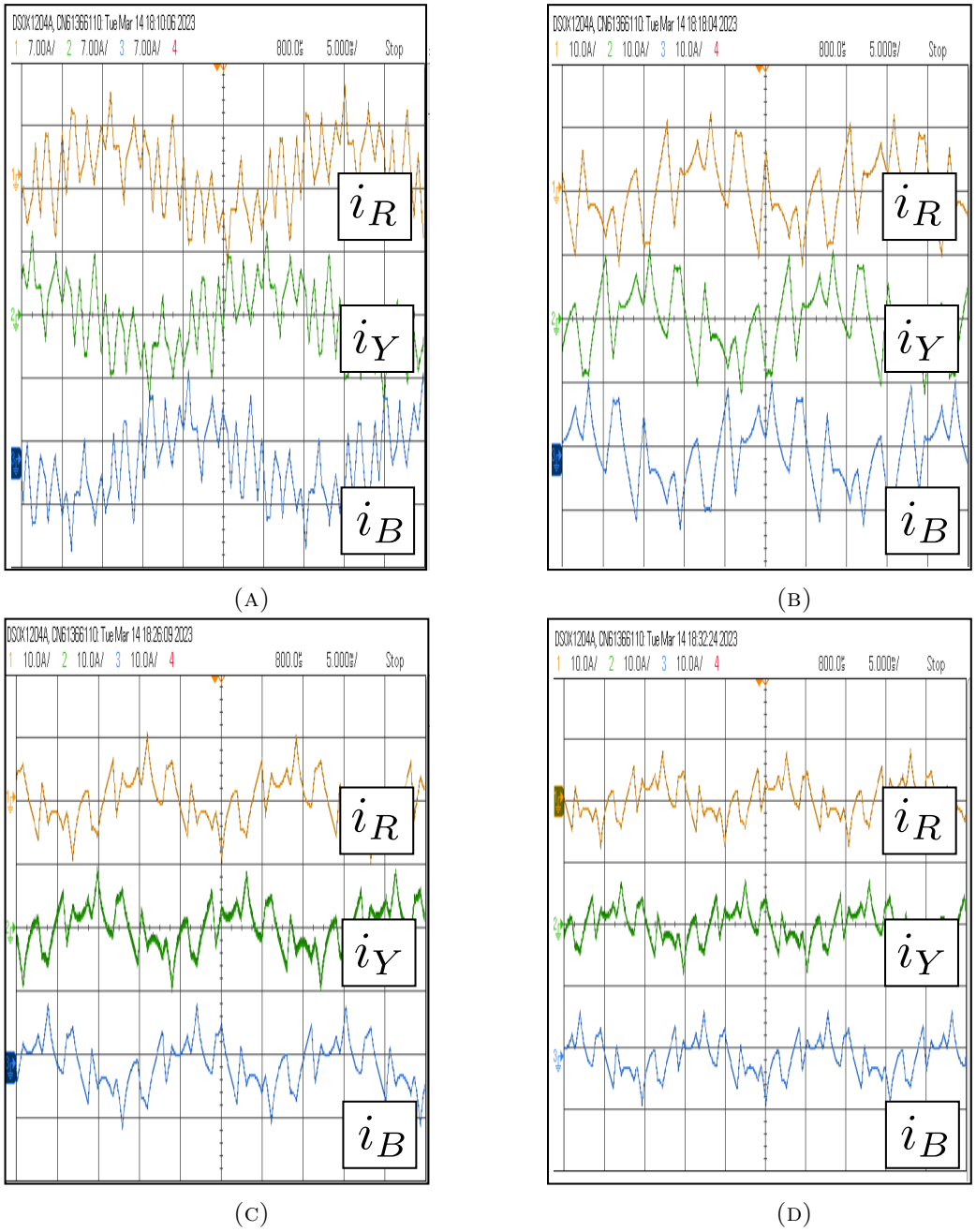


FIGURE 3.25: Measured three-phase currents pertaining to 3.7kW SCIM drive (a) f_m=35Hz (P=9) [Scale: 7A/div, 5ms/div] (b) f_m=45Hz (P=3) (c) f_m=55Hz (P=3) and (d) f_m=65Hz (P=3) under no-load [Scale: 10A/div, 5ms/div]

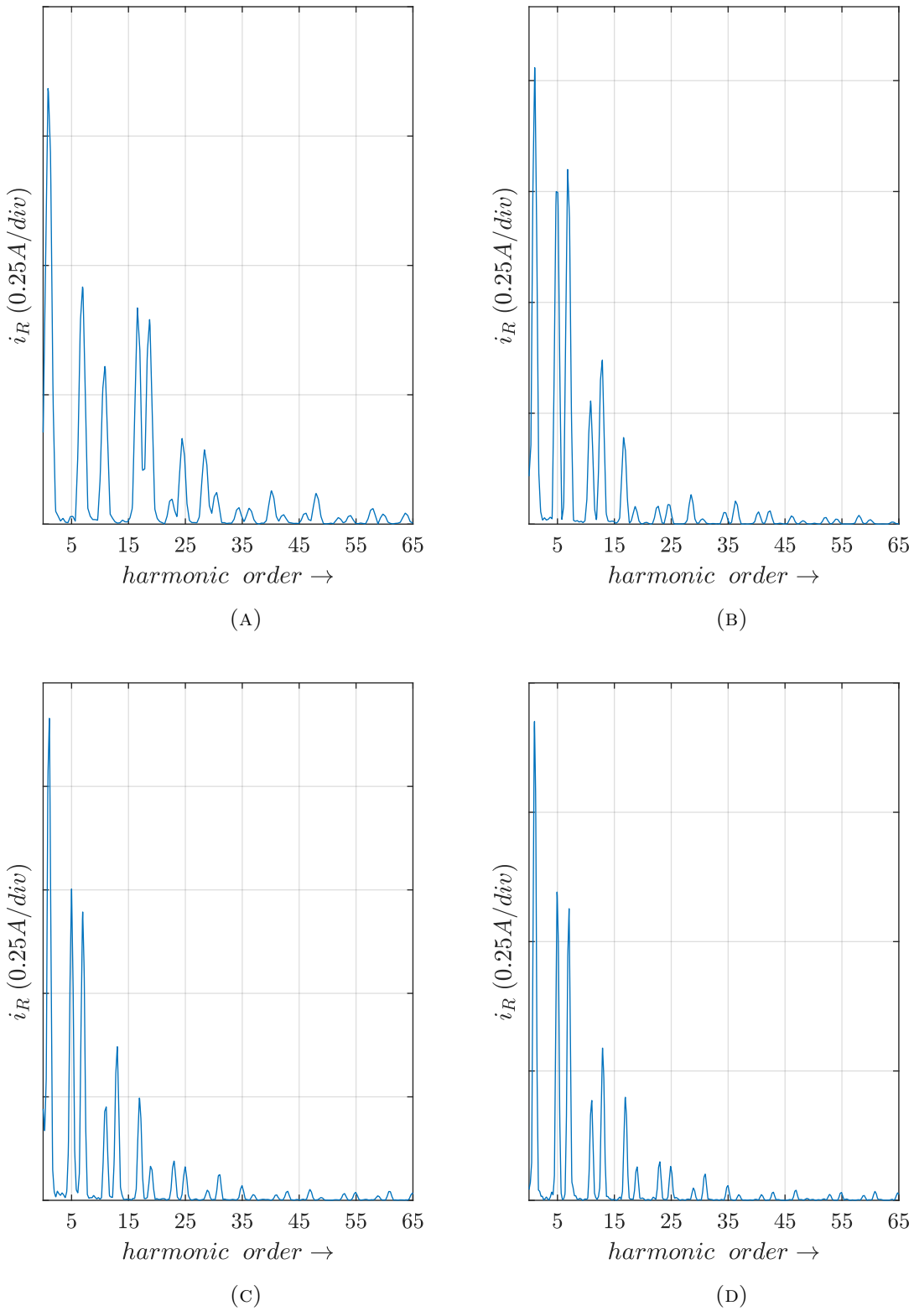


FIGURE 3.26: Measured harmonic-spectrum of i_R corresponding to (a) Fig. 3.25a (b) Fig. 3.25b (c) Fig. 3.25c and (d) Fig. 3.25d

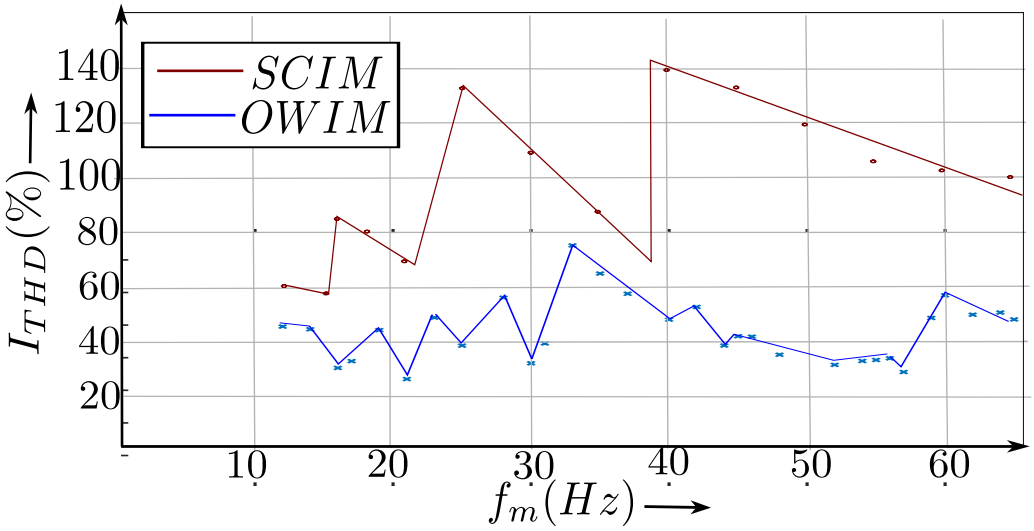


FIGURE 3.27: Comparison of experimentally measured I_{thd} under no-load condition.

drive. These confirm that three-phase line currents are balanced as stated earlier. Measured harmonic spectra of i_R, corresponding to Fig.3.22a-3.22d, are presented in Fig.3.23a-3.23d, respectively. It confirms the findings from simulation that low-order current harmonics are significantly reduced for all pulse numbers. The phase current under full-load is shown in Fig.3.24. Fig.3.25a-3.25d present measured i_R, i_Y and i_B pertaining to a standard SCIM drive at no-load corresponding to Fig.3.14a. It is found that line current is balanced but peak-peak current ripple is significantly higher compared to proposed OWIM drive. Experimentally measured harmonic spectra of i_R is shown in Fig.3.26a-3.26d corresponding to Fig.3.25a-3.25d, respectively. The presence of significant low-order harmonics is once again confirmed in the line current waveform. SCIM and OWIM based drives are further compared in terms of measured I_{THD} over complete range of f_m in Fig. 3.27 at no-load condition. As seen, SCIM drive results into I_{thd} as high as 140% under no-load condition. However, proposed OWIM drive restricts the same below 75% over complete range of f_m. Thus, proposed OWIM drive outperforms SCIM drive significantly in terms of measured I_{THD}.

3.6 Impact of Orientation of Carrier Signal with respect to the modulating signal on the harmonic performance of the drive

In the PWM scheme proposed in the previous sections, it was always ensured that the zero-crossing of the carrier signal coincides with the zero-crossing of its respective modulating signal. This is generally ensured in a Y-connected SCIM drive in order to maintain quarter-wave symmetry in the inverter pole voltages. However, it will be interesting to investigate is this remains a necessity for OWIM drive.

This section aims to investigate the impact of carrier orientation with respect to the modulating signals of both the inverters on the line-current harmonics. It has been established previously that all waveform symmetries are maintained even when even triplen and odd non-triplen P are incorporated in SST-PWM for OWIM drive. However, only one possible orientation of the carrier signal with respect to the modulating signals was considered. The other possible carrier orientations are listed below.

1. *Positive quadrature-phase Carrier:* Positive peak of the carrier coinciding with the positive zero-crossing of the modulating signal (Fig.3.28a).
2. *Negative quadrature-phase Carrier:* Negative peak of the carrier coinciding with the positive zero-crossing of the modulating signal (Fig.3.28b).
3. *In-phase Carrier:* Positive zero-crossing of the carrier coinciding with the positive zero-crossing of the modulating signal (Fig.3.28c).
4. *Out-of-phase Carrier:* Positive zero-crossing of the carrier coinciding with the negative zero-crossing of the modulating signal (Fig.3.28d).

Keeping in mind that phase-shift due to a positive quadrature-phase carrier, ϕ_R for R-phase modulating signal of inverter 1 is taken to be zero [40], the phase-shift for other carrier orientations for all three-phases is given in table 3.6.

Further, it is to be noted that the contributions to the phase shift due to various

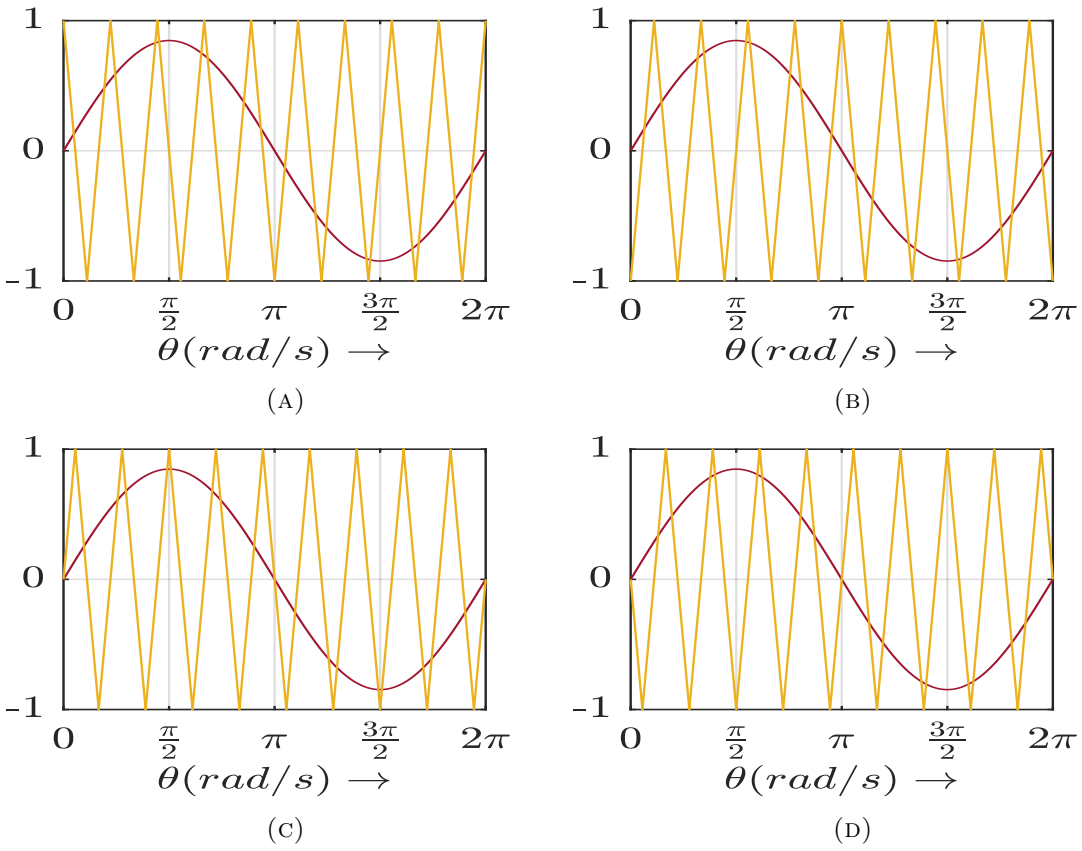


FIGURE 3.28: Various carrier configuration for 2L-VSI fed SCIM (a)Positive quadrature phase (b)Negative quadrature phase (c)In-phase (d)Out-of-phase

TABLE 3.6: ϕ_R for different carrier configuration

	ϕ_R
Pos. Quad	0
Neg. Quad	π
In-phase	$\frac{\pi}{2}$
Out-of-phase	$\frac{-\pi}{2}$

carrier orientations are same for both the inverter 1 and 2. Hence, the impact of this phase-shift is nullified in the machine phase voltage. Thus all the lower order dominant harmonics identified for in-phase carrier remain dominant for all other carrier orientations as well. Thus, it can be concluded from this analysis, that the orientation of carrier signal with respect to the modulating signals has little impact on the harmonic content of the voltage if same carrier signal is used for both the inverters in DI-OWIM drive. On the contrary, carrier orientation plays an important role for a 2L-VSI fed Y-connected SCIM drive. Thus, DI-OWIM offers an extra benefit on the flexibility on the choice of carrier orientation.

3.6.1 Validation through Simulations and Experiments

The individual inverter pole voltages (v_{Ro1}, v_{ro2}) and machine phase voltage (v_{Rr}) as obtained in simulation is shown in Fig.3.29a-3.29d respectively. The corresponding machine three-phase line currents are shown in Fog.3.30a-3.30d respectively. It is clear from Fig.3.30 that wave-shape of three-phase currents have little difference for all the four carrier-orientation. Thus, it can be argued that the harmonic content in all three of them would be the same. The same is verified through the harmonic spectrum shown in Fig.3.31a-3.31d. The harmonic spectrum for phase current remains exactly the same irrespective of carrier orientation.

Experimentally measured inverter pole voltages and machine phase voltage for same carriers for the two inverters is shown in Fig.3.32a-3.32d. The corresponding machine phase currents under no-load are shown in Fig.3.33a-3.33d. The harmonic spectrum of corresponding current in shown in Fig.3.34a-3.34d. The findings through simulations are corroborated experimentally.

3.7 Conclusion

An open-end winding induction motor (OWIM) based modified traction drive is proposed in this chapter. A multiple carrier based synchronized sine-traingle PWM is proposed to operate OWIM drive at all triplen and odd non-triplen pulse numbers (i.e. 5,6,7,9,11,12...). Performance of proposed drive is compared with standard SCIM drive through simulations on a 850kW, 65Hz traction system, in open-loop

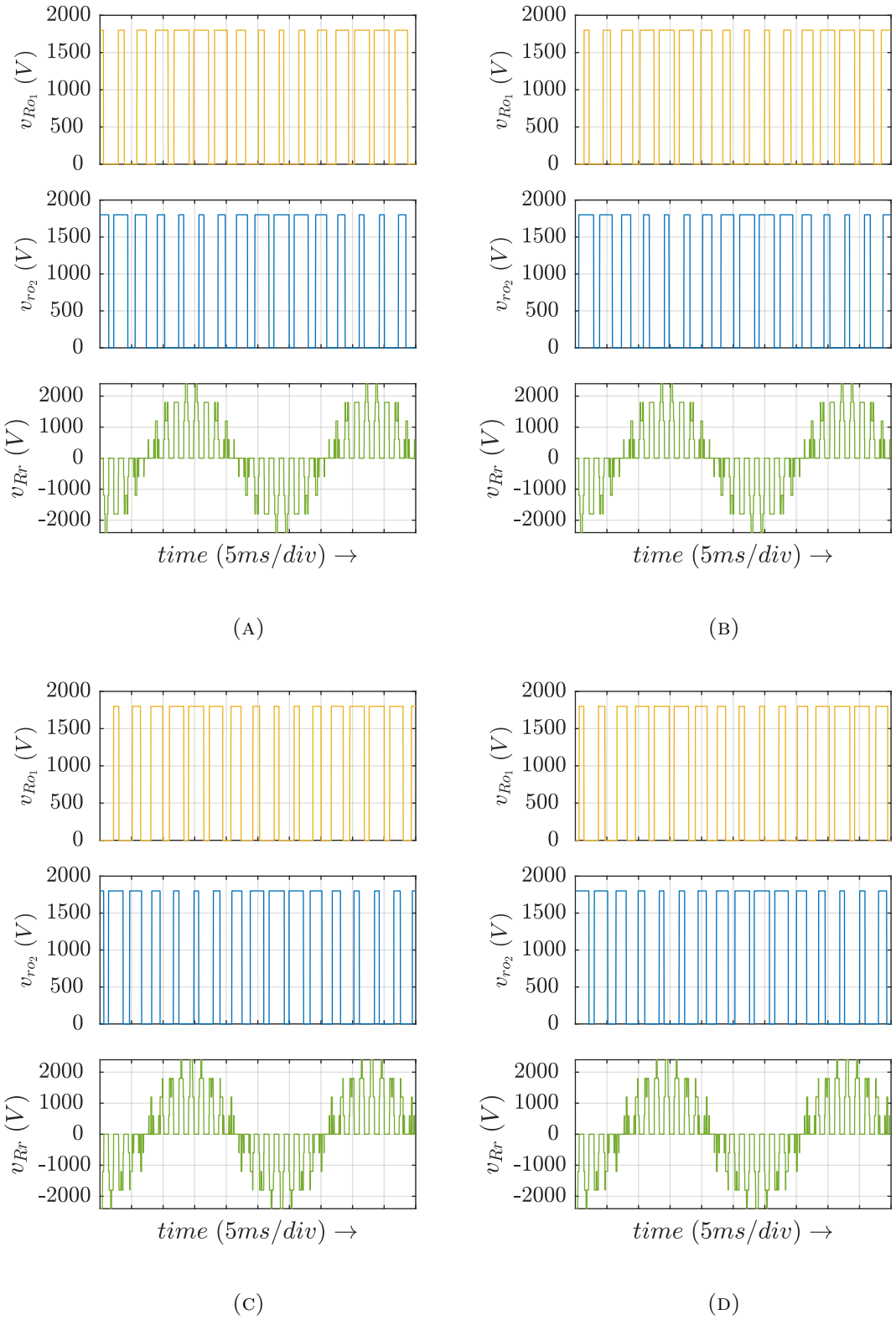


FIGURE 3.29: Individual inverter pole volatges (v_{Ro1}, v_{ro2}) and machine phase voltage (v_{Rr}) at $f_m = 35Hz$ for $P = 9$ for (a)Positive quadrature phase (b)Negative quadrature phase (c)In-phase (d)Out-of-phase carrier signals

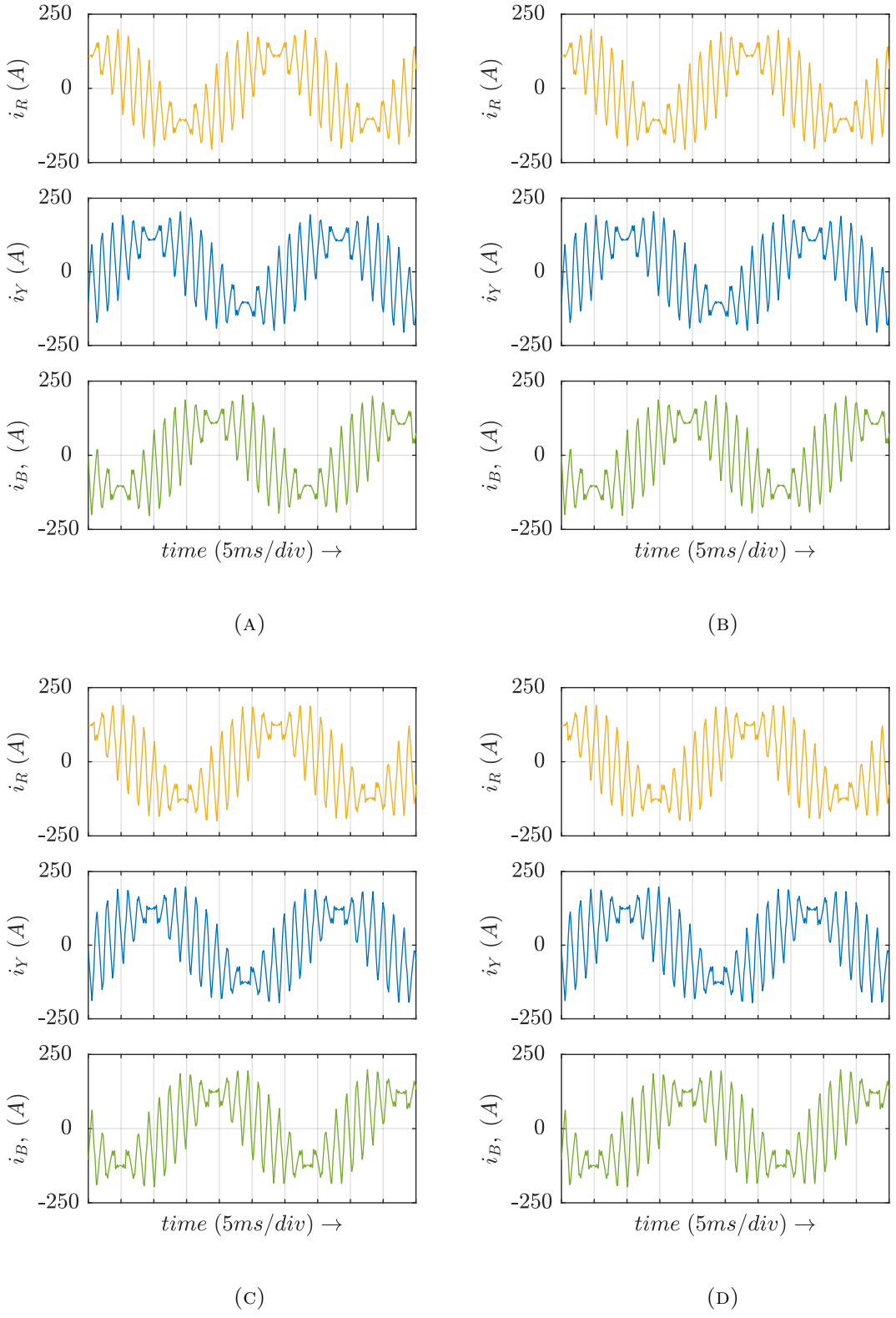


FIGURE 3.30: Three-phase line-currents (i_R, i_Y, i_B) under full-load corresponding to (a) Fig.3.29a (b) Fig.3.29b(c)Fig.3.29c(d)Fig.3.29d

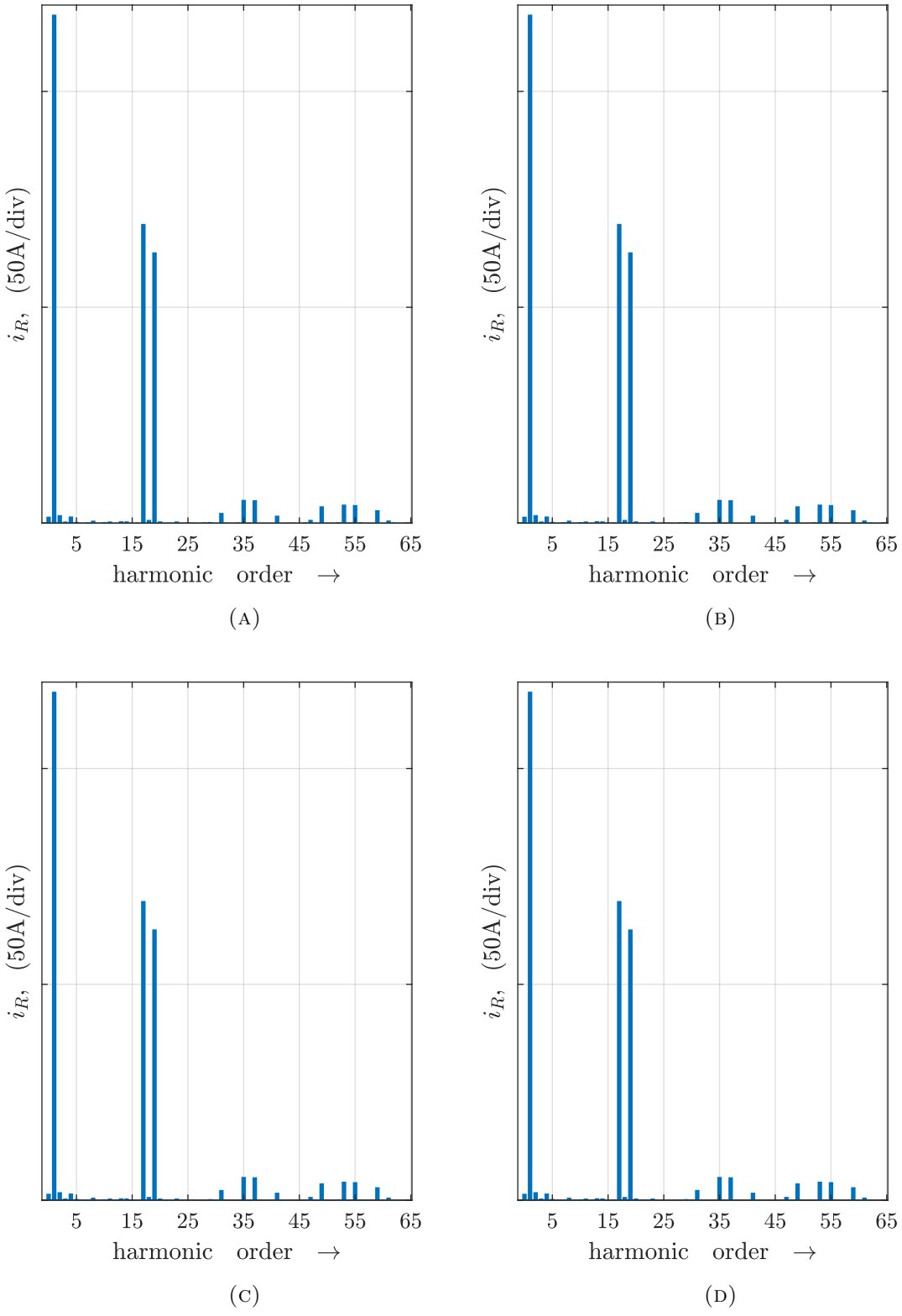


FIGURE 3.31: Harmonic spectrum of line-currents (i_R) corresponding to (a) Fig.3.30a (b) Fig.3.30b(c)Fig.3.30c(d)Fig.3.30d

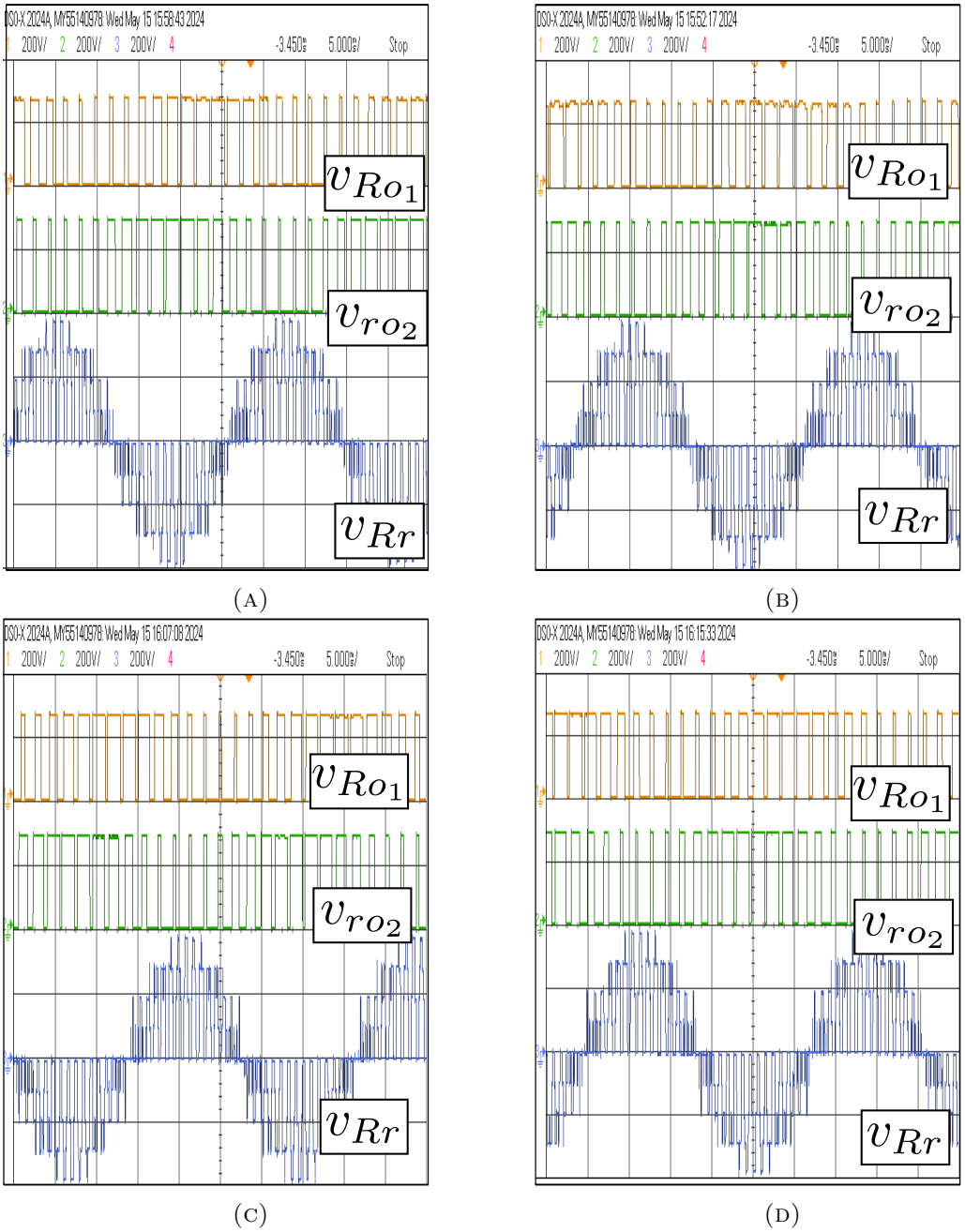
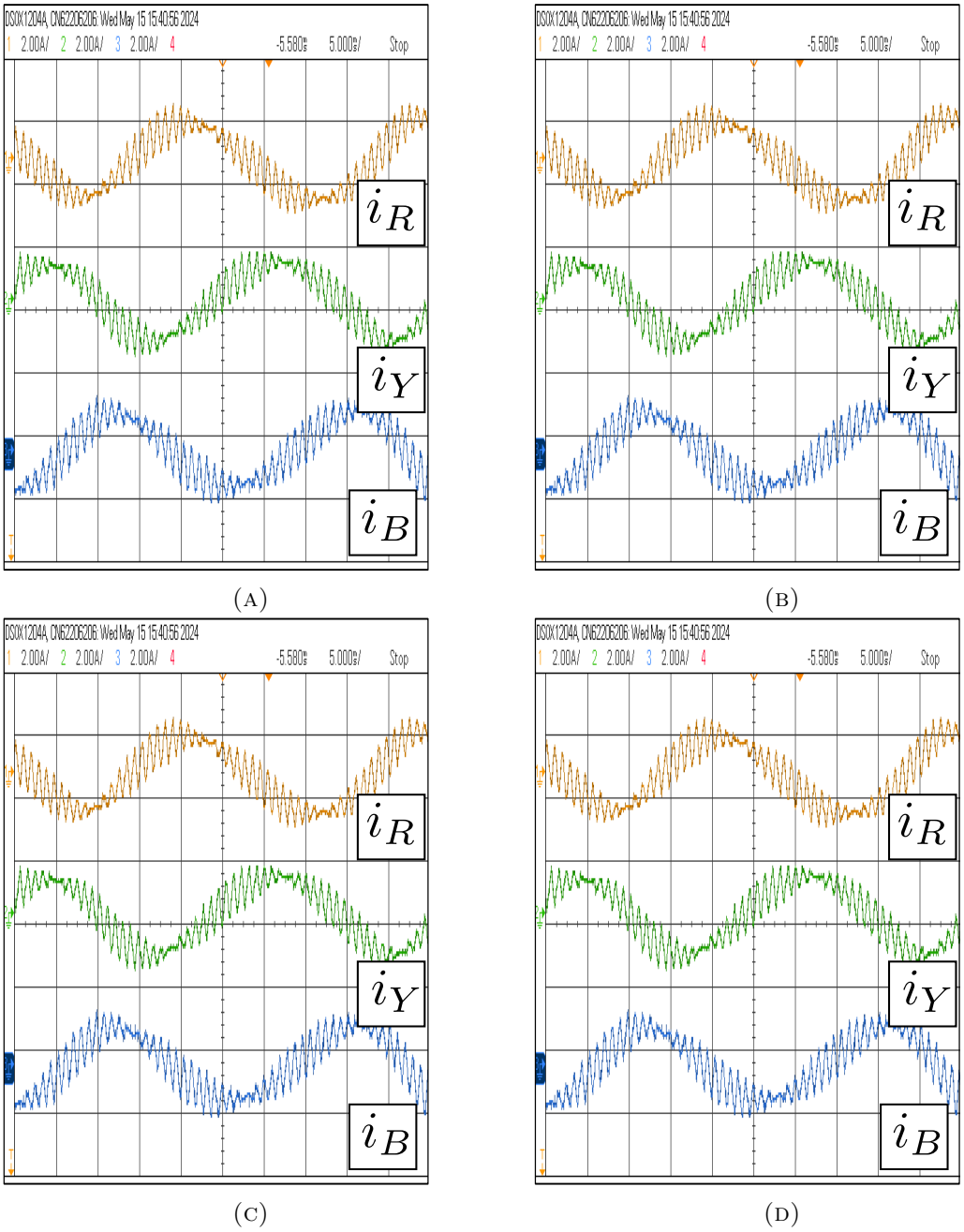


FIGURE 3.32: Experimentally measured Individual inverter pole volatges (v_{Ro1}, v_{ro2}) and machine phase voltage (v_{Rr}) at $f_m = 35Hz$ for $P = 9$ for (a)Positive quadrature phase (b)Negative quadrature phase (c)In-phase (d)Out-of-phase carrier signals [Scale: 200V/div, 5ms/div]



(A) (B)

(C) (D)

FIGURE 3.33: Experimentally measured three-phase current (i_R, i_Y, i_B) corresponding to (a)Fig.3.32a (b)Fig.3.32b (c)Fig.3.32c(d)Fig.3.32d [Scale: 5A/div, 5ms/div]

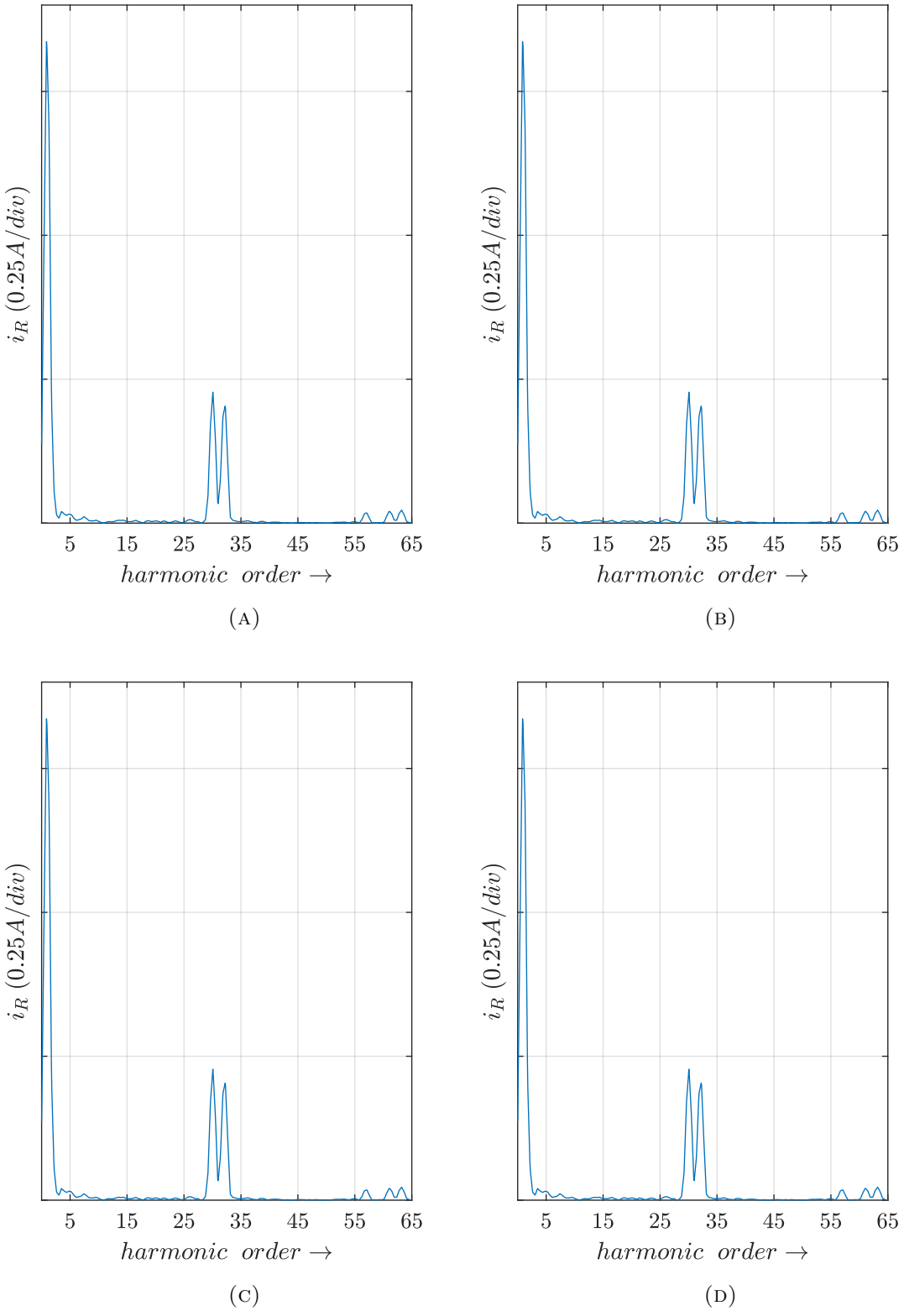


FIGURE 3.34: Experimentally measured spectrum of line-current (i_R) corresponding to (a)Fig.3.33a (b)Fig.3.33b (c)Fig.3.33c (d)Fig.3.33d.

constant V/f mode. Switching frequency (f_{sw}) for both drives is restricted below 350Hz. Despite similar thermal performances, proposed drive outperforms standard traction system significantly in terms of phase-current quality. Further, space vector and fourier-series based analyses are presented to identify the dominant voltage-harmonic components present in the proposed system. It is seen that the proposed drive maintains all the waveform symmetries in the three output phase-voltages at all pulse numbers. Further, the impact of orientation of carrier signal with respect to the modulating signal on the harmonic performance of the OWIM drive has been investigated. Simulations and analytical findings are established through experimental results on a 3.7kW, 50Hz laboratory prototype.

Chapter 4

Dissimilar Carrier based Synchronous PWM Scheme for Open-End Winding Induction Motor

4.1 Introduction

It was established in the last chapter that, OWIM drive offers more flexibilities in the implementation of carrier based SST-PWM as compared to Y-connected SCIM drive due to the presence of two inverters. All the conditions of symmetry can be maintained in the machine phase-voltage even if P takes the value of even triplen integers. Further, multi-carrier based SST PWM has been implemented when P becomes an odd non-triplen integer in case of OWIM. However, identical carrier signals are used for corresponding phases of both the VSIs of OWIM drive in literature.

In the present chapter, a SST-PWM scheme is proposed for OWIM drive which is operated at only all triplen values of P wherein dissimilar carrier signals are utilised for the two VSIs. The pulse number corresponding to each VSI, P_1 and P_2, may not necessarily remain the same. Effective pulse number of the drive is taken to be the average of P_1 and P_2, denoted by $\overline{P}$. The range of modulation index, M, over which $\overline{P}$ is maintained as an odd-triplen number, P_1 and P_2 are kept equal. Thus, P_1 and P_2 become equal to $\overline{P}$. However, a phase-shift is introduced between the two carrier signals in this case. The phase-shit is decided in order to optimize the harmonic performance of the drive. Although both P_1 and P_2 are equal in this case, the dissimilarity in the carrier signal is manifested because of the phase-shift.

Further, for the range of M for which $\overline{P}$ is maintained as an even-triplen number, P_1 and P_2 are kept as consecutive odd triplen integers. For example, in order to implement $\overline{P} = 6$, P_1 is maintained at 9 while P_2 is maintained at 3. Thus, for

the proposed PWM scheme, P_1 and P_2 are maintained only as odd-triplen integers whereas $\overline{P}$ can be both odd and even triplen integers. The mathematical background for both the cases are developed on the basis of double-fourier series (DFS) based analysis.

4.2 Proposed SST-PWM Scheme for OWIM Drive

Carrier frequency (f_c) is shown plotted against the modulating frequency (f_m) in Fig.4.1a for a conventional OWIM based high-power drive. Here, the value of f_c and P corresponding to the two inverters remain the same. The maximum allowable value of f_c is maintained at 400Hz. The drive is initially started with asynchronous PWM, where f_c remains fixed at 210Hz. At $f_m = 10Hz$, the PWM scheme is transitioned from asynchronous to synchronous with $P = 21$. Subsequently, as f_c reaches 400Hz with increase in f_m, P is changed to the next allowable value. P is maintained at $18, 15, 12, 9$ and 6 through the complete range of f_m.

SST-PWM scheme for OWIM drive proposed in this thesis utilises different carrier signals for the two inverters in OWIM drive. Similar to P_1 and P_2, f_c^{inv1} corresponds to the carrier frequency profile of inverter 1 and f_c^{inv2} corresponds to the same for inverter 2. $\overline{f_c}$ denotes the average carrier frequency profile. Mathematically, this can be depicted as

$$\overline{P} = \frac{P_1 + P_2}{2} \qquad \overline{f_c} = \frac{f_c^{inv1} + f_c^{inv2}}{2} \tag{4.1}$$

Variation of f_c^{inv1}, f_c^{inv2} and $\overline{f}_c$ with f_m is shown in Fig.4.1b. Here, the maximum value of $\overline{f}_c$ is maintained at 400Hz. With the proposed scheme, f_c^{inv1} may not necessarily be equal to f_c^{inv2} due to difference in P_1 and P_2. Table 4.1 shows the different values which P_1, P_2 and $\overline{P}$ take over different ranges of f_m. For the different spans of f_m, where both P_1 and P_2 become equal ($\overline{P}$ being odd triplen), the plot corresponding to $\overline{f_c}$, f_c^{inv1} and f_c^{inv2} coincide in Fig.4.1b. For the remaining values of f_m ($\overline{P}$ being even triplen), the plot corresponding to $\overline{f_c}$, f_c^{inv1} and f_c^{inv2} do not coincide in Fig. 4.1b. Fig.4.1b can be correlated to table 4.1.

Double-fourier Series (DFS) based mathematical framework is utilised in this

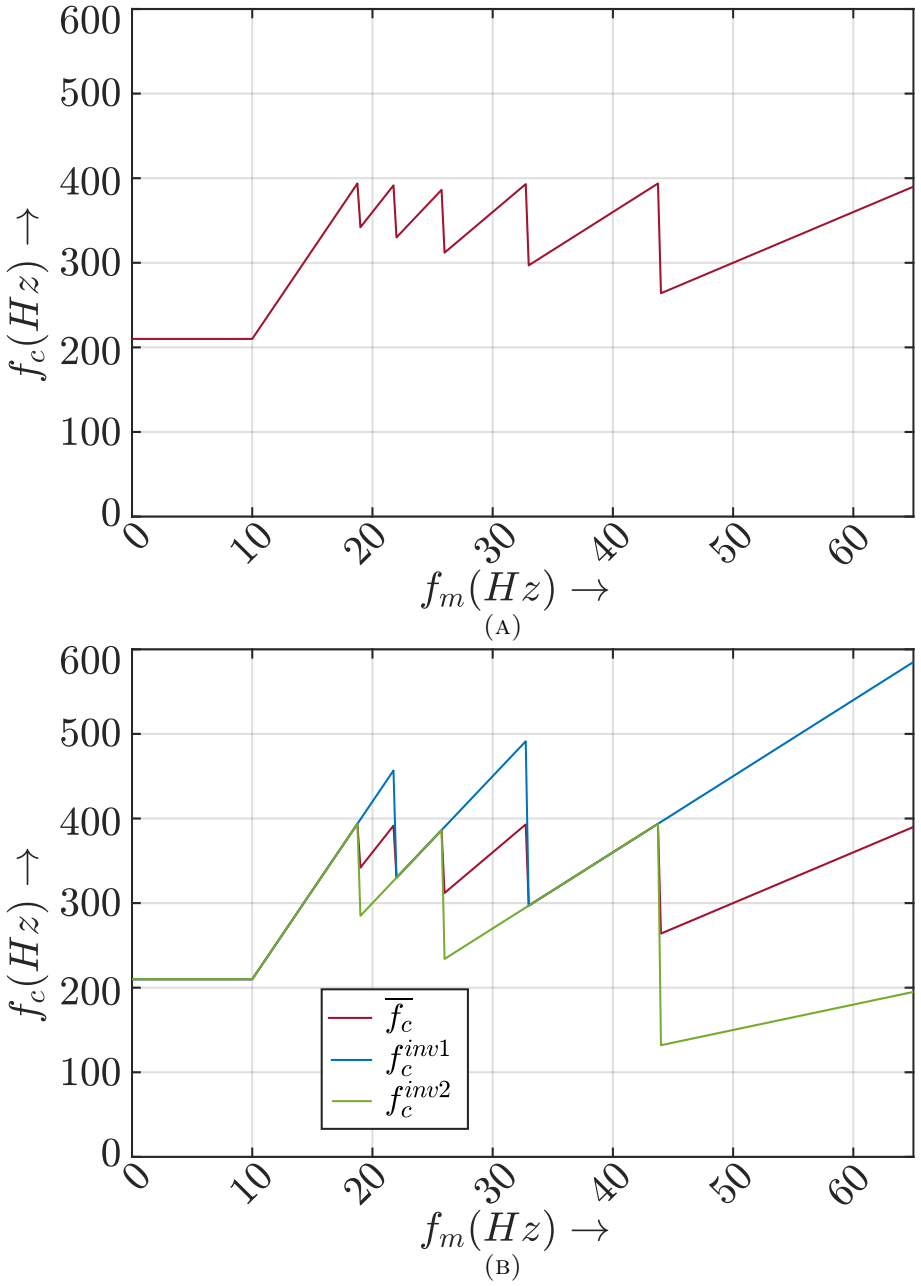


FIGURE 4.1: Variation of (a) f_c for conventional scheme and (b) f_c^{inv1}, f_2^{inv2} and $\overline{f}_c$ for proposed scheme with f_m

TABLE 4.1: Values of P_1, P_2 and $\overline{P}$ for complete range of f_m

Range of f_m	P_1	P_2	$\overline{P}$
$0Hz \leq f_m < 10Hz$	-	-	-
$10Hz \leq f_m < 19Hz$	21	21	21
$19Hz \leq f_m < 22Hz$	21	15	18
$22Hz \leq f_m < 26Hz$	15	15	15
$22Hz \leq f_m < 33Hz$	15	9	12
$33Hz \leq f_m < 44Hz$	9	9	9
$44Hz \leq f_m < 65Hz$	9	3	6

thesis in order to establish the effectiveness of the proposed PWM scheme in terms of harmonic performance. First, an expression for the phase-voltage of OWIM drive using DFS is established and then the impact of phase-shift in both carrier and modulating signals on the fundamental component of the voltage is analysed in the subsequent subsections.

4.2.1 Expression of phase-voltage of OWIM using DFS

The results given in Appendix 7 for the pole-voltages of the 2L-VSI (see (1), (2)) can be extended to obtain an expression for the resultant phase voltages (v_{Rr}, v_{Yy}, v_{Bb}) in an OWIM drive by considering inverter 2. In case of OWIM drive, the machine phase voltage is related to the pole-voltages of the two inverters as

$$v_{Xx} = v_{XO_1} - v_{xO_2} - v_{O_2O_1} \tag{4.2}$$

where $X \in \{R, Y, B\}$, $x \in \{r, y, b\}$ and $v_{o_2o_1}$ is the voltage between the negative buses of the two isolated DC sources, o_1 and o_2 (Fig.3.1b), also referred to as common-mode voltage. The same is computed as

$$v_{o_2o_1} = \frac{(v_{RO_1} + v_{YO_1} + v_{BO_1})}{3} - \frac{(v_{rO_2} + v_{yO_2} + v_{bO_2})}{3} \tag{4.3}$$

For OWIM drive, the phase-displacement corresponding to the modulating signals of inverter 1, that is, γ_R, γ_Y and γ_B are fixed at 0, $\frac{2\pi}{3}$ and $\frac{4\pi}{3}$ respectively. In order to obtain a generalised expression, a phase displacement of $\Delta\gamma$ is assumed between the modulating signals of the two inverters. Thus,the phase-displacement corresponding to the modulating signals of inverter 2, γ_r, γ_y and γ_b can be written as at $\Delta\gamma$, $\Delta\gamma + \frac{2\pi}{3}$

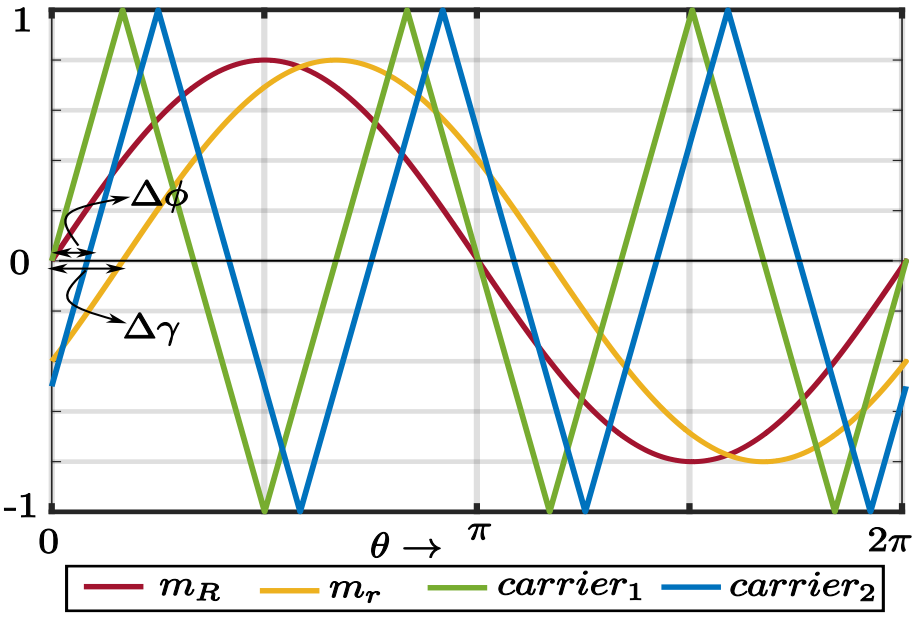


FIGURE 4.2: R-phase modulating and carrier signal for both inverter 1 and 2 showing $\Delta\phi$ and $\Delta\gamma$

and $\Delta\gamma + \frac{4\pi}{3}$. The phase-displacement corresponding to the carrier signal which is denoted by ϕ_β is fixed at $\frac{\pi}{2}$ for inverter 1. Thus, $\phi_R = \phi_Y = \phi_B = \frac{\pi}{2}$. Assuming a phase shift of $\Delta\phi$ between the carriers signals of two inverters, the value ϕ_r, ϕ_y and ϕ_b become $\frac{\pi}{2} + \Delta\phi$. The pictorial depiction of $\Delta\gamma$ and $\Delta\phi$ are shown in Fig. 4.2.

The impact of the two parameters, $\Delta\gamma$ and $\Delta\phi$ on the fundamental component of the machine phase-voltage of an OWIM drive is analysed in the next subsection.

4.2.2 Impact of phase-shift in modulating signals ($\Delta\gamma$) and carrier signals ($\Delta\phi$) on fundamental phase-voltage

The impact of creating phase shift in modulating and carrier signals on the fundamental component of the machine phase-voltage (v_{Rr_1}) is analysed for the OWIM drive in this subsection. For a given value of P, fundamental component of the pole-voltage of each VSI, v_{RO1_1} and v_{ro2_1}, can be obtained by putting $m = 0$ and $n = 1$ and appropriate values of appropriate values for γ_R and γ_r in (2). Further, substituting the expressions for v_{RO1_1} and v_{ro2_1} in (4.2), the expression for v_{Rr_1} can be obtained as,

$$v_{Rr_1} = A_0^1[cos(\omega_o t) - cos(\omega_o t + \Delta\gamma)] \tag{4.4}$$

TABLE 4.2: (m, n) giving rise k for various values of $\overline{P}$

	$k=5$	$k=7$	$k=11$	$k=13$	$k=17$	$k=19$
$\overline{P}=9$	$(1,-4)$	$(1,-2)$	$(1,2)$	$(1,4)$	$(2,-1)$	$(2,1)$
$\overline{P}=6$	$(1,-1)$	$(1,1)$	$(2,-1)$	$(2,1)$	$(3,-1)$	$(3,1)$

The magnitude of the coefficient A_0^1 can be obtained substituting the limit $m \to 0$ in (3) as shown below

$$A_0^1 = \frac{2V_{dc}}{\pi} \lim_{m \to 0} \frac{J_n\left(m\frac{M\pi}{2}\right)}{m} \tag{4.5}$$

Solving the above limit, A_0^1 becomes equal to $\frac{MV_{dc}}{2}$. Thus, substituting this in (4.4), we get

$$v_{Rr_1} = \frac{MV_{dc}}{2}[cos(\omega_o t) - cos(\omega_o t + \Delta\gamma)] \tag{4.6}$$

Thus, it is clear from (4.6) that $\Delta\gamma$ should be maintained at π for maximum DC bus utilization. Further, $\Delta\phi$ does not impact the magnitude of v_{Rr_1}. Thus, $\Delta\phi$ can be chosen based on other objectives. In the present work, $\Delta\phi$ is suitably chosen in order to minimize the total harmonic distortion in the motor line current for lower values of $\overline{P}$ such as $\overline{P}=9$. The same is explained in the next section.

4.3 Harmonic Optimization Using Phase-Shift in Carrier Signals ($\Delta\phi$) for $\overline{P}=9$

k^{th} order harmonic component present in the inverter pole-voltages is given by $k = 6q \pm 1$ where q can be any natural number, for an OWIM drive. Among these harmonic voltages, the magnitude of the lower order components, i.e. $k = 5, 7, 11, 13, 17$ and 19, play a significant role in the current and torque ripple of the motor. The total harmonic distortion (THD) in the line current can directly be correlated to the weighted THD in the voltage, V_{WTHD}. Considering the dominant lower order harmonics, V_{WTHD} can be defined as

$$V_{WTHD} = \sum_{k=5,7,11,13,17,19} \left(\frac{|v_{Rr_k}|}{k}\right)^2 \tag{4.7}$$

Here, $|v_{Rr_k}|$ is the magnitude of the k^{th} order harmonic component of the machine

phase-voltage. Taking $\Delta\gamma = \pi$ and considering a phase shift of $\Delta\phi$ between the carrier signals, the expression for the k^{th} harmonic component of phase voltage, v_{Rr_k} is given as

$$v_{Rr_k} = A_m^n cos[k\omega_o t + \frac{m\pi}{2}] - A_m^n cos[k\omega_o t + n\pi + m(\frac{\pi}{2} + \Delta\phi)] - v_{O_1O_{2_k}} \tag{4.8}$$

Here, $v_{O_1O_{2_k}}$ is the k^{th} harmonic component of the common-mode voltage. The same is obtained from (4.3) as

$$\begin{aligned} v_{O_1O_{2_k}} = & \frac{A_m^n}{3}\big(cos[k\omega_o t + \frac{m\pi}{2}] + cos[k\omega_o t + n\frac{2\pi}{3} + \frac{m\pi}{2}] + cos[k\omega_o t + n\frac{4\pi}{3} + \frac{m\pi}{2}]\big) \\ & - \frac{A_m^n}{3}\big(cos[k\omega_o t + n\pi + m(\frac{\pi}{2} + \Delta\phi)] + cos[k\omega_o t + n\frac{5\pi}{3} + m(\frac{\pi}{2} + \Delta\phi)]\big) \\ & - \frac{A_m^n}{3}\big(cos[k\omega_o t + n\frac{7\pi}{3} + m(\frac{\pi}{2} + \Delta\phi)]\big) \end{aligned} \tag{4.9}$$

It can be seen from (4.9), $v_{O_1O_{2_k}}$ becomes non-zero only if n is a multiple of 3. Table 4.2 presents the various combination of (m, n) which gives rise to particular k^{th} order harmonics two values of $\overline{P}$. It can be seen from table 4.2, n is never a multiple of 3 for any value of k for $\overline{P} = 9$. Thus, $v_{O_1O_2}^k$ can be taken to be becomes zero for this analysis.

It is proposed in this thesis, that for $\overline{P} = 9$, $\Delta\phi$ should be decided in a manner such that V_{WTHD} as given by (4.7), is minimized. Substituting the values of (m, n) from table 4.2 for $\overline{P} = 9$, the magnitude of lower order harmonics in the machine phase-voltage, normalized by the factor $\frac{4V_{dc}}{\pi}$, is given by

$$\begin{aligned} v_{Rr_5}^{\overline{P}=9} &= J_{-4}\left(\frac{\pi M}{2}\right) sin\left(-\frac{\Delta\phi}{2}\right) sin\left(5\omega_o t + \frac{\pi}{2} + \frac{\Delta\phi}{2}\right) \\ v_{Rr_7}^{\overline{P}=9} &= J_{-2}\left(\frac{\pi M}{2}\right) sin\left(-\frac{\Delta\phi}{2}\right) sin\left(7\omega_o t + \frac{\pi}{2} + \frac{\Delta\phi}{2}\right) \\ v_{Rr_{11}}^{\overline{P}=9} &= J_{2}\left(\frac{\pi M}{2}\right) sin\left(-\frac{\Delta\phi}{2}\right) sin\left(11\omega_o t + \frac{\pi}{2} + \frac{\Delta\phi}{2}\right) \\ v_{Rr_{13}}^{\overline{P}=9} &= J_{4}\left(\frac{\pi M}{2}\right) sin\left(-\frac{\Delta\phi}{2}\right) sin\left(13\omega_o t + \frac{\pi}{2} + \frac{\Delta\phi}{2}\right) \\ v_{Rr_{17}}^{\overline{P}=9} &= \frac{J_{-1}(\pi M)}{2} cos(-\Delta\phi)\, cos(17\omega_o t + \pi + \Delta\phi) \\ v_{Rr_{19}}^{\overline{P}=9} &= \frac{J_{1}(\pi M)}{2} cos(-\Delta\phi)\, cos(19\omega_o t + \pi + \Delta\phi) \end{aligned} \tag{4.10}$$

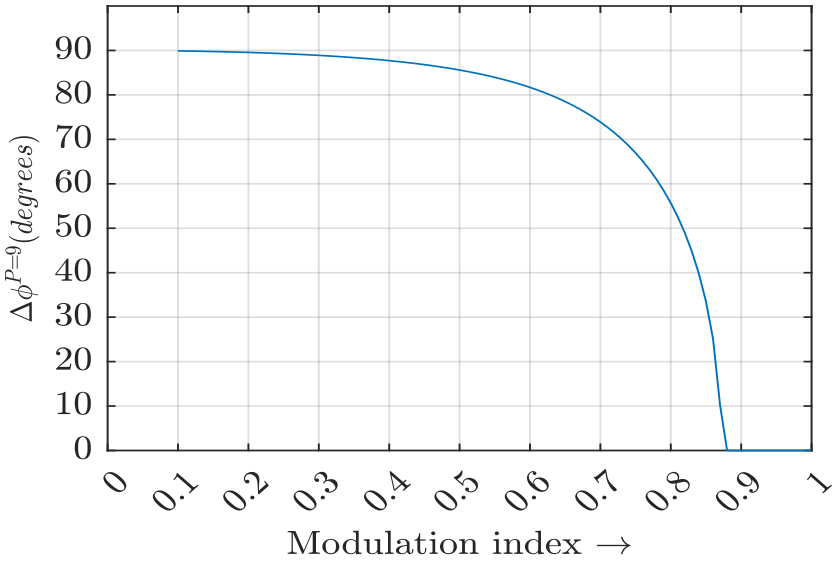


FIGURE 4.3: Variation of optimal value of $\Delta\phi$ for $\overline{P} = 9$

Substituting the values of $|v_{Rr_k}|$ from (4.10) into (4.7) and simplifying, V_{WTHD} for $\overline{P} = 9$ comes out to be

$$V_{WTHD}^{\overline{P}=9} = \alpha_1 sin^2(\frac{\Delta\phi}{2}) + \alpha_2 cos^2(\Delta\phi) \tag{4.11}$$

Here, the constants α and β are dependent on the modulation index M as,

$$\begin{aligned} \alpha_1 &= \frac{1}{25}[J_{-4}(\frac{\pi M}{2})]^2 + \frac{1}{49}[J_{-2}(\frac{\pi M}{2})]^2 + \frac{1}{121}[J_2(\frac{\pi M}{2})]^2 + \frac{1}{169}[J_4(\frac{\pi M}{2})]^2 \\ \alpha_2 &= \frac{1}{289}[\frac{J_{-1}(\pi M)}{2}]^2 + \frac{1}{361}[\frac{J_1(\pi M)}{2}]^2 \end{aligned} \tag{4.12}$$

Minimizing (4.11), by differentiating $V_{WTHD}^{p=9}$ with respect to $\Delta\phi$ and equating it 0 as, $\frac{dV_{WTHD}^{p=9}}{d\Delta\phi} = 0$, the optimal value of $\Delta\phi$ is obtained as

$$\Delta\phi^{\overline{P}=9} = cos^{-1}(\frac{\alpha_1}{4\alpha_2}) \tag{4.13}$$

Thus, for $\overline{P} = 9$, the optimal value of $\Delta\phi$ comes to be a function of M. Its variation across the complete range of modulation index is shown in Fig.4.3. Thus, varying phase-shift between the carrier signals as a function of M as shown in Fig.4.3 should lead to minimum harmonic distortion in current. The proposition regarding the improvement in harmonic performance for $\overline{P} = 6$ for the proposed scheme is analytically validated using DFS in the next section.

4.4 Harmonic performance pertaining to $\overline{P} = 6$

In the proposed PWM scheme, for even triplen values of $\overline{P}$, P_1 and P_2 are kept at different values. No phase-shift is introduced between the carrier signals. Thus, $\Delta\gamma$ is taken to π and $\Delta\phi$ is taken to be 0. For $\overline{P} = 6$, the the harmonic performance of the proposed case where $P_1 = 9$ and $P_2 = 3$, is analytically compared against the conventional case where P_1 and P_2 are both kept at 6. In the following discussion, case I would refer to the conventional method and case II would refer to the proposed method. The metric for comparison is again taken to be the weighted THD of machine phase-voltage V_{WTHD} as given by (4.7).

4.4.1 Case I: Conventional PWM, $P_1 = P_2 = 6$

The expression for V_{WTHD} when both inverter 1 and 2 are operated with $P_1 = P_2 = 6$ with $\Delta\gamma = \pi$ and $\Delta\phi = 0$ can be written by substituting the appropriate values of m and n from table 4.2 in (4.8). An interesting thing to note from table 4.2 with regards to $P_1 = P_2 = 6$ is that the value of $m + n$ for $k = 5, 7, 17$ and 19 becomes an even integer. It is clear from (3), the magnitude of A_m^n becomes zero if $m + n$ is even. Thus, for this case, the only harmonics under consideration is $k = 11$ and 13. The expression of the same normalized with respect to $\frac{4V_{dc}}{\pi}$ is given by

$$\begin{aligned} v_{Rr_{11}}^{P=6,case1} &= \frac{-J_{-1}(\pi M)}{2} cos(11\omega_o t) \\ v_{Rr_{13}}^{P=6,case1} &= \frac{-J_1(\pi M)}{2} cos(13\omega_o t) \end{aligned} \tag{4.14}$$

Thus, weighted THD for this case, $V_{WTHD}^{P=6,case1}$ is given by

$$V_{WTHD}^{P=6,case1} = \frac{1}{121}\left[J_{-1}(\pi M)\right]^2 + \frac{1}{169}\left[J_1(\pi M)\right]^2 \tag{4.15}$$

4.4.2 Case II: Proposed PWM, $P_1 = 9$ and $P_2 = 3$

The second case where $P_1 = 9$ and $P_2 = 3$ is considered now. The harmonic profile of the inverter 1 will be similar to the case of $P_1 = 9$ discussed earlier. However, in case of $P_2 = 3$, a particular order of harmonics can appear due to more than one combination of (m, n). For higher values of k, like, 17 and 19, either the value of m or n becomes greater than 4. Thus, the magnitude of the bessel function becomes insignificant and hence they can be neglected. The expression for various harmonic

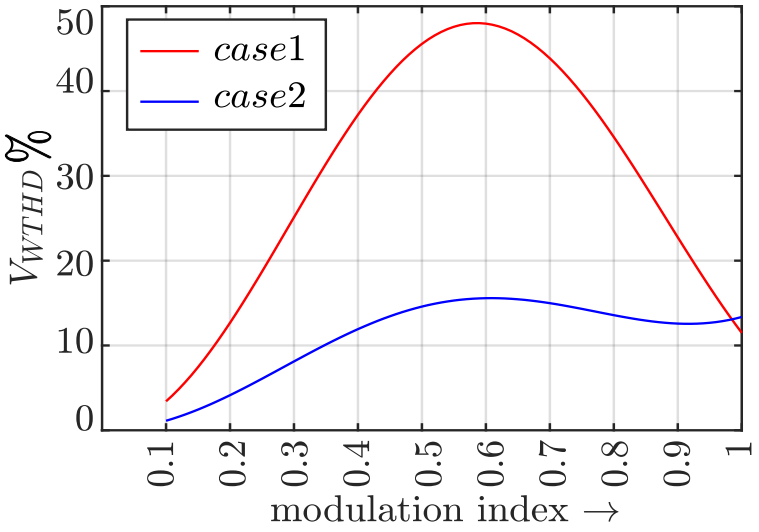


FIGURE 4.4: Comparison of V_{WTHD} for the two cases corresponding to $\overline{P} = 6$

components of the machine phase-voltage is given by

$$
\begin{aligned}
v_{Rr_5}^{P=6,case2} &= -\left(\frac{J_{-4}\left(\frac{\pi M}{2}\right)}{2} + \frac{J_2\left(\frac{\pi M}{2}\right)}{2}\right) sin\left(5\omega_o t\right) - \\
&\quad \frac{J_{-1}\left(\pi M\right)}{4} cos\left(5\omega_o t\right) \\
v_{Rr_7}^{P=6,case2} &= -\left(\frac{J_{-2} - \left(\frac{\pi M}{2}\right)}{2} + \frac{J_{-2}\left(\frac{3\pi M}{2}\right)}{6}\right) sin\left(7\omega_o t\right) + \\
&\quad \frac{J_1\left(\pi M\right)}{4} cos\left(7\omega_o t\right) \\
v_{Rr_{11}}^{P=6,case2} &= \left(-\frac{-J_{-2}\left(\frac{\pi M}{2}\right)}{2} + \frac{J_2\left(\frac{3\pi M}{2}\right)}{6}\right) sin\left(11\omega_o t\right) + \\
&\quad \frac{J_{-1}\left(2\pi M\right)}{8} cos\left(11\omega_o t\right) \\
v_{Rr_{13}}^{P=6,case2} &= -\frac{J_4\left(\frac{\pi M}{2}\right)}{2} sin\left(13\omega_o t\right) + \frac{J_1\left(2\pi M\right)}{8} cos\left(13\omega_o t\right) \\
v_{Rr_{17}}^{P=6,case2} &= \frac{J_{-1}\left(\pi M\right)}{4} cos\left(17\omega_o t\right) \\
v_{Rr_{19}}^{P=6,case2} &= \frac{J_1\left(\pi M\right)}{4} cos\left(19\omega_o t\right)
\end{aligned}
\tag{4.16}
$$

It can be seen from (4.16), there are three components corresponding to harmonic expressions for $k = 5, 7$ and 11. The first component pertains to inverter 1 with $P_1 = 9$ and the second two pertain to inverter 2 with $P_2 = 3$. There will be just two components for $k = 13$, one for each inverter. Finally one only one component

for $k = 17$ and 19, which comes from only inverter 1. Based on this discussion, the expression for various harmonics normalized with respect to $\frac{4V_{dc}}{\pi}$ can be written as

After simplifying these terms individually, the weighted THD in machine phase-voltage can be calculated using (4.7). The expression for the same for second case of $\overline{P} = 6$ is given by (4.17).

$$\begin{aligned} V_{WTHD}^{P=6,case2} = & \frac{1}{25}\left[\left(\frac{J_{-4}\left(\frac{\pi M}{2}\right)}{2}+\frac{J_2\left(\frac{\pi M}{2}\right)}{2}\right)^2+\left(\frac{J_{-1}\left(\pi M\right)}{4}\right)^2\right] \\ & +\frac{1}{49}\left[\left(\frac{J_{-2}\left(\frac{\pi M}{2}\right)}{2}-\frac{J_2\left(\frac{3\pi M}{2}\right)}{6}\right)^2+\left(\frac{J_1\left(\pi M\right)}{4}\right)^2\right] \\ & +\frac{1}{121}\left[\left(\frac{J_{-2}\left(\frac{\pi M}{2}\right)}{2}-\frac{J_2\left(\frac{3\pi M}{2}\right)}{6}\right)^2+\left(\frac{J_{-1}\left(2\pi M\right)}{8}\right)^2\right] \\ & +\frac{1}{169}\left[\left(\frac{J_4\left(\frac{\pi M}{2}\right)}{2}\right)^2+\left(\frac{J_2\left(2\pi M\right)}{8}\right)^2\right] \\ & +\frac{1}{289}\left[\frac{J_{-1}\left(\pi M\right)}{4}\right]^2+\frac{1}{361}\left[\frac{J_1\left(\pi M\right)}{4}\right]^2 \end{aligned} \tag{4.17}$$

The weighted voltage THD for both the cases of $\overline{P} = 6$ is calculated and plotted for the complete range of modulation index in Fig. 4.4. It can be seen that for almost the complete rage of modulation index, V_{WTHD} for case 2, that is implementing $\overline{P} = 6$ as an average of $P_1 = 9$ and $P_2 = 3$ yields better THD than implementing $P_1 = P_2 = 6$.

4.5 Analysis based on Stator-flux ripple

Ripple in the stator flux developed in the motor, $\tilde{\psi}_s$, due to PWM voltages is directly related to the harmonic distortion in the motor current and torque. The analysis of $\tilde{\psi}_s$ is generally done in the d-q domain where the d-axis is aligned with the voltage vector axis. The expression for d-q components of stator-flux ripple, $\tilde{\psi}_{sd}$ and $\tilde{\psi}_{sq}$, can be written in terms of voltage ripple in $\alpha - \beta$ domain, $\tilde{v}_{s\alpha}$ and $\tilde{v}_{s\beta}$, as

$$\tilde{\psi}_{sd} + j\tilde{\psi}_{sd} = \int [(\tilde{v}_{s\alpha} + j\tilde{v}_{s\beta})e^{-j\theta_s}]dt \tag{4.18}$$

Here, θ_s is angle pertaining to voltage vector. While the harmonic distortion

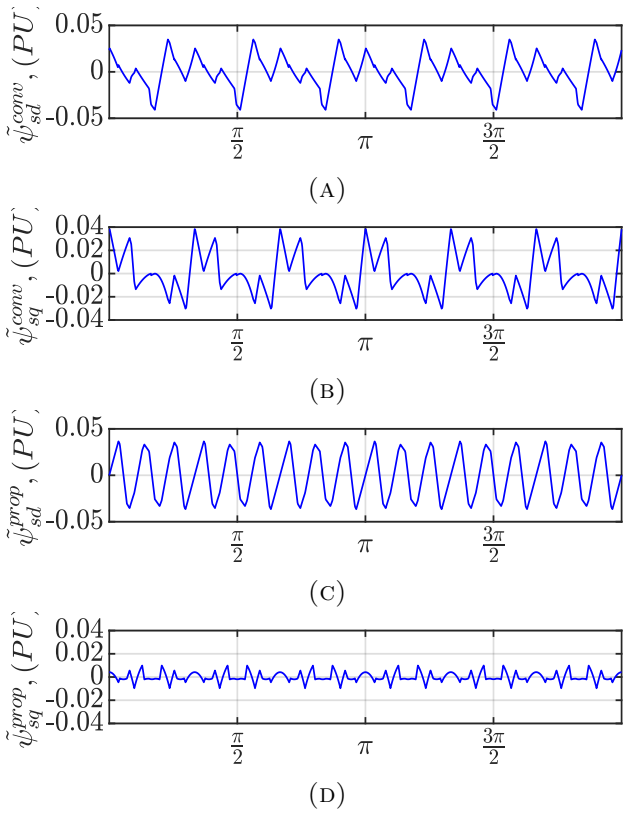


FIGURE 4.5: (a) $\tilde{\psi}_{sd}$ (b) $\tilde{\psi}_{sq}$ for conventional PWM (c) $\tilde{\psi}_{sd}$ (d) $\tilde{\psi}_{sq}$ for proposed PWM for $\overline{P} = 9$

in current is affected by both $\tilde{\psi}_{sd}$ and $\tilde{\psi}_{sq}$, the electromagnetic torque is primarily affected by $\tilde{\psi}_{sq}$ [74], [32], [33].

Normalized values of $\tilde{\psi}_{sd}$ and $\tilde{\psi}_{sq}$ for $\overline{P} = 9$ for both the conventional PWM scheme and the proposed PWM scheme for one complete fundamental cycle is shown in Fig. 4.5. $\tilde{\psi}_{sd}$ and $\tilde{\psi}_{sq}$ for the conventional PWM scheme is shown in Fig. 4.5a and 4.5b respectively while same for the proposed PWM scheme is shown in Fig. 4.5c and 4.5d respectively. It can be observed from the figure that while the peak-to-peak value of $\tilde{\psi}_{sd}$ remains almost same for both the cases, the same for $\tilde{\psi}_{sq}$ is much lesser for the proposed PWM scheme than the conventional scheme. Thus, it can be concluded that for $\overline{P} = 9$, the ripple in q-axis flux is reduced in the proposed method.

Similarly, the normalized values of $\tilde{\psi}_{sd}$ and $\tilde{\psi}_{sq}$ for $\overline{P} = 6$ is shown in Fig. 4.6 for both the conventional and the proposed PWM scheme. In this case, the peak-to-peak value of both $\tilde{\psi}_{sd}$ and $\tilde{\psi}_{sq}$ can be seen to be reduced for the proposed scheme as

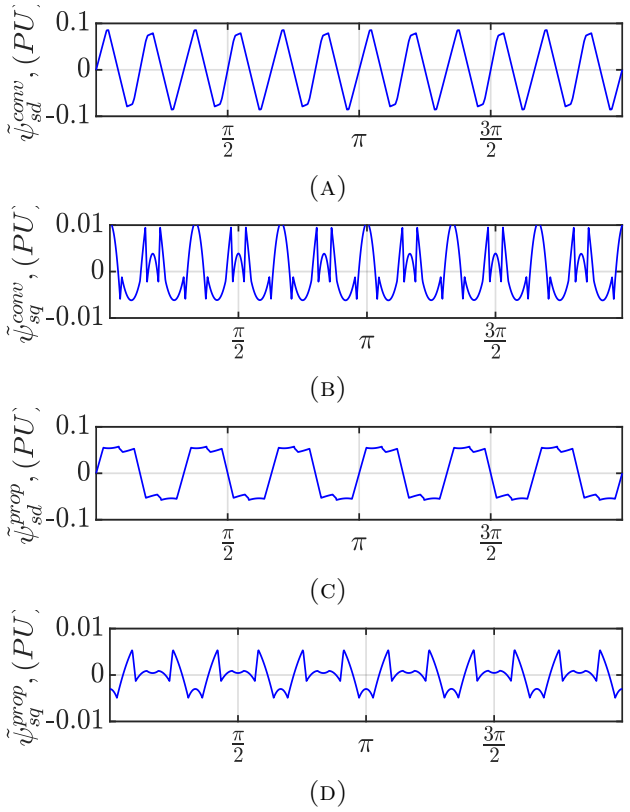


FIGURE 4.6: (a) $\tilde{\psi}_{sd}$ (b) $\tilde{\psi}_{sq}$ for conventional PWM (c) $\tilde{\psi}_{sd}$ (d) $\tilde{\psi}_{sq}$ for proposed PWM for $\overline{P} = 6$

compared to the conventional PWM scheme.

Thus, it can be concluded that the peak-to-peak value of atleast one of $\tilde{\psi}_{sd}$ and $\tilde{\psi}_{sq}$ is reduced with the proposed PWM scheme as compared to the conventional PWM scheme. Thus, the same will be reflected as an improvement in the THD in current which is validated in the next section.

4.6 Validation of Proposed PWM Technique

Improvement of the harmonic performance of an OWIM drive with the proposed PWM scheme is verified using MATLAB/Simulink based simulation of a 850kW, 2.2kV, 65Hz OWIM drive. Further, the findings of simulation are validated using experiments performed on a laboratory prototype of 7.5kW, 415V, 50Hz OWIM drive. The drive is operated using open-loop v/f control. The control algorithm and PWM techniques are implemented on TMS320f28379d DSP from Texas Instruments.

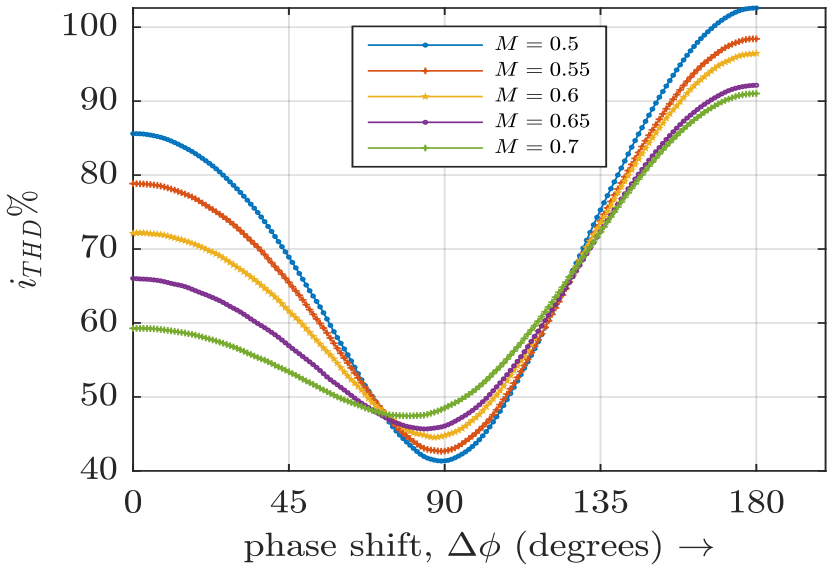


FIGURE 4.7: Variation of i_{THD} for $\overline{P} = 9$ for various modulation indices as $\Delta\phi$ is varied.

4.6.1 Simulation Results

For $\overline{P} = 9$, the effectiveness of creating a phase shift between the two carrier signals is first verified for various modulation indices, in the region in which $\overline{P} = 9$ is applied ($0.5 < M < 0.7$). This is done by measuring the corresponding phase-current THD (i_{THD}) as obtained in simulation by varying $\Delta\phi$ from 0^o to 180^o. This is shown in Fig. 4.7. The minimum value of i_{THD} for the different modulation indices comes almost at the same value of $\Delta\phi$ as obtained in Fig.4.3.

Further, waveform and harmonic spectra corresponding to the inverter pole voltages, v_{Ro_1} and v_{ro_2}, machine phase-voltage, v_{Rr} and phase-current, i_R as obtained in simulation corresponding to $M = 0.7$ are presented here. The simulation results pertaining to $\Delta\phi = 0^o$ are shown in Fig.4.8. v_{Ro_1}, v_{ro_2} and v_{Rr} are shown in Fig. 4.8a, their corresponding FFT in Fig. 4.8b, the machine phase-current (i_R) and its corresponding FFT in Fig. 4.8c and 4.8d respectively. The same quantities pertaining to $\Delta\phi = 74^o$ for the same value of M are shown in Fig. 4.9. $\Delta\phi = 74^o$ corresponds to its optimal value for $M = 0.7$ as seen in Fig.4.3. The harmonic spectrum of phase current for both the cases, that is with no phase shift and with the optimal value of

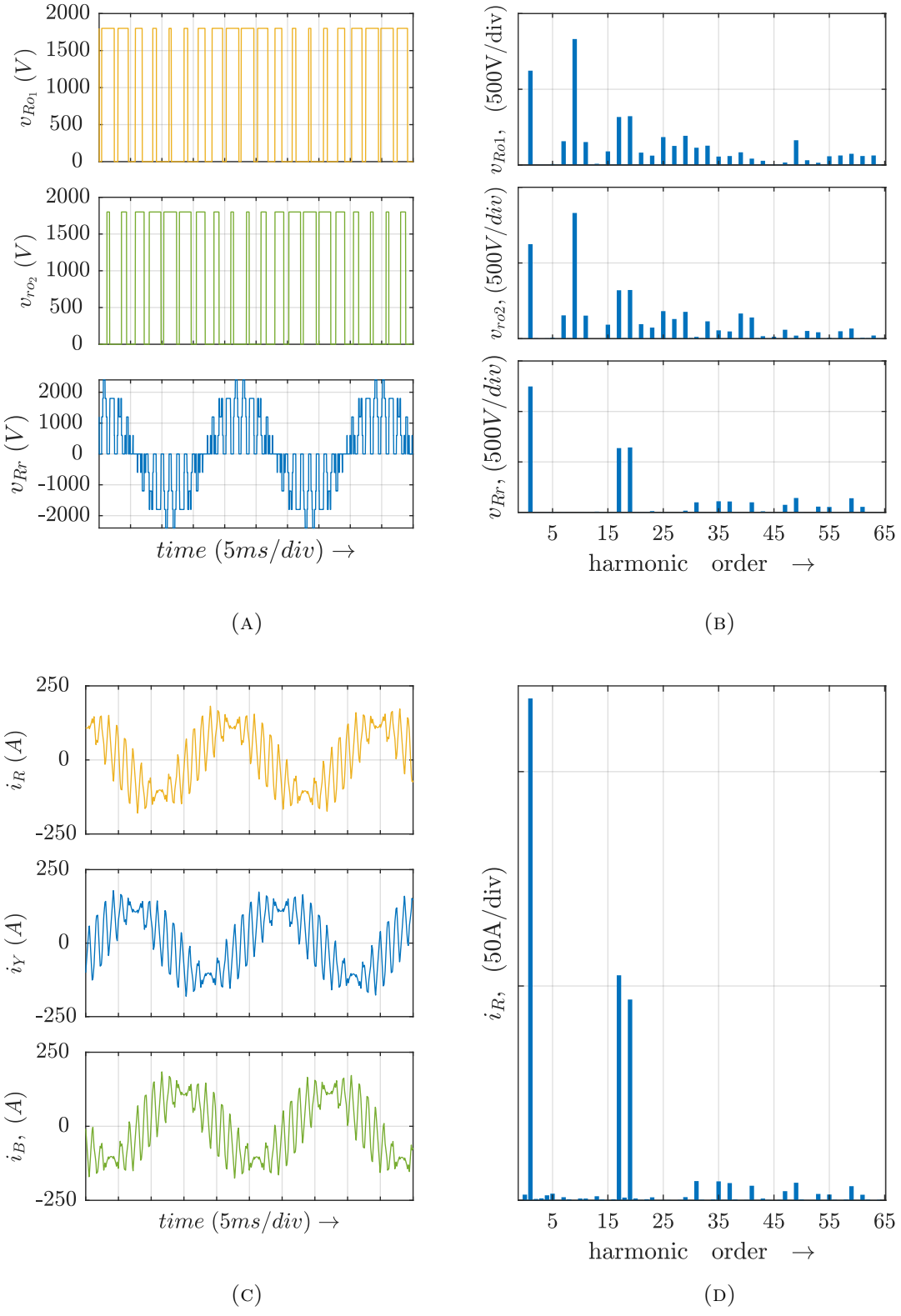


FIGURE 4.8: Simulation results for $\overline{P} = 9$ with $\Delta\phi = 0^o$ (a) pole voltages (v_{Ro1}, v_{ro2}) and phase voltage (v_{Rr}) (b) corresponding harmonic spectrum (c) three-phase current (d) corresponding harmonic spectrum.

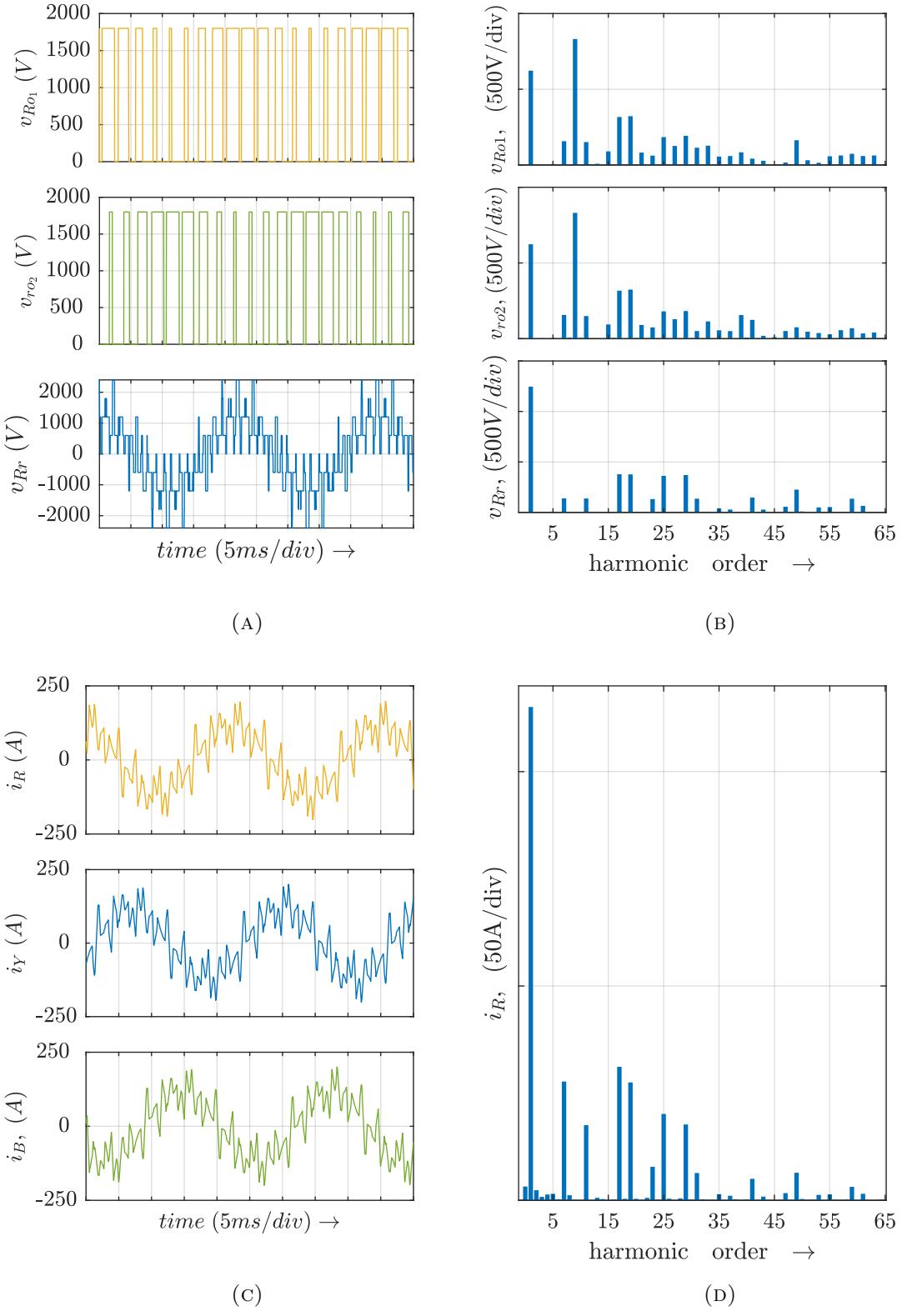


FIGURE 4.9: Simulation results for $\overline{P} = 9$ with $\Delta\phi = 74^o$ (a) pole voltages (v_{Ro1}, v_{ro2}) and phase voltage (v_{Rr}) (b) corresponding harmonic spectrum (c) three-phase current (d) corresponding harmonic spectrum.

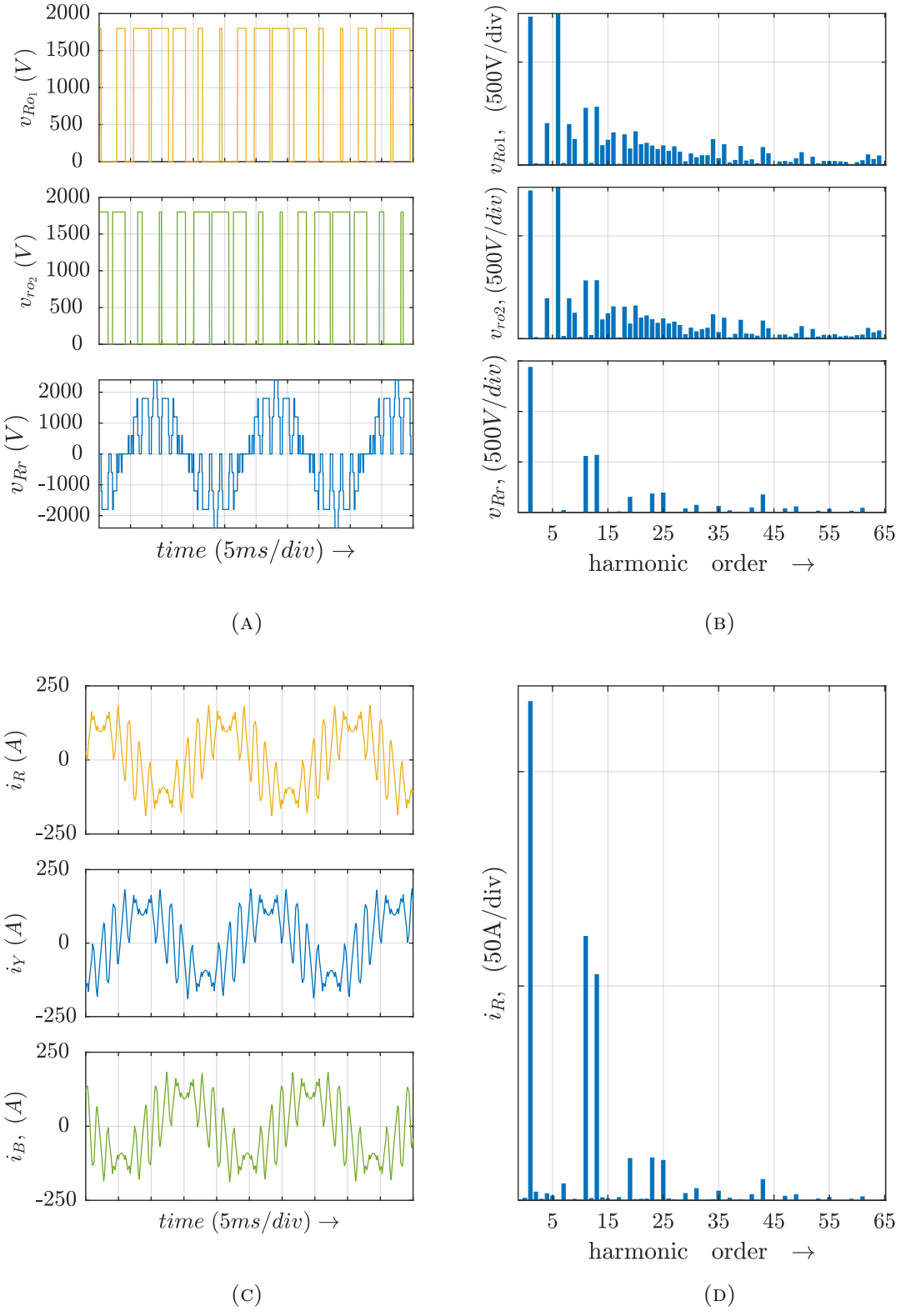


FIGURE 4.10: Simulation results for $P_1 = P_2 = \overline{P} = 6$ (a) pole voltages (v_{Ro1}, v_{ro2}) and phase voltage (v_{Rr}) (b) corresponding harmonic spectrum (c) three-phase current (d) corresponding harmonic spectrum.

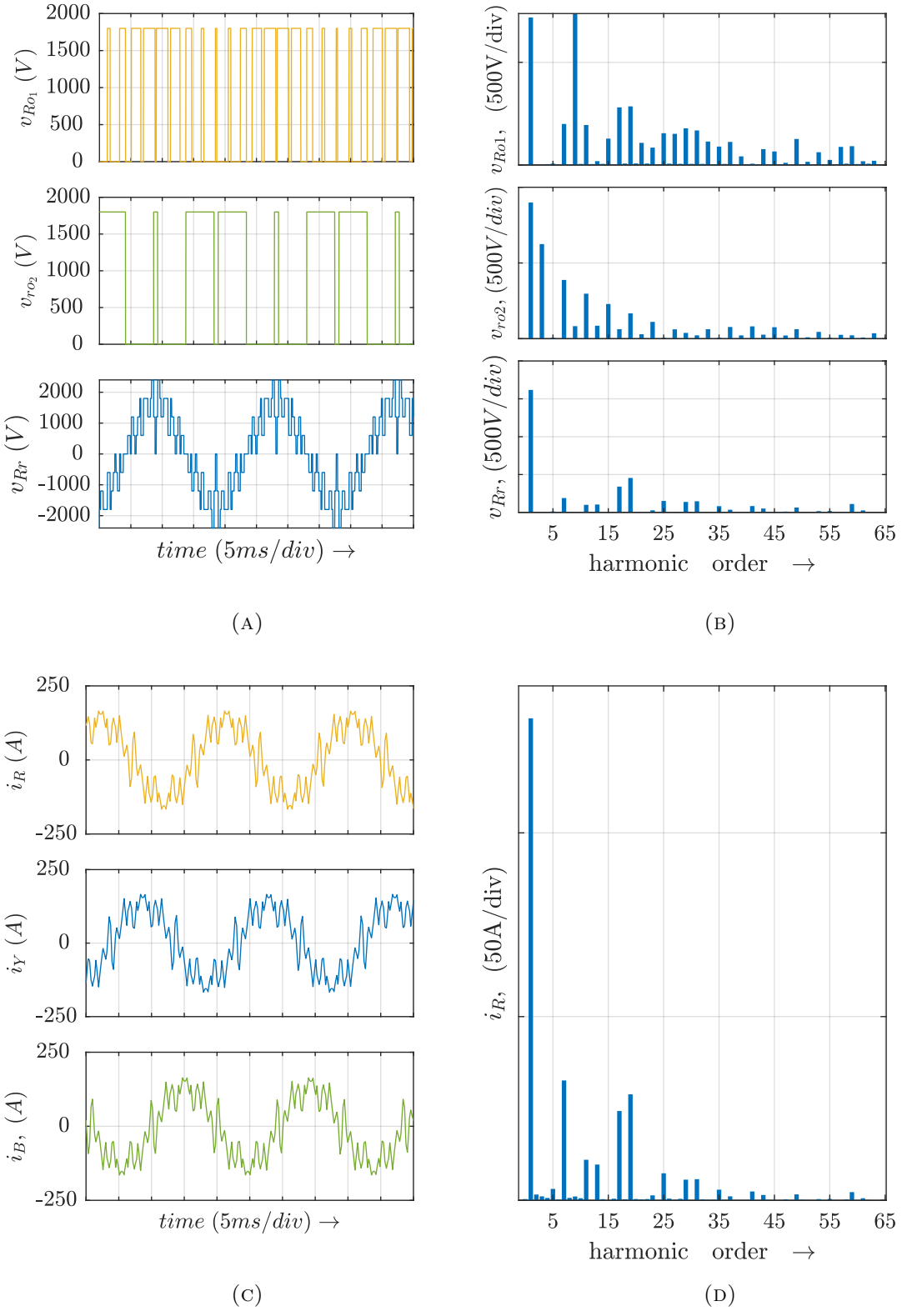


FIGURE 4.11: Simulation results for $\overline{P} = 6$, $P_1 = 9$, $P_2 = 3$ (a) pole voltages (v_{Ro1}, v_{ro2}) and phase voltage (v_{Rr}) (b) corresponding harmonic spectrum (c)three-phase current (d) corresponding harmonic spectrum.

phase shift, matches the harmonic spectrum of the respective machine phase voltage. This can be seen in Fig. 4.8d and 4.8b, and Fig. 4.9d and 4.9b respectively.

Further, it can be seen in in Fig. 4.8b, the dominant lower order harmonics come to be 17^{th} and 19^{th} for $\Delta\phi = 0^o$. All the other lower order harmonics which appear in the inverter pole voltages, that is, 7^{th}, 9^{th} and 11^{th}, they get completely cancelled in machine phase-voltage. However, 17^{th} and 19^{th} order harmonics add up in the machine phase-voltage which increases their magnitude significantly.

On the other hand, in Fig. 4.9b, for $\Delta\phi = 74^o$,lower order harmonics like 7^{th} and 11^{th} from the inverter pole-voltages do not get perfectly cancelled in the machine phase voltage. Hence, 7^{th} and 11^{th} also appear in the machine phase-voltage. However, 17^{th} and 19^{th} order harmonics from the inverter pole voltages also get cancelled in the machine phase voltage. Thus, their magnitude is reduced significantly in this case. Consequently, THD of phase current (i_{THD}) with $\Delta\phi = 74^o$ is lesser than the case with $\Delta\phi = 0^o$

Discussion related to simulation results pertaining to $\overline{P} = 6$ are presented next. The waveform and harmonic spectra corresponding to individual inverter pole-voltage v_{Ro_1}, v_{ro2}, machine phase-voltage v_{Rr} and machine phase-current i_R, i_Y, i_B corresponding to the conventional PWM wherein $P_1 = P_2 = 6$ are presented in Fig. 4.10. The same quantities corresponding to the proposed case wherein $P_1 = 9$ and $P_2 = 3$ are presented in Fig. 4.11. It can be seen that from Fig.4.10a that even order harmonics appear in the inverter pole-voltages. However, they get cancelled in the machine phase voltage. Further, the dominant lower order harmonics in the machine phase-voltage and current are 11^{th} and 13^{th} order harmonics. It can also be observed that their magnitudes add up in the machine phase-voltage.

On the other hand, it can be seen in Fig.4.11a, no even order harmonics are present in the pole-voltages of the individual inverters. However, for case 2, the voltage waveform and harmonic spectrum corresponding to individual inverter pole-voltages (Fig. 4.11a and 4.11b) are not identical. This is due to the different pulse numbers at which both the inverters are operated. The magnitude of 11^{th} and 13^{th} order

harmonics in the machine phase voltage are significantly reduced. However, some amount of 7^{th} order harmonics appear in the machine phase-voltage and current. Overall, the magnitudes of most of these harmonics are considerably smaller as compared to the 11^{th} and 13^{th} order harmonics corresponding to the conventional case. The i_{THD} corresponding to case 2 is considerably reduced as compared to case 1.

4.6.2 Experimental Results

4.6.2.1 Open-Loop Results

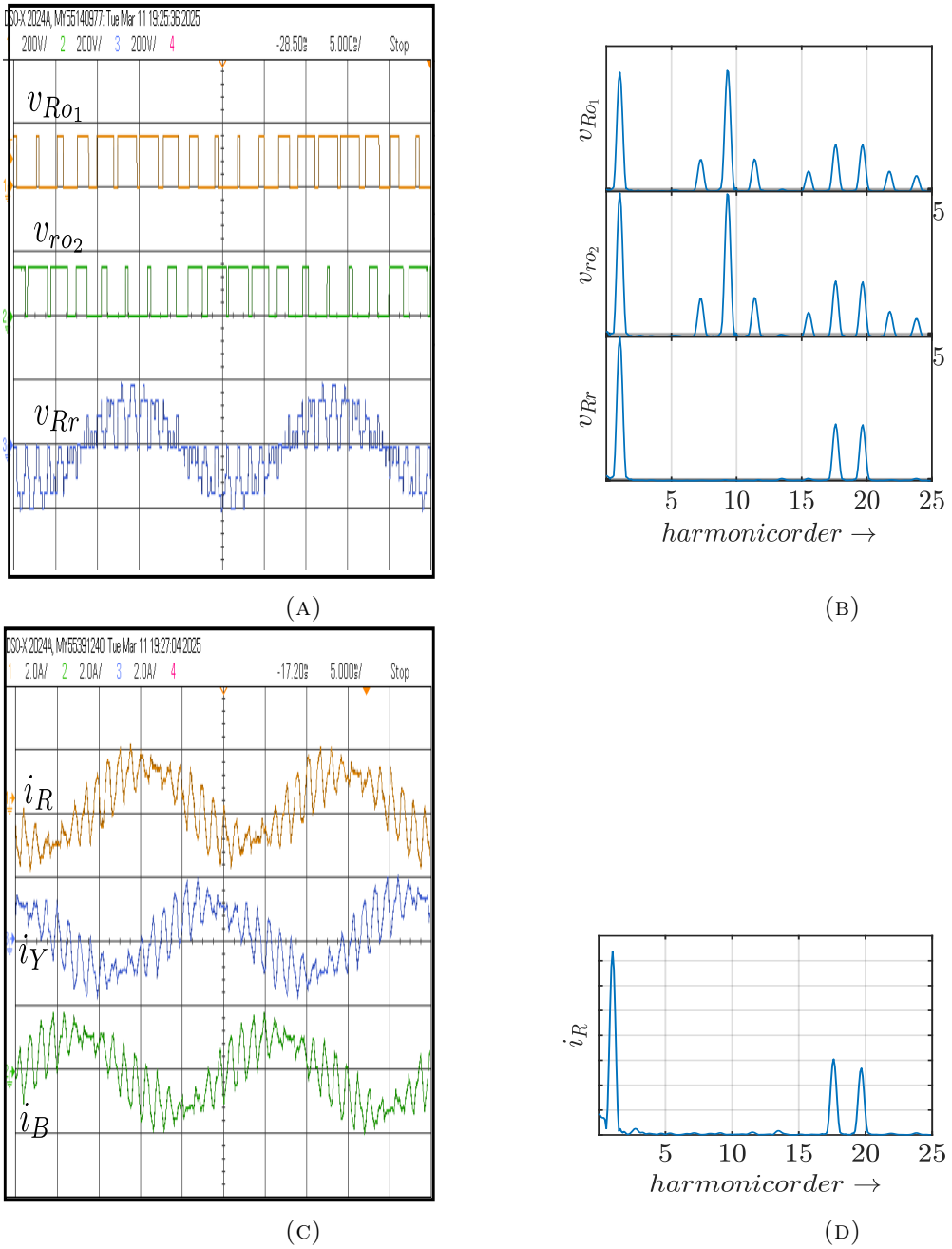
The findings of simulation are further validated experimentally on the laboratory prototype of the OWIM drive. The experimental results corresponding to v_{Ro_1}, v_{ro_2}, v_{Rr}, i_R, i_Y and i_B and their harmonic spectrum are presented here. For $\overline{P} = 9$, $\Delta\phi$ is first kept at zero and the drive is operated at $M = 0.7$ or $f_m = 35Hz$. The corresponding results are presented in Fig. 4.12. It can be seen that waveform shape and harmonic spectrum obtained through simulation match with the corresponding simulation results. Next, the drive is operated at the same modulation index making $\Delta\phi = 74^o$. All the results are presented in Fig. 4.13. The findings of simulation can be directly correlated with the experimental results.

The results pertaining to $\overline{P} = 6$ are verified experimentally next. Both the cases are implemented and the corresponding results of case 1 and 2 are shown in Fig. 4.14 and 4.15 respectively. All the findings of simulation from Fig.4.10 and 4.11 can be directly co-related with Fig. 4.14 and 4.15 respectively.

Further, the experimentally measured value of i_{THD} for both conventional and proposed PWM scheme upto $f_m = 65$Hz is shown in Fig. 4.16. Here the machine is run at reduced flux to run the machine at rated voltage at $f_m = 65$Hz. It can be clearly seen that the value of i_{THD} is much lesser for the proposed PWM scheme as compared to the conventional one.

4.6.2.2 Closed-Loop Operation

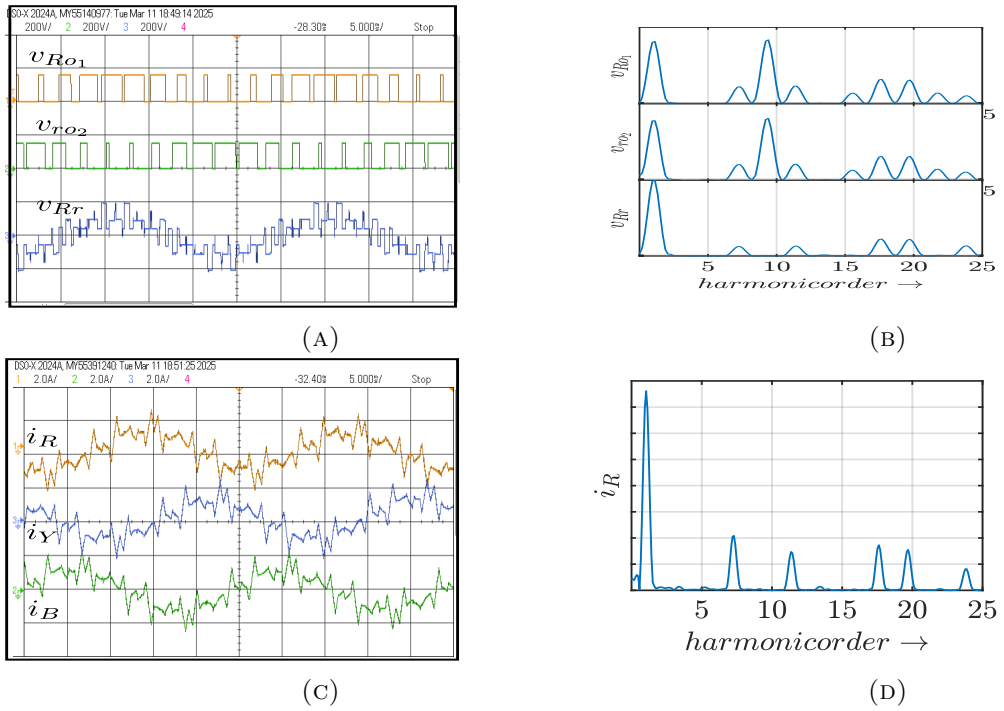
In order to establish the performance of the proposed PWM technique under dynamic conditions, the OWIM drive is operated under closed-loop control, using rotor-flux



(A) (B)

(C) (D)

FIGURE 4.12: Experimental results pertaining to $\overline{P} = 9$ and $\Delta\phi = 0$ (a) Individual inverter pole voltages (v_{Ro1}, v_{ro2}) and machine phase voltage (v_{Rr}) (500V/div, 5ms/div) (b) corresponding harmonic spectrum (c) three-phase current (2A/div, 5ms/div) (d) corresponding harmonic spectrum.



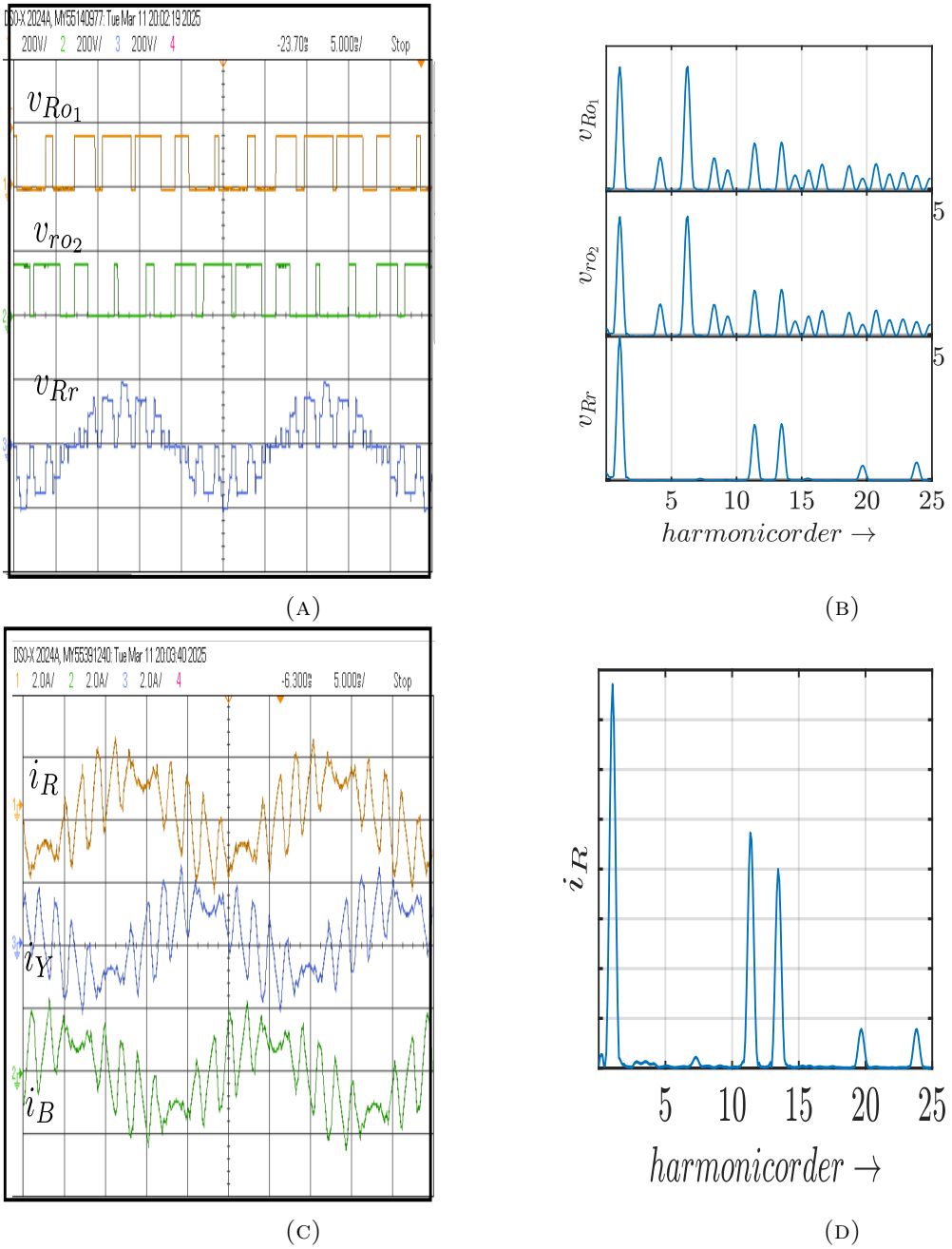
(A) (B)

(C) (D)

FIGURE 4.13: Experimental results for $\overline{P} = 9$ and $\Delta\phi = 74^o$ (a) pole voltages (v_{Ro1}, v_{ro2}) and phase voltage (v_{Rr}) (500V/div, 5ms/div) (b) corresponding harmonic spectrum (c) three-phase current (2A/div, 5ms/div) (d) corresponding harmonic spectrum.

oriented vector control method with the proposed PWM technique. The direct axis is aligned with the rotor flux vector in this case. The reference and actual values of the magnetising component of the current (i^*_{mr}, i_{mr}), direct axis component of the stator current (i^*_{sd}, i_{sd}), speed of the drive (ω^*_r, ω_r) and quadrature axis component of the stator current (i^*_{sq}, i_{sq}) are shown in Fig.4.17a-4.17d respectively. The drive is operated through the complete range of operating frequency by ramping up the reference speed from zero to rated speed and then ramping is down back to zero speed as shown in Fig.4.17c. This has been done to illustrate the performance of the drive during both acceleration and deceleration. All the actual quantities are seen to be tracking their respective reference values. Further, no unexpected transient can be seen in any of these quantities in Fig.4.17 as the transitions between various pulse-numbers in the proposed synchronous PWM takes place.

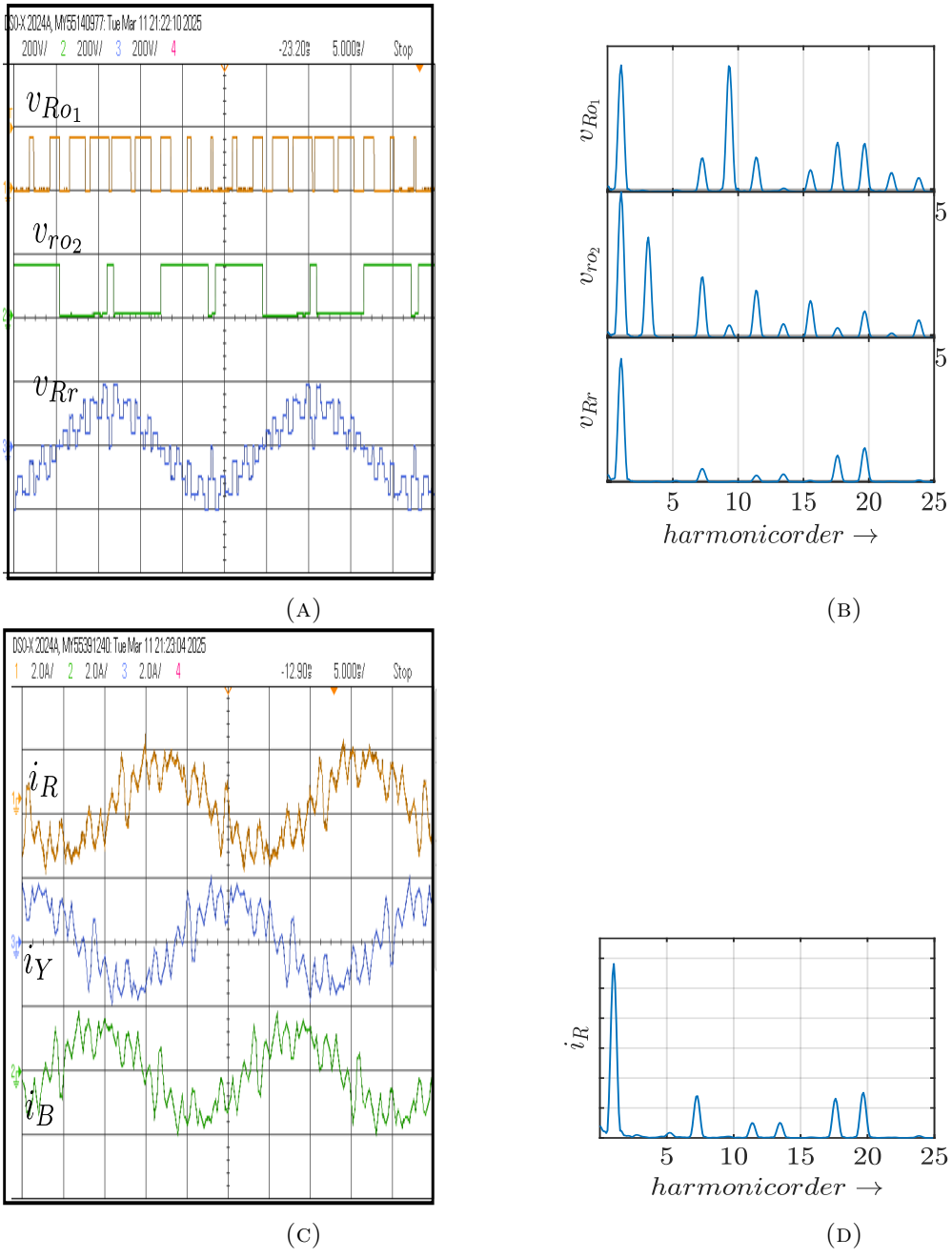
In order to further establish the smooth transitions between various pulse numbers,



(A) (B)

(C) (D)

FIGURE 4.14: Experimental results for $\overline{P} = P_1 = P_2 = 6$ (a) pole voltages (v_{Ro1}, v_{ro2}) and phase voltage (v_{Rr}) (500V/div, 5ms/div) (b) corresponding harmonic spectrum (c) three-phase current (2A/div, 5ms/div) (d) corresponding harmonic spectrum.



(A) (B)

(C) (D)

FIGURE 4.15: Experimental results for $\overline{P} == 6$, $P_1 = 9$ and $P_2 = 3$ (a) pole voltages (v_{Ro1}, v_{ro2}) and phase voltage (v_{Rr}) (500V/div, 5ms/div) (b) corresponding harmonic spectrum (c) three-phase current (2A/div, 5ms/div) (d) corresponding harmonic spectrum.

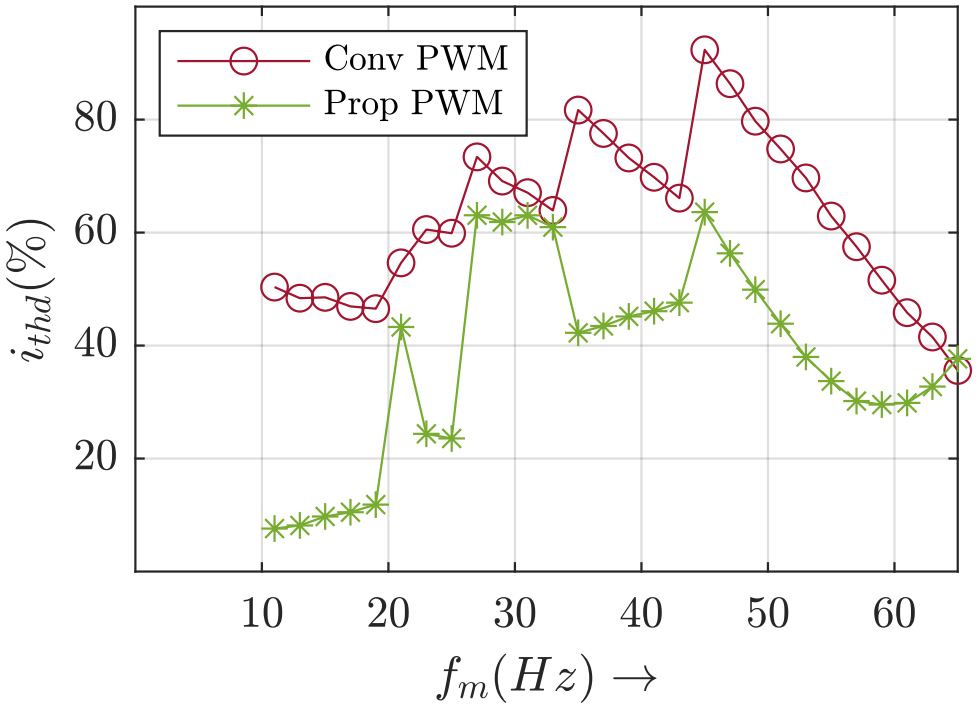


FIGURE 4.16: Comparison of i_{THD} for conventional and proposed PWM over range of f_m.

three-phase currents at the instants of transition between various pulse numbers, namely from Asynchronous PWM to proposed SST with $\overline{P} = 21$, $\overline{P} = 21$ to $\overline{P} = 18$, $\overline{P} = 12$ to $\overline{P} = 9$ and $\overline{P} = 9$ to $\overline{P} = 6$ are shown in Fig.4.18a-4.18d, respectively. All the transitions can be seen to be happening very smoothing. Only a small transient cant be seen when the transition takes place between $\overline{P} = 9$ to $\overline{P} = 6$. However, this has little impact on the performance of the drive.

4.7 Conclusion

A synchronous sine-triangle (SST) PWM scheme for open-end winding induction motor (OWIM) drive is proposed in this chapter, wherein, dissimilar carrier signals have been utilised for the two inverters in the OWIM drive. The effective pulse number, $\overline{P}$ is taken as the average of the pulse numbers of the two inverters, P_1 and P_2. For odd triplen values, such as $\overline{P} = 9$, P_1 and P_2 are kept equal. However, a suitable phase-shift, $\Delta\phi$ is introduced between the two carrier signals. The value of $\Delta\phi$ is chosen such that the harmonic performance of the drive is optimized. This is

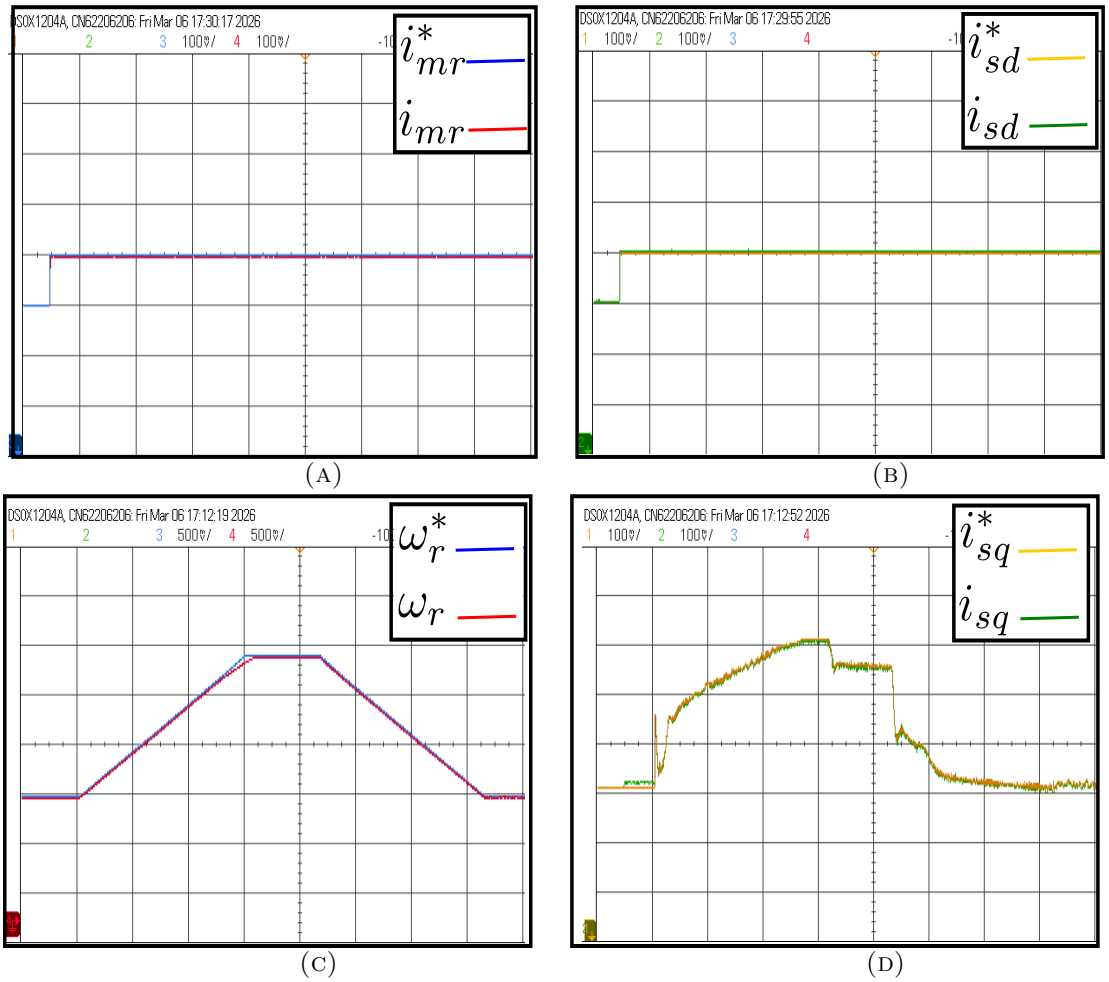


FIGURE 4.17: Experimental performance of vector controlled OWIM drive in terms of (a) i_{mr} [Scale: 3A/div, 20s/div] (b) i_{sd} [Scale: 3A/div, 20s/div] (c) speed [Scale: 500RPM/div, 20s/div]and (d) i_{sq} [Scale: 3A/div, 20s/div] with proposed PWM technique

done using double fourier series (DFS) based analysis. Further, for even-triplen values of $\overline{P}$, P_1 and P_2 are kept different. For example, for $\overline{P} = 6$, P_1 is kept at 9 and P_2 at 3. It has been shown analytically, again using DFS based mathematical framework, that implementing $\overline{P} = 6$ using this method yields better harmonic performance as compared to conventional method where both the inverters are operated are $P_1 = P_2 = 6$. Further, an analysis based on the stator flux ripple in d-q domain is done. It is found that with the proposed PWM scheme, the peak-to-peak value of q-axis flux ripple is reduced for $\overline{P} = 9$ whereas the peak-to-peak value of for both d and q-axis flux ripple is reduced for $\overline{P} = 6$. These analytical findings, pertaining to

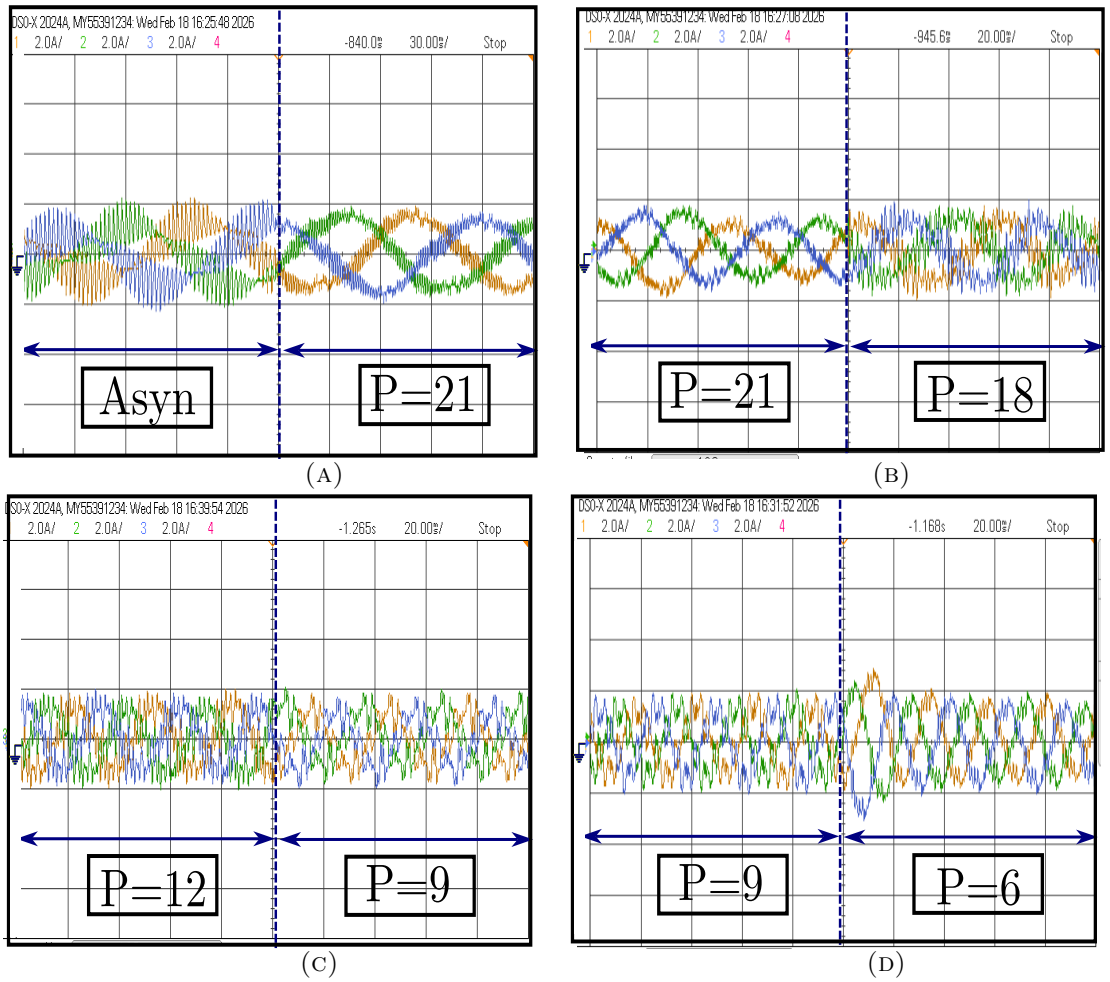


FIGURE 4.18: Experimental results showing three-phase currents at the instant of transition from (a) Asynchronous PWM to $\overline{P} = 21$ (b) $\overline{P} = 21$ to $\overline{P} = 18$ (c) $\overline{P} = 12$ to $\overline{P} = 9$ (d) $\overline{P} = 9$ to $\overline{P} = 6$ [y axis: 2A/div, x axis: 20ms/div]

$\overline{P} = 9$ and $\overline{P} = 6$, are validated using both MATLAB/Simulink based simulations on a 850-kW, 2.2 kV OWIM based traction drive and through experiments on a scaled down laboratory prototype of 415V, 7.5 kW OWIM drive. Both simulation and experimental results suggest that, the harmonic performance of the drive in terms of line-current THD is improved with the proposed PWM scheme.

Chapter 5

Speed Sensorless Control of Multi-Induction Motor Drives

5.1 Introduction

Modularity in power electronic systems provides several advantages like more reliability and easy scalability of the system [75], [76]. Modular power converter based high-power, medium voltage electric motor drives have gained high research interest in the last few decades [77]. In conventional modular motor drive systems, such as those employing cascaded H-bridge (CHB) [78] or modular multilevel converter (MMC) [79] topologies, modularity is realized primarily at the power electronic converter level. Although such configurations enhance scalability, fault tolerance and maintenance flexibility, they are typically dedicated to driving a single electric machine, resulting in a system where mechanical flexibility remains limited. On the other hand, the concept of multiple motors mechanically coupled to a common shaft introduces modularity in the mechanical drive level. Each motor operates at the same speed and collectively shares the load torque. Such a configuration enhances system-level modularity by allowing selective motor redundancy, scalability in torque/power capability, and improved fault resilience. Thus, multi-motor drive systems (MMDS) are becoming popular for high power industrial applications like industrial pumps, fans and blowers [24]. Cage-rotor induction motor (IM) drives are generally chosen for such applications due to their ruggedness and low-maintenance. Each motor in such an MMDS is driven by its dedicated power converter which can commonly be a 2-level voltage source inverter (2L-VSI). Further, rotor-flux oriented vector control algorithm is implemented for the individual motor to control the torque produced by them. Series-connected, multiphase, multi-motor drive with independent vector control is presented in [25], [26]. An IM based dual-motor drive system (DMDS) is shown in Fig. 5.1a wherein two motors are couple to the same

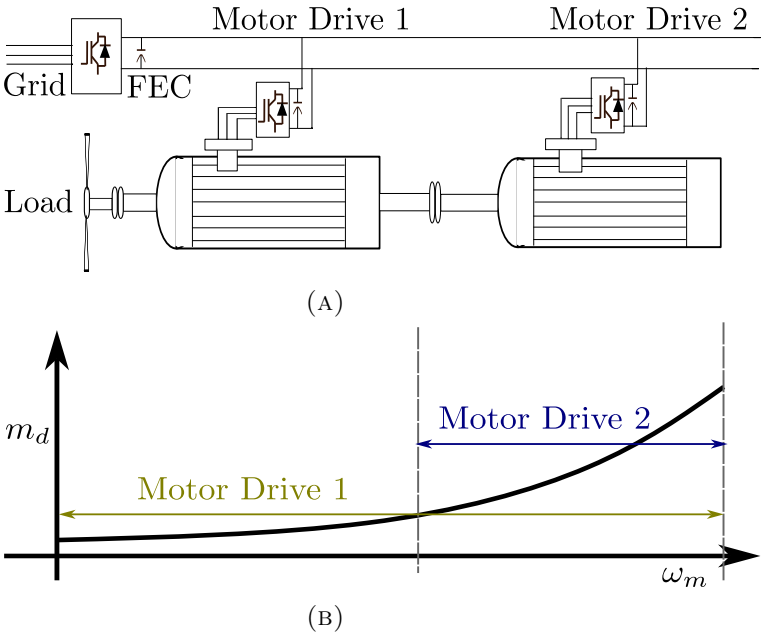


FIGURE 5.1: (a) IM based dual-motor drive system. (b) Load torque-speed profile and region of torque production of individual IM.

shaft in order to drive the load.

Speed sensorless operation of these drives is preferred in order to improve the overall reliability and robustness of the system [41]. Performance of sensorless field oriented control (FOC) of induction motor is highly dependent on the accurate estimation of stator flux vector, $\overrightarrow{\psi}_s$, using the information of applied stator voltage vector $\overrightarrow{v}_s$, stator-current vector, $\overrightarrow{i}_s$ and machine parameters. Simple integration of motor back-emf, $\overrightarrow{e}_s$, may not work due to issues like small DC-offset in measured currents [42], [43], [44]. Hence, a low-pass filter (LPF) with a small cutoff frequency ($\omega_o = 2\pi f_o$) is used to estimate the stator flux as shown below,

$$\Psi(s)_{s,\alpha} + j\Psi(s)_{s,\beta} = \frac{1}{(s+\omega_o)}[E(s)_{s,\alpha} + jE(s)_{s,\beta}] \tag{5.1}$$

Here, $\Psi(s)_{s,x}$ and $E(s)_{s,x}$, where $x \in (\alpha, \beta)$, are the s-domain transfer functions of the two quadrature components of $\overrightarrow{\psi}_s$ and $\overrightarrow{e}_s$. This method works well when the operating frequency of the motor, f_s, is fairly higher than f_o. However, at lower f_s, the phase and magnitude error in the estimated $\overrightarrow{\psi}_s$ due to the LPF becomes significant and degrades the overall performance of the sensorless drive.

The present chapter focuses on developing a PLL based technique to accurately estimate the mechanical speed of an MMDS driving loads such as a fan or a pump. For these loads, the torque requirement from the drive becomes proportional to the square of the speed. This is shown in Fig. 5.1b. Thus, all the motors in an MMDS are not required to produce torque together at lower speed. In case of a DMDS, one motor is sufficient to meet the torque demand from the load while the other motor freewheels at lower speed. The proposed technique uses a PLL implemented on the stator current vector $\overrightarrow{i}_s$ of the zero-torque producing machine to determine the mechanical speed of the drive. Since mechanical speed is same for both the motors, the accurately estimated speed is used for indirect FOC of individual motors in the DMDS. Although, the speed estimation algorithm is developed for a DMDS in the present article, it can be easily extended to an MMDS.

5.2 Sensorless Control Architecture for MMDS

Fig. 5.1a shows an IM based DMDS driving a fan load. The torque-speed characteristics for such a load is shown in Fig. 5.1b. The electrical speed of the rotor in rad/s is denoted by ω_m in this chapter. Each motor is fed by separate three-phase VSIs and can be independently controlled. The overall control philosophy of such a motor drive is explained in this section.

5.2.1 Modes of Operation of the Drive

A speed-sensorless field oriented control algorithm is developed for the IM based DMDS. This is based on the torque-speed profile of the load supplied by the drive. For the load-torque characteristics shown in Fig. 5.1b, it can very clearly be observed that both the motors are not required to produce torque together, from the beginning. As the drive starts, only one motor is sufficient to meet the torque demand. The second motor is controlled to just maintain its flux. However, as the speed builds up and the torque demand from the load increases, the second motor starts sharing the load-torque with the first one. The region in which each motor is controlled to produce torque is marked in Fig. 5.1b. Based on this, two modes of operation of the drive are defined in this work (a) Speed correction mode (SCM) when the operating

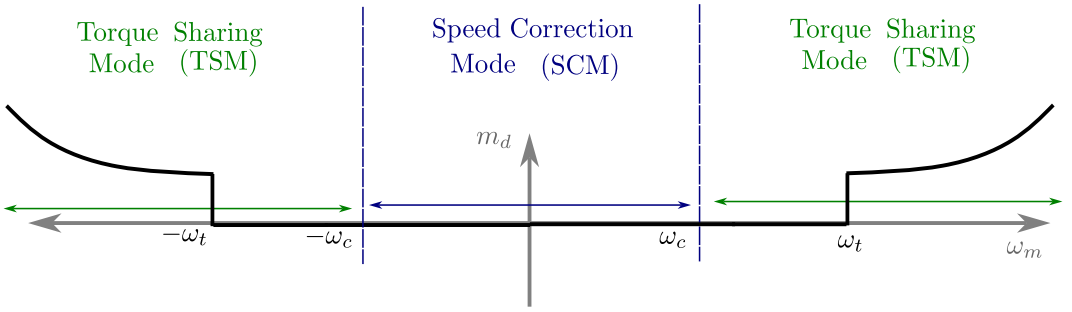


FIGURE 5.2: Torque demand from motor 2 and the corresponding modes of operation of the DMDS.

frequency is less than a pre-decided value ω_c (b) Torque sharing mode (TSM) when the operating frequency exceeds ω_c.

Voltage model of motor 1 is initially used to estimate the mechanical speed, $\tilde{\omega}_m$, of the drive. However, when the operating speed of the drive is low, accuracy of $\tilde{\omega}_m$ will be compromised. This is discussed in detail in the next section. Thus, it is proposed in this chapter that during this region of low-speed operation, the accuracy of $\tilde{\omega}_m$ can be improved by introducing a speed correction factor, $\hat{\omega}_m$ which is obtained from a PLL. This PLL is implemented on the stator current vector $\overrightarrow{i}_{s,2}$ of motor 2. In the present article, this mode of low-speed operation, when the speed-correction is done, is referred to as Speed Correction Mode (SCM). As the speed of DMDS increases, the accuracy of $\tilde{\omega}_m$ improves and beyond a predetermined speed, ω_c, speed correction is no longer required. The mode of operation beyond ω_c is referred to as Torque Sharing Mode (TSM) here. The two modes of operation are pictorially represented in Fig. 5.2.

During the initial part of TSM, motor 1 continues to supply the complete load-torque and motor 2 free-wheels. However, after a certain speed, ω_t, the torque demand becomes greater than the rated torque of a single motor, m_d^{rated}, and both the motors in the DMDS are required to share the load torque equally. The control scheme of both the motors becomes identical during TSM. In contrast, the control scheme of motor 2 is modified to obtain $\hat{\omega}_m$ during SCM. The control scheme of the DMDS throughout its complete region of operation is shown in Fig. 5.3. Here a speed PI controller gives the reference value of the total q-axis component of the stator

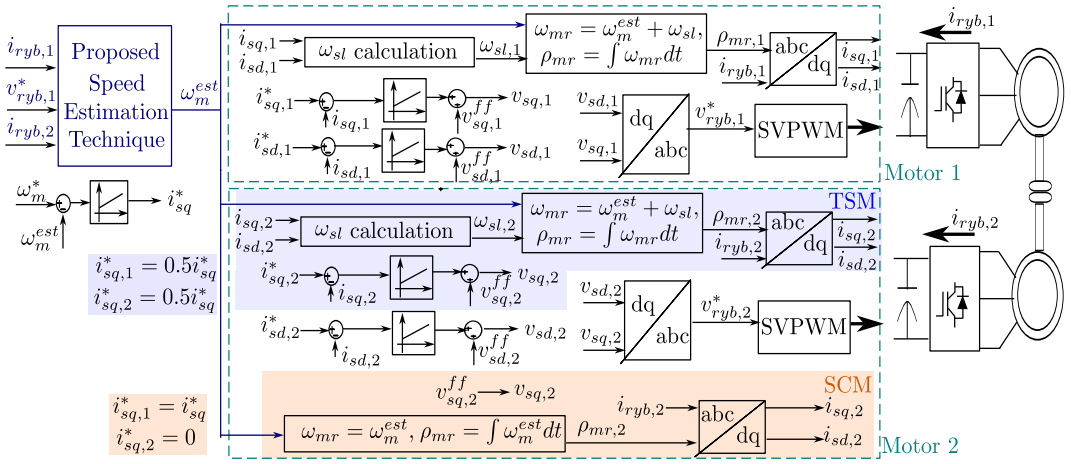


FIGURE 5.3: Proposed control block diagram for the dual motor drive system.

current, i^*_{sq} at its output. In TSM, i^*_{sq} is equally divided into $i^*_{sq,1}$ and $i^*_{sq,2}$, which are the q-axis component of the stator current of motor 1 and 2 respectively. However, in SCM, $i^*_{sq,1}$ becomes equal to i^*_{sq} whereas $i^*_{sq,2}$ is made to be 0. The control scheme employed during TSM is further explained next.

5.2.2 Control of DMDS in TSM

As the accurate mechanical speed of the drive is available, conventional rotor flux oriented indirect vector control of IM is employed to control the torque and flux of the two motors independently. The slip-speed, ω_{sl} as obtained using i_{sq} and i_{mr}, is added to the estimated mechanical speed, ω_m^{est}, to obtain the synchronous speed, ω_{mr}. The angle of the rotor flux vector, ρ_{mr} is obtained from ω_{mr}. This is shown below.

$$\omega_{mr} = \omega_{sl} + \omega_m^{est}; \;\; \rho_{mr} = \int \omega_{mr} dt \tag{5.2}$$

ρ_{mr} is further used for axes-transformation. The outer-flux controller generates the reference d-component of the stator current, i^*_{sd}. The reference q-component, i^*_{sq} is decided based on the mode of operation. The current controllers are designed based on the following dynamic equations with suitable feedforward compensation.

$$\begin{aligned} v_{sd} &= R_s i_{sd} + \sigma L_s \frac{di_{sd}}{dt} + (1-\sigma) L_s \frac{di_{mr}}{dt} - \sigma L_s \omega_{mr} i_{sq} \\ v_{sq} &= R_s i_{sq} + \sigma L_s \frac{di_{sq}}{dt} + \sigma L_s \omega_{mr} i_{sd} + (1-\sigma) L_s \omega_{mr} i_{mr} \end{aligned} \tag{5.3}$$

ρ_{mr} is again used to obtain the three-phase reference voltages, v^*_{ryb} from v^*_{sd} and v^*_{sq}. Carrier based implementation of space vector PWM technique is used to generate

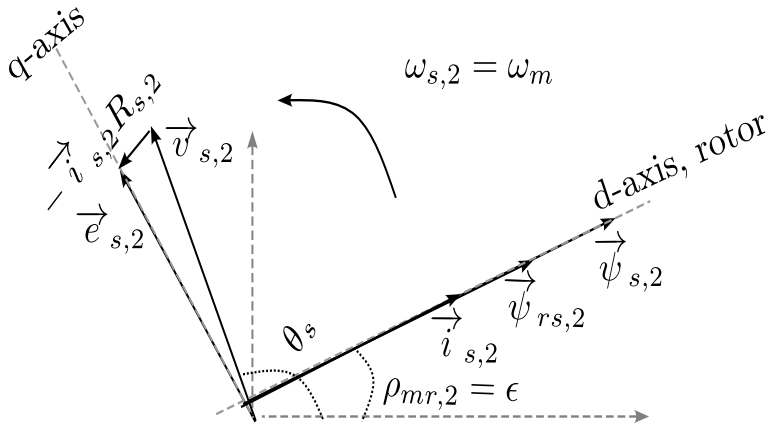


FIGURE 5.4: Phasor diagram of IM under no-load

the desired pole voltages from the 2L-VSI. The complete control block diagram is shown in Fig.5.3.

5.3 Proposed Speed Estimation Technique

The technique for accurate speed estimation of DMDS proposed in this chapter and the related control scheme of motor 2 during both SCM and TSM are explained in this section. Further, various aspects of the proposed scheme like design of the PLL, its stability and its performance under parametric variation are also discussed. Finally, an analysis regarding the power flow in the two machines both in SCM and TSM has been done.

5.3.1 PLL Based Speed Estimation Scheme

At low speed, the drive is operated in SCM and the torque requirement from motor 2 is zero (Fig. 5.2). The phasor diagram of an IM under no-load is shown in Fig. 5.4. Under no-load, q-axis component of the stator current of motor 2, $i_{sq,2}$ becomes zero. This implies that the vector $\overrightarrow{i}_{s,2}$ will be aligned along its rotor-flux vector $\overrightarrow{\psi}_{rs,2}$. Moreover, redthe q-axis component of the stator-flux $\psi_{sq,2}$, as derived in (1.5), is given by

$$\psi_{sq,2} = (L_{s,2} - \frac{L_{m,2}^2}{L_{r,2}})i_{sq,2} \tag{5.4}$$

Thus, $\psi_{sq,2}$ also becomes zero. Thus, the angle between the stator flux vector, $\overrightarrow{\psi}_{s,2}$ and $\overrightarrow{\psi}_{rs,2}$ will also be zero. Thus, all the three vectors, $\overrightarrow{i}_{s,2}$, $\overrightarrow{\psi}_{rs,2}$ and $\overrightarrow{\psi}_{s,2}$ will be in the same direction. Further, since the slip of the motor is zero, $\omega_{mr,2}$ which

is the frequency associated with $\overrightarrow{\psi}_{rs,2}$ will become equal to the rotor speed, ω_m. Consequently, their respective angles, that is $\rho_{mr,2}$ and ϵ also become equal. Thus, the vector $\overrightarrow{i}_{s,2}$ aligns along the rotor axis, as shown in Fig. 5.4. Hence, under such condition, a PLL designed to determine the phase and frequency of $\overrightarrow{i}_{s,2}$ will give ω_m and angle ρ_{mr}.

A general control block diagram for a PLL is shown in Fig. 5.5. In case of grid-connected converters, a PLL is implemented on the grid voltage in order to extract the grid frequency and voltage angle information. Further, it is well established in literature that the performance of the PLL can be improved by adding the nominal frequency of the grid at the output of the PI controller. This offers two-fold advantages. Firstly, it gives an initial estimate of the frequency. Secondly, in this case, the PI controller is required to act only on the small deviation in frequencies rather than the full value [80]. However, in case of motor drives, the operating frequency changes with the mechanical speed. Thus, adding a fixed value of the nominal frequency of the motor at the output of the PI does not solve its purpose. In some cases, it is suggested to augment the performance of the PLL by adding the reference speed at the output of the PLL. Such an idea may work, when the reference speed is ramped up gradually, where the actual speed is close to the reference speed. However, in cases where a reference speed signal changes in a step manner, adding the same to the output of the PLL may not serve the purpose of improving the performance of the PLL.

Thus, the performance of the PLL is required to be improved in some other way. It is proposed in this chapter, that the performance of this PLL can be improved by adding an erroneous estimate of the operating speed, $\tilde{\omega}_m$, at the output of the PI. In this case, the PLL will be required to act on only the error between $\tilde{\omega}_m$ and the actual rotor speed, ω_m. $\tilde{\omega}_m$ can be obtained using the voltage model of motor 1 as done in conventional speed-sensorless control. Estimation of the same is discussed in detail in the next subsection.

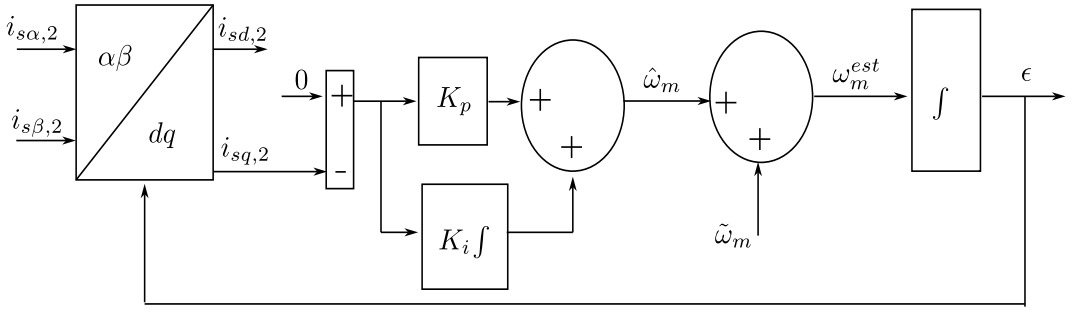


FIGURE 5.5: Control block diagram for stator current based PLL

5.3.2 Estimation of Erroneous Operating Speed, $\tilde{\omega}_m$

The erroneous operating speed, $\tilde{\omega}_m$, is found using the voltage model of motor 1. This is done by estimating the $\alpha - \beta$ components of the stator-flux vector of motor 1, $\tilde{\psi}_{s\alpha,1}$ and $\tilde{\psi}_{s\beta,1}$ from the motor back-emf, $e_{s\alpha,1}$ and $e_{s\beta,1}$ using (5.1). The cutoff frequency of the low-pass filter, f_o is kept at 5 Hz ($\omega_o = 2\pi 5$ rad/s). Following this, the $\alpha - \beta$ components of the rotor flux vector referred to the stator for motor 1, $\tilde{\psi}_{rs\alpha,1}$ and $\tilde{\psi}_{rs\beta,1}$, are estimated from the stator-flux and current information as shown below.

$$\tilde{\psi}_{rsx,1} = \frac{L_{r,1}}{L_{m,1}}(\tilde{\psi}_{sx,1} - \sigma L_s i_{sx,1}) \quad x \in (\alpha, \beta) \tag{5.5}$$

Further, the unit-vectors $\sin(\tilde{\rho}_{mr,1})$ and $\cos(\tilde{\rho}_{mr,1})$ are calculated from $\tilde{\psi}_{rs\alpha,1}$ and $\tilde{\psi}_{rs\beta,1}$. The d-q components of the current, $\tilde{i}_{sd,1}$ and $\tilde{i}_{sq,1}$, are obtained using the three-phase currents and unit vectors. Further, the frequency of the rotor-flux vector, $\tilde{\omega}_{mr,1}$, is also estimated from $\sin(\tilde{\rho}_{mr,1})$ and $\cos(\tilde{\rho}_{mr,1})$. $\tilde{i}_{sq,1}$ and $\tilde{i}_{mr,1}$ are used to calculate the slip of the motor, $\tilde{\omega}_{sl,1}$ using (5.6). Here, $T_{r,1}$ is the rotor time-constant of motor 1. Finally, $\tilde{\omega}_m$ is obtained by subtracting $\tilde{\omega}_{sl}$ from $\tilde{\omega}_{mr}$.

$$\tilde{\omega}_{sl,1} = \frac{\tilde{i}_{sq,1}}{T_{r,1}\tilde{i}_{mr,1}} \qquad \tilde{\omega}_m = \tilde{\omega}_{mr,1} - \tilde{\omega}_{sl,1} \tag{5.6}$$

Owing to the inaccuracies in stator flux estimation, $\tilde{\omega}_m$ will be inaccurate specially in low-speed region. It is also to be noted that, not just $\tilde{\omega}_m$ but all the quantities pertaining to motor 1, estimated using this voltage model are inaccurate and are denoted by a over-head $\tilde{}$ in this article. This inaccuracy is attributed to using $\frac{1}{s+\omega_o}$ instead of $\frac{1}{s}$ in flux estimation from the motor back-emf. The effect is more prominent

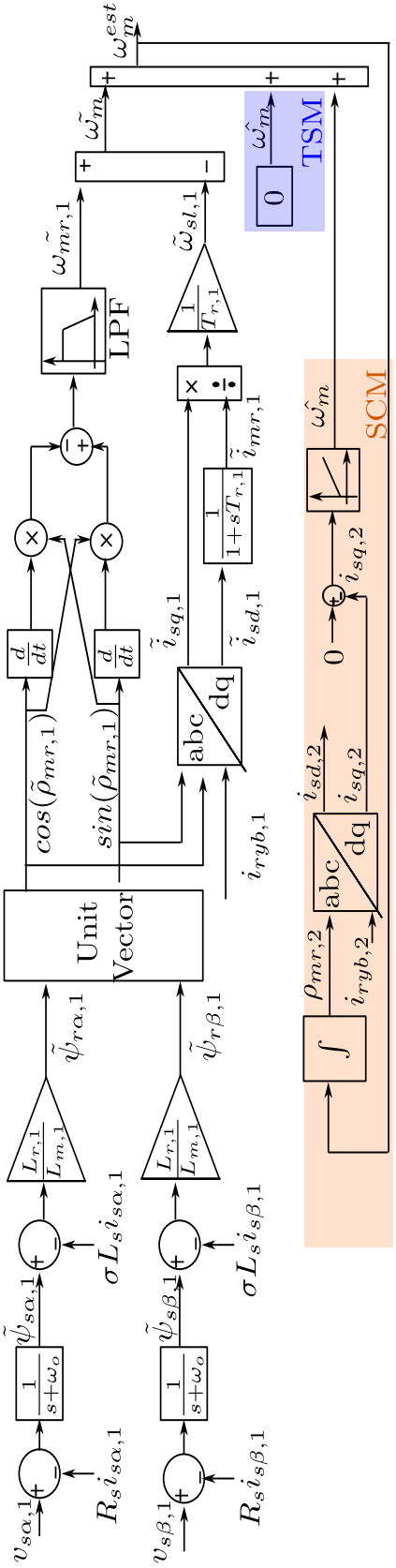


FIGURE 5.6: Proposed speed estimation technique

in low-speed region. Thus, the impact of operating frequency on the accuracy of the stator-flux estimation is analysed in the next subsection.

Fig.5.6 presents the block diagram of the proposed speed estimation scheme. Estimation of $\tilde{\omega}_m$ is shown in the upper part of the figure. $\tilde{\omega}_m$ is added to the output of the PLL in SCM. However, in TSM, the PLL is deactivated and $\tilde{\omega}_m$ is taken to be the estimated mechanical speed, ω_m^{est}.

5.3.3 Impact of Operating Frequency on the Estimation of $\tilde{\omega}_m$

The impact of the operating frequency on the accuracy of $\tilde{\omega}_m$ is analysed by looking at its impact on the estimated $\overrightarrow{\psi}_{s,1}$. Since quantities pertaining to motor 1 are under consideration, the $\alpha - \beta$ components of $\overrightarrow{e}_{s,1}$, which is the input to (5.1), can be considered to be sinusoidal signals with angular frequency, $\omega_{mr,1}$. The same can be denoted by $e_1(t)_{s,x} = A \sin[\omega_{mr,1} t + \phi]\, u(t)$, where $x \in (\alpha, \beta)$. Here, the phase ϕ has been included for generalization and $u(t)$ is the unit-step function. Taking Laplace transform, the corresponding s-domain transfer functions, $E_1(s)_{s,x}$, are given by,

$$E_1(s)_{s,x} = A \sin(\phi) \frac{s + \omega_{mr,1} \cot(\phi)}{s^2 + \omega_{mr,1}^2} \quad x \in (\alpha, \beta) \tag{5.7}$$

According to (5.1), the s-domain transfer function of output, $\Psi_1(s)_{s,x}$, is given by,

$$\Psi_1(s)_{s,x} = A \sin(\phi) \frac{s + \omega_{mr,1} \;\; cot(\phi)}{(s^2 + \omega_{mr,1}^2)(s + \omega_o)} \quad x \in (\alpha, \beta) \tag{5.8}$$

Taking the inverse laplace transform of $\Psi_1(s)_{s,x}$, $\psi_1(t)_{s,x}$ in time-domain is given by,

$$\psi_1(t)_{s,x} = \frac{A}{\sqrt{\omega_o^2 + \omega_{mr,1}^2}} \left[\sin(\omega_{mr,1} t + \phi - \theta) + A_2 e^{-\omega_o t}\right] \tag{5.9}$$

Here, A_2 is the constant pertaining to transient part of the solution. θ is the phase shift between the input and the output signal that comes as result of this low-pass filtering and is given by,

$$\theta = \tan^{-1} \frac{\omega_{mr,1}}{\omega_o} \tag{5.10}$$

Ideally, for a pure integrator, θ comes out to be $\frac{\pi}{2}$. However, for an LPF, θ

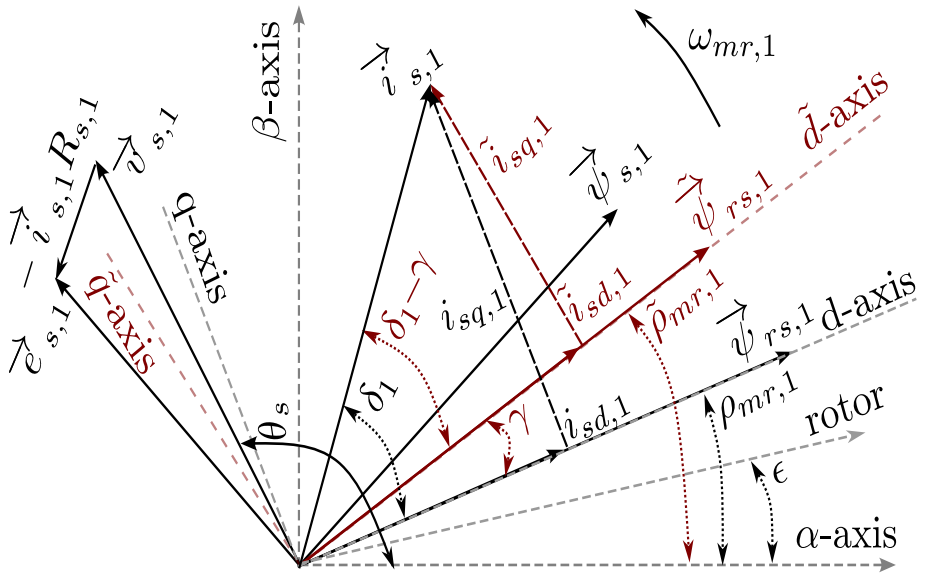


FIGURE 5.7: Inaccuracy in ρ_{mr} estimation

deviates from $\frac{\pi}{2}$. This deviation depends upon the ratio, $\frac{\omega_{mr,1}}{\omega_o}$ as shown in (5.10). Thus, the difference between the angle of actual flux and estimated flux can be written as

$$\gamma = 90^o - \tan^{-1}\frac{\omega_{mr,1}}{\omega_o} \tag{5.11}$$

Thus, it can be inferred that for $\omega_{mr,1} >> \omega_o$, $\gamma \approx 0$. Thus, during higher operating frequencies, $\overrightarrow{\psi}_s$ is more accurately estimated. Consequently, the accuracy of $\tilde{\omega}_m$ is fairly good.

On the other hand, when $\omega_{mr,1}$ is low, θ becomes much lower than $\frac{\pi}{2}$. The value of γ is significant when $\omega_{mr,1}$ becomes lower than ω_o. Thus, it is preferred to keep ω_o low. However, keeping a very low value of ω_o, would lead to a very slow decay of the transient term in (5.9). This, too, leads to incorrect estimation of $\overrightarrow{\psi}_{s,1}$. Moreover, for any non-zero small value of ω_o, there will exist a phase-error in the estimated flux during low-speed operation where $\omega_{mr,1} < \omega_o$.

The phase-error in estimation of $\overrightarrow{\psi}_{s,1}$ leads to subsequent phase-error in $\overrightarrow{\psi}_{rs,1}$ as can be seen from (5.5). This is depicted in Fig. 5.7. The phasor quantities shown in black are the actual positions of the respective quantities whereas those depicted in red color are incorrectly estimated positions. It can be seen that due to incorrectly

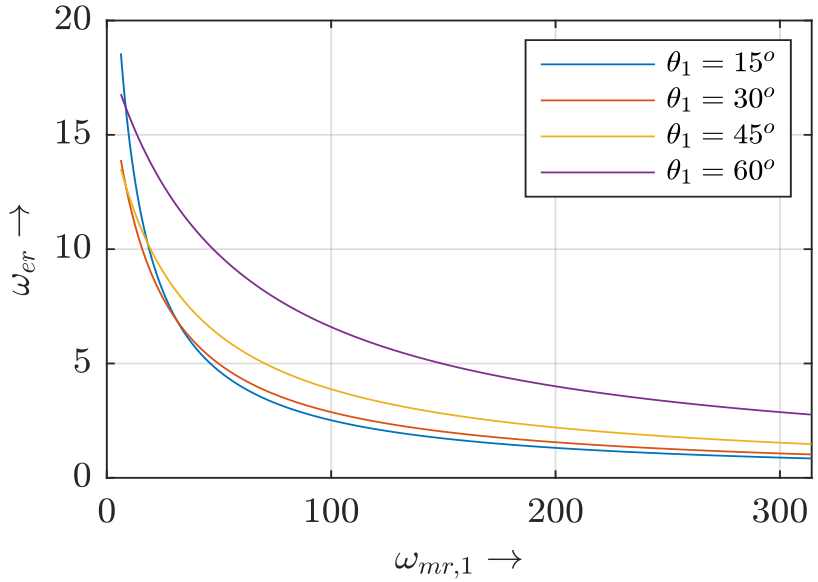


FIGURE 5.8: Variation in ω_{er} with $\omega_{mr,1}$

estimated angle, $\tilde{\rho}_{mr,1}$, the d and q-components of $\overrightarrow{i}_{s,1}$ would be wrongly estimated. Thus, the slip-speed, $\tilde{\omega}_{sl,1}$ calculation using (5.6) will be incorrect and so will be the estimation of $\tilde{\omega}_m$.

As flux developed in the machine settles down, $i_{sd,1}$ becomes equal to $i_{mr,1}$. Thus, the correct value of slip would correspond to the ratio between $i_{sq,1}$ and $i_{sd,1}$ (Fig. 5.7). This ratio can be written as $\tan(\delta_1)$ where δ_1 is the angle between $\overrightarrow{i}_{s,1}$ and $\overrightarrow{\psi}_{rs,1}$. However, in case of incorrect value of slip, $\tilde{\omega}_{sl,1}$ estimated using $\tilde{i}_{sq,1}$ and $\tilde{i}_{sd,1}$, the angle $\delta_1 - \gamma$ (Fig. 5.7) will be accounted. This is shown below.

$$\omega_{sl,1} = \frac{\tan(\delta_1)}{T_{r,1}}; \qquad \tilde{\omega}_{sl,1} = \frac{\tan(\delta_1 - \gamma)}{T_{r,1}} \tag{5.12}$$

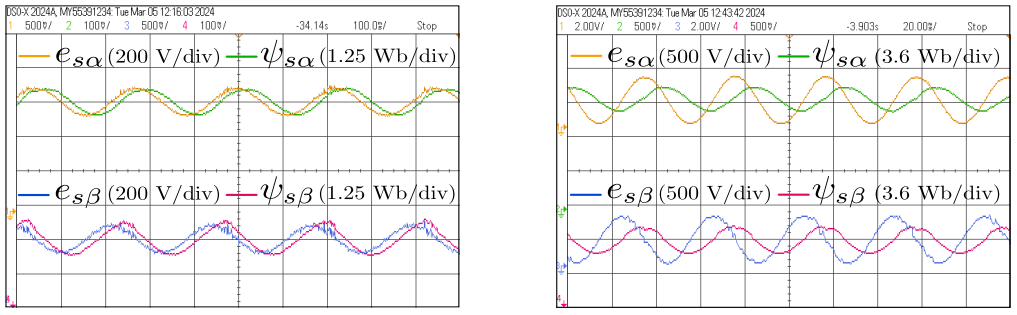
Thus, the error in slip-speed, ω_{er} can be simplified as

$$\omega_{er} = \omega_{sl} - \tilde{\omega}_{sl} = \frac{\tan(\delta_1) - \tan(\delta_1 - \gamma)}{T_{r,1}} \tag{5.13}$$

Substituting the value of γ from (5.11) in (5.13) and using trigonometric identities, ω_{er} can be written as

$$\omega_{er} = \frac{1}{T_{r,1}} \frac{\tan\delta_1 + \cot\delta_1}{1 + \frac{\omega_{mr,1}}{\omega_o} \cot\delta_1} \tag{5.14}$$

The variation of ω_{er} with $\omega_{mr,1}$ is shown in Fig. 5.8 for different values of θ_1, which is a direct indicator of the load on the motor. It can be seen that ω_{er} falls



(A) (B)

FIGURE 5.9: Experimentally obtained $\alpha - \beta$ components of $\overrightarrow{e}_s$ and estimated $\overrightarrow{\psi}_s$ when the drive operates at (a) $f_s = 4$ Hz [x-axis scale: 100 ms/div] (b) $f_s = 24$ Hz [x-axis scale: 20 ms/div].

steeply with $\omega_{mr,1}$ which again indicates towards the improvement in accuracy of $\tilde{\omega}_m$ at higher operating frequencies.

Further, the inaccuracy in estimation of $\overrightarrow{\psi}_s$ is experimentally validated and shown in Fig. 5.9. An SCIM is run at $\omega_{mr,1} = 8\pi$ rad/s using sensorless FOC using $\omega_o = 10\pi$ rad/s. $\psi(t)_{s,x}$ and $e(t)_{s,x}$ where $x \in (\alpha, \beta)$ are shown in Fig. 5.9a. It can be seen that $\psi(t)_{s,x}$ is nearly in phase with $e(t)_{s,x}$ which is highly inaccurate. $e(t)_{s,x}$ shown in the figure is obtained by subtracting the stator resistance drop from the stator voltages. Thus, the phase-shift between the two signals should be exactly $\frac{\pi}{2}$ as the deviation due to resistance drop will be zero. The same setup is run at $\omega_{mr,1} = 48\pi$ rad/s and shown in Fig. 5.9b. Here, $\psi(t)_{s,x}$ can be seen lagging $e(t)_{s,x}$ by almost $\frac{\pi}{2}$. Thus, it is established that speed-estimation using the voltage model of SCIM works fairly accurately at high speed whereas it is not so at low speed.

5.3.4 Design of the PLL

As stated earlier, the erroneously estimated speed, $\tilde{\omega}_m$ is added to the output of the PI controller present in the PLL in order to improve the performance of the PLL. Thus, it is imperative to include this variable in the design of this PLL. In this direction, $\tilde{\omega}_m$ is required to be obtained as a function of ω_m^{est}. $\tilde{\omega}_m$ can be obtained by adding ω_{er} and ω_m^{est}. (5.14) gives ω_{er} as function of $\omega_{mr,1}$. Thus, $\omega_{mr,1}$ can be substituted as the sum of ω_{est} with $\omega_{sl,1}$ in (5.14). Further, $\omega_{sl,1}$ can be written as $\frac{\tan\delta_1}{T_r}$. Thus, mathematically it can be represented as,

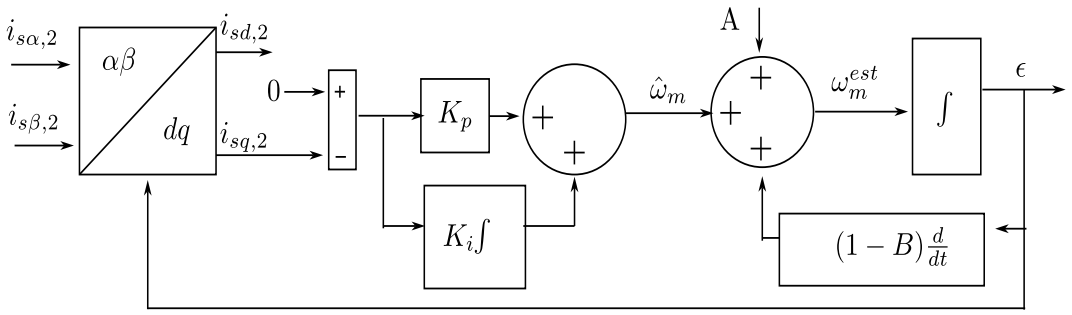


FIGURE 5.10: Control block diagram for PLL with $\tilde{\omega}_m$

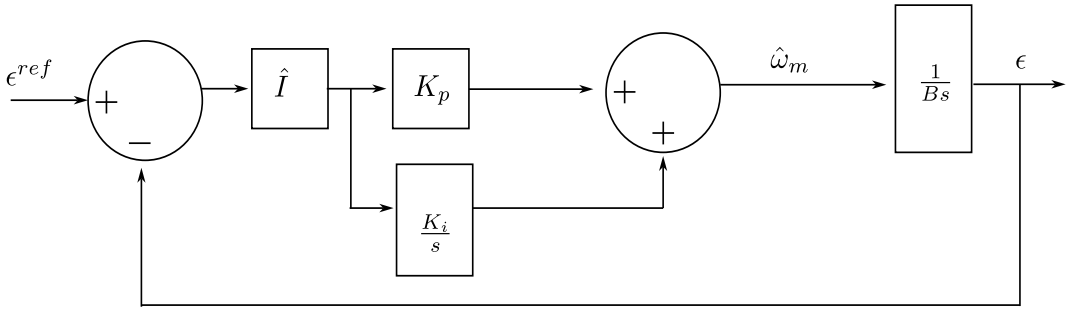


FIGURE 5.11: Small signal model for PLL

$$\omega_{mr,1} = \omega_{est} + \omega_{sl,1} = \omega_{est} + \frac{\tan\delta_1}{T_r} \tag{5.15}$$

Substituting this value of ω_{mr} in (5.14), ω_{er} can be written in terms of ω_m^{est} as shown below

$$\omega_{er} = \frac{1}{T_{r,1}}\left(\frac{\tan\delta_1 + \cot\delta_1}{1 + \frac{1}{\omega_o T_{r,1}} + \frac{\cot\delta_1}{\omega_o}\omega_m^{est}}\right) \tag{5.16}$$

As, ω_{er} is obtained as a function of ω_m^{est}, $\tilde{\omega}_m$ can be then further written as

$$\tilde{\omega}_m = \omega_m^{est} + \frac{1}{T_{r,1}}\left(\frac{\tan\delta_1 + \cot\delta_1}{1 + \frac{1}{\omega_o T_{r,1}} + \frac{\cot\delta_1}{\omega_o}\omega_m^{est}}\right) \tag{5.17}$$

(5.17) is a non-linear function of $\tilde{\omega}_m$ in ω_m^{est}. However, since this PLL is operational only in SCM, that is low-speed range, (5.17) can linearized about $\omega_m^{est} = 0$ using Taylor's approximation as shown below.

$$\tilde{\omega}_m = A + (1 - B)\omega_m^{est} \tag{5.18}$$

The coefficients A and B are given as,

$$A = \frac{\tan\delta_1 + \cot\delta_1}{T_{r,1} + \frac{1}{\omega_o}}; \quad B = \frac{T_{r,1}\omega_o \mathrm{cosec}^2\delta_1}{(1 + T_{r,1}\omega_o)^2} \tag{5.19}$$

Using (5.18), Fig. 5.5 can be modified into Fig. 5.10. The constant A can be eliminated using feedforward compensation. Thus, the small-signal model pertaining to the PLL as shown in Fig. 5.11 is obtained from the block diagram of Fig. 5.10. Further, i_{sq} can be normalized with respect to the magnitude of the current and $\hat{I}$ becomes equal to 1. With this, the loop-gain (G_{ol}^{PLL}) and closed-loop transfer function (G_{cl}^{PLL}) of the PLL are given by (5.20).

$$G_{ol}^{PLL} = \frac{K_p s + K_i}{B s^2}; \quad G_{cl}^{PLL} = \frac{\frac{K_p}{B} s + \frac{K_i}{B}}{s^2 + \frac{K_p}{B} s + \frac{K_i}{B}} \tag{5.20}$$

The closed-loop transfer function given in (5.20) pertains to a second-order system and the value of K_p and K_i can be obtained by choosing a suitable bandwidth, ω_{bw} and damping coefficient, ζ. Since the PLL under consideration is used to determine the speed of the drive, ω_{bw} can be kept sufficiently low as mechanical quantities like speed do not undergo rapid changes. Further, ζ is kept high, in order to mitigate any adverse effects of the ripple components of the current. Thus, ζ is taken as 5 and ω_{bw} is kept at 10π rad/s.

The parameter B is dependent on rotor time constant of motor 1, $T_{r,1}$ and the angle δ_1. This angle is computed from the nominal values of $i_{sq,1}$ and $i_{mr,1}$ while designing the PLL. The value of δ_1 comes around 70^o. However, this angle changes with load. Thus, the performance of the PLL has to be established as δ_1 varies. Further, effect of variation in $T_{r,1}$ on the closed-loop performance of the PLL is investigated next.

5.3.5 Impact of Variation in $T_{r,1}$ and δ_1 on the Closed-Loop Performance of the PLL

As stated earlier, the parameter B in the transfer function of the PLL is dependent on both δ_1 and $T_{r,1}$. δ_1 varies with load whereas $T_{r,1}$ may vary because of variation in rotor resistance, $R_{r,1}$. As the drive is operated for long duration, rise in temperature leads to change in $R_{r,1}$. Thus, it is imperative to analyse the impact of the variation of these parameters on the closed-loop performance of the PLL. The bode-plots pertaining to the loop gain, G_{ol}^{PLL}, with different values of B corresponding to different

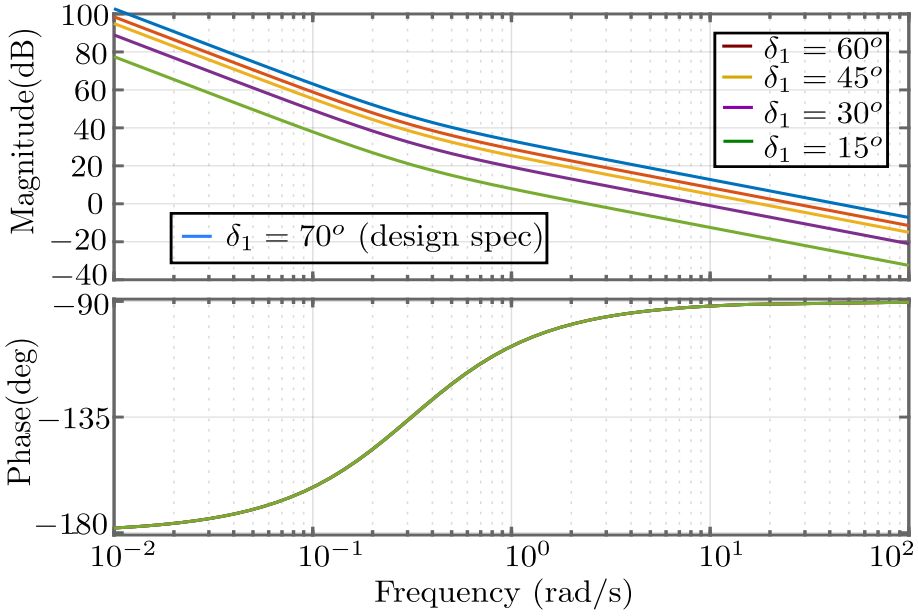


FIGURE 5.12: Bode plot of G_{ol}^{PLL} for variation in δ_1

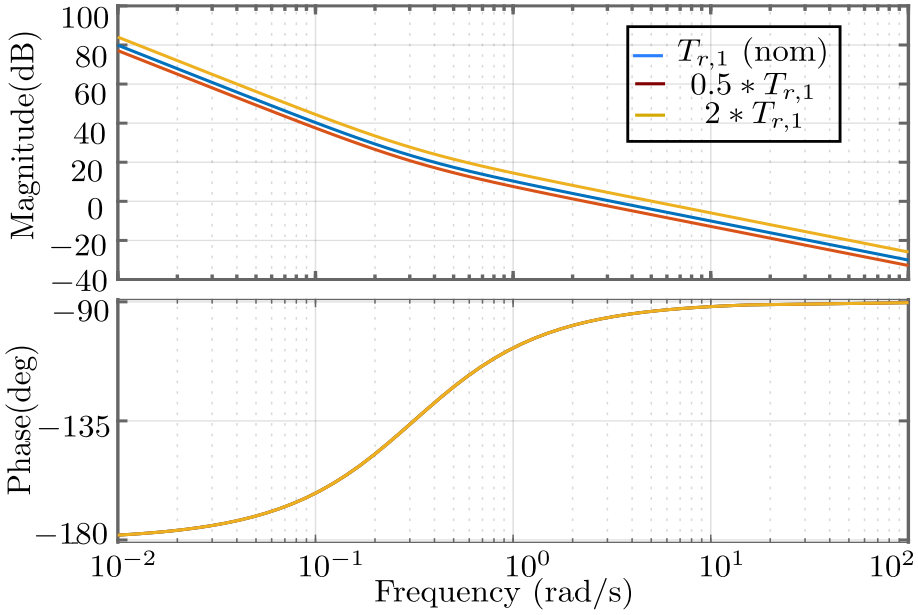


FIGURE 5.13: Bode plot of G_{ol}^{PLL} for variation in $T_{r,1}$

values of δ_1 are shown in Fig. 5.12. The controller gains, K_p and K_i are kept to be same in each case corresponding to the design specification. It can be seen in Fig. 5.12, as δ_1 reduces the magnitude plot shifts towards left. However, the phase-plot remains the same. This indicates that the gain cross-over frequency reduces as δ_1 comes down. However, since the phase plot is almost flat in that frequency range, the phase margin remains almost the same. This guarantees stability of the PLL as δ_1 reduces. However, the response of the PLL might get slower. However, since the PLL tracks the speed of the drive which is a mechanical quantity, a slower response does not significantly impact its performance. This is further verified through experiments in a later section.

The rotor time constant, $T_{r,1}$, is defined as the ratio between rotor inductance and rotor resistance. Rotor resistance changes with rise in temperature as the drive is operated for a long duration. Thus, impact of the variation in $T_{r,1}$ on the performance of the PLL is analysed next. The bode-plot of G_{ol}^{PLL} corresponding to three cases, with nominal value of $T_{r,1}$, half the value of $T_{r,1}$ and twice the value of $T_{r,1}$ is plotted and shown in Fig. 5.13. As $T_{r,1}$ reduces, the gain cross-over frequency comes down making the system slower. However, in this case the change in gain cross-over frequency is so small, that it will have insignificant impact on the closed-loop performance of the PLL.

Both the parameters, $T_{r,1}$ and δ_1 are varied and the bandwidth of the closed-loop transfer function of the PLL, G_{cl}^{PLL} is plotted in Fig. 5.14. It can be seen that the bandwidth reduces as both $T_{r,1}$ and δ_1 reduce. This aligns with the previously done analysis where the gain cross-over frequency of G_{ol}^{PLL} was reducing with both of these parameters.

Further, the loop transfer function pertaining to the PLL has no dependence on the stator resistance, $R_{s,1}$ and parameters of the second motor like its stator and rotor-resistance. Thus, it is expected that any variation in these parameters will have insignificant impact on the performance of the PLL. The impact of variation in both rotor and stator resistance on the performance of the drive is validated

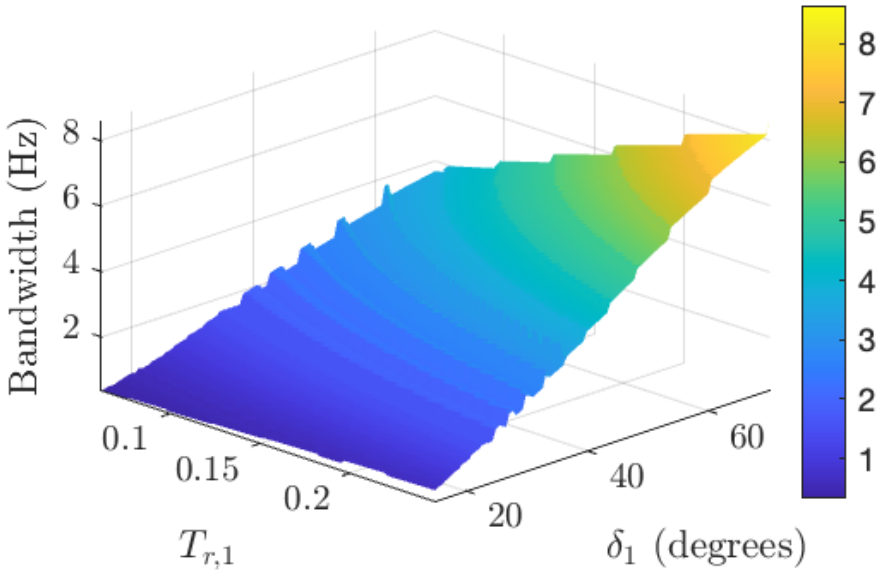


FIGURE 5.14: Variation in bandwidth of the G_{cl}^{PLL} with δ_1 and $T_{r,1}$

experimentally later.

5.3.6 Control of DMDS in SCM

The conventional method of maintaining $i_{sq,2}$ at zero is to use a PI controller with reference q-axis current, $i^*_{sq,2} = 0$. However, if the stator of motor 2 is supplied with a three-phase voltage of frequency, $\omega_{mr,2}$ which is maintained same as the mechanical speed of the rotor i.e. ω_m, then $\omega_{sl,2}$ will become zero. As a result of this, $i_{sq,2}$ will also be zero as shown below,

$$\omega_{mr,2} - \omega_m = \omega_{sl,2} = \frac{1}{T_{r,2}} \frac{i_{sq,2}}{i_{mr,2}} = 0 \tag{5.21}$$

The total current flowing through the stator of motor 2 will be used to establish the flux. $i_{sd,2}$ can be controlled at its rated value using a PI controller which gives the d-component $v_{sd,2}$, of the voltage vector, $\overrightarrow{v}_{s,2}$. The corresponding q-component $v_{sq,2}$, should be equal to the magnitude of the back-emf due to the developed flux. This is equal to the feedforward terms as shown below;

$$v_{sq,2} = v^{ff}_{sq,2} = \sigma L_s \omega^{est}_m i_{sd,2} + (1-\sigma) L_s \omega^{est}_m i_{mr,2} \tag{5.22}$$

Thus, the required modifications to be done in the control algorithm of motor 2 in SCM are

1. The stator frequency of motor 2 is set to be same as the estimated mechanical frequency by making $\omega_{mr,2} = \omega_m^{est}$.
2. The q-axis voltage, $v_{sq,2}$ for motor 2 should just be equal to the feedforward terms.
3. The d-axis voltage, $v_{sd,2}$ for motor 2 is obtained as usual using a PI controller with suitable feedforward compensation.

5.3.7 Transition from SCM to TSM

As the mechanical speed of the drive becomes greater than 1.5-2 times ω_o, the accuracy of $\tilde{\omega}_m$ improves. Thus a cutoff frequency, $\omega_c = 1.5\omega_o$ is set. Beyond ω_c, the mode of operation of the drive is changed from SCM to TSM. This is achieved by making $\hat{\omega}_m = 0$ in the speed estimation algorithm as shown in Fig. 5.6. Simultaneously, the PI controller pertaining to $i_{sq,2}$ is modified to give voltage as output. Moreover, slip of motor 2, $\omega_{sl,2}$ is included in the estimation of $\omega_{mr,2}$ and $\rho_{mr,2}$. As this happens, $i_{sq,2}$ is made zero by controlling $v_{sq,2}$. The output of $i_{sq,2}$ controller is added to the feedforward terms to get the q-axis voltage, $v_{sq,2}$. After this transition, $i^*_{sq,2}$ may remain zero for a while. As the speed increases beyond ω_t, motor 2 is required to produce torque and $i^*_{sq,2}$ becomes non-zero. All the changes required to be done in the control algorithm of motor 2 are highlighted by a change of color in Fig. 5.3 and Fig. 5.6.

5.3.8 Power Flow Analysis

It is also imperative to analyse the flow of electric power through motor 1 and motor 2 when the drive operates in SCM. The input electric power, P_{in}, is divided into stator losses, P_{loss}^{stator} and air-gap power, P_{ag}, which is further divided into rotor losses, P_{loss}^{rotor} and mechanical output-power, P_{out}^{mech} (5.18). P_{out}^{mech} also consists of all the mechanical losses occurring in the drive.

$$\begin{aligned} P_{in} &= P_{loss}^{stator} + P_{ag} \\ P_{ag} &= P_{loss}^{rotor} + P_{out}^{mech} \end{aligned} \tag{5.23}$$

However, P_{out}^{mech} for motor 2 will be zero when the drive is in SCM. This is because it neither produces any output mechanical torque nor it supplies to any mechanical

losses. This is because of the fact that, the torque angle δ_2 for motor 2, is made zero. Moreover, the rotor speed and stator-supply frequency of motor 2 are kept the same during SCM. As a result, there will be no EMF induced in its rotor and consequently rotor current in motor 2 will be zero. As a result, P_{loss}^{rotor} for motor 2 will also be zero. Thus, P_{ag} will be zero for motor 2 and the P_{in} drawn by motor 2 will just be used supply its P_{loss}^{stator} as shown below.

$$P_{in,2} = P_{loss,2}^{stator} \tag{5.24}$$

Although a dual motor drive system is discussed in this chapter, the proposed speed estimation technique can easily be extended to an IM based multi-motor drive. In an MMDS, the stator current of any one of the freewheeling motors can be used to implement the PLL to correct the speed estimated using the voltage model of any one of the torque producing motors. Thus, the proposed technique works for a multi-induction motor drive.

5.4 Torque-sharing strategy for minimum copper loss

During TSM, a suitable torque-sharing strategy is required to be developed in order to distribute the total load torque demand into the two individual motors in a DMDS, specially under reduced load conditions. The objective for the torque-sharing strategy developed in this section is to reduce the total copper losses occurring in the DMDS. The core-loss occurring in an IM drive mainly depends on its operating frequency [38], which further depends on the speed of the drive. Thus, the core loss becomes nearly constant at a certain speed. However, the total copper losses can be minimized by optimally distributing the load torque between two motors.

The copper-loss occurring in the individual IM, $P_{loss,i}^{cu}$, can be divided into rotor copper loss and stator copper loss. Thus, the same can be estimated using the d-q components of the stator ($i_{sd,i}$ and $i_{sq,i}$) and rotor current ($i_{rd,i}$ and $i_{rq,i}$) of individual motors as shown below,

$$P_{loss,i}^{cu} = R_{s,i}(i_{sd,i}^2 + i_{sq,i}^2) + R_{r,i}(i_{rd,i}^2 + i_{rq,i}^2), \;\; i \in 1, 2 \tag{5.25}$$

Here, $R_{s,i}$ and $R_{r,i}$ are the stator and rotor resistance of the individual motors respectively. However, for a rotor flux oriented vector controlled drive, $i_{rd,i} = 0$ and $i_{sq,i}$ and $i_{rq,i}$ are related to each other as,

$$i_{rq,i} = \frac{L_{m,i}}{L_{r,i}} i_{sq,i} \tag{5.26}$$

Here, $L_{m,i}$ and $L_{r,i}$ are the mutual and rotor inductances of the individual motors respectively. Using these relations, (5.25) can be further simplified as

$$P^{cu}_{loss,i} = R_{s,i} i^2_{sd,i} + (R_{s,i} + R_{r,i} \frac{L^2_{m,i}}{L^2_{r,i}}) i^2_{sq,i} \tag{5.27}$$

The total copper-loss, $P^{cu}_{loss,tot}$ can be modelled as

$$P^{cu}_{loss,tot} = \sum_{i=1,2} [R_{s,i} i^2_{sd,i} + (R_{s,i} + R_{r,i} \frac{L^2_{m,i}}{L^2_{r,i}}) i^2_{sq,i}] \tag{5.28}$$

The motors are generally operated at rated flux below the base speed. This is done in order to achieve maximum torque per ampere (MTPA) operation of the motors [81]. Thus, $i_{sd,i}$ for the individual motors is kept constant. Hence, in order to minimize $P^{cu}_{loss,tot}$, the term pertaining to $i_{sq,i}$ has to be minimized. Moreover, the minimization of this term must happen under the torque constraint as explained next.

The total torque demand, m^*_d, from the multi-motor drive system comes as the output of a speed controller. This torque reference is then divided into the torque reference of individual motors, $m^*_{d,i}$, $i = 1, 2$. Thus, the torque produced by the individual motors must satisfy the constraint

$$m^*_d = \sum_{i=1,2} m^*_{d,i} \tag{5.29}$$

Here, $m^*_{d,i}$ is the torque produced by individual motors and is given by

$$m^*_{d,i} = \frac{2}{3} \frac{P}{2} \frac{L^2_{m,i}}{L_{r,i}} i_{mr,i} i_{sq,i} \tag{5.30}$$

Since, $i_{mr,i}$ remains constant, the constraint presented in (5.29) can directly be written in terms of $i_{sq,i}$ as

$$m^*_d = \sum_{i=1,2} \beta_i i_{sq,i} \tag{5.31}$$

Here, $\beta_i = \frac{2}{3} \frac{P}{2} \frac{L^2_{m,i}}{L_{r,i}} i_{mr,i}$.

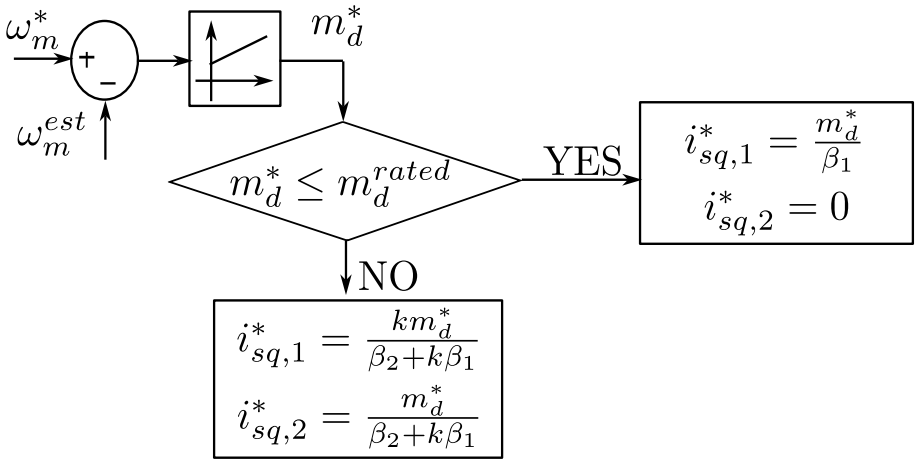


FIGURE 5.15: Flowchart depicting the torque sharing strategy.

Thus the torque sharing strategy can be framed as a minimization of a loss function, L, under the torque constraint as shown below

$$\begin{aligned} &\text{Minimize:} \qquad L = \sum_{i=1,2} \alpha_i i_{sq,i}^2 \\ &\text{Constraint:} \qquad m_d^* = \sum_{i=1,2} \beta_i i_{sq,i} \end{aligned} \tag{5.32}$$

Here, $\alpha_i = R_{s_i} + R_{r_i} \frac{L_{m,i}^2}{L_{r_1}^2}$.

The loss function, L can be written in terms of only $i_{sq,1}$ and a minima can be obtained by differentiating it with respect to $i_{sq,1}$ and equating the result to zero as shown below

$$\frac{dL}{di_{sq,1}} = \frac{d[\alpha_1 i_{sq,1}^2 + \frac{\alpha_2}{\beta_2^2}(m_d^* - \beta_1 i_{sq,1})^2]}{di_{sq,1}} = 0 \tag{5.33}$$

Solving the above equation, the optimal ratio, k, between $i_{sq,1}$ and $i_{sq,2}$ for minimum copper loss under the torque constraint is thus obtained as

$$\frac{i_{sq,1}}{i_{sq,2}} = k = \frac{\alpha_2 \beta_1}{\alpha_1 \beta_2} \tag{5.34}$$

If the two motors in the dual-motor drive are identical, then k becomes 1 which implies equal torque sharing would lead to minimum $P_{loss,tot}^{cu}$ in a dual motor drive. However, if the motors are non-identical, the individual q-axis current reference can be written as

$$i_{sq,1}^* = \frac{km_d^*}{\beta_2 + k\beta_1} \qquad i_{sq,2}^* = \frac{m_d^*}{\beta_2 + k\beta_1} \tag{5.35}$$

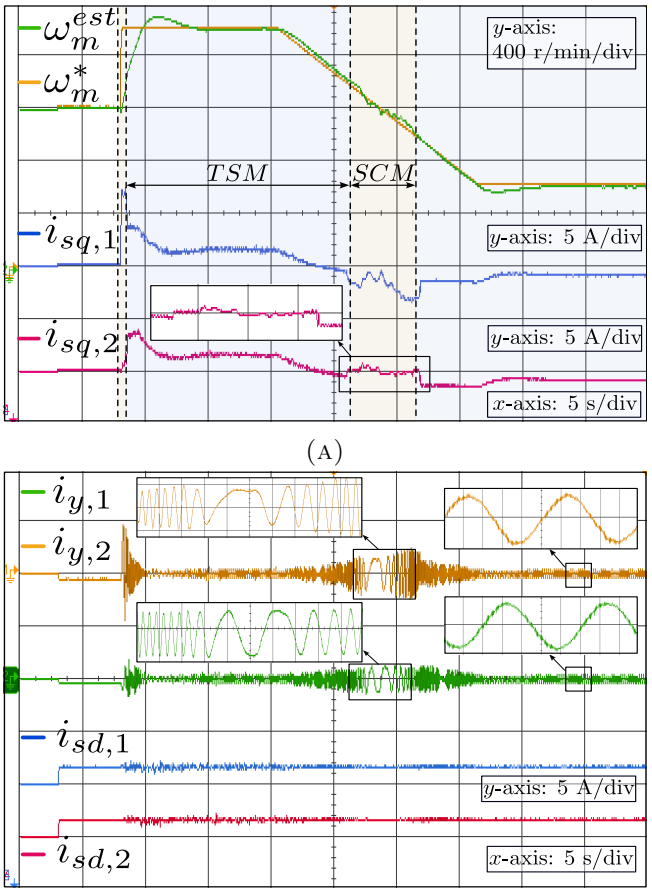


FIGURE 5.16: Experimentally obtained (a) ω_m^*, ω_m^{est} , $i_{sq,1}$ and $i_{sq,2}$ (b) $i_{y,1}$ and $i_{y,2}$ and $i_{sd,1}$ and $i_{sd,2}$ for motor 1 and 2 for a positive speed command of $\omega_m^* =$ 600 r/min followed by reversal command upto $\omega_m^* = -600$ r/min.

The flowchart presented in Fig. 5.15 elucidates the torque sharing strategy developed above. When the load-torque demand is less than the rated torque of individual motors, m_d^{rated}, only one of the two motors supply the load torque. This happens in SCM and initial part of TSM. However, when the torque demand becomes greater than m_d^{rated}, it is divided among the two motors as per the ratio obtained before.

5.5 Validation of Proposed Algorithm

The proposed speed estimation technique is experimentally validated on a drive system where two induction motors are coupled together in the same shaft. The complete experimental setup is shown in Appendix 7 (Fig.4). The two motors are

TABLE 5.1: Controller parameters

	K_p	K_i
PLL	5.7523	1.8071
Speed Controller	1.7767	3.4885
Current Controller	11.7698	102.22

marked as IM-1 and IM-2 in the figure. The dual-motor drive is coupled with a DC machine which can be operated as generator in order to load the complete drive. The parameters of both the IMs are given in Appendix 7 (Table 3). Although both induction motors have the same power rating and manufacturer, their parameters differ slightly. Both the motors are connected to separate IGBT based 2L-VSI from SEMIKRON marked as VSI-1 and VSI-2. A common DC bus is created using a three-phase diode bridge rectifier connected to a three-phase auto-transformer. The complete control algorithms for both the motors and speed estimation technique are implemented on TI based TMS320F28379D digital launchpad with inbuilt ADC and EPWM modules. LEM based current sensors (LA-55) are utilised to measure the motor currents. An external four-channel DAC (MAX5250B6APT) is used to visualize the internal signals. Two 4-channel oscilloscopes from KEYSIGHT have been used.

At lower operating speed, IM-1 is controlled to meet the load torque demand and IM-2 freewheels. An LPF with $\omega_o = 2\pi 5$ rad/s is used to estimate $\tilde{\omega}_m$ using the voltage-model of motor 1. Keeping this in mind, the drive is operated in SCM up to $\omega_c = \pm 2\pi 8$ rad/s. Beyond this frequency, the mode is changed to TSM. However, the load torque is shared equally between the two motors when the operating frequency crosses $\omega_t = \pm 2\pi 15$ rad/s. The complete control algorithm consists of four PI controllers, one for the PLL, two for the current loops and one for the speed loop. The values of the proportional constant (K_p) and integral constant (K_i) for these controllers are given in Table 5.1.

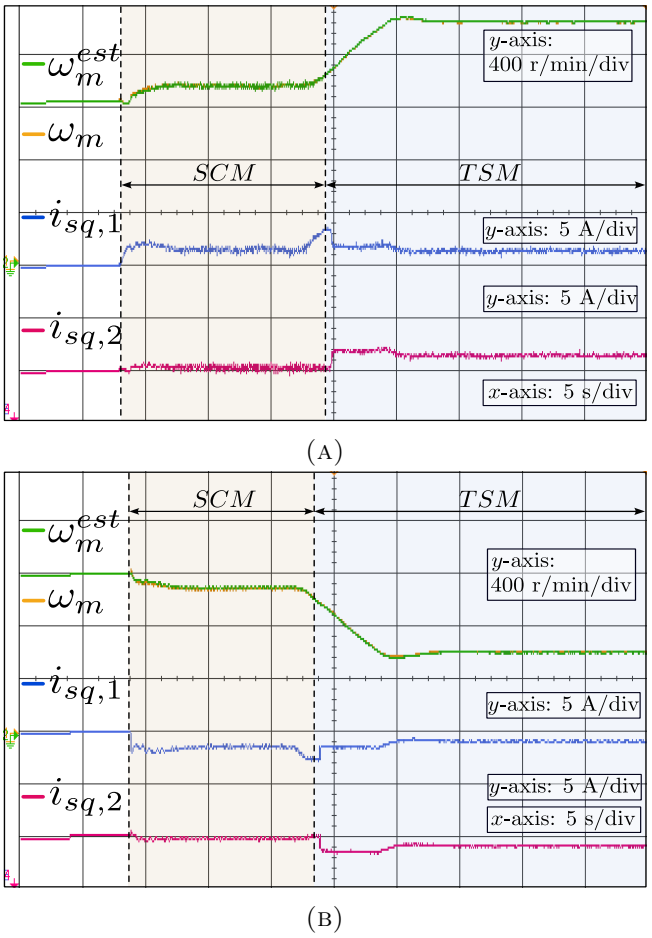


FIGURE 5.17: Experimentally measured ω_m, ω_m^{est}, $i_{sq,1}$ and $i_{sq,2}$ for motor 1 and 2 for a initial speed command of $\omega_m^* = 200$ r/min followed by a speed command of 600 r/min in (a) positive and (b) negative direction.

5.5.1 Smooth Starting and Speed Reversal

In order to establish the smooth starting of the drive, a speed command of 600 r/min is given to the drive. The reference (ω_m^*) and estimated speed (ω_m^{est}), and q-axis currents of both the motors, $i_{sq,1}$ and $i_{sq,2}$ are shown in Fig. 5.16a for $\omega_m^* = 600$ r/min. The y-phase currents, $i_{y,1}$ and $i_{y,2}$ and d-axis currents for both the motors $i_{sd,1}$ and $i_{sd,2}$ are shown in Fig. 5.16b. It can be observed, that as the speed command is given, i_{sq1} reaches an initial high value and i_{sq2} is 0. In this zone, the drive is in SCM and the complete load-torque is supplied by motor 1. Very quickly, i_{sq1} falls and i_{sq2} rises and both of them become equal and the load torque is shared between the two motors. This establishes that the drive starts smoothly as it receives a speed

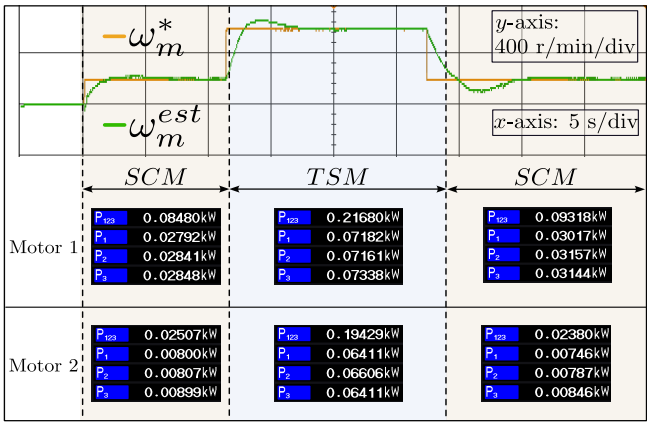


FIGURE 5.18: Active power-flow as the mode changes from SCM to TSM and vice versa.

command. Next, the operation of the drive in negative speed region is established.

As the speed reaches the reference value, a speed reversal command is given in a ramp manner as shown in Fig. 5.16. The reference is set at $\omega_m^* = -600$ r/min. Fig. 5.16a shows that the estimated speed tracks the reference speed which is ramped down. As the speed falls below ω_c, the drive automatically goes to SCM from TSM. This can be observed from $i_{sq,2}$ as it becomes zero. As the speed rises in the negative direction, the mode of operation of the drive again changes from SCM to TSM. The phase currents and d-axis currents for both the motors remain stable throughout as seen in Fig. 5.16b.

5.5.2 Smooth Operation in SCM and Transition to TSM

Smooth operation of the drive both during SCM and during the transition between SCM and TSM is established in Fig. 5.17. In order to establish the efficacy of the speed estimation algorithm, the actual speed (ω_m) of the drive is measured using an encoder of METRONIX make and shown in Fig 5.17. A low speed command of $\omega_m^* =$ 200 r/min is given initially so that the drive operates in SCM (Fig. 5.17a). During SCM, $i_{sq,2}$ can be seen to be maintained at zero in Fig. 5.17a with the PI controller pertaining to $i_{sq,2}$ deactivated. Both speed, ω_m and ω_m^{est} overlap each other. This establishes the accuracy of the speed-estimation algorithm. Following this, in order to initiate the transition to TSM, the speed command is increased to $\omega_m^* = 600$ r/min.

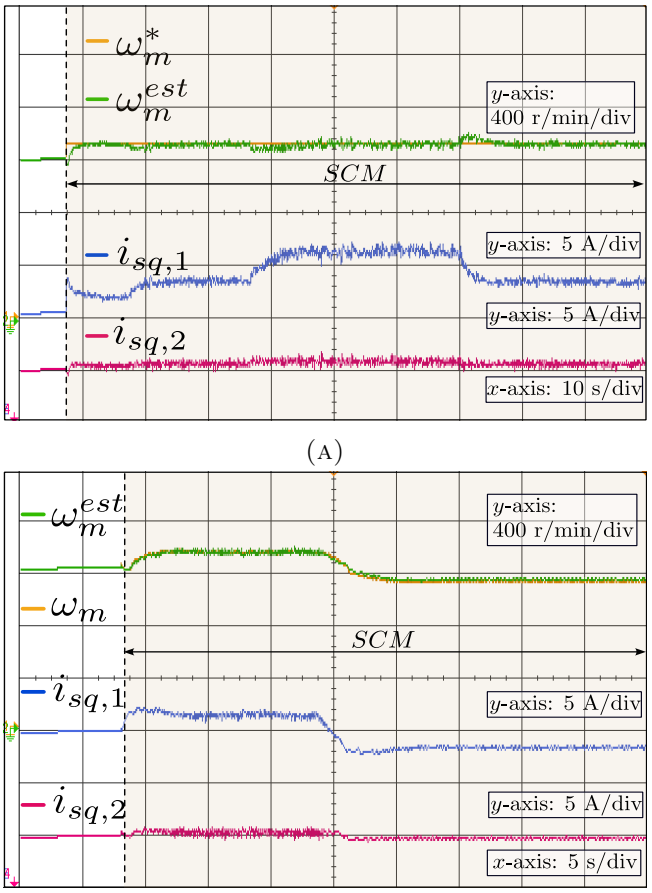


FIGURE 5.19: (a) Experimentally measured ω_m^*, ω_m^{est}, $i_{sq,1}$ and $i_{sq,2}$ during load dynamics at low speed (b) ω_m, ω_m^{est}, $i_{sq,1}$ and $i_{sq,2}$ during speed reversal command at low speed.

As the transition from SCM to TSM happens, $i_{sq,2}$ increases. The transition happens very smoothly with no disturbance in speed or q-axis current as seen in Fig. 5.17a. It is also imperative to establish the effectiveness of the same in negative direction of speed. The same is shown in Fig. 5.17b. The same sequence of operations are performed but in negative direction and the performance of the drive can be seen to be smooth.

In order to validate the analysis done regarding the active power flow through the two machines during SCM and TSM, the drive is operated first with $\omega_m^* = 200$ r/min (SCM mode) and then with $\omega_m^* = 600$ r/min (TSM mode) and then again setting ω_m^* back to 200 r/min. The three-phase active power flowing through each

machine is measured using a power analyser from HIOKI (PW6001). The total active power (P_{123}) and power through each phases (P_1, P_2, P_3) for both the motors under steady-state are shown in Fig. 5.18. It can be seen that at low speed (SCM), the power flowing through IM-2 ($\approx$ 25 W) is smaller compared to motor 1 ($\approx$ 90 W). However, at higher speed (TSM), power flow through them becomes equal ($\approx$ 200 W). Thus, this validates the conclusion that during SCM, most of the active power flows through motor 1 and motor 2 only draws the small power pertaining to the stator resistive losses. While, in TSM the active power is almost equally shared.

5.5.3 Low-Speed Operation of the Drive

Since the proposed algorithm improves the low-speed operation of the drive, extensive experiments have been conducted to establish its effectiveness in the low-speed region as shown in Fig. 5.19. The performance of the drive under load dynamics while it operates in SCM is shown in Fig. 5.19a. For a speed command of 200 r/min (SCM), a load torque of 0.2 pu is initially applied and then later removed. It can be seen in Fig. 5.19a, that in this region of operation, complete load torque is developed by motor 1 as the drive is in SCM. This is clearly established in Fig. 5.19a as only $i_{sq,1}$ rises and falls with the load. $i_{sq,2}$ is controlled at zero throughout. Further, another interesting aspect to be noted is that as the drive is loaded in SCM, the angle δ_1 changes. Thus, the performance of the PLL with change in δ_1 remains satisfactory as established analytically in previous section.

Another aspect of interest during the low speed region is the performance of the drive during speed reversal from a low positive value of speed to a low negative value of the speed. The same is shown in Fig. 5.19b. Here, the drive is initially started with a positive speed reference of $\omega_m^* = 200$ r/min. Then after sometime, a speed reversal command is given for $\omega_m^* = -100$ r/min. The measured speed using an encoder is shown along with the estimated speed in Fig. 5.19b. This is done in order to further establish the accuracy of the speed-estimation technique mainly in the low speed region. $i_{sq,1}$ can be seen to be changing from positive to negative. However, $i_{sq,2}$ is maintained at zero throughout.

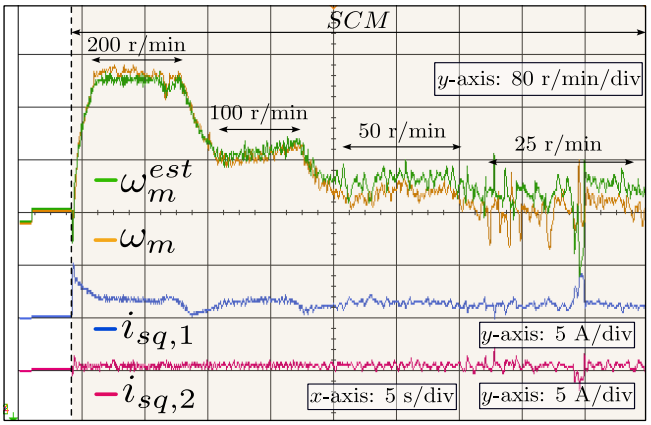


FIGURE 5.20: Performance of the drive with successive low speed command.

In order to experimentally determine the lowest speed upto which the performance of the PLL remains satisfactory, the drive is started with $\omega_m^* = 200$ r/min and then its value is successively reduced to 100 r/min, 50 r/min and then finally to 25 r/min. Estimated and actual speed of the drive and q-axis currents of both the motors are presented in Fig. 5.20. It can seen in the figure that the performance of the speed estimation technique remains reasonably well till 100 r/min. However, the same deteriorates at about 50 rpm and 25 r/min with disturbances in both actual and estimated speed. Thus, it can concluded that the speed estimation technique works satisfactorily till about 100 r/min which is quite low.

5.5.4 Comparison with Conventional Sensorless Algorithm

The performance of the proposed algorithm is experimentally compared with the performance of conventional sensorless algorithm and the result is presented in Fig. 5.21. Here, the speed of such a dual-motor drive when operated with conventional sensorless algorithm where the speed is estimated using just the voltage model of one of the motors is shown in the upper half of Fig. 5.21. The reference ω_m^*, estimated ω_m^{est} and actual ω_m speeds are shown in the same figure. It is observed that with the conventional algorithm, even though ω_m^{est} can seen to be tracking the ω_m^*, ω_m is not building up in any direction. In the experimental set-up, the motor just vibrates without rotating in any direction. On the other hand, with the proposed algorithm, ω_m and ω_m^{est} both follow each other and they track ω_m^*. In the experimental set-up,

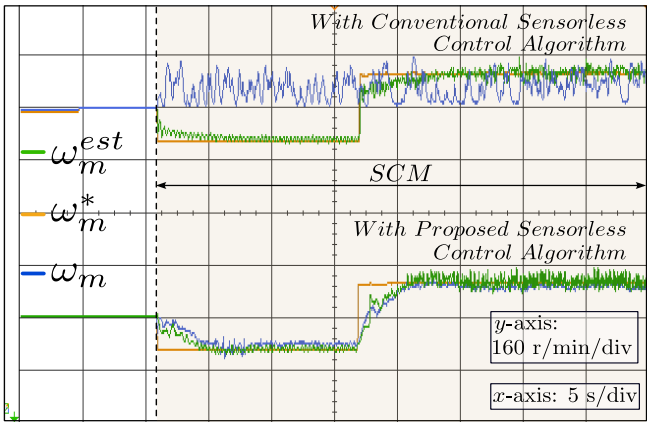


FIGURE 5.21: Experimental comparison of performance between proposed and conventional sensorless algorithm in low speed of operation.

TABLE 5.2: Code execution time

Conventional sensorless control for one motor	8 μs
Conventional sensorless control for DMDS	13.6 μs
Proposed sensorless control for DMDS	14.2 μs

the motor rotates in negative direction and then in positive direction. This clearly establishes the superior performance of the proposed algorithm over conventional sensorless algorithms specially in low-speed region.

Further, it is also important to compare the execution time of the program in one interrupt cycle for the proposed speed estimation algorithm with the conventional speed sensorless algorithm of a single motor and multi-motor drive. Table 5.2 presents the same for all three cases that is, for conventional sensorless control for a single motor and for DMDS and the proposed control algorithm for a DMDS. A difference of about 0.6 μs is observed between the conventional sensorless control and the proposed sensorless control for the DMDS. This can be attributed to the implementation of the PLL which is the only extra feature in the proposed control.

5.5.5 Performance of the Drive Under Load Dynamics

The performance of the drive under load dynamics at near rated speed is shown in Fig. 5.22. This is done to establish the performance of the drive during TSM. The drive is operated at 1000 r/min and almost half rated load is applied and then

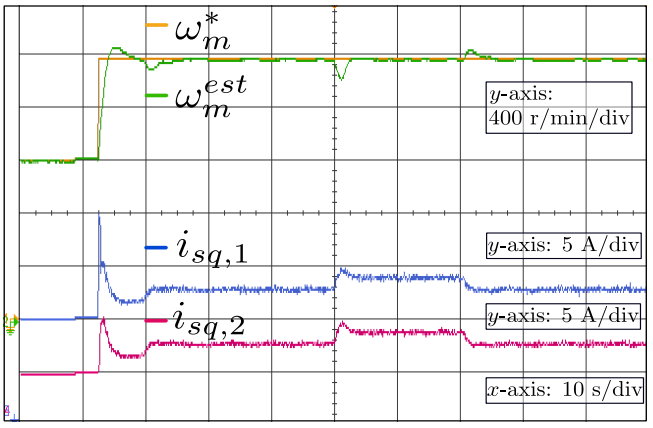


FIGURE 5.22: Experimentally obtained ω_m^*, ω_m^{est}, $i_{sq,1}$ and $i_{sq,2}$ during load dynamics in TSM.

TABLE 5.3: Error in ω_m^{est} with variation in $R_{r,1}$

Percentage Variation in $R_{r,1}$	Error in ω_m^{est}
100%	25 r/min
50%	10 r/min

removed by electrically loading the coupled DC machine. Since the drive is in TSM at this speed, both $i_{sq,1}$ and $i_{sq,2}$ can be seen to be increased with the load and then reduced as the load is removed as shown in Fig. 5.22.

5.5.6 Impact of Parameter Variation on Drive Performance

Impact of the variation in machine parameters, namely, stator and rotor resistances of both the motors, on the performance of the proposed speed estimation technique is experimentally studied in this subsection. It has been established analytically that the effect of variation in $R_{r,1}$, $R_{s,1}$, $R_{r,2}$ and $R_{s,2}$ is insignificant in the performance of the PLL. For all these cases, the drive is first operated with no external load with a speed command of 200 r/min, where the mode of operation is SCM and then the speed command is increased to 600 r/min, which changes the mode to TSM. The performance of the drive with variation in $R_{r,1}$ is shown in Fig. 5.23. In a practical situation, the actual values of resistances may increase due to thermal effects, while the values of these parameters used in the control algorithm may remain lower at their respective nominal values. Thus, in order to emulate a similar situation, the

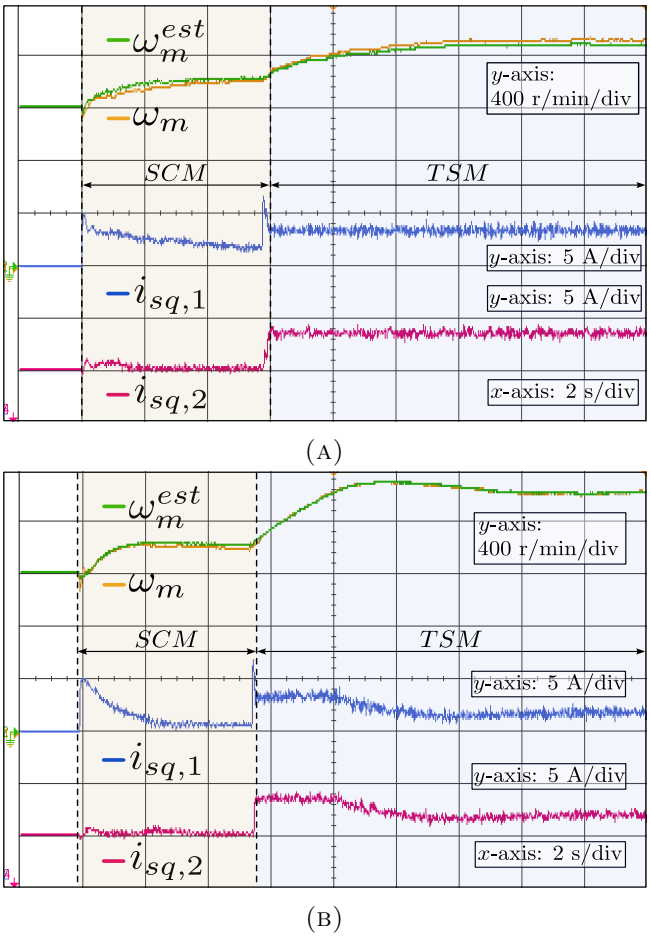


FIGURE 5.23: Performance of the drive with (a) 100% (b) 50% variation in $R_{r,1}$.

value of $R_{r,1}$ used in the control program is reduced to 0.5 times the nominal value. This leads to a 100% variation in the value of the parameter. The response of the drive is shown in Fig. 5.23a. The accuracy of the speed estimation technique is not significantly compromised as ω_m^{est} closely tracks ω_m. A small error of about 25 r/min can be seen between ω_m^{est} and ω_m in Fig. 5.23a.

In order to further validate the impact of the change in $R_{r,1}$, the same experiment is conducted with a 50% change in the value of $R_{r,1}$. This has been done to see if the error in ω_m^{est} reduces with reduction in magnitude of variation in $R_{r,1}$. This is shown in Fig. 5.23b. It can be seen that with 50% change in the value of $R_{r,1}$, the error has reduced significantly. Experimentally the measured error comes out to be only 10 r/min. The error found in ω_m^{est} with various degrees of variation in $R_{r,1}$

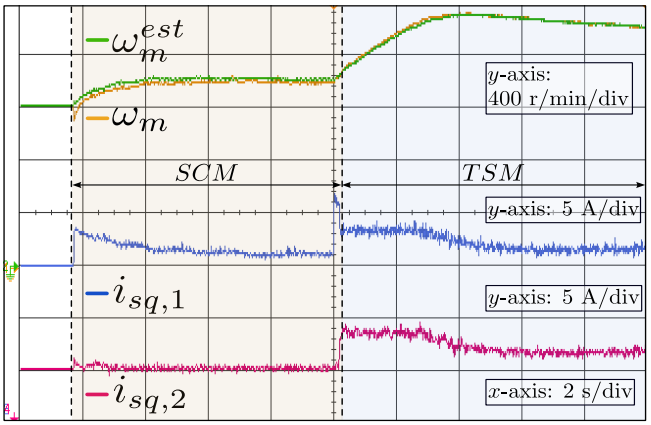


FIGURE 5.24: Performance of the drive with 100% variation in $R_{s,1}$

has been tabulated in Table 5.3. Moreover, it also interesting to note the change in dynamic behaviour of the drive with increased mismatch in $R_{r,1}$. It can be seen that the dynamic response of the drive becomes relatively slower as the error in $R_{r,1}$ increases, as is expected in indirect vector control.

Similar studies have been conducted for $R_{s,1}$ as well. $R_{s,1}$ is utilised in the voltage model of machine-1 to estimate $\tilde{\omega}_m$ which is added as a feedforward term in the PLL. The value of $R_{s,1}$ used in the control program is reduced to 0.5 times of its nominal value. The response of the drive under such a situation is shown in Fig. 5.24. It can be clearly seen from the figure that the impact of such a variation is insignificant in performance of both the speed estimation technique and overall dynamic performance of the drive.

As stated earlier, the stator resistance of machine 2, $R_{s,2}$ is not used in the control algorithm. Thus, only the rotor resistance of machine 2, $R_{r,2}$ is varied and its impact is studied experimentally. Similar to the other parameters, $R_{r,2}$ is varied to 0.5 times its nominal value in the control algorithm and the performance of the drive is shown in Fig. 5.25. The performance of the speed estimation scheme is satisfactory even with the variation as can be seen in the figure.

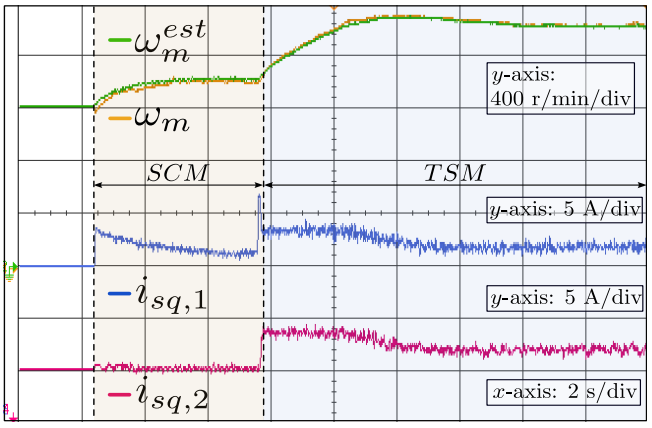


FIGURE 5.25: Performance of the drive with 100% variation in $R_{r,2}$

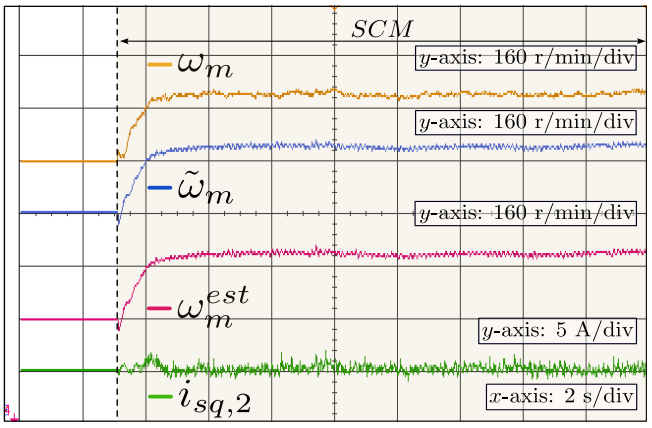


FIGURE 5.26: Accuracy in speed estimation with $\omega_o = 2$ Hz.

5.5.7 Impact of LPF Cutoff Frequency, ω_o on Drive Performance

It has been stated earlier that the operating speed of the drive is incorrectly estimated ($\tilde{\omega}_m$) using the voltage model of machine 1 and added to the PLL as a feedforward term. This involves a low-pass filter with a cutoff frequency ω_o which is kept at $2\pi 5$ rad/s in the present work. Keeping a lower value of ω_o improves the accuracy of $\tilde{\omega}_m$ but makes it more susceptible to practical issues like offset in current measurement. The performance of the drive with $\omega_o = 2\pi 2$ rad/s is shown in Fig. 5.26. For a speed command of 200 r/min, $\tilde{\omega}_m$ seems to be actually following the measured speed, ω_m. Thus, the accuracy of $\tilde{\omega}_m$ itself is very good.

However, with such a low value of ω_o, any offset in the measured current can

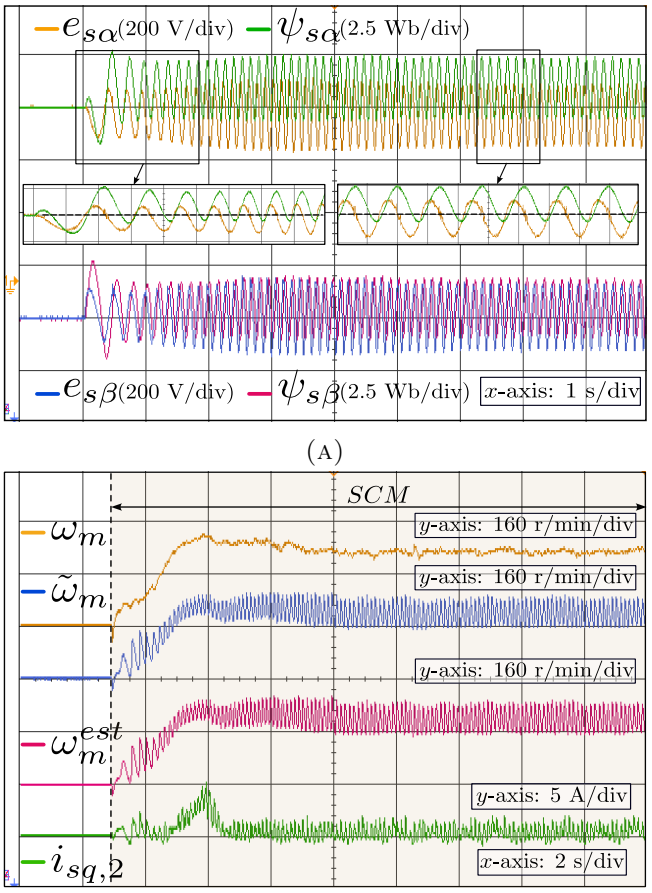


FIGURE 5.27: Performance of the drive with $\omega_o = 2$ Hz with offset in R-phase current

lead to error in flux estimation and impact the performance of the drive. In order to validate this, a small offset of 0.05 pu is added to the measured current of R-phase in machine 1. The response of the drive in terms of estimated flux and speed is shown in Fig. 5.27. A clear offset can be seen in the estimated $\psi_{s\alpha}$ in Fig. 5.27a. The offset can be seen to be present even in steady-state. This is translated into a sustained oscillation in $\tilde{\omega}_m$ and ω_m^{est} as seen in Fig. 5.27b.

The drive is operated with the same value of offset in R-phase current with $\omega_o = 10\pi$ rad/s. The response of the drive in terms of estimated flux and speed is shown in Fig. 5.28. It can be seen in Fig. 5.28a, that the offset in $\psi_{s\alpha}$ slowly decays down with negligible offset in steady-sate. The oscillations in $\tilde{\omega}_m$ and ω_m^{est} are also reduced as shown in Fig. 5.28b.

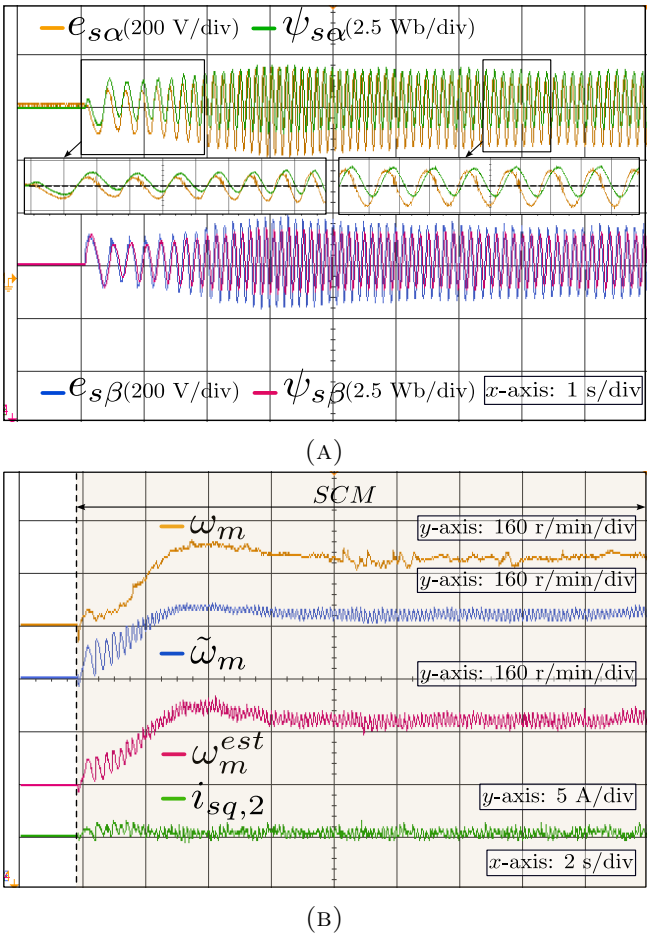


FIGURE 5.28: Performance of the drive with $\omega_o = 5$ Hz with offset in R-phase current

Further, the performance of the PLL without $\tilde{\omega}_m$ as the feedforward term is shown in Fig. 5.29. For a speed command of 400 r/min, the PLL is unable to track the speed which increases in a ramp manner. Thus, it is clear that adding this feedforward term is crucial for satisfactory performance of PLL.

5.5.8 Experimental validation of torque sharing strategy

The torque sharing strategy developed in the chapter is experimentally validated by gradually loading the dual-motor drive at rated speed. This is shown in Fig. 5.30. In the first case, the torque is shared equally between the two motors which is optimal for the dual-motor drive under consideration as shown in Fig. 5.30a. Then, in the next case, an unequal sharing (60-40 percentage) of load torque between the two motors is done. This is shown in Fig. 5.30b. The total copper loss, $P_{loss,tot}^{Cu}$ is

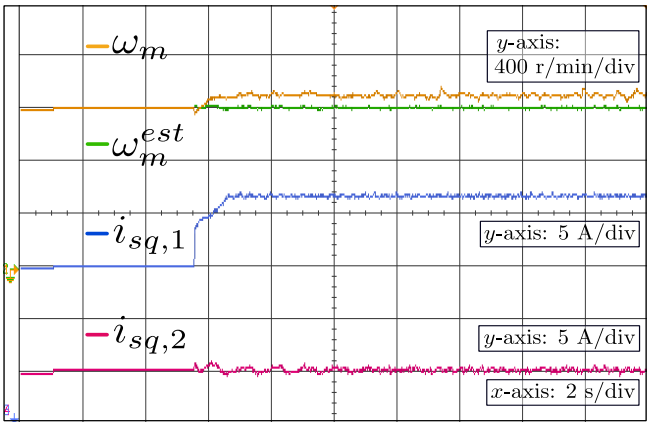


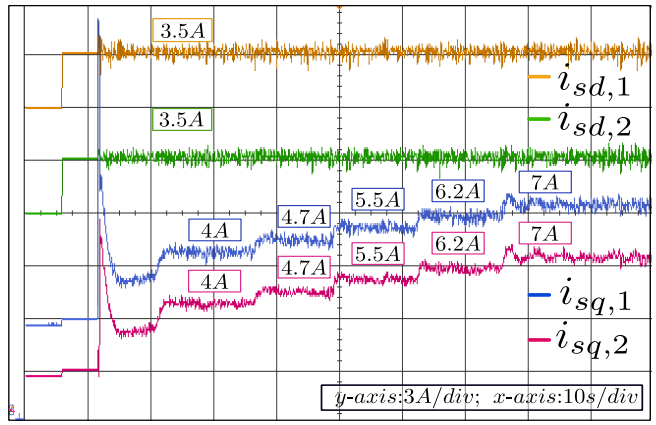
FIGURE 5.29: Performance of the PLL without $\tilde{\omega}_m$ as feedforward

estimated using (5.28) in both the cases and plotted in Fig. 5.30c. It can be clearly seen that the copper loss for equal sharing of load torque is less than the unequal sharing for all operating points. This establishes that the copper loss is reduced when the load-torque is shared in the ratio obtained in the chapter as opposed to when the ratio is kept arbitrary.

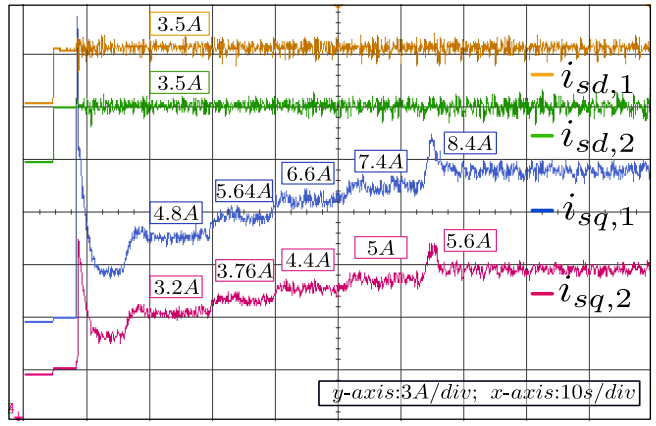
5.5.9 Simulation based validation

Some simulation (MATLAB/Simulink) based validation of the proposed algorithm under extreme conditions has also been done to to test the limit of the proposed estimation method without damaging the hardware setup. The results are presented in Fig.5.31.

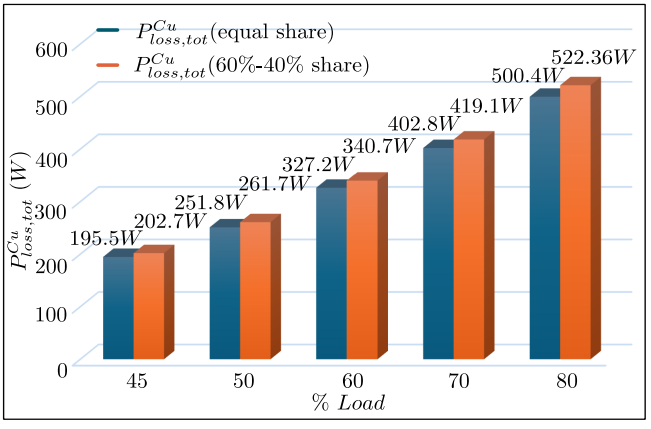
First the simulation result pertaining to the performance of the conventional sensorless method at low speed is shown in Fig.5.31a. The conventional method is not effective to estimate the speed of the drive at low speed range. Then the speed of the drive is ramped up and down at much faster space in Fig.5.31b. It can be seen in the figure that during deceleration, the performance of the speed controller is poor. However, the estimated speed closely tracks the actual speed. Finally, instead of using the inaccurately estimated speed from the open-loop estimator to augment the output of the PLL, the reference speed can also be added to augment the output the PLL because in case the reference, if increased in a slow ramp manner closely tracks the actual speed. However, in extreme cases, such as when a step change is



(A)



(B)



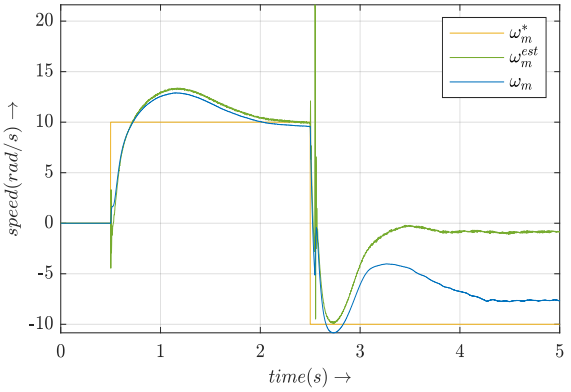
(C)

FIGURE 5.30: Experimentally obtained $i_{sd,1}$, $i_{sd,2}$, $i_{sq,1}$ and $i_{sq,2}$ for (a) equal and (b) unequal sharing of torque as the load is increased sequentially. (c) Estimated copper loss using (5.28) for both the cases.

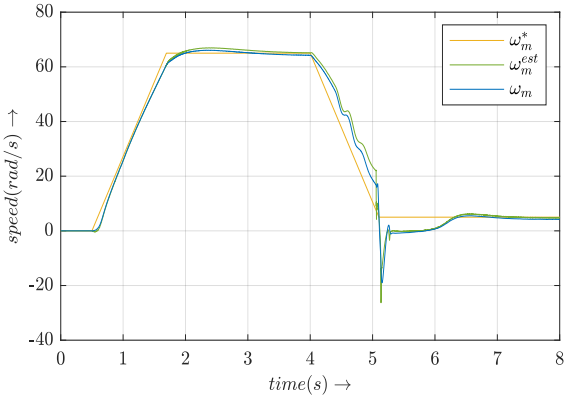
given, the reference speed and actual speed may not necessarily remain close to each to other and thus the reference speed cannot be used to augment the output of PLL. This condition is simulated and results are shown in Fig.5.31c. As expected, the performance of the drive is severely impacted in this case.

5.6 Conclusion

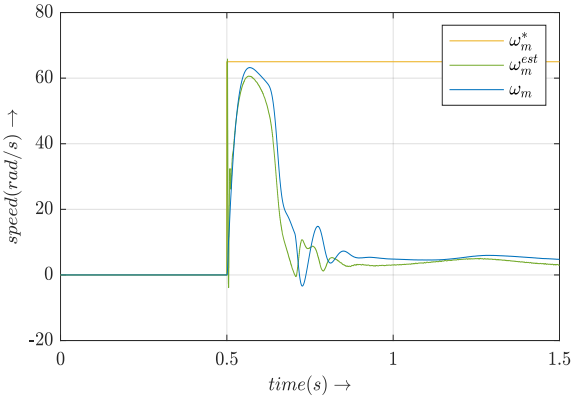
A speed sensorless vector control scheme is proposed for a multi-induction motor drive for applications wherein the torque demand from the drive is low at lower speed. For such applications, atleast one of the motors in the multi-motor drive systems is not required to produce torque when the operating frequency is low. A phase-locked loop (PLL) based on the stator current of the non-torque producing machine is used to estimate the speed of the drive. The performance of the PLL is enhanced by adding a factor, $\tilde{\omega}_m$, as a feedforward term. $\tilde{\omega}_m$ is basically the speed of the drive estimated from the voltage model of the torque producing motor. As the operating frequency increases, accuracy of $\tilde{\omega}_m$ improves. Thus, beyond a specific value of operating frequency, ω_c, the PLL is no longer required. As the operating frequency exceeds ω_c, all the motors can contribute to meet the torque demand from the load. Thus, based on this, the operation of the drive can be divided into two modes- speed correction mode (SCM) and torque sharing mode (TSM). Detailed analysis regarding the design of the PLL and impact of variation in machine parameters on the performance of the speed-estimation scheme has been done in this present work. Further, a torque sharing strategy for a dual-motor drive system for reduced copper loss has been developed. Finally, the proposed speed estimation algorithm is validated experimentally on a drive system consisting of two 3.7-kW induction motors coupled together. The performance of the drive during low-speed, during transition between SCM and TSM , under load dynamics and with variation in machine parameters and the torque sharing strategy have been studied experimentally. Although, the algorithm is developed and validated for a drive consisting of two induction motors coupled together to drive a common load, the same can be easily extended to a multi-induction motor drive system.



(A)



(B)



(C)

FIGURE 5.31: ω_m^*, ω_m^{est} and ω_m obtained through simulation to (a) validate the performance of conventional sensorless algorithm at low speed (b) to test the proposed algorithm with faster rates of change of speed (c) to test the performance of PLL with reference speed added to the output of PLL

Chapter 6

Conclusion and Future Scope

6.1 General

Various aspects of a high-power induction motor drive are investigated in this thesis. Three configurations of induction motor drives are considered in this thesis, namely, Y-connected SCIM drive, open-end winding induction motor drives and multi-induction motor drives. For high-power application, the switching frequency of the voltage source inverter is kept low. This is done to curb the switching energy losses occurring in the drive. Synchronous pulse-width modulation techniques are employed for such cases. For a Y-connected SCIM drive, the transition from $P = 9$ to $P = 3$ was first investigated. It was found that under closed-loop control, such transition made the operation of the drive unstable. Thus, a synchronous optimal hybrid PWM scheme is proposed. Along with that, a pulse transition strategy is also proposed which ensures smooth transition from one pulse number to the next. Next, a multi-carrier based synchronous sine-triangle PWM scheme is proposed for open-end winding induction motor drive which incorporates all triplen values of P along with odd non-triplen values of P also. Double-fourier series based analysis has been done to predict the harmonic profile of the resultant machine phase voltage and current. Next, a PWM strategy for OWIM drive is proposed wherein dissimilar carrier signals have been utilised for the two inverters in the OWIM drive. Finally, a PLL based technique is developed for a multi-induction motor drive which results in improved low-speed operation of the drive.

6.2 Major Conclusions

1. For a SCIM drive, operation with non triplen values of P, such as $P = 7$ and $P = 5$ is not feasible with simple SST PWM scheme. A combination of SST PWM and SO PWM works best for such a drive. For higher values of P, SST PWM is employed whereas for lower values of P, SO PWM is implemented.

2. The transients observed in the current during pulse pattern transition arise mainly due to the mismatch in the instantaneous current vector for the incoming and outgoing pulse patter. If the transition is ensured to happen at an instant where the current vector for the incoming and outgoing pulse pattern match, the transients will be diminished.

3. Since the stator current is difficult to estimate, matching of stator-flux trajectory based pulse transition strategy also gives satisfactory performance.

4. In the present structure of traction drives in Indian Railways, two single phase active front-end converters are present. On the AC side, these converters are connected to the grid through a three-winding transformer. Thus, essentially, on the DC side they can be considered two isolated DC sources. Thus, it concluded in this thesis, that, double-inverter fed open-end winding induction motor drive is very suitable choice for this application. Thus, OWIM based modified railway traction drive has been proposed in this thesis.

5. Further, a multi-carrier based SST PWM technique has been proposed for a double inverter fed OWIM drive which incorporates all triplen values of P and odd non-triplen values of P. It was shown analytically that for such drives, all conditions of the waveform symmetry are maintained in the machine phase-voltage for even triplen values of P and odd non-triplen values of P, along with odd triplen values of P.

6. The two VSIs present in the OWIM can operate independent of each other. It was mathematically shown that, for maximum DC bus utilisation, the phase-shift between the modulating signals of the two VSIs should be kept at π. However, the phase-shift between the carrier signals of the two VSIs has no impact on the fundamental component of the phase-voltage. Thus, this parameter can be utilised to achieve some other objective.

7. For odd triplen values of P, the phase shift between the triangular carriers of the two VSIs has been optimized in order to improve the harmonic performance of the OWIM drive. This is done using a double fourier series based mathematical

framework.

8. For even triplen values of P, it is proposed in this thesis that the two VSIs can be operated at different values of P. They can be mainatined at two consecutive odd triplen values and the resultant average pulse number will be a even triplen integer. Thus, a SST PWM scheme for OWIM drives is proposed where dissimilar carrier signals are utilised to operate the drive at all triplen values of P.

9. Another configuration of high-power drive, which is multi-induction motor drive is considered next. It is observed that for particular loads like fans and pumps, all the motors in a MMDS are not required to produce torque at low speed. The non-torque producing motor just rotates to maintain its flux. Under such situation, it has been shown, in the present thesis, that the stator current vector of the non torque producing motor aligns with the rotor reference frame. Thus, a PLL designed to obtain the angle and phase information of the stator current would also give the information pertaining rotor speed. Thus, a speed sensorless control algorithm has been developed for a IM based MMDS.

6.3 Future Scope

PWM techniques and control methodologies for three configurations of induction motor drives, namely, Y-connected SCIM drive, OWIM drive and multi-induction motor drives have been discussed in this thesis. The possibility of further research exist in this area. Some of areas that can be explored in future work are

1. The closed-loop control technique employed for SCIM drives while operating with SST and SOH PWM techniques were sensored field-oriented control. The sensorless control algorithm developed for the MMDS worked well with switching frequency at 1.5kHz. Challenges associated with speed-sensorless control algorithms at low switching frequency, ($f_{sw} \leq 500Hz$) can be investigated and suitable solutions can be proposed.

2. Applicability of Direct torque and flux control for induction motors under low f_{sw} can be explored.
3. Control aspects like field-weakening control with low f_{sw} of the VSI can be studied further.
4. Optimal PWM techniques for OWIM drives can be explored further.
5. The impact of non-linearities on the performance of the PLL for speed estimation of induction motor drives and the design of the PLL using geometric large signal stability based concepts can be explored.
6. Total loss minimization in multi-induction motor by considering the core-losses and using a Lagrangian formulation can be explored.

Bibliography

[1] A. Tripathi and G. Narayanan, "Investigations on optimal pulse width modulation to minimize total harmonic distortion in the line current," *IEEE Transactions on Industry Applications*, vol. 53, no. 1, pp. 212–221, 2017.

[2] D. G. Holmes, B. P. McGrath, and S. G. Parker, "Current regulation strategies for vector-controlled induction motor drives," *IEEE Transactions on Industrial Electronics*, vol. 59, no. 10, pp. 3680–3689, 2012.

[3] H. Swami and A. K. Jain, "A novel e/f controller for squirrel cage induction motor based on rotor flux orientation," *IEEE Journal of Emerging and Selected Topics in Industrial Electronics*, vol. 6, no. 2, pp. 643–653, 2025.

[4] S. Kouro, M. Malinowski, K. Gopakumar, J. Pou, L. G. Franquelo, B. Wu, J. Rodriguez, M. A. Pérez, and J. I. Leon, "Recent advances and industrial applications of multilevel converters," *IEEE Transactions on Industrial Electronics*, vol. 57, no. 8, pp. 2553–2580, 2010.

[5] A. Nabae, I. Takahashi, and H. Akagi, "A new neutral-point-clamped pwm inverter," *IEEE Transactions on Industry Applications*, vol. IA-17, no. 5, pp. 518–523, 1981.

[6] T. Meynard and H. Foch, "Multi-level conversion: high voltage choppers and voltage-source inverters," in *PESC '92 Record. 23rd Annual IEEE Power Electronics Specialists Conference*, pp. 397–403 vol.1, 1992.

[7] F. Z. Peng, "A generalized multilevel inverter topology with self voltage balancing," *IEEE Transactions on Industry Applications*, vol. 37, no. 2, pp. 611–618, 2001.

[8] A. Lesnicar and R. Marquardt, "An innovative modular multilevel converter topology suitable for a wide power range," in *2003 IEEE Bologna Power Tech Conference Proceedings,*, vol. 3, pp. 6 pp. Vol.3–, 2003.

[9] K. Mohapatra, K. Gopakumar, V. Somasekhar, and L. Umanand, "A harmonic elimination and suppression scheme for an open-end winding induction motor

drive," *IEEE Trans. on Ind. Electron.*, vol. 50, no. 6, pp. 1187–1198, 2003.

[10] M. Baiju, K. Mohapatra, R. Kanchan, and K. Gopakumar, "A dual two-level inverter scheme with common mode voltage elimination for an induction motor drive," *IEEE Trans. on Power Electron.*, vol. 19, no. 3, pp. 794–805, 2004.

[11] A. Amerise, M. Mengoni, L. Vancini, G. Rizzoli, L. Zarri, and A. Tani, "Overmodulation strategies for an open-end winding induction motor drive with a floating capacitor bridge," *IEEE Trans. on Ind. Electron.*, pp. 1–10, 2022.

[12] S. Pramanick, N. A. Azeez, R. Sudharshan Kaarthik, K. Gopakumar, and C. Cecati, "Low-order harmonic suppression for open-end winding im with dodecagonal space vector using a single dc-link supply," *IEEE Trans. on Ind. Electron.*, vol. 62, no. 9, pp. 5340–5347, 2015.

[13] A. Edpuganti and A. K. Rathore, "New optimal pulsewidth modulation for single dc-link dual-inverter fed open-end stator winding induction motor drive," *IEEE Trans. on Power Electron.*, vol. 30, no. 8, pp. 4386–4393, 2015.

[14] A. Edpuganti and A. K. Rathore, "Optimal pulsewidth modulation for common-mode voltage elimination scheme of medium-voltage modular multilevel converter-fed open-end stator winding induction motor drives," *IEEE Trans. on Ind. Electron.*, vol. 64, no. 1, pp. 848–856, 2017.

[15] K. Lee and Y. Han, "Simple discontinuous pulse-width modulation scheme for the loss reduction of a dual inverter fed an open-end winding induction motor," *IEEE Trans. on Energy Conv.*, pp. 1–12, 2022.

[16] G. Poddar and V. Ranganathan, "Sensorless field-oriented control for double-inverter-fed wound-rotor induction motor drive," *IEEE Transactions on Industrial Electronics*, vol. 51, no. 5, pp. 1089–1096, 2004.

[17] G. Poddar and V. Ranganathan, "Direct torque and frequency control of double-inverter-fed slip-ring induction motor drive," *IEEE Transactions on Industrial Electronics*, vol. 51, no. 6, pp. 1329–1337, 2004.

[18] N. K. Bajjuri and A. K. Jain, "Mathematical modeling and current-oriented

control of double-inverter-fed wound rotor im emulated as two virtual cage rotor ims," *IEEE Transactions on Industrial Electronics*, vol. 68, no. 11, pp. 10 488–10 497, 2021.

[19] N. K. Bajjuri and A. K. Jain, "An improved dual dtc of double-inverter-fed wrim drive with reduced torque ripple by emulating equivalent 3l npc vsc," *IEEE Transactions on Industrial Electronics*, vol. 69, no. 6, 2022.

[20] C. Jain, N. Vaishnav, and A. K. Jain, "Mtpa control of double inverter fed wound rotor induction motor drive," *IEEE Transactions on Energy Conversion*, vol. 38, no. 4, pp. 2326–2343, 2023.

[21] A. Verma and A. K. Jain, "A dual-vsi dfig-dc voltage generation system based on series connected dc-link," *IEEE Transactions on Industrial Electronics*, vol. 71, no. 11, pp. 13 670–13 681, 2024.

[22] G. Esfandiari, M. Ebrahimi, A. Tabesh, and M. Esmaeilzadeh, "Dynamic modeling and analysis of cascaded dfims in an arbitrary reference frame," *IEEE Transactions on Energy Conversion*, vol. 30, no. 3, pp. 999–1007, 2015.

[23] M. E. Achkar, R. Mbayed, G. Salloum, N. Patin, and E. Monmasson, "Voltage control of a stand-alone cascaded doubly fed induction generator," *IEEE Transactions on Industrial Electronics*, vol. 66, no. 1, pp. 762–771, 2019.

[24] C. Gong, Y. R. Li, and N. R. Zargari, "An overview of advancements in multimotor drives: Structural diversity, advanced control, specific technical challenges, and solutions," *Proc. IEEE*, vol. 112, no. 3, pp. 184–209, 2024.

[25] M. Mengoni, A. Tani, L. Zarri, G. Serra, and D. Casadei, "Position control of a multi-motor drive based on series-connected five-phase tubular pm actuators," *IEEE Transactions on Industry Applications*, vol. 48, no. 6, pp. 2048–2058, 2012.

[26] E. Levi, M. Jones, S. Vukosavic, and H. Toliyat, "A novel concept of a multiphase, multimotor vector controlled drive system supplied from a single voltage source inverter," *IEEE Transactions on Power Electronics*, vol. 19, no. 2, pp. 320–335, 2004.

[27] A. Birda, J. Reuss, and C. M. Hackl, "Simple fundamental current estimation and smooth transition between synchronous optimal pwm and asynchronous svm," *IEEE Trans. on Ind. Electron.*, vol. 67, no. 8, pp. 6354–6364, 2020.

[28] A. Edpuganti and A. K. Rathore, "A survey of low switching frequency modulation techniques for medium-voltage multilevel converters," *IEEE Trans. on Ind. Appl.*, vol. 51, no. 5, pp. 4212–4228, 2015.

[29] L. Xiao, J. Li, Y. Xiong, J. Chen, and H. Gao, "Strategy and implementation of harmonic-reduced synchronized svpwm for high-power traction machine drives," *IEEE Trans. on Power Electron*, vol. 35, no. 11, pp. 12 457–12 471, 2020.

[30] S. K. Sahoo and T. Bhattacharya, "Rotor flux-oriented control of induction motor with synchronized sinusoidal pwm for traction application," *IEEE Trans. on Power Electron.*, vol. 31, no. 6, pp. 4429–4439, 2016.

[31] N. Oikonomou and J. Holtz, "Closed-loop control of medium-voltage drives operated with synchronous optimal pulsewidth modulation," *IEEE Trans. on Ind. Appl.*, vol. 44, no. 1, pp. 115–123, 2008.

[32] A. Tripathi and G. Narayanan, "Evaluation and minimization of low-order harmonic torque in low-switching-frequency inverter-fed induction motor drives," *IEEE Trans. on Ind. Appl.*, vol. 52, no. 2, pp. 1477–1488, 2016.

[33] A. Tripathi and G. Narayanan, "Analytical evaluation and reduction of torque harmonics in induction motor drives operated at low pulse numbers," *IEEE Trans. on Ind. Electron.*, vol. 66, no. 2, pp. 967–976, 2019.

[34] J.-S. Kim, D.-H. Kim, J.-H. Lee, and J.-S. Lee, "Smooth pulse number transition strategy considering time delay in synchronized svpwm," *IEEE Trans. on Power Electron.*, vol. 38, no. 2, pp. 2252–2261, 2023.

[35] H. Yang, Y. Zhang, G. Yuan, P. D. Walker, and N. Zhang, "Hybrid synchronized pwm schemes for closed-loop current control of high-power motor drives," *IEEE Trans. on Ind. Electron.*, vol. 64, no. 9, pp. 6920–6929, 2017.

[36] X. Wu, W. Huang, and C. Huang, "Flux trajectory tracking based implementation of synchronized space vector modulation for induction motors," *IEEE Trans. on Ind. Electron.*, vol. 69, no. 7, pp. 6624–6634, 2022.

[37] G. Narayanan and V. Ranganathan, "Two novel synchronized bus-clamping pwm strategies based on space vector approach for high power drives," *IEEE Trans. on Power Electron.*, vol. 17, no. 1, pp. 84–93, 2002.

[38] H. Zhang, W. Liu, Z. Chen, and N. Jiao, "Smooth transition of multimode synchronous modulation for ipmsm sensorless drives in rail-transit applications," *IEEE Trans. on Ind. Electron.*, vol. 68, no. 1, pp. 128–138, 2021.

[39] A. M. Alcaide, H. Yan, X. Wang, J. I. Leon, R. Portillo, G. Buticchi, S. Vazquez, V. G. Monopoli, M. Liserre, and L. G. Franquelo, "Common-mode voltage mitigation technique in motor drive applications by applying a sampling-time adaptive multi-carrier pwm method," *IEEE Access*, vol. 9, pp. 56 115–56 126, 2021.

[40] A. M. Alcaide, V. G. Monopoli, E. Zafra, G. Buticchi, J. I. Leon, S. Vazquez, M. Liserre, and L. G. Franquelo, "Generalized multicarrier pwm technique for two-level voltage source inverters," *IEEE Transactions on Industrial Electronics*, vol. 70, no. 5, pp. 4345–4355, 2023.

[41] L. Carbone, M. Marchesoni, M. Passalacqua, G. Postiglione, L. Vaccaro, and C. Vitaloni, "Sensorless control of medium voltage induction motor with lc filter and long cable in oil pump applications," *IEEE Transactions on Energy Conversion*, pp. 1–12, 2024.

[42] G.-J. Jo and J.-W. Choi, "Rotor flux estimator design with offset extractor for sensorless-driven induction motors," *IEEE Transactions on Power Electronics*, vol. 37, no. 4, pp. 4497–4510, 2022.

[43] S. Mukherjee and G. Poddar, "Fast control of filter for sensorless vector control sqim drive with sinusoidal motor voltage," *IEEE Transactions on Industrial Electronics*, vol. 54, no. 5, pp. 2435–2442, 2007.

[44] K. Hurst, T. Habetler, G. Griva, and F. Profumo, "Zero-speed tacholess im torque control: simply a matter of stator voltage integration," *IEEE Transactions on Industry Applications*, vol. 34, no. 4, pp. 790–795, 1998.

[45] J. Hu and B. Wu, "New integration algorithms for estimating motor flux over a wide speed range," *IEEE Transactions on Power Electronics*, vol. 13, no. 5, pp. 969–977, 1998.

[46] J. Holtz, "Sensorless control of induction machines - with or without signal injection?" *IEEE Transactions on Industrial Electronics*, vol. 53, no. 1, pp. 7–30, 2006.

[47] M. K. Metwaly, N. I. Elkalashy, M. S. Zaky, and T. M. Wolbank, "Slotting saliency extraction for sensorless torque control of standard induction machines," *IEEE Transactions on Energy Conversion*, vol. 33, no. 1, pp. 68–77, 2018.

[48] R. Raute, C. Caruana, C. S. Staines, J. Cilia, M. Sumner, and G. M. Asher, "Sensorless control of induction machines at low and zero speed by using pwm harmonics for rotor-bar slotting detection," *IEEE Transactions on Industry Applications*, vol. 46, no. 5, pp. 1989–1998, 2010.

[49] L. Harnefors and M. Hinkkanen, "Complete stability of reduced-order and full-order observers for sensorless im drives," *IEEE Transactions on Industrial Electronics*, vol. 55, no. 3, pp. 1319–1329, 2008.

[50] S. Maiti, C. Chakraborty, Y. Hori, and M. C. Ta, "Model reference adaptive controller-based rotor resistance and speed estimation techniques for vector controlled induction motor drive utilizing reactive power," *IEEE Transactions on Industrial Electronics*, vol. 55, no. 2, pp. 594–601, 2008.

[51] H. Wang, Y. Yang, X. Ge, Y. Zuo, Y. Yue, and S. Li, "Pll- and fll-based speed estimation schemes for speed-sensorless control of induction motor drives: Review and new attempts," *IEEE Transactions on Power Electronics*, vol. 37, no. 3, pp. 3334–3356, 2022.

[52] R. Zhao, Z. Xin, P. C. Loh, and F. Blaabjerg, "A novel flux estimator based

on multiple second-order generalized integrators and frequency-locked loop for induction motor drives," *IEEE Transactions on Power Electronics*, vol. 32, no. 8, pp. 6286–6296, 2017.

[53] L. Zhao, J. Huang, J. Chen, and M. Ye, "A parallel speed and rotor time constant identification scheme for indirect field oriented induction motor drives," *IEEE Transactions on Power Electronics*, vol. 31, no. 9, pp. 6494–6503, 2016.

[54] J. Chen and J. Huang, "Stable simultaneous stator and rotor resistances identification for speed sensorless im drives: Review and new results," *IEEE Transactions on Power Electronics*, vol. 33, no. 10, pp. 8695–8709, 2018.

[55] J. Chen and J. Huang, "Globally stable speed-adaptive observer with auxiliary states for sensorless induction motor drives," *IEEE Transactions on Power Electronics*, vol. 34, no. 1, pp. 33–39, 2019.

[56] M. Hinkkanen, L. Harnefors, and J. Luomi, "Reduced-order flux observers with stator-resistance adaptation for speed-sensorless induction motor drives," *IEEE Transactions on Power Electronics*, vol. 25, no. 5, pp. 1173–1183, 2010.

[57] A. N. Smith, S. M. Gadoue, and J. W. Finch, "Improved rotor flux estimation at low speeds for torque mras-based sensorless induction motor drives," *IEEE Transactions on Energy Conversion*, vol. 31, no. 1, pp. 270–282, 2016.

[58] S. M. Gadoue, D. Giaouris, and J. W. Finch, "Mras sensorless vector control of an induction motor using new sliding-mode and fuzzy-logic adaptation mechanisms," *IEEE Transactions on Energy Conversion*, vol. 25, no. 2, pp. 394–402, 2010.

[59] M. S. Zaky, M. K. Metwaly, H. Z. Azazi, and S. A. Deraz, "A new adaptive smo for speed estimation of sensorless induction motor drives at zero and very low frequencies," *IEEE Transactions on Industrial Electronics*, vol. 65, no. 9, pp. 6901–6911, 2018.

[60] Z. Yin, G. Li, Y. Zhang, J. Liu, X. Sun, and Y. Zhong, "A speed and flux observer of induction motor based on extended kalman filter and markov chain," *IEEE Transactions on Power Electronics*, vol. 32, no. 9, pp. 7096–7117, 2017.

[61] C. Caruana, G. Asher, and M. Sumner, "Performance of hf signal injection techniques for zero-low-frequency vector control of induction machines under sensorless conditions," *IEEE Transactions on Industrial Electronics*, vol. 53, no. 1, pp. 225–238, 2006.

[62] V. V. Reddy, N. Aarzoo, G. Poddar, and S. Sau, "Improved sensorless operation of double inverter fed wound rotor induction machine with seamless mode transitions," *IEEE Transactions on Industrial Electronics*, vol. 70, no. 11, pp. 11 078–11 086, 2023.

[63] R. Cardenas, R. Pena, J. Proboste, G. Asher, and J. Clare, "Mras observer for sensorless control of standalone doubly fed induction generators," *IEEE Transactions on Energy Conversion*, vol. 20, no. 4, pp. 710–718, 2005.

[64] S. Yang, X. Sun, M. Ma, X. Zhang, and L. Chang, "Fault detection and identification scheme for dual-inverter fed oewim drive," *IEEE Transactions on Industrial Electronics*, vol. 67, no. 7, pp. 6112–6123, 2020.

[65] H. Liu, Y. Yan, F. Bu, W. Huang, W. Jiang, Y. Tan, and Z. Qian, "Sensorless control with adaptive speed observer using power winding information for dual-stator winding induction starter/generator," *IEEE Transactions on Industrial Electronics*, vol. 71, no. 2, pp. 1388–1398, 2024.

[66] *Final Draft technical specification for upgradation of WAG9H locomotive.* ELECTRICAL DIRECTORATE,RDSO,Ministry of Railways, Government of India, Apr. 2017.

[67] J. Holtz, "Advanced pwm and predictive control-an overview," *IEEE Transactions on Industrial Electronics*, vol. 63, no. 6, pp. 3837–3844, 2016.

[68] X. Qi and J. Holtz, "Modeling and control of low switching frequency high-performance induction motor drives," *IEEE Transactions on Industrial Electronics*, vol. 67, no. 6, pp. 4402–4410, 2020.

[69] Y. Xu, C. Morito, and R. D. Lorenz, "Accurate discrete-time modeling for improved torque control accuracy for induction machine drives at very low

sampling-to-fundamental frequency ratios," *IEEE Transactions on Transportation Electrification*, vol. 6, no. 2, pp. 668–678, 2020.

[70] K. He, J. Li, L. Xiao, Y. Lu, L. Wu, and H. Chen, "Synchronous optimal pwm with continuous switching-to-fundamental frequency ratio," *IEEE Journal of Emerging and Selected Topics in Power Electronics*, vol. 11, no. 2, pp. 1466–1476, 2023.

[71] J. Holtz and X. Qi, "Optimal control of medium voltage drive- an overview," *IEEE Transactions on Industrial Electronics*, vol. 60, no. 12, pp. 5472–5481, 2013.

[72] A. Karuvaril Vijayan, D. Xiao, B. Nahid-Mobarakeh, and A. Emadi, "Synchronous optimal pulsewidth modulation for high-power ac motor drives: A review," *IEEE Transactions on Transportation Electrification*, vol. 10, no. 2, pp. 3976–3990, 2024.

[73] V. Kumar, A. Tripathi, and G. Narayanan, "Experimental determination of mechanical parameters in sensorless vector-controlled induction motor drive," *Sadhana*, pp. 1285–1297, 12 2017.

[74] G. Narayanan and V. Ranganathan, "Analytical evaluation of harmonic distortion in pwm ac drives using the notion of stator flux ripple," *IEEE Transactions on Power Electronics*, vol. 20, no. 2, pp. 466–474, 2005.

[75] P. Purgat, J. Gerber-Popovic, and P. Bauer, "Modularity in power electronics: Conceptualization, classification and outlook," in *IECON 2017 - 43rd Annual Conference of the IEEE Industrial Electronics Society*, pp. 1307–1312, 2017.

[76] A. B. Acharya, M. Ricco, D. Sera, R. Teoderscu, and L. E. Norum, "Performance analysis of medium-voltage grid integration of pv plant using modular multilevel converter," *IEEE Transactions on Energy Conversion*, vol. 34, no. 4, pp. 1731–1740, 2019.

[77] J. Pan, Z. Ke, M. Al Sabbagh, H. Li, K. A. Potty, W. Perdikakis, R. Na, J. Zhang, J. Wang, and L. Xu, "7-kv 1-mva sic-based modular multilevel converter

prototype for medium-voltage electric machine drives," *IEEE Transactions on Power Electronics*, vol. 35, no. 10, pp. 10 137–10 149, 2020.

[78] H. Patel, S. Bhawal, and K. Hatua, "Solid state transformer (sst) based high frequency mv propulsion drive with new modulation technique," *IEEE Transactions on Transportation Electrification*, pp. 1–1, 2025.

[79] N. Aarzoo and G. Poddar, "Sensorless control of wound field synchronous machine drive using current source-based modular multilevel converter," *IEEE Transactions on Industrial Electronics*, vol. 70, no. 11, pp. 10 946–10 956, 2023.

[80] S. Golestan, J. M. Guerrero, and J. C. Vasquez, "Three-phase plls: A review of recent advances," *IEEE Transactions on Power Electronics*, vol. 32, no. 3, pp. 1894–1907, 2017.

[81] S.-H. Kim and S.-K. Sul, "Maximum torque control of an induction machine in the field weakening region," *IEEE Transactions on Industry Applications*, vol. 31, no. 4, pp. 787–794, 1995.

[82] L. Xiao, J. Li, J. Chen, R. Qu, and Y. Xiong, "Synchronous svpwm for field-oriented control of pmsm using phase-lock loop," in *2017 IEEE Energy Conversion Congress and Exposition (ECCE)*, DOI 10.1109/ECCE.2017.8096745, pp. 4324–4331, 2017.

[83] M. Strop and D. Zimmer, "Intelligent operating strategy for an internal rubber mixer's multi-motor drive system based on artificial neural network," in *2016 IEEE 21st International Conference on Emerging Technologies and Factory Automation (ETFA)*, pp. 1–9, 2016.

[84] H. Stemmler and P. Guggenbach, "Configurations of high-power voltage source inverter drives," in *1993 Fifth European Conference on Power Electronics and Applications*, pp. 7–14 vol.5, 1993.

[85] J. Holtz and N. Oikonomou, "Synchronous optimal pulsewidth modulation and stator flux trajectory control for medium-voltage drives," *IEEE Trans. on Ind. Appl.*, vol. 43, no. 2, pp. 600–608, 2007.

[86] J. W. Kimball and M. Zawodniok, "Reducing common-mode voltage in three-phase sine-triangle pwm with interleaved carriers," *IEEE Transactions on Power Electronics*, vol. 26, no. 8, pp. 2229–2236, 2011.

[87] D. Zhang, D. Cittanti, P. Sun, J. Huber, R. I. Bojoi, and J. W. Kolar, "Detailed modeling and in-situ calorimetric verification of three-phase sparse npc converter power semiconductor losses," *IEEE Journal of Emerging and Selected Topics in Power Electronics*, vol. 11, no. 3, pp. 3409–3423, 2023.

[88] Y. Ali, M. Lashkevich, E. Stolyarov, A. Zharkov, E. Kulik, and A. Anuchin, "Nearly contant losses current regulation strategy for an open-end winding traction induction motor," in *2022 IEEE 1st Industrial Electronics Society Annual On-Line Conference (ONCON)*, pp. 1–5, 2022.

[89] G. Grandi, V. Oleschuk, and F. Dragonas, "Synchronized pwm control of asymmetrical dual-inverter fed open-end winding traction drive," in *2012 Electrical Systems for Aircraft, Railway and Ship Propulsion*, pp. 1–8, 2012.

[90] H. Matsumori, T. Kosaka, N. Matsui, and S. Saha, "Alternative pwm switching strategy implementation for a dual inverter fed open winding motor drive system for an electric vehicle application," *IEEE Transactions on Industry Applications*, vol. 59, no. 5, pp. 5957–5970, 2023.

[91] A. Guha and G. Narayanan, "Impact of dead time on inverter input current, dc-link dynamics, and light-load instability in rectifier-inverter-fed induction motor drives," *IEEE Transactions on Industry Applications*, vol. 54, no. 2, pp. 1414–1424, 2018.

Appendix A: Double Fourier Series

For naturally sampled PWM, the double-Fourier expansion for the pole voltages for a 2L-VSI is given by (1), where O is the reference point on the negative DC bus. Here, n and m are two integers which represent the order of harmonic frequency band due to the modulating signal and carrier signal respectively. Further, in (1), γ_β is the phase shift of the modulating signal of a particular phase with respect to the position zero-crossing of the m_R. Similarly, ϕ_β is the phase shift of the carrier signal with respect to the m_R. ϕ_β is taken to be zero when the positive zero crossing of m_R coincide with the positive peak of the carrier [40]. In case, the zero-crossing of the carrier signal and m_R coincide, ϕ_β becomes equal to $\frac{\pi}{2}$. ω_o and ω_c in (1) refer to angular frequency in electrical rad/s for the modulating signal and carrier signal respectively.

$$v_{\beta o}(t) = \frac{A_0^0}{2} + \sum_{m=0}^{\infty}\sum_{n=-\infty}^{\infty}\left(A_m^n cos\big(n(\omega_o t + \gamma_\beta) + m(\omega_c t + \phi_\beta)\big)\right), \beta \in \{R, Y, B, r, y, b\} \tag{1}$$

In case of SST PWM, ω_o and ω_c are related with pulse number P as $\omega_c = P * \omega_o$. Thus, considering this relation, (1) is simplified to (2).

$$v_{\beta o}(t) = \frac{A_0^0}{2} + \sum_{m=0}^{\infty}\sum_{n=-\infty}^{\infty}\left(A_m^n cos\big((mP+n)\omega_o t + n\gamma_\beta + m\phi_\beta\big)\right), \quad \beta \in \{R, Y, B, r, y, b\} \tag{2}$$

The coefficient A_m^n in (2) is given by (3) where J_n is the bessel function of first kind of order n.

$$A_m^n = \frac{2V_{dc}}{m\pi} J_n\left(\frac{m\pi}{2}M\right) sin\left(\frac{(m+n)\pi}{2}\right) \tag{3}$$

It can be seen from (2), a combination of (m, n, P) gives rise to k^{th} order harmonics in the pole voltages. Here, $k = mP + n$. The value of J_n in (3) becomes very small as both $|n|, |m| > 3$. Thus, the values of m, n only in the range of $-3 \leq m, n \leq 3$ leads to harmonics of significant magnitude in the pole voltages.

Further, it can be seen from (3) that the combination of (m, n) for which $m + n$ becomes an even integer, A_m^n becomes zero and the corresponding order to harmonics disappear from the inverter pole-voltages. Since, P is maintained as an odd integer,

it can be established that for any combination of (m, n) for which k is an even integer, the sum corresponding to $m + n$ will always be an even integer. Thus, even order harmonics are not present in the inverter-pole voltages. On the contrary, all odd order harmonics (triplen or non-triplen) are present in the inverter pole-voltages.

Appendix B: Controller Design

The design of the inner current controllers, namely, i_{sd} and i_{sq} and the outer speed controller is discussed in this Appendix. Both the inner and outer controllers have been designed according to the method presented in [73].

Design of Inner Current Controllers

With suitable feed-forward compensation, the induction motor can be considered as a simple $R-L$ circuit with the resistance being equal to R_s and inductance being σL_s, while designing the inner current loop. Thus, the transfer function of the motor can be written as

$$G_{IM}(s) = \frac{\frac{1}{R_s}}{1 + s\frac{\sigma L_s}{R_s}} \tag{4}$$

For applications where the switching frequency of the 2L-VSI is considerably high $(2-5kHz)$, the power converter can simply be modelled as as gain. However, for applications with reduced switching frequency, the delay caused by the 2L-VSI becomes significant to be considered in the design of the current controllers. The time delay of the inverter, T_d, is taken to be $\frac{3}{4}T_{sw}$ where T_{sw} is the complete switching period [73]. Thus, the transfer function pertaining to the 2L-VSI can be written as

$$G_{VSI}(s) = \frac{1}{1 + sT_d} \tag{5}$$

Generally, a PI controller is used for the inner current control loop. The transfer function of the same is given by,

$$G_C(s) = \frac{K_{ic}(1 + sT_{ic})}{sT_{ic}} \tag{6}$$

The control loop for the current controller is shown in Fig.1a. The time constant of the controller, T_{ic} is chosen such that the largest time constant in the control loop is cancelled.

$$T_{ic} = \frac{\sigma L_s}{R_s} \tag{7}$$

With such a choice, the closed-loop transfer function, for say d-axis current loop becomes

$$\frac{i^*_{sd}(s)}{i_{sd}(s)} = \frac{K_{ic}}{(s^2 + s\frac{1}{T_d} + \frac{K_ic}{R_s T_{ic} T_d})R_s T_{ic} T_d} = G_{ic}(s) \tag{8}$$

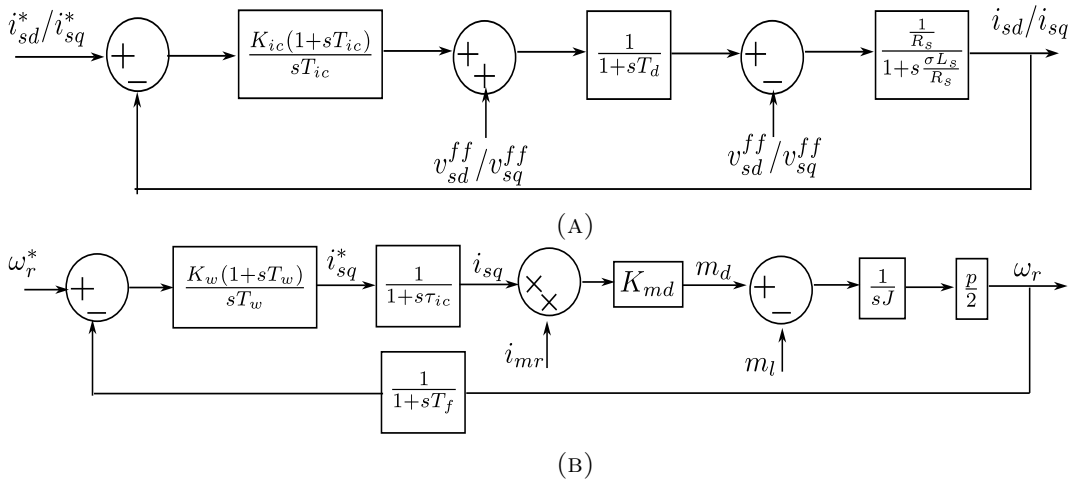


FIGURE 1: (A) Inner current control loop (B) Outer speed control loop

It is to be noted, that the transfers function becomes a second order transfer function with natural frequency ω_n and damping coefficient ζ given by

$$\omega_n = \sqrt{\frac{K_i c}{R_s T_{ic} T_d}} \tag{9}$$

$$2\zeta\omega_n = \frac{1}{T_d} \tag{10}$$

Further, the bandwidth of a second order system, ω_{bw} is related to ω_n and ζ as

$$\omega_{bw} = \omega_n \sqrt{[1 - 2\zeta^2] + \sqrt{1 + [1 - 2\zeta^2]^2}} \tag{11}$$

The value of ζ is chosen first to decide the value of K_{ic}, which is given by

$$K_{ic} = \frac{1}{4\zeta^2} \frac{R_s T_{ic}}{T_d} \tag{12}$$

Further, using the chosen value of ζ and K_{ic}, the natural frequency, ω_n and bandwidth of the system, ω_{bw} are calculated for the system. In most of the work presented in this thesis, the bandwidth of the current controller is kept low, in the range of 50-60 Hz. This is done because of reduced switching frequency constraint in the chosen applications.

Design of Outer Speed Controller

The outer speed loop is designed using the popular symmetric optimum method. The inner q-axis current loop is approximated using a first order transfer function, as,

$$\frac{i^*_{sd}(s)}{i_{sd}(s)} = G_{ic}(s) = \frac{1}{a + s\tau_{ic}} \quad \text{where} \quad \tau_{ic} = \frac{2\zeta}{\omega_n} = \frac{R_s T_{ic}}{K_{ic}} \tag{13}$$

The control loop is shown in Fig.1b. A low-pass filter with a time constant T_f is placed in the feed-back loop and K_{md} is a constant given by

$$K_{md} = \frac{2}{3}\frac{p}{2}\frac{L_m^2}{L_r} \tag{14}$$

The open-loop transfer function is given by

$$\frac{\omega_r^*(s)}{\omega_r(s)} = \frac{K_w}{T_w}\frac{1}{J}\frac{p}{2}K_{md}i_{mr}^*\frac{1}{s^2}\frac{1}{(1+sT_f)}\frac{(1_+sT_w)}{(1+s\tau_{ic})} \tag{15}$$

The gains K_w and T_w as decided using symmetric optimum method as described in [73]. The bandwidth of the speed controller is kept very low (1-2 Hz) because of the high-inertia of these high-power motor drives.

Appendix C: Experimental Setups and Parameters

Experimental setup and parameters of Y-connected SCIM Drive

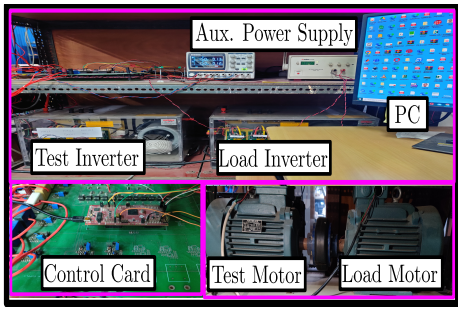


FIGURE 2: Experimental setup of Y-connected SCIM

TABLE 1: Machine parameters for Y-connected SCIM

		Simulation	Experiments
Rated Power	P_N	$850kW$	$3.7kW$
DC-Bus Votage	V_{dc}	$3600V$	$600V$
Rated Voltage	V_{rated}	$2200V$	$415V$
Rated Frequency	f_r	$65Hz$	$65Hz$
Pole Pairs	P	6	6
Stator Resistance	R_s	0.0727Ω	4.95Ω
Rotor Resistance	R_r	0.0693Ω	4.82Ω
Mutual Inductance	L_m	$0.03667H$	$0.55582H$
Stator Inductance	L_s	$0.037979H$	$0.58642H$
Rotor Inductance	L_r	$0.037945H$	$0.58642H$
Mechanical Inertia	J	$20kgm^2$	$0.2kgm^2$

Experimental setup and parameters of OWIM Drive

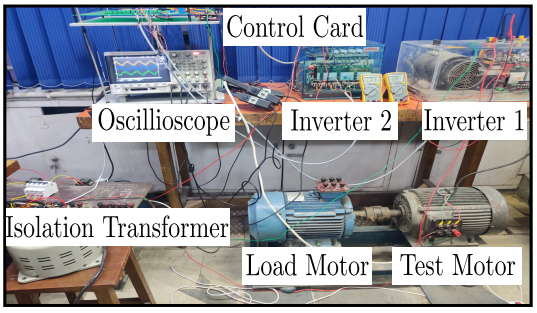


FIGURE 3: Experimental set-up for OWIM drive

TABLE 2: Machine parameters for OWIM Drive

		Simulation	Experiments
Rated Power	P_N	$850kW$	$7.5kW$
Rated Frequency	f_r	$65Hz$	$50Hz$
Stator Resistance	R_s	0.0727Ω	4.95Ω
Rotor Resistance	R_r	0.0693Ω	4.82Ω
Mutual Inductance	L_m	$0.03667H$	$0.55582H$
Stator Inductance	L_s	$0.037979H$	$0.58642H$
Rotor Inductance	L_r	$0.037945H$	$0.58642H$
Mechanical Inertia	J	$20kgm^2$	$0.2kgm^2$

Experimental setup and parameters of Multi-induction motor drive

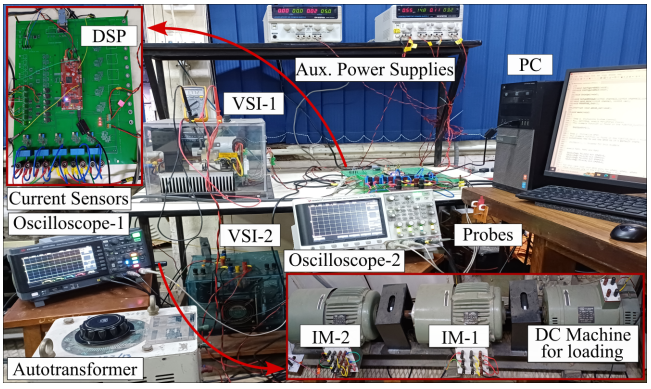


FIGURE 4: Experimental setup for MMDS

TABLE 3: Machine parameters for MMDS

		Motor 1	Motor 2
Rated Power	P_r	3.7 kW	3.7 kW
Rated Voltage	V_r	415 V	415 V
Rated current	I_r	7.2 A	7.2 A
Rated speed	ω_m	1440 r/min	1440 r/min
Rated Frequency	f_r	50 Hz	50 Hz
Poles	P	4	4
Stator Resistance	R_s	2 Ω	1.9 Ω
Rotor Resistance	R_r	2.9 Ω	2.8 Ω
Mutual Inductance	L_m	0.5761 H	0.54588 H
Stator Inductance	L_s	0.5952 H	0.56424 H
Rotor Inductance	L_r	0.5952 H	0.56424 H
Mechanical Inertia	J	$20kgm^2$	$0.2kgm^2$

List of Publications

• International Journals

- **S. Chaudhuri**, A. Tripathi and A. K. Jain, "OWIM Drive Operated With Synchronized PWM With Odd-Non-Triplen and All-Triplen Pulse Numbers for Railway Traction Application," in *IEEE Transactions on Industrial Electronics*, vol. 71, no. 9, pp. 10366-10376, Sept. 2024,
- **S. Chaudhuri**, P. Kumari, A. Tripathi and A. Kumar Jain, "Synchronous Optimal Hybrid PWM Technique With Smooth Pulse Pattern Transition Strategy for IM-Based High-Power Railway Traction Drive," in *IEEE Transactions on Transportation Electrification*, vol. 11, no. 6, pp. 13391-13403, Dec. 2025
- **S. Chaudhuri**, K. R. Gopan and A. K. Jain, "Sensorless Vector Controlled Multi-Induction Motor Drive using Stator-Current based Phase-Locked Loop for Pump Application," in *IEEE Transactions on Energy Conversion*,
- One work is under review in *IEEE Trans.*

• International Conferences

- **S. Chaudhuri**, A. Tripathi and A. K. Jain, "Impact of Orientation and Phase-shift in Carrier Signals on Line-Current Harmonics for an OWIM Drive Operated with Synchronous PWM," IECON 2024 - 50th Annual Conference of the IEEE Industrial Electronics Society, Chicago, IL, USA, 2024, pp. 1-6,
- K. R. Gopan, **S. Chaudhuri** and A. K. Jain, "Modelling and Torque Estimation of an Inverse Connected Cascaded WRIM in Rotor Reference Frame Operated with a Constant V/f Ratio," IECON 2024 - 50th Annual Conference of the IEEE Industrial Electronics Society, Chicago, IL, USA, 2024 **(Received SYPA travel Grant, Best Paper Presentation Award)**
- **S. Chaudhuri**, A. Tripathi and A. K. Jain, "Performance Evaluation

of IM Drive Operated with Synchronous Sine-Triangle PWM with Odd Non-Triplen Pulse Number," 2025 IEEE Energy Conversion Congress & Exposition Asia (ECCE-Asia), Bengaluru, India, 2025, pp. 1-6 **(Received SYPA travel Grant, Best Paper Presentation Award)**

– K. R. Gopan, **S. Chaudhuri** and A. K. Jain, "Dual-CPU DSP Based Implementation of Instantaneous Torque Ripple Estimation in Inverse Connected Cascaded WRIM," 2025 IEEE Energy Conversion Congress & Exposition Asia (ECCE-Asia), Bengaluru, India, 2025, pp. 1-6

– **S. Chaudhuri**, K. R. Gopan and A. Kumar Jain, "Torque-Sharing Strategy for Reduced Copper-Loss in a Vector-Controlled Dual-Induction Motor Drive," IECON 2025 – 51st Annual Conference of the IEEE Industrial Electronics Society, Madrid, Spain, 2025, pp. 1-6

Biography

Shayak Chaudhuri received his B.Tech in Electrical engineering from Delhi Technological University (2016) and M.Tech in Machine Drives and Power Electronics from IIT, Kharagpur (2019).

After finishing his Masters degree, he was working with Mercedes Benz Research and Development, India, Bangaluru. He has finished his PhD from the Department of Electrical Engineering, IIT, Delhi in the area of Electric Motor Drives. He is the recipient of the prestigious Prime Minister's Research Fellowship (PMRF). His research interests are high-power AC drives, high-power electronic converters and electrical machines.